

SYNTHESIS, EVALUATION OF FUNCTIONAL METHACRYLATES AND A  
COMPUTATIONAL APPROACH TO THE REACTIONS OF MOLECULES WITH  
BIOLOGICAL POTENTIAL

by

Sesil Çınar

B.S., Chemistry, Boğaziçi University, 2009

M.S., Chemistry, Boğaziçi University, 2011

Submitted to the Institute for Graduate Studies in  
Science and Engineering in partial fulfillment of  
the requirements for the degree of  
Doctor of Philosophy

Graduate Program in Chemistry

Boğaziçi University

2017

SYNTHESIS, EVALUATION OF FUNCTIONAL METHACRYLATES AND A  
COMPUTATIONAL APPROACH TO THE REACTIONS OF MOLECULES WITH  
BIOLOGICAL POTENTIAL

APPROVED BY:

Prof. Duygu Avcı Semiz .....  
(Thesis Supervisor)

Prof. Viktorya Aviyente .....  
(Thesis Co-supervisor)

Assoc. Prof. Şaron Çatak .....

Prof. Nilhan Kayaman Apohan .....

Prof. A. Neren Ökte .....

Prof. Nurcan Tüzün .....

DATE OF APPROVAL: 22.06.2017

## ACKNOWLEDGEMENTS

First I want to present my great appreciation to my thesis supervisor, Prof. Viktorya Aviyente for her continuous support, motivation, help, patience and grace. She has guided and encouraged me throughout my graduate years both academically and socially. I would also like to thank my second supervisor, Prof. Duygu Avcı Semiz for giving the opportunity to study with her and enlarge my vision with her guidance and understanding. I always feel lucky for being their student, I have learnt a lot from them.

I also wish to appreciate to my examining committee, Assoc. Prof. Şaron Çatak (Boğaziçi University) for her valuable advices, contributions and friendship, Prof. Nurcan Tüzün (İstanbul Technical University) and Prof. Nilhan Kayaman Apohan (Marmara University) for their helpful comments and Prof. A. Neren Ökte (Boğaziçi University) for her encouragement and support.

I acknowledge the TÜBİTAK BİDEB graduate student scholarship for the financial support and TÜBİTAK ULAKBİM High Performance Computing Center as well as the Istanbul Technical University National Center for High Performance Computing-UHEM (Project number- 5004052016) for computational resources. Finally, I also want to thank to Bogazici University Research Fund (7940) for their financial support for my research.

I would like to acknowledge the people that made my graduate years more cheerful. I feel very lucky to have them in my life, Burcu Dedeoğlu, İlke Uğur Marion, Melis Çağdaş, Gülşah Çifci Bağatır and Tuğba Özaltın. They always have been a part of my most important moments.

I would like to thank all the members of Chemistry Department for warm family environment. Especially, I would like to remark the former and current members of CCBG family and also my dear Avcı Group lab mates, Melek Naz Güven, Ece Akyol,

Tuğçe Nur Eren, Betül Bingöl and Seçkin Altuncu.

Last but not least, my deep and sincere gratitude to my family for their endless love and support. I am forever grateful to my father for giving me the opportunities that have made me who I am. My mom is my role model, she has dedicated her all life to the successes of her children. She was dreaming about getting my PhD degree with my daughter, as today. Even I get my PhD title, I would always be mamma's little girl. I am also thankful to my brother for always being there for me as a friend even though the long distances between us. I would like to thank my mother-in-law because of being there whenever I need during my studies. My closest friend and my love, Sayat, I could not achieve this degree without you. You made everything easier and have been the light of my way.

This journey would not have been possible without these great people and I dedicate this milestone to them, especially to my little miracle Sirun.

## ABSTRACT

# SYNTHESIS, EVALUATION OF FUNCTIONAL METHACRYLATES AND A COMPUTATIONAL APPROACH TO THE REACTIONS OF MOLECULES WITH BIOLOGICAL POTENTIAL

In this dissertation, experimental and computational methods are used to investigate the molecules which are biologically active and have potential in pharmaceutical field. This study sheds light on the synthesis procedures of methacrylate based monomers, characterization of the synthesized materials, and also detection of reaction mechanisms, calculations of thermodynamic properties in several reactions. In the first three chapters, several methacrylate monomers were investigated which have various biomedical applications. The synthesis and photoinitiating abilities of six novel methacrylate-based monomeric photoinitiators (MPIs) has been carried out. In order to make useful predictions on the reactivities of methacrylates, a relationship between reactivities of 21 methacrylates in free radical polymerization and their chemical structures were built by a non-linear expression. Finally, methacrylates were used to prepare PEG-based carboxylic-acid functionalized monomers which were incorporated into hydrogel scaffolds for biomedical applications. In the last three chapters, the reactions of biologically active molecules were analyzed by computational tools. The exo-stereoselectivity of norbornene in the synthesis of thiazolidine derivatives which have diverse biological potential, are clarified by means of Density Functional Theory (DFT). Another biologically active molecule, diclofenac that is used as a drug, was examined to enlighten the degradation mechanism and byproduct formations. Finally, the reactions of cyclohexanone with 3-methyl indole and N-methyl indole, which are the basis of many biologically active compounds, are modeled to determine the origins of regioselectivities.

## ÖZET

# FONKSİYONEL METAKRİLATLARIN SENTEZ VE DEĞERLENDİRİLMESİ İLE BİYOLOJİK POTANSİYELE SAHİP MOLEKÜLLERİN TEPKİMELERİNE HESAPSAL YAKLAŞIM

Bu tezde, biyoaktif ve ilaç alanında potansiyele sahip moleküller deneysel ve hesapsal yöntemler kullanılarak incelenmiştir. Bu çalışma, (met)akrilat bazlı monomerlerin sentez metotları ve karakterizasyonları ile tepkime mekanizmalarının tayini ve çeşitli tepkimelerin de termodinamik özelliklerinin hesaplanması açısından önem taşımaktadır. İlk üç başlıkta, biyomedikal uygulamalarda kullanılabilen çeşitli metakrilat monomerleri araştırılmıştır. Altı yeni metakrilat bazlı monomerik fotobaşlatı sentezlenmiş ve bunların akrilat polimerizasyonlarını fotobaşlatma etkinlikleri çalışılmıştır. Metakrilatların reaktivitelerinin doğru öngörülebilmesi için, 21 tane metakrilat özellikli monomerin serbest radikal polimerizasyonundaki reaktiviteleri ile kimyasal yapıları arasındaki ilişki, doğrusal olmayan bir korelasyon oluşturularak açıklanmıştır. Son olarak da, metakrilatlar kullanılarak biyomedikal uygulamalarda önemli bir yeri olan hidrojel iskeletlerinin hazırlanmasında kullanılmak üzere PEG-bazlı karboksilik asit fonksiyonelli monomerler sentezlenmiştir. Son üç bölümde de biyoaktif moleküllerin tepkimeleri hesapsal yöntemlerle araştırılmıştır. Norbornenin biyolojik potansiyeli bulunan tiyazolidin ile verdiği hetero Diels-Alder tepkimelerindeki exo-stereoseçicilik Yoğunluk Fonksiyonel Teorisi (YFT) çalışmaları ile açıklığa kavuşmuştur. Bir diğer biyoaktif molekül ve aynı zamanda ilaç türevidir olan diklofenakın bozunma mekanizması ve yan ürünlerinin oluşumu da YFT ile aydınlatılmıştır. Son olarak da, birçok biyoaktif molekülün kökünde bulunan 3-metil indol ve N-metil indolün sikloheksanon ile verdiği tepkimeler bölgesel seçiciliklerinin belirlenebilmesi için modellenmiştir.

## TABLE OF CONTENTS

ACKNOWLEDGEMENTS . . . . .	iii
ABSTRACT . . . . .	v
ÖZET . . . . .	vi
LIST OF FIGURES . . . . .	xi
LIST OF TABLES . . . . .	xix
LIST OF SYMBOLS . . . . .	xxii
LIST OF ACRONYMS/ABBREVIATIONS . . . . .	xxiii
1. INTRODUCTION . . . . .	1
2. OBJECTIVE AND SCOPE . . . . .	3
3. THEORETICAL BACKGROUND . . . . .	4
3.1. Quantum Mechanics . . . . .	4
3.2. Hartree-Fock Theory . . . . .	7
3.3. Density Functional Theory . . . . .	8
3.3.1. Local Density Approximation . . . . .	10
3.3.2. Generalized Gradient Approximation . . . . .	12
3.3.3. Time-Dependent Density Functional Theory . . . . .	13
3.4. Basis Sets . . . . .	14
3.5. Continuum Solvation Models . . . . .	15
4. STRUCTURE-REACTIVITY RELATIONSHIPS OF NOVEL MONOMERIC PHOTOINITIATORS . . . . .	18
4.1. Introduction . . . . .	19
4.2. Materials and Characterization . . . . .	22
4.2.1. Materials . . . . .	22
4.2.2. Characterization . . . . .	22
4.3. Synthesis of Monomeric Photoinitiators . . . . .	23
4.3.1. Synthesis of MPI1 . . . . .	23
4.3.2. Synthesis of MPI2 . . . . .	23
4.3.3. Synthesis of MPI3 . . . . .	24
4.3.4. Synthesis of MPI4 . . . . .	25

4.3.5.	Synthesis of MPI5 . . . . .	25
4.3.6.	Synthesis of MPI6 . . . . .	26
4.4.	Experimental Work . . . . .	27
4.4.1.	Photopolymerization Experiments . . . . .	27
4.4.2.	ESR Spin Trapping (ESR-ST) Experiments . . . . .	27
4.4.3.	Computational Calculations . . . . .	28
4.4.4.	Migration Study . . . . .	28
4.5.	Results and Discussions . . . . .	29
4.5.1.	Synthesis and Characterization of Photoinitiators . . . . .	29
4.5.2.	Light Absorption Properties of the Novel Photoinitiators . . . . .	32
4.5.3.	Molecular Modeling . . . . .	33
4.5.4.	Electron Spin Resonance (ESR) Experiments . . . . .	37
4.5.5.	Photoinitiating Activities . . . . .	38
4.5.6.	Migration Study . . . . .	44
4.6.	Conclusions . . . . .	44
5.	RELATIONSHIP BETWEEN THE FREE RADICAL POLYMERIZATION RATES OF METHACRYLATES AND THE CHEMICAL PROPERTIES OF THEIR MONOMERIC RADICALS . . . . .	46
5.1.	Introduction . . . . .	47
5.2.	Computational Details . . . . .	49
5.3.	Experimental Methods . . . . .	51
5.4.	Results and Discussions . . . . .	52
5.5.	Conclusions . . . . .	60
6.	SYNTHESIS AND EVALUATION OF NOVEL CARBOXYLIC ACID FUNC- TIONALIZED METHACRYLATES FOR HYDROGELS IN BIOMEDICAL APPLICATIONS . . . . .	62
6.1.	Introduction . . . . .	63
6.2.	Materials and Characterization . . . . .	65
6.2.1.	Materials . . . . .	65
6.2.2.	Characterization . . . . .	65
6.3.	Synthesis of Monomers . . . . .	65



6.4. Synthesis of Hydrogels . . . . .	66
6.4.1. Gelation Percentage . . . . .	67
6.4.2. Equilibrium Swelling Ratio (ESR) . . . . .	67
6.4.3. Contact Angle Measurements . . . . .	68
6.4.4. Mineralization of Hydrogels . . . . .	68
6.4.5. Measurement of Ca <sup>2+</sup> Content . . . . .	68
6.5. Results and Discussion . . . . .	69
6.5.1. Synthesis of Monomers . . . . .	69
6.5.2. Photopolymerization . . . . .	72
6.5.3. Synthesis and Characterization of Hydrogels . . . . .	72
6.5.3.1. Swelling Properties . . . . .	74
6.5.3.2. Contact Angle Measurements . . . . .	75
6.5.3.3. Mineralization of Hydrogels . . . . .	76
6.6. Conclusion . . . . .	78
7. ORIGINS OF EXO-STEREOSELECTIVITY OF NORBORNENE IN HET- ERO DIELS-ALDER REACTIONS . . . . .	80
7.1. Introduction . . . . .	82
7.2. Computational Methodology . . . . .	84
7.3. Results and Discussion . . . . .	86
7.3.1. Rotational Barriers of 1b and 2b . . . . .	87
7.3.2. Hetero Diels-Alder Reactions of 3b with Norbornene . . . . .	89
7.3.3. Rotational Barrier of the Hetero Diels-Alder Adduct (4b) . . . . .	96
7.4. Conclusion . . . . .	97
8. ASSESSMENT OF THE DEGRADATION MECHANISM AND TOXICITY OF DICLOFENAC AND ITS BYPRODUCTS . . . . .	99
8.1. Introduction . . . . .	100
8.2. Computational Methodology . . . . .	102
8.2.1. Quantum Chemical Calculations . . . . .	102
8.2.2. Toxicity Assessment . . . . .	103
8.3. Results and Discussion . . . . .	104
8.3.1. Initial Reactions of Diclofenac with ·OH . . . . .	104

8.3.2. Fragmentation of DCF/DCF <sup>-</sup> . . . . .	109
8.3.3. Analysis of the Degradation Byproducts . . . . .	110
8.3.4. Toxicity . . . . .	116
8.4. Conclusions . . . . .	120
9. COMPUTATIONAL INVESTIGATION OF DISPROPORTIONATIVE CON- DENSATION REACTIONS OF INDOLES WITH CYCLIC KETONES . .	122
9.1. Introduction . . . . .	123
9.2. Computational Details . . . . .	126
9.3. Experimental Results . . . . .	126
9.4. Results and Discussion . . . . .	127
9.5. Conclusions . . . . .	132
10. CONCLUDING REMARKS . . . . .	133
11. FUTURE WORK SUGGESTIONS . . . . .	136
REFERENCES . . . . .	137

## LIST OF FIGURES

Figure 4.1.	Excitation process upon irradiation of a photoinitiator. . . . .	19
Figure 4.2.	Formation of radicals by homolytic cleavage of type-I photoinitiators.	20
Figure 4.3.	Formation of radicals by photolysis of type-II photoinitiators. . . .	20
Figure 4.4.	Structures of synthesized MPIs. . . . .	21
Figure 4.5.	Synthesis of MPIs from TBBr. . . . .	30
Figure 4.6.	Synthesis of MPIs from IEM. . . . .	30
Figure 4.7.	The FTIR spectra of MPI1, MPI2 and MPI3. . . . .	31
Figure 4.8.	<sup>1</sup> H NMR spectra of MPI1, MPI3 and MPI4. . . . .	32
Figure 4.9.	<sup>13</sup> C NMR spectrum of MPI6. . . . .	33
Figure 4.10.	Absorption spectra of (A) group 1 and (B) group 2 photoinitiators in CHCl <sub>3</sub> (4 x 10 <sup>-5</sup> M) solution. . . . .	34
Figure 4.11.	Transition molecular orbitals of the photoinitiators. . . . .	35
Figure 4.12.	Calculated/Theoretical UV spectra of the photoinitiators for (a) group 1 and (b) group 2. (TD-DFT B3LYP/6-31G(d) in CHCl <sub>3</sub> )..	37

Figure 4.13. ESR spectra of the radicals generated in (a) MPI6/EDB and (b) MPI5 irradiated by LED@385 nm exposure and trapped by PBN in <i>tert</i> -butylbenzene. The hyperfine constants are shown for each spectra. . . . .	39
Figure 4.14. Rate-time plots for the photopolymerization of HEMA under nitrogen initiated by MPI1, MPI2, MPI5 and Irgacure 2959 (PI concentration is 2 mol%). . . . .	41
Figure 4.15. Rate-time plots for the photopolymerization of HDDA under nitrogen initiated by MPI1, MPI3, MPI5, Irgacure 2959 and Irgacure 184 (PI concentration is 2 mol%). . . . .	42
Figure 4.16. Rate-time plots for the photopolymerization of TMPTA under nitrogen initiated by (A) MPI1, MPI5 and Irgacure 2959 (PI concentration is 2 mol%); (B) MPI4/DMAEM, MPI6/DMAEM, BP/DMAEM and AP/DMAEM (PI and DMAEM concentrations are 1 and 3 mol%). . . . .	43
Figure 4.17. Conversion values of MPIs in photopolymerization of HDDA, HEMA and TMPTA. . . . .	44
Figure 4.18. UV-vis absorption spectra of Irgacure 2959, MPI1, MPI2 and MPI5 extracted with chloroform from the polymer samples. . . . .	45
Figure 5.1. General structure of methacrylates. . . . .	52
Figure 5.2. List of methacrylate monomers, investigated in this study. . . . .	53
Figure 5.3. Formation of the monomeric radicals via methyl radical attack to the ethylenic double bond of the monomer. . . . .	54

Figure 5.4.	Correlation between the experimental rates of polymerization $R_{p,exp}$ and the electrophilicity index descriptor $(\omega - \omega_0)^2$ for Series 1-3. . . . .	57
Figure 5.5.	Correlation between the predicted and the experimental rates of polymerization, according to Table 5.2. Series 1-3 are in blue, and Series 4 is in black. R13 from Series 4 was included in the correlation given by the blue marks. . . . .	57
Figure 5.6.	Correlation between the slopes of the correlation equations of Figure 5.3 and the average $\Delta stab$ values for each of the corresponding Series 1-3. . . . .	59
Figure 5.7.	Comparison between the predicted (Equation 5.8) and the experimental rates of polymerization for the monomeric radicals of Series 1 (blue), Series 2 (red), and Series 3 (green). . . . .	59
Figure 6.1.	Chemical structures of materials that can be photopolymerized to create crosslinked hydrogel networks. . . . .	63
Figure 6.2.	Natural bone synthesis with synthetic polymers. . . . .	64
Figure 6.3.	Synthesis of carboxylic acid-functionalized monomers 1 and 2. . . . .	70
Figure 6.4.	FTIR spectra of monomers 1 and 2. . . . .	70
Figure 6.5.	$^1H$ NMR spectra of monomers 1a and 2a. . . . .	71
Figure 6.6.	$^1H$ NMR spectra of monomers 1 and 2. . . . .	71
Figure 6.7.	Rate-time and conversion-time plots for copolymerizations of 1 and 2 with PEGDA and HEMA at 40 °C using DMPA. . . . .	73

Figure 6.8.	pH response of the hydrogel composition “H2” (15% monomer 1 incorporation). . . . .	75
Figure 6.9.	Images and angles taken from contact angle measurements. . . . .	76
Figure 6.10.	SEM images of hydrogels (a) H2, (b) H4, (c) mineralized H2, and (d) mineralized H4. . . . .	77
Figure 6.11.	SEM images and EDX spectra of (a) mineralized H2 and (b) mineralized H4. . . . .	77
Figure 6.12.	Ca <sup>2+</sup> deposition assay measured as the total Ca <sup>2+</sup> content in the mineralized hydrogels. . . . .	78
Figure 7.1.	Parent system of the Diels-Alder reaction . . . . .	80
Figure 7.2.	Molecular orbital representation of Diels-Alder reactions with normal and inverse electron demand. . . . .	81
Figure 7.3.	Examples for exo and endo stereoisomers in Diels-Alder reaction. . . . .	82
Figure 7.4.	Synthesis of 2, 3 and 4. . . . .	83
Figure 7.5.	The inverse-electron demand Diels-Alder reaction of 5-benzylidene-3-phenyl-2-phenyliminothiazolidine-4-thione (3a) with norbornene yielding endo and exo products. . . . .	87
Figure 7.6.	Rotational transition state structures with NPA charges and dipole moments ( $\mu$ ) for 1b and 2b in toluene (M06-2X/6-31+G(d))/B3LYP/6-31+G(d)). . . . .	89

Figure 7.7.	Experimental results for the adduct. . . . .	90
Figure 7.8.	Transition structures for the reaction between 3b and norbornene.	91
Figure 7.9.	Optimized structure for norbornene in CH <sub>2</sub> Cl <sub>2</sub> (M06-2X/6-31+G(d) //B3LYP/6-31+G(d)) . . . . .	93
Figure 7.10.	Newman projections for the cycloadditions of norbornene to thione with exo and endo faces (M06-2X/6-31+G(d)//B3LYP/6-31+G(d) in CH <sub>2</sub> Cl <sub>2</sub> ). . . . .	94
Figure 7.11.	Reaction profile for the reaction 3b with norbornene resulting in 4b (M06-2X/6-31+G(d)// B3LYP/6-31+G(d)). . . . .	95
Figure 7.12.	Plot of activation energies versus distortion energies of the reac- tions of thione derivatives and norbornene calculated by M06-2X/6- 31+G(d)//B3LYP/6-31+G(d). Values in kcal/mol. . . . .	96
Figure 7.13.	Gibbs Free Energy profile (kcal/mol) for the interconversion of (M,S,R,R)-x to (P,S,R,R)-x in CH <sub>2</sub> Cl <sub>2</sub> at room temperature (M06- 2X/6-31+G(d)//B3LYP/6-31+G(d)). . . . .	97
Figure 8.1.	Structure of DCF (2-(2,6-dichloroanilino)phenylacetic acid) . . . . .	99
Figure 8.2.	Molecular structures of some of the common degradation byprod- ucts of diclofenac . . . . .	101
Figure 8.3.	Optimized structures of diclofenac in neutral (DCF) and anionic forms (DCF-) (B3LYP/6-31+G(d) in water). . . . .	104

- Figure 8.4. H-abstraction by OH from DCF, generating radical intermediate ( $R_{abs}$ ). . . . . 105
- Figure 8.5. OH-addition of  $\cdot\text{OH}$  to DCF, generating radical intermediate ( $R_{add}$ ). 106
- Figure 8.6. Gibbs free energies of the reaction ( $\Delta G_{rxn}$ ) of  $\cdot\text{OH}$  with  $\text{DCF}^-$  to give H-abstraction intermediates ( $R_{abs}$ ) on the left (red path) and OH-addition intermediates ( $R_{add}$ ) on the right (orange path). . . . 108
- Figure 8.7. Gibbs free energies of the reaction of  $\cdot\text{OH}$  with DCF to give H-abstraction intermediates ( $R_{abs}$ ) on the left (orange path) and OH-addition intermediates ( $R_{add}$ ) on the right (green path). . . . . 108
- Figure 8.8. Schematic representation of the generation of degradation byproducts by (I) rearrangement and (II) in the presence of  $\bullet\text{OH}$  using  $\text{DCF}^-$  (except for P2 where DCF has been utilized) Gibbs free energies are given in kcal/mol. . . . . 111
- Figure 8.9. Degradation mechanism and reaction profile yielding P2 starting from DCF. Gibbs free energies are given in kcal/mol. . . . . 112
- Figure 8.10. Degradation mechanism and reaction profile yielding P3 starting from decarboxylated DCF. Gibbs free energies are given in kcal/mol. 113
- Figure 8.11. Reaction profile of the degradation product P4 starting from  $\text{DCF}^-$  and DCF in parenthesis. Gibbs free energies are given in kcal/mol. 114
- Figure 8.12. Degradation mechanism and reaction profile yielding P1 starting from  $\text{DCF}^-$  and DCF in parenthesis. Gibbs free energies are given in kcal/mol. (\*Transition state could not be located.) . . . . . 115



Figure 8.13.	Degradation mechanism and reaction profile yielding P5 starting from P1. Gibbs free energies are given in kcal/mol. . . . .	116
Figure 8.14.	Degradation mechanism and reaction profile yielding P6 starting from P5. Gibbs free energies are given in kcal/mol. . . . .	117
Figure 8.15.	Degradation mechanism and reaction profile yielding P7 starting from DCF <sup>-</sup> and DCF in parenthesis. Gibbs free energies are given in kcal/mol. . . . .	118
Figure 8.16.	Degradation mechanism and reaction profile yielding P8 starting from DCF <sup>-</sup> and DCF in parenthesis. Gibbs free energies are given in kcal/mol. . . . .	119
Figure 8.17.	Degradation mechanism and reaction profile yielding P9 starting from P8 (neutral form is shown in parenthesis). Gibbs free energies are given in kcal/mol. . . . .	120
Figure 9.1.	Structure of indole. . . . .	122
Figure 9.2.	Resonance structures of indole. . . . .	122
Figure 9.3.	Electrophilic attack to C3 and C2 positions. . . . .	123
Figure 9.4.	Representatives of some indole alkaloids and synthesized indoles. . .	124
Figure 9.5.	Vinylogous iminium or azafulvenium type reactivity of indole. . .	125
Figure 9.6.	Reactions carried out by Saraçoğlu group. . . . .	127

Figure 9.7.	Gibbs Free energy profile for the formation of 12b (M06-2X/6-31+G(d,p) in cyclohexanone). . . . .	128
Figure 9.8.	Gibbs Free energy profile for the formation of 26 (M06-2X/6-31+G(d,p) in cyclohexanone). . . . .	129
Figure 9.9.	The formation mechanism of 26 from 23 and 11. Possible H shifts.	130
Figure 9.10.	Possible cycloadduct structures for the Diels-Alder reaction of 26 and 29. . . . .	130
Figure 9.11.	Gibbs Free Energy profile for [1,5] and [1,7] H-shift. . . . .	131
Figure 9.12.	Transition state structures of Diels-Alder reaction between 26 and 29 with 1,5- and 1,6-addition. Activation free energies, activation enthalpies, reaction energies and reaction enthalpies are given in kcal/mol. . . . .	131

## LIST OF TABLES

Table 4.1.	Solubilities of MPIs. . . . .	31
Table 4.2.	Absorption properties in $\text{CHCl}_3$ solution, energies(eV) and wavelength (nm) of experimental absorption bands, and the most important electronic transitions calculated with B3LYP/ 6-31G(d). . . . .	36
Table 4.3.	Photopolymerization data of HEMA, HDDA and TMPTA initiated by commercial PIs or synthesized MPIs. . . . .	40
Table 5.1.	Experimental rates of polymerization $R_{p,exp}$ of the monomers (M1-M21) and the property values of the corresponding radicals (R1-R21): the electrophilicity index $\omega$ in eV, the stability values $stab$ based on the combination of R and $\text{CH}_2\text{OH}$ , H and F, the average stability values $stab_{av}$ (Equation 3), and the stability difference values $\Delta stab$ relative to the most stable radical R18. All stability values are in $\text{kJ mol}^{-1}$ . . . . .	55
Table 5.2.	The electrophilicity index descriptor $(\omega - \omega_0)^2$ in $\text{eV}^2$ , the predicted rate of polymerization $R_{p,pred1}$ ( $\text{s}^{-1}$ ) the difference $\Delta R_p$ ( $\text{s}^{-1}$ ) with the experimental rate of polymerization $R_{p,exp}$ ( $\text{s}^{-1}$ ) for Series 1-4, with $a = 0.3209 \text{ eV}^{-2} \text{ s}^{-1}$ and $b = 0.0021 \text{ s}^{-1}$ , $a = 0.1971 \text{ eV}^{-2} \text{ s}^{-1}$ and $b = -0.0024 \text{ s}^{-1}$ , $a = 0.0805 \text{ eV}^{-2} \text{ s}^{-1}$ and $b = 0.0023 \text{ s}^{-1}$ , for Series 1, 2, 3 of the monomeric radicals, respectively. . . . .	56
Table 5.3.	The predicted rates of polymerization $R_{p,pred2}$ and $R_{p,pred3}$ ( $\text{s}^{-1}$ ) resulting from Equation 5.7. . . . .	60
Table 6.1.	Compositions of the synthesized hydrogels (H0-H4). . . . .	74

Table 7.1.	Rotational barriers (kcal/mol) of 1b and 2b around the N3-C <sub>aryl</sub> bond. Toluene is used as a solvent at T=333K. . . . .	88
Table 7.2.	Activation energies ( $\Delta G^\ddagger = G(\text{TS}) - G(3b) - G(\text{norbornene})$ ), reaction energies ( $\Delta G_{rxn} = G(\text{Product}) - G(3b) - G(\text{norbornene})$ ), dihedral angles and distortion-interaction energies for the transition states. (M06-2X/6-31+G(d)//B3LYP/6-31+G(d) in CH <sub>2</sub> Cl <sub>2</sub> ) . . .	92
Table 8.1.	Activation Gibbs free energies ( $\Delta G^\ddagger$ ), activation enthalpies ( $\Delta H^\ddagger$ ), reaction Gibbs free energies ( $\Delta G_{rxn}$ ), reaction enthalpies ( $\Delta H_{rxn}$ ) for the R <sub>abs</sub> intermediates calculated from Equation 8.2 and RSE values calculated from Equation 8.3 (MPWB1K/6-311+G(3df,2p)//B3LYP/6-31+G(d), kcal mol <sup>-1</sup> ). Values in parentheses have been calculated with B3LYP/6-31+G(d) in water. . . . .	105
Table 8.2.	Activation Gibbs free energies ( $\Delta G^\ddagger$ ), activation enthalpies ( $\Delta H^\ddagger$ ), reaction Gibbs free energies ( $\Delta G_{rxn}$ ), reaction enthalpies ( $\Delta H_{rxn}$ ) for the R <sub>add</sub> intermediates calculated from Equation 8.2 and RSE values calculated from Equation 8.3 (MPWB1K/6-311+G(3df,2p)//B3LYP/6-31+G(d), kcal mol <sup>-1</sup> ). Values in parentheses have been calculated with B3LYP/6-31+G(d) in water. . . . .	107
Table 8.3.	Reaction Gibbs free energies ( $\Delta G_{rxn}$ ) for the fragments of DCF/DCF <sup>-</sup> calculated with Equation 8.4 (MPWB1K/6-311+G(3df,2p)//B3LYP/6-31+G(d), kcal mol <sup>-1</sup> ). Values in parentheses have been calculated with B3LYP/6-31+G(d) in water. . . . .	109
Table 8.4.	Toxicity classification according to the Globally Harmonized System (GHS) of Classification and Labelling of Chemical . . . . .	117

Table 8.5. Toxicity values of DCF/ DCF <sup>-</sup> and its degradation byproducts P1-P9 to aquatic organisms (mg L <sup>-1</sup> ) using ECOSAR. . . . .	118
---	-----



## LIST OF SYMBOLS

$E_x^{exact}$	Exact exchange energy
$E_c[\rho]$	Correlation energy
$E_x[\rho]$	Exchange energy
$J[\rho]$	Coulomb energy
$T[\rho]$	Kinetic energy of interacting electrons
$T_s[\rho]$	Kinetic energy of non-interacting electrons
$U_{x\sigma}$	Exchange energy density
$V_{ee}[\rho(r)]$	Interelectronic interactions
$V_{ext}(r)$	External potential
$V_{KS}$	Kohn-Sham potential
$\Delta E$	Electronic energy
$\Delta E^\ddagger$	Electronic activation energy
$\Delta G_{rxn}$	Gibbs free energy of reaction
$\Delta G^\ddagger$	Gibbs free energy of activation
$\Delta H_p$	Heat released per mole of double bonds reacted
$\Delta H_{rxn}$	Heat of reaction
$\epsilon$	Extinction coefficient
$\lambda_{max}$	The wavelengths for maximum absorption
$\rho(r)$	Electron density
$v(r)$	External potential
$\Phi$	Number of propagation chains initiated per light photon absorbed
$\psi$	Wavefunction

**LIST OF ACRONYMS/ABBREVIATIONS**

AP	Acetophenone
B3LYP	Becke-3-parameter Lee-Yang-Parr functional
BMK	Boese-Martin for Kinetics
BP	Benzophenone
DFT	Density functional theory
DMAEM	N,N-dimethylaminoethyl methacrylate
DSC	Differential Scanning Calorimetry
ESR	Electron Spin Resonance
FT-IR	Fourier Transform Infrared Spectroscopy
GGA	Generalized gradient approximation
GTO	Gaussian type orbital
HDDA	Hexane-1,6-diol diacrylate
HEMA	2-hydroxyethyl methacrylate
HF	Hartree-Fock theory
HOMO	Highest occupied molecular orbital
IEFPCM	Integral equation formalism polarizable continuum model
IEM	2-Isocyanatoethyl methacrylate
IRC	Intrinsic reaction coordinate
Irgacure 184	1-Hydroxy-cyclohexyl-phenyl-ketone
Irgacure 2959	2-Hydroxy-1-[4-(2-hydroxyethoxy)phenyl]-2-methyl-1-Propanone
LDA	Local density approximation
LUMO	Lowest unoccupied molecular orbital
M06-2X	Hybrid meta exchange-correlation functional
MPI	Monomeric photoinitiator
MPWB1K	Modified Perdew-Wang-Becke 1 Parameter Method for Kinetic
NMR	Nuclear Magnetic Resonance spectroscopy
NPA	Natural population analysis

PEG	Poly(ethylene) glycol
PEGDA	Poly(ethylene) glycol diacrylate
PI	Photoinitiator
$R_p$	Rate of polymerization
RHMA	Alkyl $\alpha$ -hydroxymethacrylate
SCF	Self consistent field
SEM	Scanning Electron Microscope
STO	Slater type orbital
TBBr	Tert-butyl $\alpha$ -bromomethacrylate
TBHMA	Tert-butyl $\alpha$ -hydroxymethacrylate
TD-DFT	Time-dependent density functional theory
TEA	Triethylamine
TFA	Trifluoroacetic acid
THF	Tetrahydrofuran
TMPTA	Trimethylolpropane triacrylate



## 1. INTRODUCTION

Experimental and computational studies are strong partners in the different fields of chemistry. Computational chemistry is not a replacement for experimental studies, but has a crucial role in explaining and verifying the known chemistry. It allows us to make predictions before running the experiments, especially for the ones that are too difficult to find or too expensive to purchase.

In this dissertation, experimental and computational studies are combined to explore the reactions of methacrylates (in the first three chapters) and molecules with biological potential (in the last three chapters).

Photoinitiated free-radical polymerization has a great interest because of wide range of applicability on acrylate-based resins. In photopolymerization, the most important components are photoinitiators and polymerizable monomers. Using suitable photoinitiator with good initiation ability and minimum toxicity is important in order to have polymers with good mechanical and chemical properties. In recent years, the synthesis of novel photoinitiators has a great interest in the development of photopolymerization studies. Acrylates and methacrylates are most frequently used monomers in photopolymerization due to their acrylic double bonds that exhibit higher reactivity compared to other double bonds, no yellowing property and good adhesion. Incorporation of functional groups into the methacrylate based monomers improves the properties of the synthesized polymers. Polymers of the acid-functionalized methacrylate monomers show adhesion properties especially in biomaterials. In this dissertation, the syntheses of novel photoinitiators and novel acid-functionalized monomers originated from methacrylates have been disclosed.

The potential of a structure to undergo chemical change is called reactivity. Some structures are more prone to react than others because of the chemical properties they exhibit. The reactivities of several methacrylate monomers in free radical polymerization are analyzed and a relationship with their structure is established. In order to

define their chemical properties some monomer reactivity descriptors have been used; electrophilicity, radical stability and electronegativity.

Understanding of the key factors that determine the selectivity of the reactions is very important for the development of reliable models that explain the origins of the organic reactions. Selectivity is classified as stereoselectivity and regioselectivity. The first results from different ratios of isomers in the reaction products and the latter arises from the preferred reaction sites. Steric and electronic factors in the reactions determine the stereo- and regioselectivities leading to different products. In this thesis, selectivities in hetero Diels-Alder and disproportionative condensation reactions have been investigated. Also the regioselectivity in the hydroxyl radical mediated degradation of diclofenac in aqueous medium have been explored in order to determine the byproducts.

Overall, this dissertation includes both practical and theoretical insight to the polymerization and organic reactions. In six chapters, synthesis, development, evaluation and theoretical investigation of several reactions have been represented which play an important role in polymer science and biomedical applications.

## 2. OBJECTIVE AND SCOPE

This work consists of experimental and theoretical studies on investigation of molecules with biological activity like methacrylates and the ones with pharmaceutical potential. In the first three chapters, the features of methacrylates have been investigated in terms of the synthesis and characterization of methacrylate-based monomeric photoinitiators (Chapter 4), constructing a relationship between their polymerization rates and chemical properties (Chapter 5), and also the synthesis and evaluation of carboxylic acid-functionalized methacrylates for hydrogels (Chapter 6).

In the last three chapters, molecules with biological activities have been modeled in terms of their reaction mechanisms and energetics by computational tools. Firstly, the origins of *exo*-stereoselectivity of norbornene in the synthesis of thiazolidine derivatives via hetero-Diels-Alder reactions were investigated (Chapter 7). Then, the analysis on degradation mechanism of diclofenac shed light to production of its byproducts (Chapter 8). And lastly, the mechanism of disproportionative condensation reactions of indoles with cyclic ketones was assessed (Chapter 9).

### 3. THEORETICAL BACKGROUND

Computational chemistry is a set of techniques for investigating chemical problems on a computer. There are five main classes of methods used in examination of these problems;

- Molecular mechanics (MM) is based on a ball (atoms) and springs (bonds) model of a molecule. MM will calculate the geometries and energies of very large molecules quickly but does not give any information on electronic properties.
- Ab initio calculations are based on Schrodinger equation, which describes how the electrons in a molecule behave. Ab initio methods do not consult to fitting to experiment.
- Semiempirical (SE) calculations are based on Schrodinger equation as in ab initio, but experimental values are used for parametrization.
- In Density Functional Theory (DFT), Schrodinger equation is used also, but instead of calculating a wavefunction it derives electron density function (distribution) directly.
- Molecular dynamics (MD) calculations apply the laws of motion to molecule.

This chapter gives the details on the most commonly used methods in this dissertation including Quantum Mechanics, Hartree-Fock Theory, Semiempirical calculations and Density Functional Theory.

#### 3.1. Quantum Mechanics

Molecules are composed of nuclei and electrons, and quantum chemistry concerns principally the motion of these electrons under the electromagnetic field caused by nuclear charges. Electronic properties of molecules and thus their structures and

reactions, are described basically by Schrödinger equation,

$$H\psi = E\psi \quad (3.1)$$

where  $H$  is the Hamiltonian operator,  $E$  is the total energy of the system and  $\psi$  is the wave function that describes the amplitude of the particle/wave at a distance  $x$  from some chosen origin. The Hamiltonian operator is a sum of all energy terms involved kinetic and potential energies. The kinetic energies belong to the nuclei ( $E_I^{kin}$ ) and electrons ( $E_i^{kin}$ ). The potential energies stem from the Coulomb interactions by nucleus-electron ( $U_{Ii}$ ), electron-electron ( $U_{ij}$ ) and nucleus-nucleus ( $U_{IJ}$ ),

$$H = E_I^{kin} + E_i^{kin} + U_{Ii} + U_{ij} + U_{IJ} \quad (3.2)$$

$$H = - \sum_I \frac{\hbar^2}{2m_I} \nabla_I^2 - \sum_i \frac{\hbar^2}{2m_e} \nabla_i^2 - \sum_i \sum_I \frac{e^2 Z_I}{r_{iI}} + \sum_{i<j} \frac{e^2}{r_{ij}} + \sum_{I<J} \frac{e^2 Z_I Z_J}{r_{IJ}}. \quad (3.3)$$

where  $m_I$  and  $m_i$  are the masses of the nuclei and the electron, respectively,  $\hbar$  is the Planck's constant divided by  $2\pi$ ,  $\nabla^2$  is the Laplacian operator,  $e$  is the charge on the electron,  $Z$  is an atomic number and  $r$  is the distance between the particles.

Because nuclei are far more massive than electrons, their movements compared to the electrons are negligible. This means that the positions of nuclei are considered to be frozen. Born-Oppenheimer approximation suggests that the terms connected with nuclei can be eliminated and therefore by taking the nuclear kinetic energy term independent of the electrons, and considering the nuclear-nuclear potential energy term constant, Hamiltonian operator becomes,

$$H_e l = E_I^{kin} + U_{Ii} + U_{ij} \quad (3.4)$$

As a result, Schrödinger equation with respect to Born-Oppenheimer approximation is defined as,

$$(H_{el} + V_{nn})\psi_{el} = E_{el}\psi_{el} \quad (3.5)$$

where  $V_{nn}$  is the nuclear-nuclear repulsion energy constant, and the eigenvalue,  $E_{el}$  is called the ‘electronic energy’.

Schrödinger equation is powerful to describe almost all properties of systems, but it is too complicated to solve. The equation can be solved exactly only for a few systems like particle in a box, the hydrogen atom and the hydrogen molecule ion. For the solution of all the other systems, the variational method can be used. In Equation 3.1, multiplying both sides by  $\psi$  gives,

$$\psi H\psi = \psi E\psi \quad (3.6)$$

For many electron systems, integration of the both sides in a volume ( $d\tau$ ) results in,

$$E = \frac{\int \psi H\psi d\tau}{\int \psi^2 d\tau} \quad (3.7)$$

When Hamiltonian is exact, energy calculated from Equation 3.7 will also be exact. In the Hamiltonian, each interaction term decreases the energy. Once an approximate energy is obtained, the calculation will be repeated by modifying the Hamiltonian. The identification of the energy value close to the actual one involves a minimization process of calculated energy. This principle is called variational method which is considered to be one of the most useful tools for finding approximate solutions of the Schrödinger equation.

The Schrödinger equation of a simple 2-D square potential or a hydrogen atom, can be solved exactly in order to get the wavefunction determine the allowed energy states of the system. Unfortunately it is impossible to solve the Schrödinger equation for a multi electron system. Some approximations should be involved in order to solve the problem like Hartree-Fock (HF) theory and Density Functional Theory (DFT).

### 3.2. Hartree-Fock Theory

Hartree-Fock theory is the simplest wavefunction-based method and called also as 'Molecular Orbital Approximation'. It is a modification of the Hartree method where single electron approximation technique is used for multi electron systems. In HF method, many-electron wavefunction is defined as a Slater determinant of one-electron wavefunctions. Each electron experiences a Coulombic repulsion due to the average positions of electrons. The single Slater determinant is constructed from a set of  $N$  single-electron wave functions as an approximation to the wavefunction.

$$\psi_{SD} = \frac{1}{\sqrt{N!}} \begin{vmatrix} \chi_1(1) & \cdots & \chi_N(1) \\ \vdots & \ddots & \vdots \\ \chi_1(N) & \cdots & \chi_N(N) \end{vmatrix} \quad (3.8)$$

In Equation 3.8,  $N$  is the total number of electrons in the molecule and  $\chi$  a spin-orbital equal to the spin function multiplied by the spatial wave function.

Minimum energy will be calculated through the optimization of the spin orbitals,  $\chi$ , by applying the variational method to Slater determinant. For this purpose Hartree-Fock equation is used which determines the best spin orbital for which will reach its lowest value. Hartree-Fock equation can be written as,

$$f_i \chi_i = \varepsilon_i \chi_i \quad (3.9)$$

where  $f_i$  is the Fock operator,  $\chi_i$  is an eigenfunction of  $f_i$  and  $\varepsilon_i$  is the corresponding energy of the orbital. The one electron Fock-operator is defined for each electron  $i$  as,

$$f_i = -\frac{1}{2}\nabla_i^2 - \sum_k^{nuclei} \frac{Z_k}{r_{ik}} + V_{HF}(i) \quad (3.10)$$

where the final term  $V_{HF}(i)$  is the Hartree-Fock potential.  $V_{HF}(i)$  represents the average repulsive potential experienced by each electron due to the other electrons.

The HF equations form a set of pseudo-eigenvalue equations. The HF equations are solved iteratively; starts with a guess and calculates the energy then improves the guess and recalculates. A set of orbitals that is a solution to the HF equations are called Self-consistent Field (SCF) orbitals.

Hartree-Fock theory neglects correlation between electrons. The electrons are subject to an average non-local potential arising from the other electrons, which can lead to a poor description of the electronic structure. Hartree-Fock theory is insufficiently accurate to make accurate quantitative predictions. There are methods based on the calculation of the wave function including the electron correlation effects, but these methods are computationally very expensive. By considering the inadequacy of HF and cost of higher methods, density functional methods offer a cheaper solution of this problem.

### 3.3. Density Functional Theory

Density functional theory (DFT) [1] is a method to obtain an approximate solution to the Schrödinger equation for many electron systems which based on Kohn-Hohenberg theorems proposed in 1964 [2, 3]. DFT uses electron density as a fundamental property unlike HF theory. Electron density is a functional which is a function of space and time.



The wavefunction of many-electron system is a function of  $3N$  variables, the coordinates of all  $N$  atoms in the system, whereas the electron density is only a function of only three variables ( $x, y, z$ ). Kohn-Hohenberg theorem claims that the density of the system determines all ground-state properties of it. Total ground state electronic energy is the sum of the nucleus-electron attraction potential energies, the electron kinetic energies, and the electron-electron repulsion potential energies and each is a functional of the ground-state electron density  $\rho(r)$  [4],

$$E[\rho(r)] = \int V(r) \rho(r) dr + T[\rho(r)] + V_{ee}[\rho(r)] \quad (3.11)$$

$$\rho(r) = N \int \dots \int |\psi(r_1, r_2, \dots, r_n)|^2 dr_1 dr_2 \dots dr_n \quad (3.12)$$

where  $r$  represents both spin and spatial coordinates of electrons.

To utilize Equation 3.11, Kohn and Sham introduced the idea of a reference system of noninteracting electrons. The electronic energy may be rewritten as,

$$E[\rho(r)] = \int V(r) \rho(r) d(r) + T_{ni}[\rho(r)] + J[\rho(r)] + E_{XC}[\rho(r)] \quad (3.13)$$

where  $J[\rho]$  is the coulomb energy,  $T_{ni}[\rho]$  is the kinetic energy of the non-interacting electrons and  $E_{XC}[\rho]$  is the exchange-correlation energy functional. The Coulomb energy term describes the unfavorable electron-electron repulsion energy and therefore disfavors the total electronic energy. Exchange-correlation energy functional contains a kinetic energy term from the kinetic energy difference between the interacting and non-interacting electron systems. Therefore, it is expressed as the sum of an exchange functional  $E_X[\rho]$  and a correlation functional  $E_C[\rho]$ .

In Kohn-Sham density functional theory, one-body potential  $V_{KS}$  yielding the same density as the real fully-interacting system is considered. A set of independent reference orbitals  $\psi_i$  satisfying the following independent particle Schrödinger equation are imagined.

$$\left[ -\frac{1}{2}\nabla^2 + V_{KS} \right] \psi_i = \varepsilon_i \psi_i \quad (3.14)$$

with the one-body potential  $V_{KS}$  is defined as

$$V_{KS} = v(r) + \frac{\partial J[\rho]}{\partial \rho(r)} + \frac{\partial E_{xc}[\rho]}{\partial \rho(r)} \quad (3.15)$$

$$V_{KS} = v(r) + \frac{\rho(r')}{|r-r'|} dr' + v_{xc}(r) \quad (3.16)$$

where  $V_{xc}(r)$  is the exchange-correlation potential. The independent orbitals  $\psi_i$  are known as Kohn-Sham orbitals and give the exact density by

$$\rho(r) = \sum_i^N |\psi_i|^2 \quad (3.17)$$

if the exact form of the exchange-correlation functional is known. However, the exact form of this functional is not known and approximate forms are developed starting with the local density approximation (LDA).

### 3.3.1. Local Density Approximation

The local density approximation (LDA) is the basis of all approximate exchange-correlation functionals. At the center of this model is the idea of an uniform electron gas, a system in which electrons move on a positive background charge distribution

such that the total ensemble is neutral. The energy expression is,

$$E[\rho] = T_s[\rho] + \int \rho(r) v(r) dr + J[\rho] + E_{xc}[\rho] + E_b \quad (3.18)$$

where  $E_b$  is the electrostatic energy of the positive background. Since the positive charge density is the negative of the electron density due to uniform distribution of particles, the energy expression is reduced to

$$E[\rho] = T_s[\rho] + E_{xc}[\rho] \quad (3.19)$$

$$E[\rho] = T_s[\rho] + E_x[\rho] + E_c[\rho] \quad (3.20)$$

The kinetic energy functional can be written as

$$T_s[\rho] = C_F \int \rho(r)^{5/3} dr \quad (3.21)$$

where  $C_F$  is a constant equal to 2.8712. The exchange functional is given by

$$E_x[\rho] = -C_x \int \rho(r)^{4/3} dr \quad (3.22)$$

with  $C_x$  being a constant equal to 0.7386. The correlation energy,  $E_c[\rho]$ , for a homogeneous electron gas comes from the parametrization of the results of a set of quantum Monte Carlo calculations.

The LDA method underestimates the exchange energy by about 10 percent and does not have the correct asymptotic behavior. The exact asymptotic behavior of the

exchange energy density of any finite many-electron system is given by

$$\lim_{x \rightarrow \infty} U_x^\sigma = -\frac{1}{r} \quad (3.23)$$

$U_x^\sigma$  being related to  $E_x[\rho]$  by

$$E_x[\rho] = \frac{1}{2} \sum_{\sigma} \int \rho_{\sigma} U_x^{\sigma} dr \quad (3.24)$$

In LDA the electron density is assumed to be the same everywhere, but the constant value of the electronic density is not consistent with the rapid variation of densities in a molecule. Generalized gradient approximation (GGA) methods take into account the inhomogeneous nature of the electron density by making the exchange and correlation energies dependent not only on the density but also on its gradient.

### 3.3.2. Generalized Gradient Approximation

Generalized Gradient Approximation (GGA) functionals improve the accuracy provided by Local Density Approximation. GGA functionals depend not just on the value of the density at a point (as in the LDA case) but also on its gradient.

$$E_{XC}^{GGA}[n] = \int n(r) \epsilon_{XC}(n(r), |\nabla n(r)|) dr \quad (3.25)$$

Most GGA functionals are constructed in the form of a correction term which is added to the LDA functional,

$$E_{X/C}^{LDA}[n] = E_{X/C}^{LDA}[n] + \Delta \epsilon_{XC} \left[ \frac{|\nabla(r)|}{n^{4/3}(r)} \right] \quad (3.26)$$

There are several improvements over GGA functionals, hybrid-GGA and meta-GGA. Hybrid density functional methods are alternative approaches that combine the exchange-correlation of GGA method with a percentage of HF exchange. Most famous hybrid density functional is B3LYP [5,6] which is a mix between LDA and GGA functionals taken from the DFT and HF methods as shown below,

$$E_{XC}^{B3LYP} = (1 - a)E_X^{LSDA} + aE_X^{HF} + b\Delta E_X^B + (1 - c)E_C^{LSDA} + cE_C^{LYP} \quad (3.27)$$

where a, b, and c were optimized to 0.20, 0.72, and 0.81, respectively using a set of atomization energies, ionization potentials, proton affinities and total atomic energies and LSDA (Local Spin Density Approximation), HF (Hartree-Fock), B (Becke) and LYP (Lee-Yang-Parr) are the functionals.

M06-2X [7] is another hybrid functional introduced by Zhao *et al.* and this hybrid functional is extensively used in this thesis. The hybrid exchange-correlation can be written as follows:

$$E_{XC}^{hyb} = \frac{X}{100}E_X^{HF} + \left(1 - \frac{X}{100}\right)E_X^{DFT} + E_C^{DFT} \quad (3.28)$$

where X (X=54 in the case of M06-2X functional) is the percentage of Hartree-Fock exchange in the hybrid functional and corresponds to a in Equation 3.28.

### 3.3.3. Time-Dependent Density Functional Theory

Time-dependent density functional theory (TD-DFT) is an extension of DFT to the time-dependent domain. TD-DFT is very useful in modeling energies, structures and properties of electronically excited states (ES). The applications of TD-DFT enclose the simulation of vertical transition states, determination of excited state structures, emission wavelengths, atomic point charges and simulation of photochemical

reactions.

Runge-Gross theorem [8] is the fundamental theory of TD-DFT. Runge-Gross theorem states that the existence of a one-to-one correspondence between a given external potential and an associated electronic density up to a purely time-dependent function.

### 3.4. Basis Sets

Basis set is a set of one-particle functions which are used to build up molecular orbitals (MOs). Basis sets were first developed by Slater. Linear combination of atomic orbitals (LCAO-MO) approximation is used to define molecular orbitals from atomic orbitals.

$$\phi_i = \sum_{\mu=1}^K c_{\mu i} f_{\mu} \quad (3.29)$$

where the functions  $\phi_i$  are molecular orbitals,  $f_{\mu}$  are atomic orbitals,  $c_{\mu i}$  are coefficients and  $K$  is the total number of atomic orbital functions, basis functions.

There are two types of basis sets, Slater-type orbitals (STOs) and Gaussian-type orbitals (GTOs). Hydrogen-like AO functions (STOs) are very suitable for expanding MOs because they have the correct shape. Because GTOs allow for efficient computation of molecular integrals with a simpler formula, in modern DFT GTOs are preferred in practice.

In minimal basis sets, all orbitals are taken into account as to be the same shape. Because this is not realistic, double-zeta basis set considers each atomic orbital separately and expresses as the sum of two Slater-type orbitals (STOs). However, to calculate a double-zeta for every orbital is costly. In order to reduce computational cost, split-valence basis set method is used which is developed by Pople. In this method,

two different basis sets are used for core and valence electrons of an atom. Because the core electrons are less affected by the chemical environment than the valence electrons, core electrons are treated with a minimal basis set while the valence electrons are treated with a larger basis set. Examples for the split-valence basis set are 3-21G and 6-31G where the number on the left hand-side of the dash shows the number of Gaussian functions for inner shell orbitals and the one on the right hand-side for the valence electrons.

The size of basis sets can be improved by polarization and diffuse functions in order to get closer to the exact electronic energy. Polarization functions add higher angular momentum orbital to all heavy atoms designated with a \* or (d). Hydrogen atoms can be polarized as well, this would be done by \*\* or (d,p). Polarization functions are not fully occupied in molecules, they are included to improve the flexibility of the basis set, and to represent better the electron density in bonding regions.

Diffuse functions, represented by a “+”, allow orbitals to occupy larger spaces. It is generally used for the atoms holding loose electrons, the ones in their anion or excited state. One '+' means only 'p' orbitals are considered, while '++' means both 'p' and 's' orbitals are taken into account.

The selection of appropriate functionals and basis set for quantum chemical calculations is very important. The more complex basis sets are more accurate but, they use up a great deal of computing time. Basis set should be chosen according to the desired level of accuracy with reasonable computational cost.

### 3.5. Continuum Solvation Models

Continuum solvation models are the most efficient way to include condensed-phase effects into quantum mechanical calculations [9]. The advantage of these models is that they decrease the number of the degrees of freedom of the system by describing them in a continuous way, usually by means of a distribution function [10, 11]. In continuum solvation models, the solvent is represented as a polarizable medium

characterized by its static dielectric constant and the solute is embedded in a cavity surrounded by this dielectric medium. The total solvation free energy is defined as,

$$\Delta G_{solvation} = \Delta G_{cavity} + \Delta G_{dispersion} + \Delta G_{electrostatic} + \Delta G_{repulsion} \quad (3.30)$$

where  $\Delta G_{cavity}$  is the energetic cost of placing the solute in the medium. Dispersion interactions between solvent and solute are expressed as  $\Delta G_{dispersion}$ , this adds stabilization to solvation free energy.  $\Delta G_{electrostatic}$  is the electrostatic component of the solute-solvent interaction energy.  $\Delta G_{repulsion}$  is the exchange solute-solvent interactions not included in the cavitation energy.

The central problem of continuum solvent models is the electrostatic problem described by the general Poisson equation:

$$-\vec{\nabla} \left[ \epsilon(\vec{r}) \nabla \vec{V}(\vec{r}) \right] = 4\pi \rho_M(\vec{r}) \quad (3.31)$$

simplified to

$$-\nabla^2 V() = 4\pi \rho_M(\vec{r}) \quad \text{within C} \quad (3.32)$$

$$-\epsilon \nabla^2 V(\vec{r}) = 0 \quad \text{outside C} \quad (3.33)$$

where C is the portion of space occupied by cavity,  $\epsilon$  is dielectric function, V is the sum of electrostatic potential  $V_M$  generated by the charge distribution  $\rho_M$  and the reaction potential  $V_R$  generated by the polarization of the dielectric medium:

$$V(\vec{r}) = V_M(\vec{r}) + V_R(\vec{r}) \quad (3.34)$$



Polarizable Continuum Model (PCM) belongs to the class of polarizable continuum solvation models [12]. In PCM, the solute is embedded in a cavity defined by a set of spheres centered on atoms (sometimes only on heavy atoms), having radii defined by the van der Waals radii of the atoms multiplied by a predefined factor (usually 1.2). The cavity surface is then subdivided into small domains (called tesserae), where the polarization charges are placed. There are three different approaches to carry out PCM calculations. The original method is called Dielectric PCM (D-PCM), the second model is the Conductor-like PCM (C-PCM) [13] in which the surrounding medium is modeled as a conductor instead of a dielectric, and the third one is an implementation whereby the PCM equations are recast in an integral equation formalism (IEF-PCM) [14, 15].

## 4. STRUCTURE-REACTIVITY RELATIONSHIPS OF NOVEL MONOMERIC PHOTOINITIATORS

Photopolymerization has been the subject of growing interest in polymer science and technology due to a wide range of application areas in coatings, adhesives, inks, printing plates, dental materials and microelectronics [16–18]. Photopolymerization processes are advantageous over the thermal polymerization processes, because of shorter curing times due to high rate of polymerization at ambient temperatures, lower energy requirements and also having reduced VOC emissions due to solvent-free formulations [19]. These advantages make it useful in daily life and in industry. Photopolymerization in areas such as coatings, adhesives, inks, paints, varnishes, microelectronics, optics, 3D printing, nanotechnology and dental fillings are just the few areas that photopolymerization is used quite a lot [16, 17].

Requirements for a photopolymerization reaction to occur are a polymerizable medium like a monomer or an oligomer, a photoinitiator or a photoinitiating system, and a light source. Photoinitiators are small in mass but have a major role in polymerization medium. A photoinitiator absorbs the energy from the light and generates the reactive species, free radicals or cations. The formed reactive species initiate the polymerization by attacking monomers/oligomers and then converts them into a linear polymer or crosslinked network [20]. Photoinitiators also have The physical and mechanical properties of the cured network depending on the identity of the photoinitiators.

Upon irradiation of photoinitiators, electrons get excited from a bonding ( $\pi$ ) or nonbonding orbital (n) to an antibonding orbital ( $\pi^*$ ). n- $\pi^*$  transitions appear generally in the range of 300-380 nm and have low absorption properties. However  $\pi$ - $\pi^*$  transitions are seen in the shorter wavelengths and have higher absorption properties [18]. Irradiation transfers an electron from the ground state to an excited state if only the states have the same multiplicity. Since ground states are singlet, the first

excitation will generate excited singlet states ( $S_1, S_2 \dots S_n$ ) with an unchanged spin. From there the excited molecule could either return to the ground state by internal conversion (e.g. fluorescence) or move to the triplet state by intersystem crossing. The radical formation occurs through cleavage of the excited molecule on the triplet state (Figure 4.1).

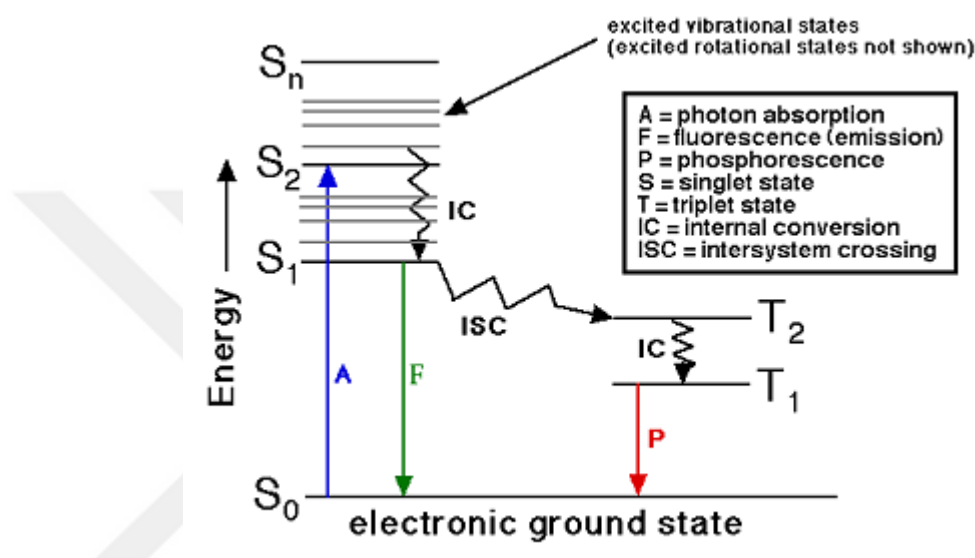


Figure 4.1. Excitation process upon irradiation of a photoinitiator.

#### 4.1. Introduction

Choice of suitable photoinitiator to photopolymerize the monomer at the desired medium is very important. The following requirements are desirable for photoinitiators: high absorptivity in the spectral region of lamp emission, good solubility in the formulation, high quantum yield, high photoreactivity, low odor, low toxicity, no yellowing due to the presence of migrating residues in the polymer, and good storage stability [4]. Small molecular weight commercial photoinitiators do not exhibit all of these properties. Therefore, in recent years, the development of monomeric (MPI) [21–28] and polymeric photoinitiators (PPIs) [29–41] which include the desired properties, has become an important issue.

Photoinitiators produce radicals upon absorption of light by either (i) direct fragmentation via bond cleavage (Type-I), or (ii) a bimolecular reaction where the excited molecule abstracts a hydrogen atom from another molecule play an important role in these processes (Type-II). A Type I photoinitiator is cleaved homolytically by absorbing photons ( $\alpha$ -cleavage), and generates free radicals capable of inducing polymerization (Figure 4.2).

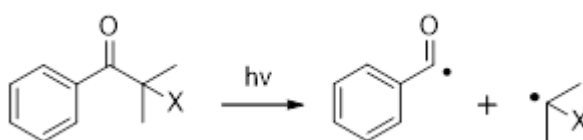


Figure 4.2. Formation of radicals by homolytic cleavage of type-I photoinitiators.

Type II photoinitiation mechanism involves two initiating radical species which are formed by a hydrogen abstraction from a H-donor (coinitiator) such as an amine, alcohol or ether upon light exposure. Upon irradiation, two radicals are produced, a ketyl radical from the carbonyl compound and an alkyl radical from the hydrogen donor. The ketyl radical formed from BP is not reactive toward double bonds because of steric hindrance and delocalization of the unpaired electron (Figure 4.3).

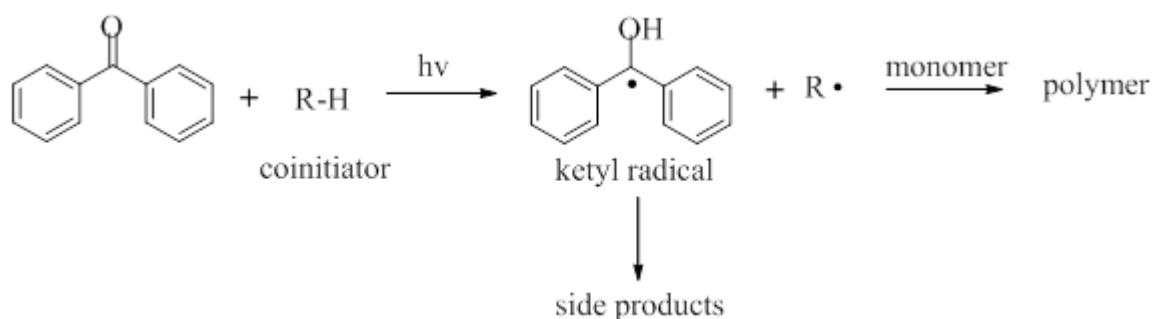


Figure 4.3. Formation of radicals by photolysis of type-II photoinitiators.

During photopolymerization, unreacted photoinitiators or their fragments, which are toxic, may migrate out of the materials. It is important to design a photoinitiator with low migration and high photoinitiation activity for biomedical applications. For that reason, in recent years, polymerizable, oligomeric or polymeric photoinitiators (PPIs) meeting the mentioned requirements received great interest due to their advantages in comparison with their corresponding low molecular weight non-monomeric

analogues. In the present work, both Type I and Type II photoinitiators were attached

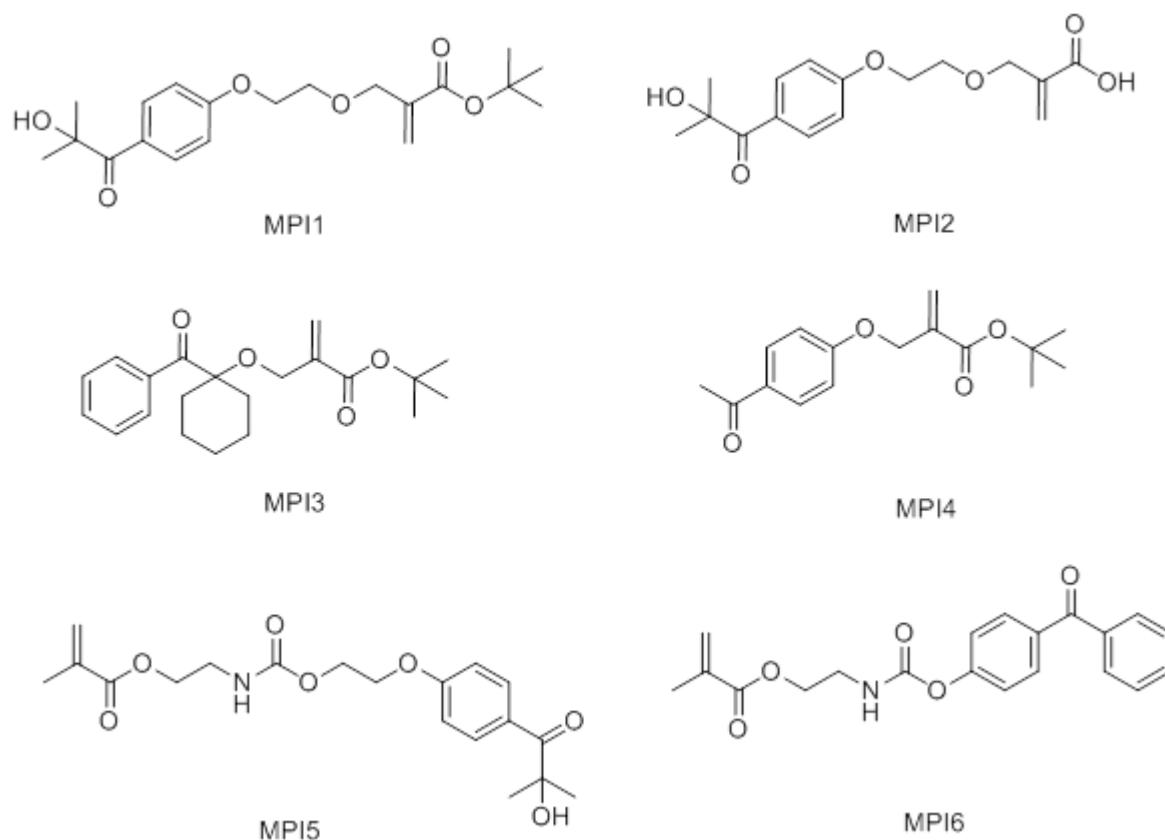


Figure 4.4. Structures of synthesized MPIs.

to two different methacrylates, *tert*-butyl  $\alpha$ -bromomethacrylate and 2-isocyanatoethyl methacrylate (IEM), in order to combine the advantages of polymerizability with the advantageous properties of commercial photoinitiators (Figure 4.4). It was also aimed to investigate the effect of attaching the same photoinitiator to different monomers. The Type I photoinitiators utilized are 2-hydroxy-1-[4-(2-hydroxyethoxy)phenyl]-2-methyl-1-propanone (Irgacure 2959) and 1-hydroxy-cyclohexyl-phenyl-ketone (Irgacure 184), and the Type II photoinitiators are, 4-hydroxy-benzophenone (BP) and acetophenone (AP). In particular, one of the photoinitiators (from TBBr) also has an adhesion promoter carboxylic acid group, which might make it important for metal, glass and hyperbranched polymer surface applications. Monomers MPI1-MPI4 are novel and MPI5 and MPI6 are mentioned in two different patents [42, 43]. Their photoinitiating abilities in the polymerizations of hexane-1,6-diol diacrylate (HDDA), 2-hydroxyethyl methacrylate (HEMA) and trimethylolpropane triacrylate (TMPTA) were studied us-

ing photodifferential scanning calorimeter and the kinetic parameters were correlated with the structures of the photoinitiating systems. Besides photoinitiating activities, also their light absorption properties, electron spin resonance experiments and amount of migrations were investigated.

## 4.2. Materials and Characterization

### 4.2.1. Materials

Irgacure 2959 (2-Hydroxy-1-[4-(2-hydroxyethoxy) phenyl]-2-methyl-1-propanone), Irgacure 184 (1-Hydroxycyclohexyl-1-phenyl methanone), 4-hydroxybenzophenone, 4-hydroxyacetophenone, 2-isocyanatoethyl methacrylate (IEM), 1,6-hexanediol diacrylate (HDDA), 2-hydroxyethyl methacrylate (HEMA) and trimethylolpropane triacrylate (TMPTA), ethyl 4-(dimethylamino)benzoate (EDB), trifluoroacetic acid (TFA), acetophenone (AP), N,N-dimethylaminoethyl methacrylate (DMAEM), benzophenone (BP), and the other reagents were obtained from Sigma-Aldrich and used as received without further purification. Triethyl amine (TEA), dichloromethane (CH<sub>2</sub>Cl<sub>2</sub>), chloroform (CHCl<sub>3</sub>), tetrahydrofuran (THF) and dimethylformamide (DMF) were purchased from Merck and dried over activated molecular sieves (4 Å). *tert*-Butyl  $\alpha$ -bromomethacrylate (TBBr) was synthesized according to literature procedures [44,45].

### 4.2.2. Characterization

<sup>1</sup>H and <sup>13</sup>C NMR spectra were recorded on a Varian Gemini (400 MHz) spectrometer with deuterated chloroform (CDCl<sub>3</sub>) or methanol (MeOD) as solvents. IR spectra were obtained on a Nicolet 6700 FTIR spectrometer. Combi Flash Companion Teledyne ISCO Flash Chromatography was used for purification of the acid monomer. The UV-Vis spectra were obtained by using a Shimadzu UV-2450 spectrophotometer. Photopolymerizations were carried out on a TA Instruments Q100 differential photocalorimeter (DPC). Mass spectrometry (MS) experiments were carried out on a LC-MS-2020-Mass Spectrometer System.

### 4.3. Synthesis of Monomeric Photoinitiators

#### 4.3.1. Synthesis of MPI1

To an ice-cold solution of Irgacure 2959 (1.12 g, 4.99 mmol) and TEA (1.92 g, 18.97 mmol) in 2.5 mL of dry THF under nitrogen, TBBr (1.10 g, 4.98 mmol) in 2.5 mL dry THF was added dropwise. The solution was stirred at 60 °C for 24 h under nitrogen. After evaporation of the solvent, the residue was diluted with 15 mL of CH<sub>2</sub>Cl<sub>2</sub> and then extracted with distilled water (3 x 4 mL). The organic layer was dried over anhydrous sodium sulfate, filtered and evaporated under reduced pressure. The residue was purified by recrystallization from methanol to give the pure product as a white solid (mp = 46 °C) in 76% yield.

<sup>1</sup>H NMR (CDCl<sub>3</sub>, 400 MHz,  $\delta$ ): 1.42 (s, 9H, CH<sub>3</sub>), 1.56 (s, 6H, CH<sub>3</sub>), 3.81 (t, 2H, CH<sub>2</sub>-O), 4.15 (t, 2H, CH<sub>2</sub>-O), 4.19 (s, 2H, CH<sub>2</sub>-O), 5.75 (s, 1H, CH<sub>2</sub>=C), 6.14 (s, 1H, CH<sub>2</sub>=C), 6.90 (d, 2H, Ar-H), 7.98 (d, 2H, Ar-H) ppm.

<sup>13</sup>C NMR (CDCl<sub>3</sub>, 400 MHz,  $\delta$ ): 28.04 (CH<sub>3</sub>), 28.68 (C(CH<sub>3</sub>)<sub>3</sub>), 67.57, 68.98, 69.65 (CH<sub>2</sub>-O), 75.74 (C-OH), 80.99 (C(CH<sub>3</sub>)<sub>3</sub>), 115.00 (Ar-CH), 124.84 (CH<sub>2</sub>=C), 125.98 (Ar-C), 132.32 (Ar-CH), 138.41 (C=CH<sub>2</sub>), 162.65 (Ar-C-O), 165.03 (C=O, ester), 202.56 (C=O, ketone) ppm.

FTIR (ATR, cm<sup>-1</sup>): 3420 (OH), 2970 (C-H), 1720 (C=O, ester), 1663 (C=O, ketone), 1133 (C-O).

#### 4.3.2. Synthesis of MPI2

TFA (1.23 g, 10.79 mmol) was added to MPI1 (0.98 g, 2.69 mmol) dropwise in an ice-bath and under nitrogen. After stirring at room temperature for 24 hours, the volatile components were removed under reduced pressure. The crude product was purified by reversed-phase flash chromatography on C<sup>18</sup>, eluting with water/acetonitrile system to give MPI2 as a white crystalline solid (mp = 83 °C) in 50% yield.

$^1\text{H}$  NMR (MeOD, 400 MHz,  $\delta$ ): 1.41 (s, 6H,  $\text{CH}_3$ ), 3.78 (t, 2H,  $\text{CH}_2\text{-O}$ ), 4.14 (t, 2H,  $\text{CH}_2\text{-O}$ ), 4.19 (s, 2H,  $\text{CH}_2\text{-O}$ ), 5.81 (s, 1H,  $\text{CH}_2=\text{C}$ ), 6.18 (s, 1H,  $\text{CH}_2=\text{C}$ ), 6.90 (d, 2H, Ar-H), 8.10 (d, 2H, Ar-H) ppm.

$^{13}\text{C}$  NMR (MeOD, 400 MHz,  $\delta$ ): 27.18 ( $\text{CH}_3$ ), 67.34, 68.82, 69.16 ( $\text{CH}_2\text{-O}$ ), 76.97 ( $\text{C-CH}_3$ ), 113.75 (Ar-CH), 125.18 (Ar-C), 127.51 ( $\text{CH}_2=\text{C}$ ), 132.31 (Ar-CH), 137.71 ( $\text{C}=\text{CH}_2$ ), 162.44 (Ar-C-O), 167.57 ( $\text{C}=\text{O}$ , acid), 203.08 ( $\text{C}=\text{O}$ , ketone) ppm.

FTIR (ATR,  $\text{cm}^{-1}$ ): 3400 (OH, alcohol), 2969 (C-H), 2937 (OH, acid), 1707 ( $\text{C}=\text{O}$ , acid), 1656 ( $\text{C}=\text{O}$ , ketone), 1152 (C-O).

MS ( $m/z$ ): Calcd for  $\text{C}_{16}\text{H}_{20}\text{O}_6$ , 308.13. Found: 308.90  $[\text{M}+\text{H}]^+$ .

### 4.3.3. Synthesis of MPI3

Irgacure 184 (0.51 g, 2.50 mmol) in 3 mL of dry DMF was added on to NaH (60% dispersion in mineral oil, 0.14 g, 5.8 mmol) dropwise at 0 °C under nitrogen. After stirring 45 minutes at room temperature, TBBr (1.27 g, 5.8 mmol) in 2 mL of dry DMF was added dropwise and the solution was stirred at room temperature for 24 h. The reaction was quenched by addition of water and the resulting white precipitate was isolated, washed with hexane ( $3 \times 10$  mL) and dried under reduced pressure to give the crude product. Final purification by column chromatography on silica gel using hexane initially and gradually changing to  $\text{CH}_2\text{Cl}_2$  as eluent, afforded the pure product as a viscous liquid in 40% yield.

$^1\text{H}$  NMR ( $\text{CDCl}_3$ , 400 MHz,  $\delta$ ): 1.37 (s, 9H,  $\text{CH}_3$ ), 1.50-1.78 (m, 6H,  $\text{CH}_2$ ), 2.06 (d, 4H, ring- $\text{CH}_2$ ), 3.88 (s, 2H,  $\text{CH}_2\text{-O}$ ), 5.75 (s, 1H,  $\text{CH}_2=\text{C}$ ), 6.12 (s, 1H,  $\text{CH}_2=\text{C}$ ), 7.32 (t, 2H, Ar-H-m), 7.43 (t, 1H, Ar-H-p), 8.15 (d, 2H, Ar-H-o) ppm.

$^{13}\text{C}$  NMR ( $\text{CDCl}_3$ , 400 MHz,  $\delta$ ): 21.44 ( $\text{CH}_2$ ), 25.49 ( $\text{CH}_2$ ), 28.01 ( $\text{CH}_3$ ), 32.55 ( $\text{CH}_2$ ), 61.88 ( $\text{CH}_2\text{-O}$ ), 80.97 ( $\text{C}(\text{CH}_3)_3$ ), 84.05 (C- $\text{CH}_2$ ), 124.54 ( $\text{CH}_2=\text{C}$ ), 128.19 (Ar-CH-m), 129.58 (Ar-CH-o), 132.61 (Ar-CH-p), 135.28 (Ar-C), 138.81 ( $\text{C}=\text{CH}_2$ ), 164.91 ( $\text{C}=\text{O}$ ,



ester), 203.80 (C=O, ketone) ppm.

FTIR (ATR,  $\text{cm}^{-1}$ ): 2927 (C-H), 1694 (C=O, ester), 1672 (C=O, ketone), 1147 (C-O).

#### 4.3.4. Synthesis of MPI4

To a mixture of 4-hydroxyacetophenone (1.63 g, 12.00 mmol) and  $\text{K}_2\text{CO}_3$  (18.04 g, 130.50 mmol) in acetone (25 mL) under nitrogen, TBBr (2.88 g, 13.00 mmol) was added dropwise at room temperature. After stirring at 60 °C for 48 h, the solvent was removed under reduced pressure.  $\text{CH}_2\text{Cl}_2$  (5 mL) was added and the solution was extracted with water ( $3 \times 5$  mL). The organic phase was dried over anhydrous sodium sulfate, filtered and the solvent was evaporated under reduced pressure. The residue was purified by recrystallization from methanol to give the pure product as a white solid (mp = 44-45 °C) in 51% yield.

$^1\text{H-NMR}$  ( $\text{CDCl}_3$ , 400 MHz,  $\delta$ ): 1.45 (s, 9H,  $\text{CH}_3$ ), 2.48 (s, 3H,  $\text{CH}_3\text{-C=O}$ ), 4.71 (s, 2H,  $\text{CH}_2\text{-O}$ ), 5.82 (s, 1H,  $\text{CH}_2=\text{C}$ ), 6.24 (s, 1H,  $\text{CH}_2=\text{C}$ ), 6.89 (d, 2H, Ar-H), 7.86 (d, 2H, Ar-H) ppm.

$^{13}\text{C}$  NMR ( $\text{CDCl}_3$ , 400 MHz,  $\delta$ ): 26.32 ( $\text{CH}_3$ ), 28.05 ( $\text{C}(\text{CH}_3)_3$ ), 66.32 ( $\text{CH}_2\text{-O}$ ), 81.50 ( $\text{C}(\text{CH}_3)_3$ ), 114.42 (Ar-CH), 125.59 ( $\text{CH}_2=\text{C}$ ), 130.56 (Ar-C), 130.64 (Ar-CH), 136.74 ( $\text{C}=\text{CH}_2$ ), 162.22 (Ar-C-O), 164.48 (C=O, ester), 196.67 (C=O, ketone) ppm.

FTIR (ATR,  $\text{cm}^{-1}$ ): 2971 (C-H), 1713 (C=O, ester), 1670 (C=O, ketone), 1148 (C-O).

MS (m/z): Calcd for  $\text{C}_{16}\text{H}_{20}\text{O}_4$ , 276.14. Found: 276.90  $[\text{M}+\text{H}]^+$ .

#### 4.3.5. Synthesis of MPI5

To a solution of the Irgacure 2959 (3.09 g, 13.80 mmol) in anhydrous  $\text{CH}_2\text{Cl}_2$  (6 mL), a 1% solution of dibutyltin dilaurate in anhydrous  $\text{CH}_2\text{Cl}_2$  (4 mL) followed by IEM (13.80 mmol) were added dropwise under nitrogen. The solution was stirred for

3 h at room temperature and concentrated under reduced pressure to leave the crude product. The crude product was purified by column chromatography on silica gel using hexane initially and gradually changing to ethyl acetate as eluent. The pure product was obtained as a white solid (mp = 81-82 °C) in 50% yield.

$^1\text{H-NMR}$  ( $\text{CDCl}_3$ , 400 MHz,  $\delta$ ): 1.56 (s, 6H,  $\text{CH}_3$ ), 1.86 (s, 3H,  $\text{CH}_3$ ), 3.45 (t, 2H,  $\text{CH}_2\text{-N}$ ), 4.17 (t, 4H,  $\text{CH}_2\text{-O}$ ), 4.39 (t, 2H,  $\text{CH}_2\text{-O}$ ), 5.52 (s, 1H,  $\text{CH}_2\text{=C}$ ), 6.04 (s, 1H,  $\text{CH}_2\text{=C}$ ), 6.89 (d, 2H, Ar-H), 7.99 (d, 2H, Ar-H) ppm.

$^{13}\text{C-NMR}$  ( $\text{CDCl}_3$ , 400 MHz,  $\delta$ ): 18.28 ( $\text{CH}_3$ ), 28.67 ( $\text{CH}_3\text{-C-OH}$ ), 40.28 ( $\text{CH}_2\text{-N}$ ), 63.04, 63.60, 66.53 ( $\text{CH}_2\text{-O}$ ), 75.82 ( $\text{CH}_3\text{-C-OH}$ ), 113.33 (Ar-CH), 126.09 ( $\text{CH}_2\text{=C}$ ), 126.28 (Ar-C), 132.39 (Ar-CH), 135.89 ( $\text{C=CH}_2$ ), 156.02 ( $\text{C=O}$ , urethane), 162.30 (Ar-C-O), 167.24 ( $\text{C=O}$ , ester), 202.58 ( $\text{C=O}$ , ketone) ppm.

FTIR (ATR,  $\text{cm}^{-1}$ ) : 3433 (N-H), 3364 (O-H), 2958 (C-H), 1723 ( $\text{C=O}$ , ester), 1699 ( $\text{C=O}$ , urethane), 1666 ( $\text{C=O}$ , ketone), 1155 (C-O).

MS (m/z): Calcd for  $\text{C}_{19}\text{H}_{25}\text{NO}_7$ , 379.16. Found: 379.90  $[\text{M}+\text{H}]^+$ .

#### 4.3.6. Synthesis of MPI6

To a solution of 4-hydroxybenzophenone (2.74 g, 13.80 mmol) in anhydrous  $\text{CH}_2\text{Cl}_2$  (6 mL), a 1% solution of dibutyltin dilaurate in anhydrous  $\text{CH}_2\text{Cl}_2$  (4 mL) followed by IEM (13.80 mmol) were added dropwise under nitrogen. The solution was stirred for 3 h at room temperature and concentrated under reduced pressure to leave the crude product. The crude product was recrystallized from methanol and the pure product was obtained as a white solid (mp= 109-110 °C) in 68% yield.

$^1\text{H-NMR}$  ( $\text{CDCl}_3$ , 400 MHz,  $\delta$ ): 1.91 (s, 3H,  $\text{CH}_3$ ), 3.56 (t, 2H,  $\text{CH}_2\text{-N}$ ), 4.27 (t, 2H,  $\text{CH}_2\text{-O}$ ), 5.57 (s, 1H,  $\text{CH}_2\text{=C}$ ), 6.10 (s, 1H,  $\text{CH}_2\text{=C}$ ), 7.19 (d, 2H, Ar-H), 7.42 (t, 2H, Ar-H-m), 7.53 (t, 1H, Ar-H-p), 7.73 (d, 2H, Ar-H), 7.77 (d, 2H, Ar-H-o) ppm.

$^{13}\text{C}$ -NMR ( $\text{CDCl}_3$ , 400 MHz,  $\delta$ ): 18.18 ( $\text{CH}_3$ ), 40.40 ( $\text{CH}_2\text{-N}$ ), 63.26 ( $\text{CH}_2\text{-O}$ ), 121.14 ( $\text{Ar-CH}$ ), 126.16 ( $\text{C}=\text{CH}_2$ ), 128.19 ( $\text{Ar-CH-m}$ ), 129.80 ( $\text{Ar-CH-o}$ ), 131.51 ( $\text{Ar-CH}$ ), 132.32 ( $\text{Ar-CH-p}$ ), 134.30 ( $\text{Ar-C}$ ), 135.76 ( $\text{C}=\text{CH}_2$ ), 137.39 ( $\text{Ar-C}$ ), 153.83 ( $\text{C}=\text{O}$ , urethane), 154.18 ( $\text{Ar-C-O}$ ), 167.23 ( $\text{C}=\text{O}$ , ester), 195.60 ( $\text{C}=\text{O}$ , ketone) ppm.

FTIR (ATR,  $\text{cm}^{-1}$ ): 3350 (N-H), 2963 (C-H), 1743 ( $\text{C}=\text{O}$ , ester), 1700 ( $\text{C}=\text{O}$ , urethane), 1659 ( $\text{C}=\text{O}$ , ketone), 1185 (C-O).

MS ( $m/z$ ): Calcd for  $\text{C}_{20}\text{H}_{19}\text{NO}_5$ , 353.13. Found: 353.95  $[\text{M}+\text{H}]^+$ .

## 4.4. Experimental Work

### 4.4.1. Photopolymerization Experiments

Monomer (HDDA, TMPTA or HEMA) samples (3-4 mg) containing 2 mol% of Type I photoinitiator or 1/3 mol% of Type II photoinitiator/amine (DMAEM) formulation were irradiated at 40 °C under nitrogen with a mercury lamp (light intensity of 20  $\text{mW}/\text{cm}^2$ ). Rates of polymerization were calculated according to the following formula:

$$\text{Rate} = \frac{\left(\frac{\text{Q}}{\text{s}}\right)\text{M}}{n\Delta H_p m} \quad (4.1)$$

where  $\text{Q}/\text{s}$  is the heat flow per second,  $\text{M}$  the molar mass of the monomer,  $n$  the number of double bonds per monomer molecule,  $\Delta H_p$  the heat released per mole of double bonds reacted and  $m$  the mass of monomer in the sample. The theoretical value used for  $\Delta H_p$  was 13.1 kcal/mol for methacrylate double bonds.

### 4.4.2. ESR Spin Trapping (ESR-ST) Experiments

ESR-ST experiments were carried out using a Bruker EMX-plus spectrometer (X-band). The radicals were produced at room temperature upon irradiation by LED

at 385 nm under nitrogen and trapped by phenyl-N-tert-butyl nitron (PBN) according to a procedure described in the literature [46]. The ESR spectra simulations were carried out using the WINSIM software.

#### 4.4.3. Computational Calculations

All calculations were carried out with the Gaussian 09 series of programs [47]. Geometry optimizations were done with density functional theory at B3LYP/6-31G(d) level after detailed conformational search for all photoinitiators. The electronic absorption spectra of the compounds were calculated with the time-dependent density functional theory at the B3LYP/6-31G(d) level on their most stable conformation in chloroform.

#### 4.4.4. Migration Study

HDDA in the presence of MPI1, MPI2, MPI5 and Irgacure 2959 ( $1.12 \times 10^{-5}$  mol  $\text{g}^{-1}$ ) was photopolymerized under air in teflon molds for 30 minutes. The crosslinked polymers were ground into small particles and immersed in 25 mL of chloroform for 7 days. The amount of extracted photoinitiators was determined by UV-vis spectroscopy. The concentration ( $c$ ) of extracted photoinitiator was determined according to the Beer-Lambert law, and the weight ( $m$ ) was calculated by,

$$m = McV_{\text{solution}} = \frac{MA10^{-2}}{\varepsilon l} \quad (4.2)$$

where  $\varepsilon$  was molar extinction coefficient of photoinitiator in acetonitrile,  $l$  was optical path length,  $A$  was absorbance and  $M$  was molecular weight of photoinitiator [25].

## 4.5. Results and Discussions

### 4.5.1. Synthesis and Characterization of Photoinitiators

To synthesize the first group of MPIs, three commercial photoinitiators, Irgacure 2959, Irgacure 184 and 4-hydroxyacetophenone were separately attached to TBBr. The nucleophilic substitution reaction of Irgacure 2959 with TBBr in the presence of TEA gave MPI1 as a white solid in 76% yield (Figure 4.5). Cleavage of the *tert*-butyl groups of MPI1 using TFA and purification of the crude product using reversed-phase flash chromatography on C18 gave MPI2 as a white solid in 50% yield. Our attempt to perform reaction of Irgacure 184 with TBBr under identical conditions with Irgacure 2959 was unsuccessful and gave very low yield of MPI3. This result can be attributed to the sterically hindered structure of Irgacure 184 (3° alcohol). Therefore, the standard Williamson synthesis method, namely reaction of alkoxide ion with TBBr via an S<sub>N</sub>2 reaction was used to give MPI3 as viscous liquid in good yields. The last monomer of this group (MPI4) was also obtained through nucleophilic substitution reaction of 4-hydroxyacetophenone with TBBr under basic conditions as a white solid with melting point of 44-45 °C in 51% after recrystallization from methanol.

To synthesize the second group of MPIs, two commercial photoinitiators, Irgacure 2959, and 4-hydroxybenzophenone were separately attached to IEM to give MPI5 or MPI6, respectively, in a one-pot reaction in dry CH<sub>2</sub>Cl<sub>2</sub> under stoichiometric conditions (Figure 4.6). Analysis of the reaction by FTIR showed disappearance of the NCO (around 2160 cm<sup>-1</sup>) peak and the photoinitiators were obtained with quantitative yield after 3 h of reaction. MPI5 and MPI6 were obtained as white solids with melting points of 81-82 °C and 109-110 °C, respectively.

The photoinitiators were characterized on the basis of their <sup>1</sup>H, <sup>13</sup>C NMR and FTIR spectroscopic data (Figure 4.7- 4.9). In the FTIR spectrum of the photoinitiators, the absorptions at 1700-1740, 1700 and 1660-1670 cm<sup>-1</sup> were assigned to the ester, urethane and ketone carbonyl bonds (Figure 4.7). In addition, MPI1 and MPI2 displayed a sharp peak at around 3400 cm<sup>-1</sup> due to OH stretching vibrations.

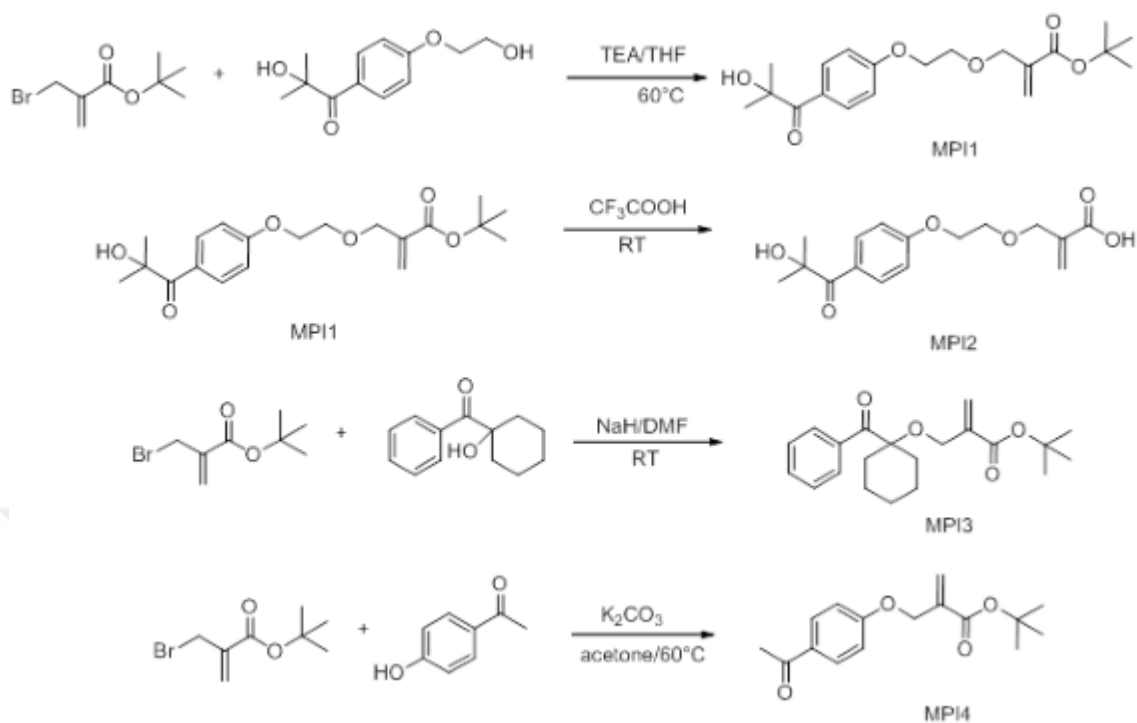


Figure 4.5. Synthesis of MPIs from TBBBr.

The <sup>1</sup>H NMR spectrum of MPI1 showed peaks characteristic of two different methyl protons at 1.42 and 1.56 ppm, methylene protons adjacent to oxygens at 3.81, 4.15 and 4.19 ppm, double bond protons at 5.75 and 6.14 ppm and aromatic protons at 6.90 and 7.98 ppm (Figure 4.8). In the <sup>1</sup>H NMR of MPI2, the absence of *tert*-butyl peak confirmed the purity of this monomer. The <sup>1</sup>H NMR spectrum of MPI3 shows peaks between 1.37 and 2.06 due to cyclohexyl and *tert*-butyl protons (Figure 4.8). In the <sup>1</sup>H NMR spectrum of MPI4 the singlet at 2.48 ppm corresponds to the methyl protons of the AP group (Figure 4.8).

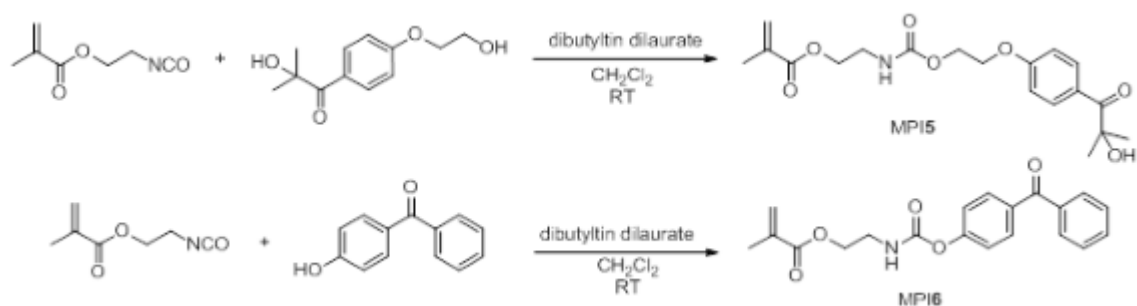


Figure 4.6. Synthesis of MPIs from IEM.

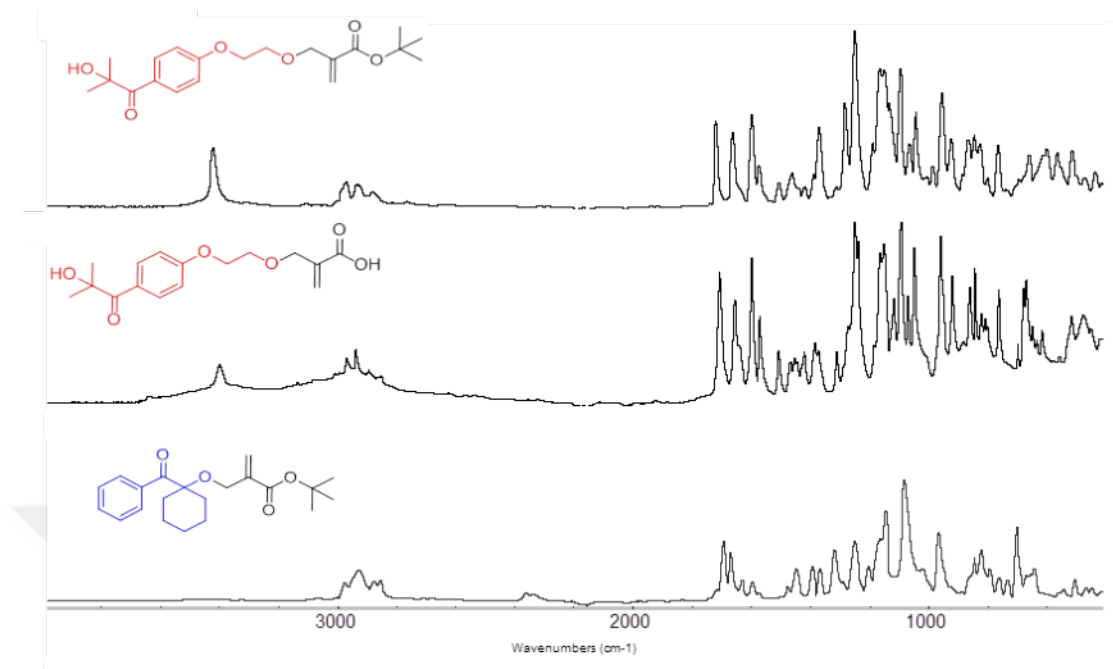


Figure 4.7. The FTIR spectra of MPI1, MPI2 and MPI3.

Table 4.1. Solubilities of MPIs.

MPIs	H <sub>2</sub> O	Methanol	CH <sub>2</sub> Cl <sub>2</sub>	THF	Acetone	Ether	Hexane
MPI1	-	+	+	+	+	+	-
MPI2	-	+	+*	+	+	-	-
MPI3	-	+	+	+	+	-	+
MPI4	-	+	+	+	+	+	+
MPI5	-	+	+	+	+	-	-
MPI6	-	+	+	+	+	+	-

\*partially soluble

The <sup>13</sup>C NMR spectrum of MPI6 showed two different carbonyl carbon peaks at 167.23 and 195.60 ppm due to ester and ketone groups (Figure 4.9).

MPIs show high solubility in common organic solvents such as acetone, THF and methanol and good compatibility with commercial acrylate monomers such as HDDA, HEMA and TMPTA (except MPI2 with HDDA and TMPTA) (Table 4.1).

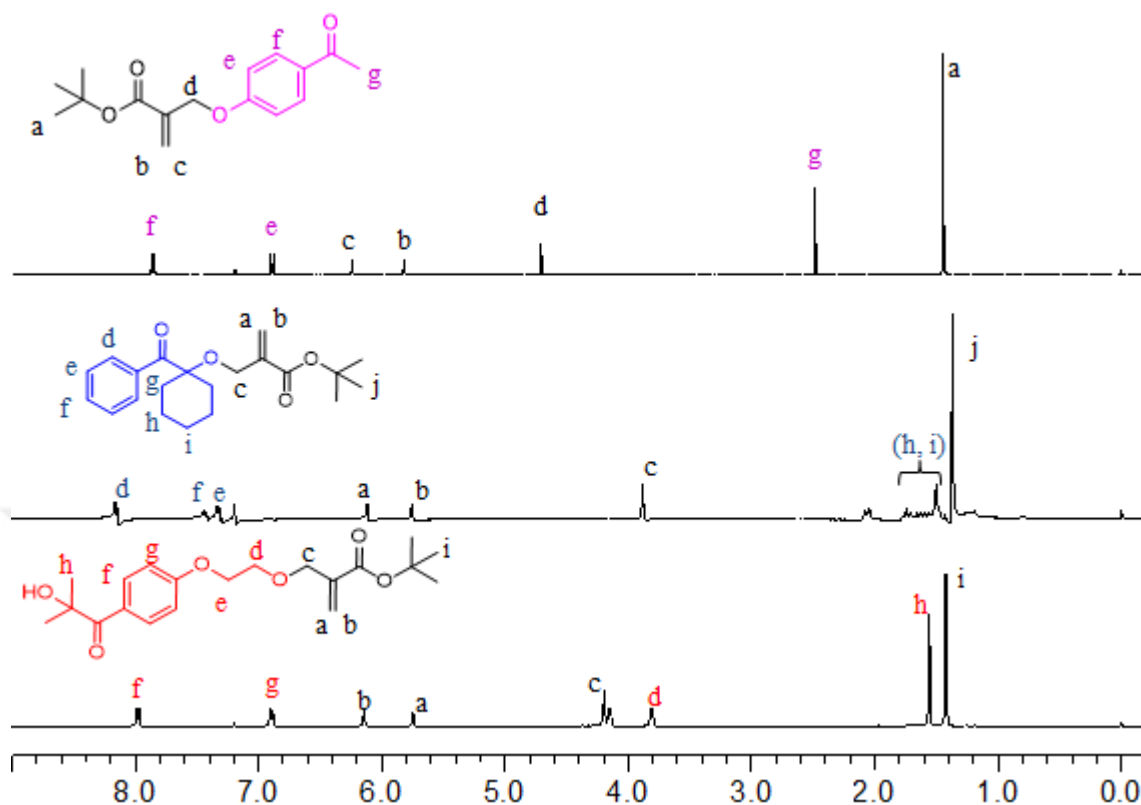


Figure 4.8.  $^1\text{H}$  NMR spectra of MPI1, MPI3 and MPI4.

#### 4.5.2. Light Absorption Properties of the Novel Photoinitiators

The UV absorption spectra (Figure 4.10) of the synthesized photoinitiators and the commercial ones as references were measured in  $\text{CHCl}_3$ . The wavelengths of maximum absorptions ( $\lambda_{max}$ ) and molar extinction coefficients ( $\epsilon$ ) are summarized in Table 4.2. Irgacure 2959-containing MPIs (MPI1, MPI2 and MPI5) exhibit strong  $\pi \rightarrow \pi^*$  absorption maxima at  $\lambda_{max}$  values (276-280 nm) similar to Irgacure 2959 ( $\lambda_{max} = 276$  nm). The extinction coefficients of these MPIs were also found to be similar to that of their commercial analogue except MPI2. Although MPI3 exhibits strong  $\pi \rightarrow \pi^*$  absorption maximum at  $\lambda_{max}$  similar to Irgacure 184, its extinction coefficient was found to be much lower compared to it. BP-containing MPI6 also exhibits strong  $\pi \rightarrow \pi^*$  absorption maximum with  $\lambda_{max}$  and  $\epsilon$  values similar to BP, with a peak broadened toward higher wavelength. The absorption of MPI4 is red shifted ( $\lambda_{max} = 270$  nm) compared to AP ( $\lambda_{max} = 244$  nm), which may be due to the effect of the oxygen atom attached to AP. Also, its extinction coefficient ( $\epsilon = 17415 \text{ M}^{-1} \text{ cm}^{-1}$ ) was found to



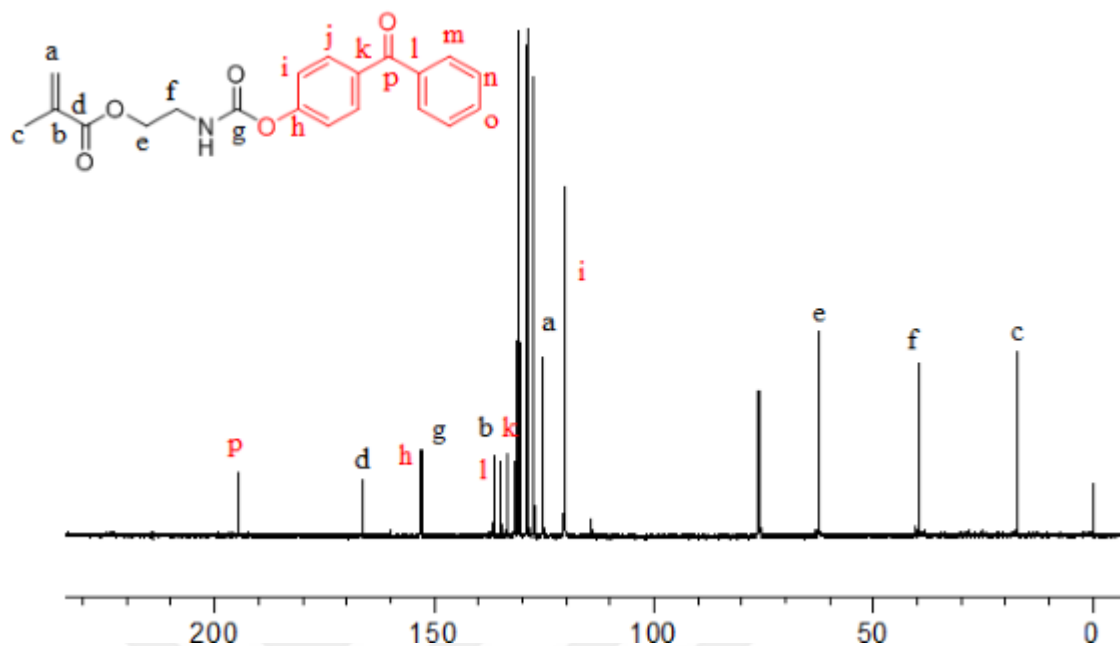


Figure 4.9.  $^{13}\text{C}$  NMR spectrum of MPI6.

be higher than AP ( $\epsilon = 12963 \text{ M}^{-1} \text{ cm}^{-1}$ ). Molecular orbital calculations confirm this red-shift e.g. for MPI4 ( $\lambda_{max} = 266 \text{ nm}$ ,  $f = 0.4942$ ) vs AP ( $\lambda_{max} = 239 \text{ nm}$ ,  $f = 0.3117$ ), being the oscillator strength characterizing the intensity of the transition. In general,  $n \rightarrow \pi^*$  transitions are at 300-350 nm with a low extinction coefficient due to the spin-forbidden transition. In all initiators except BP and MPI6, no obvious  $n \rightarrow \pi^*$  transition was observed, we believe since that wavelength region is dominated by the strong  $\pi \rightarrow \pi^*$  transition peak.

#### 4.5.3. Molecular Modeling

Molecular orbital calculations (using TD-DFT at B3LYP/6-31G(d) level with SCRF solvent model in  $\text{CHCl}_3$ ) showed that, for all of the photoinitiators, the excellent absorption properties are associated with a HOMO to LUMO charge transfer transition with a  $\pi \rightarrow \pi^*$  character. In Figure 4.11, it can be noticed that the HOMO and LUMO are mainly localized on the fragments of the benzene groups as donor moiety and carbonyl groups as acceptor moiety. The calculated most important electronic transitions are tabulated in Table 4.2. The calculated spectra are in good agreement with the experimental ones (Figure 4.12).

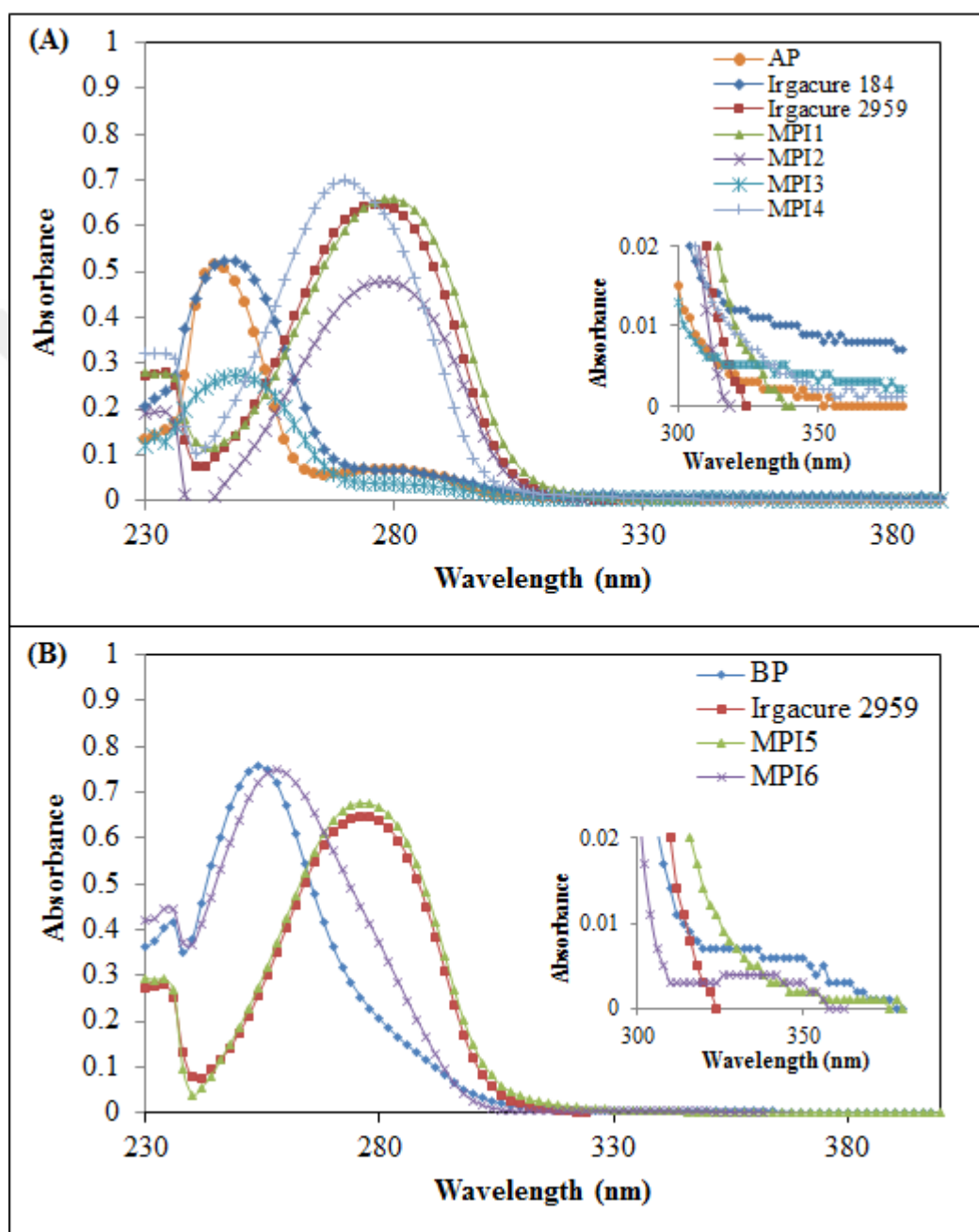


Figure 4.10. Absorption spectra of (A) group 1 and (B) group 2 photoinitiators in  $\text{CHCl}_3$  ( $4 \times 10^{-5} \text{ M}$ ) solution.

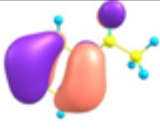
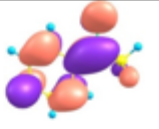

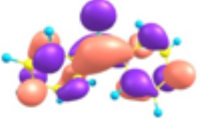
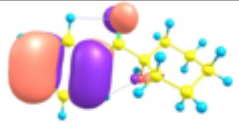
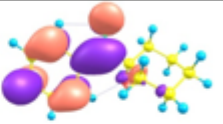

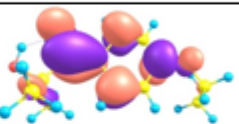
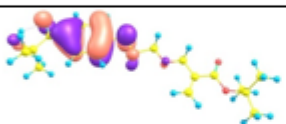
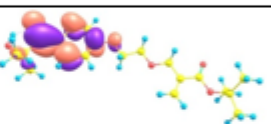

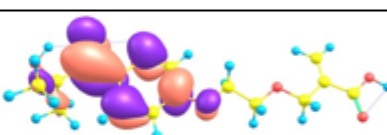
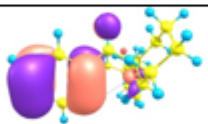
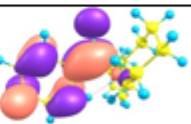
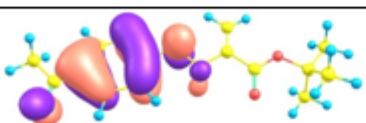
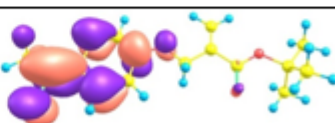

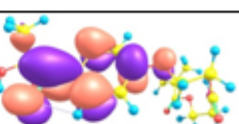
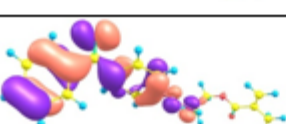
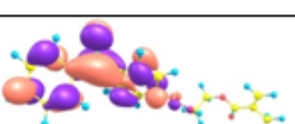
PIs	HOMO (-1/-2)	LUMO
AP		
BP		
Irgacure 184		
Irgacure 2959		
MPI1		
MPI2		
MPI3		
MPI4		
MPI5		
MPI6		

Figure 4.11. Transition molecular orbitals of the photoinitiators.

Table 4.2. Absorption properties in  $\text{CHCl}_3$  solution, energies(eV) and wavelength (nm) of experimental absorption bands, and the most important electronic transitions calculated with B3LYP/ 6-31G(d).

PI	Excitations	Character	$\lambda(\text{nm})$	E(eV)	$f$	Exp. $\lambda(\text{nm})[\epsilon]$
AP	H-2 $\rightarrow$ L	$\pi(\text{Ph}) \rightarrow \pi^*(\text{Ph})$	238.96	5.1884	0.3117	244 [12963]
BP	H-3 $\rightarrow$ L	$\pi(\text{Ph}) \rightarrow \pi^*(\text{Ph})$ $\text{n}(\text{C=O}) \rightarrow \pi^*(\text{C=O})$	266.93	4.6449	0.3240	254 [18938]
Irg184	H-2 $\rightarrow$ L	$\pi(\text{Ph}) \rightarrow \pi^*(\text{Ph})$	249.45	4.9703	0.3387	248 [9685]
Irg2959	H $\rightarrow$ L	$\pi(\text{Ph}) \rightarrow \pi^*(\text{Ph})$	281.47	4.4048	0.4387	276 [16495]
MPI1	H $\rightarrow$ L	$\pi(\text{Ph}) \rightarrow \pi^*(\text{Ph})$	279.90	4.4296	0.4662	280 [16657]
MPI2	H $\rightarrow$ L	$\pi(\text{Ph}) \rightarrow \pi^*(\text{Ph})$	280.88	4.4142	0.4721	278 [11990]
MPI3	H-2 $\rightarrow$ L	$\pi(\text{Ph}) \rightarrow \pi^*(\text{Ph})$	249.07	4.9779	0.2528	258 [317]
MPI4	H $\rightarrow$ L	$\pi(\text{Ph}) \rightarrow \pi^*(\text{Ph})$	266.13	4.6589	0.4942	270 [17415]
MPI5	H $\rightarrow$ L	$\pi(\text{Ph}) \rightarrow \pi^*(\text{Ph})$	279.92	4.4292	0.4707	276 [16876]
MPI6	H-1 $\rightarrow$ L	$\pi(\text{Ph}) \rightarrow \pi^*(\text{Ph})$ $\text{n}(\text{C=O}) \rightarrow \pi^*(\text{C=O})$	281.12	4.4104	0.5143	258 [19133]

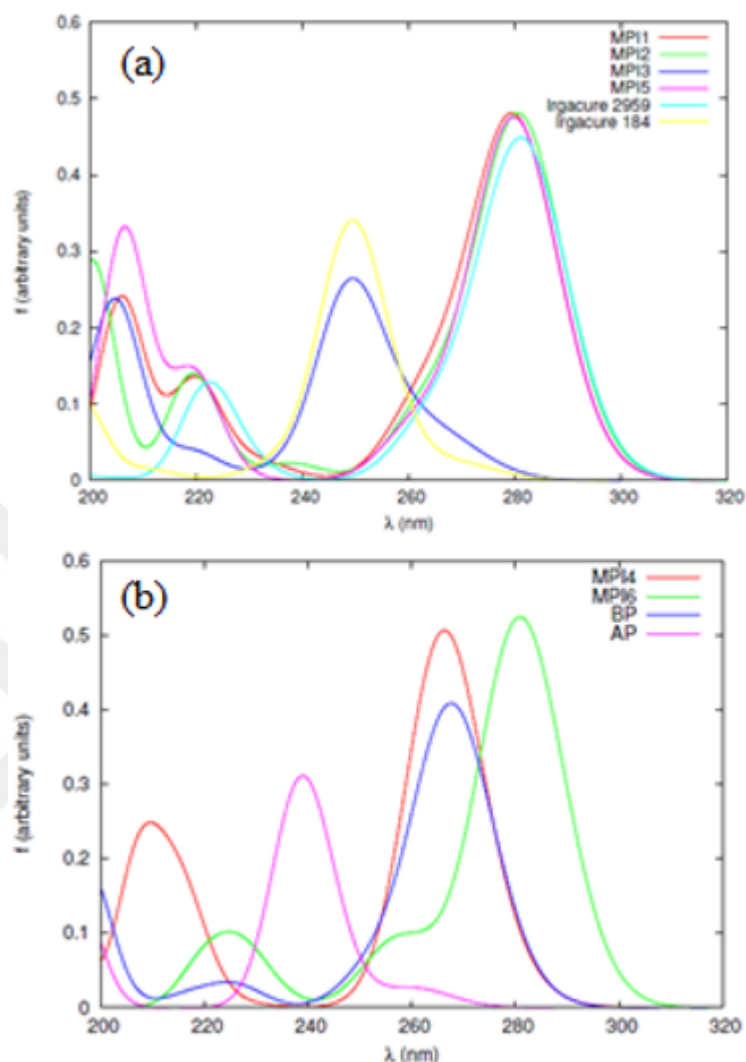
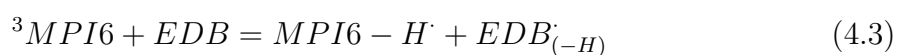


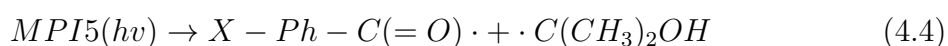
Figure 4.12. Calculated/Theoretical UV spectra of the photoinitiators for (a) group 1 and (b) group 2. (TD-DFT B3LYP/6-31G(d) in  $\text{CHCl}_3$ ).

#### 4.5.4. Electron Spin Resonance (ESR) Experiments

ESR-spin trapping experiments were carried out on MPI5 and MPI6 as representative derivatives of Irgacure 2959 (Type I) and BP (Type II) derivatives. MPI6/EDB solution leads to a radical which corresponds to aminoalkyl radical ( $\text{EDB}_{(-H)}\cdot$ ) (Figure 4.13; PBN/ $\text{EDB}_{(-H)}\cdot$  adduct:  $a_N = 14.40$  G;  $a_H = 2.42$  G; reference values [48]) in agreement with Equation 4.3:



MPI5 solution spectrum shows substituted-benzoyl ( $a_N = 14.2$  G,  $a_H = 4.6$  G [49]) as major radical trapped by PBN in agreement with a Type I behavior for this compound (Equation 4.4). A minor radical is also observed (characterized by  $a_N = 14.1$  G,  $a_H = 1.8$  G) that is not fully identified but can perhaps be associated with the addition the radical onto methacrylate double bond of MPI5 leading to methacrylate derived radical after 2 minutes of irradiation.



#### 4.5.5. Photoinitiating Activities

The photoinitiating activities of synthesized monomeric photoinitiators (MPI1, MPI2, MPI3, MPI4/DMAEM, MPI5 and MPI6/DMAEM) were tested toward a monofunctional methacrylate (HEMA) and/or multifunctional acrylates (HDDA and TMPTA) with photo-DSC under nitrogen at 40 °C, in combinations that can be seen in Table 4.4. The rates of polymerizations (Figure 4.14- 4.16) and conversions (Figure 4.17) were compared with the commercial photoinitiators BP, AP, Irgacure 184 and Irgacure 2959 under the same conditions.

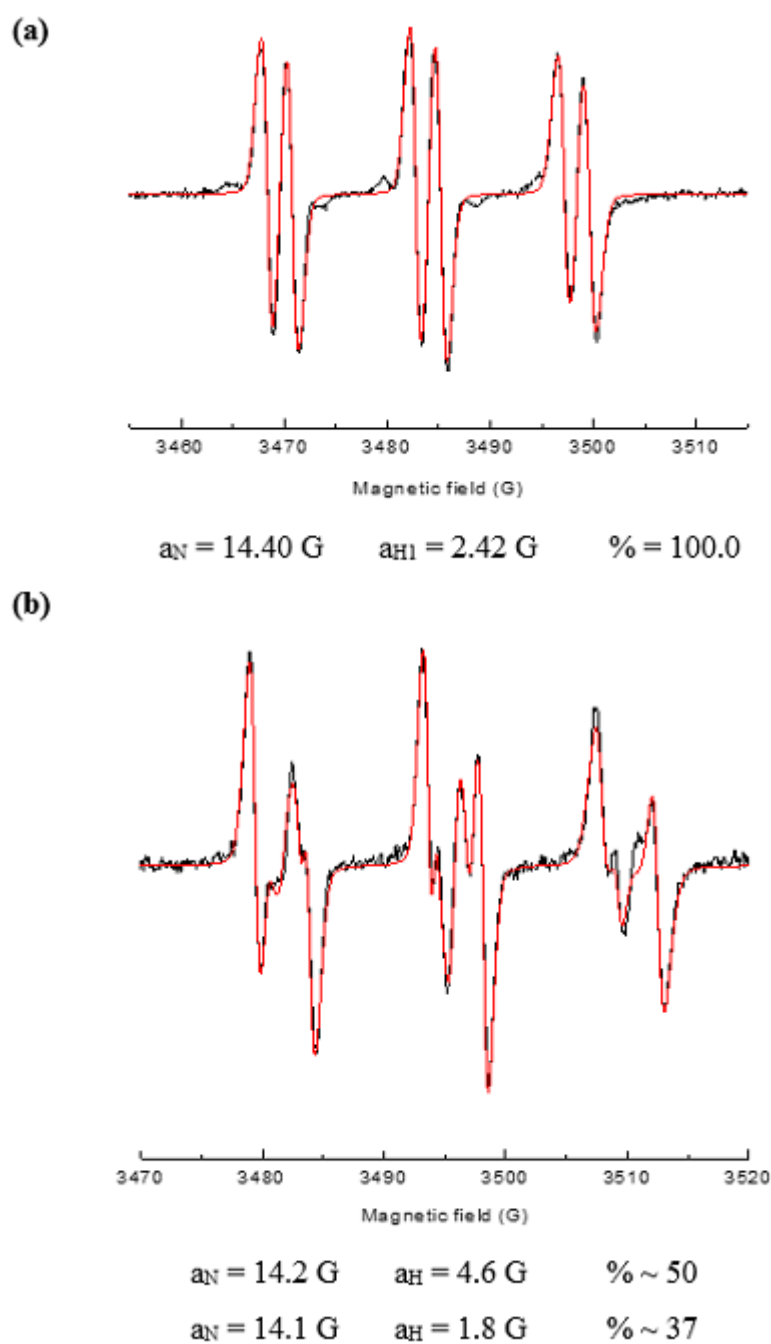


Figure 4.13. ESR spectra of the radicals generated in (a) MPI6/EDB and (b) MPI5 irradiated by LED@385 nm exposure and trapped by PBN in *tert*-butylbenzene. The hyperfine constants are shown for each spectra.

Table 4.3. Photopolymerization data of HEMA, HDDA and TMPTA initiated by commercial PIs or synthesized MPis.

PI <sub>s</sub>	HEMA			HDDA			TMPTA		
	$R_{pmax}$ (s <sup>-1</sup> )	Conversion (%)	$t_{max}$ (s)	$R_{pmax}$ (s <sup>-1</sup> )	Conversion (%)	$t_{max}$ (s)	$R_{pmax}$ (s <sup>-1</sup> )	Conversion (%)	$t_{max}$ (s)
MPI1	0.012	83	157	0.060	68	63	0.031	47	63
MPI2	0.015	72	160	-	-	-	-	-	-
MPI3	-	-	-	0.071	69	63	-	-	-
MPI5	0.014	81	140	0.060	68	63	0.030	48	63
Irgacure 2959	0.011	85	166	0.060	75	65	0.030	47	63
Irgacure 184	-	-	-	0.073	70	63	-	-	-
MPI4 /DMAEM	-	-	-	0.004	49	139	0.005	24	70
MPI6 /DMAEM	0.003	66	227	0.020	57	76	0.025	35	63
AP /DMAEM	-	-	-	0.012	53	83	0.008	32	68
BP /DMAEM	0.002	35	225	0.015	59	74	0.026	40	63



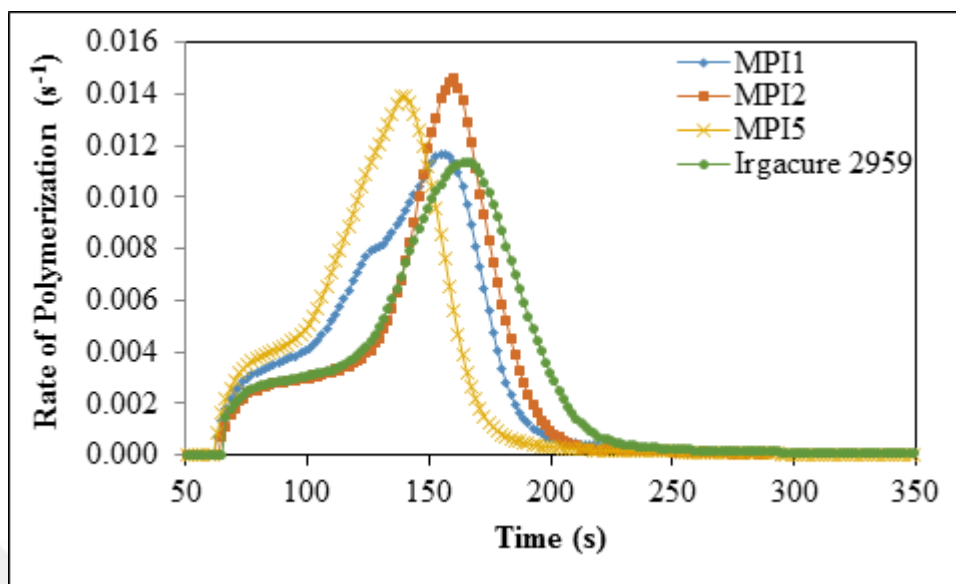


Figure 4.14. Rate-time plots for the photopolymerization of HEMA under nitrogen initiated by MPI1, MPI2, MPI5 and Irgacure 2959 (PI concentration is 2 mol%).

The photopolymerization profiles of HEMA with Irgacure 2959-based photoinitiators (MPI1, MPI2 and MPI5) together with Irgacure 2959 are shown in Figure 4.14. MPI2 and MPI5 gave increased  $R_{pmax}$  value (0.0146 and 0.0139  $s^{-1}$ ) compared to Irgacure 2959 (0.0114  $s^{-1}$ ) and MPI1 (0.0117  $s^{-1}$ ) (Table 4.3). The conversions reached were similar and around 81-85% except MPI2. The lowest conversion obtained with MPI2 (72 %) is due to the presence of the carboxylic acid groups in its structure which increases the rigidity of the system by additional hydrogen bonding. Also, it can be easily observed that the time to reach the maximum polymerization rate,  $t_{max}$  of MPI5 was improved by 16 % compared to Irgacure 2959. The photopolymerizations of HDDA and TMPTA initiated by the synthesized photoinitiators except insoluble MPI2 were also investigated (Figure 4.15, Figure 4.16 and Table 4.3). The performances of MPI1 and MPI5, were found to be very similar to Irgacure 2959, and MPI3 performed similar to Irgacure 184; the attachment of different monomeric structures (backbones) to Irgacure 2959 or Irgacure 184 seems to have only a small effect on the polymerization efficiency. This similarity can be understood as due to multiple double bonds of HDDA and TMPTA whose reaction rates are too fast to be modified by small differences in MPI structures, and the absence of hydrogen bonding between monomer and MPI; in contrast to HEMA where the said hydrogen bonding can modify the polymerization

rate, which is already smaller due to its single double bond.

The photopolymerization results of HEMA, HDDA and TMPTA initiated by the Type II MPIs, MPI6 and BP, showed that MPI6 gave significantly increased, somewhat increased and similar  $R_{pmax}$  values compared to BP for the three respective monomers (Table 4.3). The advantage of MPI6 therefore decreases with increasing monomer functionality. However, attachment of TBBr to AP to get MPI4 causes a decrease both in  $R_{pmax}$  and conversion values of HDDA and TMPTA (Table 4.3).

Overall, it was observed that the initiators MPI4 and MPI6 exhibited lower reactivity than the Type I systems due to different photoinitiation mechanisms, which require an electron donating agent such as tertiary amines to initiate the hydrogen abstraction mechanism. This slowness gives time for the different structures of photoinitiating groups to bring out their effects on photoefficiencies.

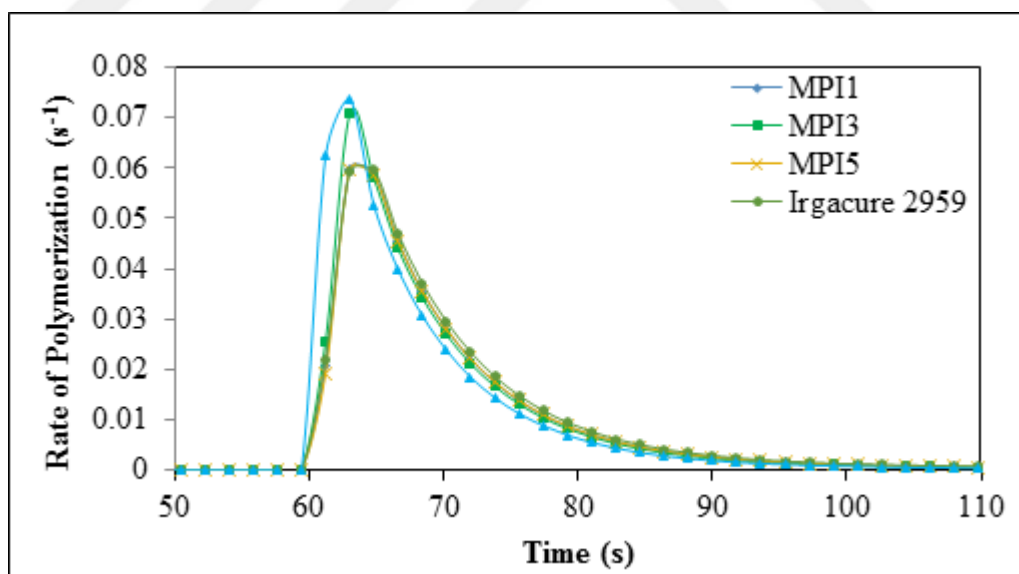


Figure 4.15. Rate-time plots for the photopolymerization of HDDA under nitrogen initiated by MPI1, MPI3, MPI5, Irgacure 2959 and Irgacure 184 (PI concentration is 2 mol%).

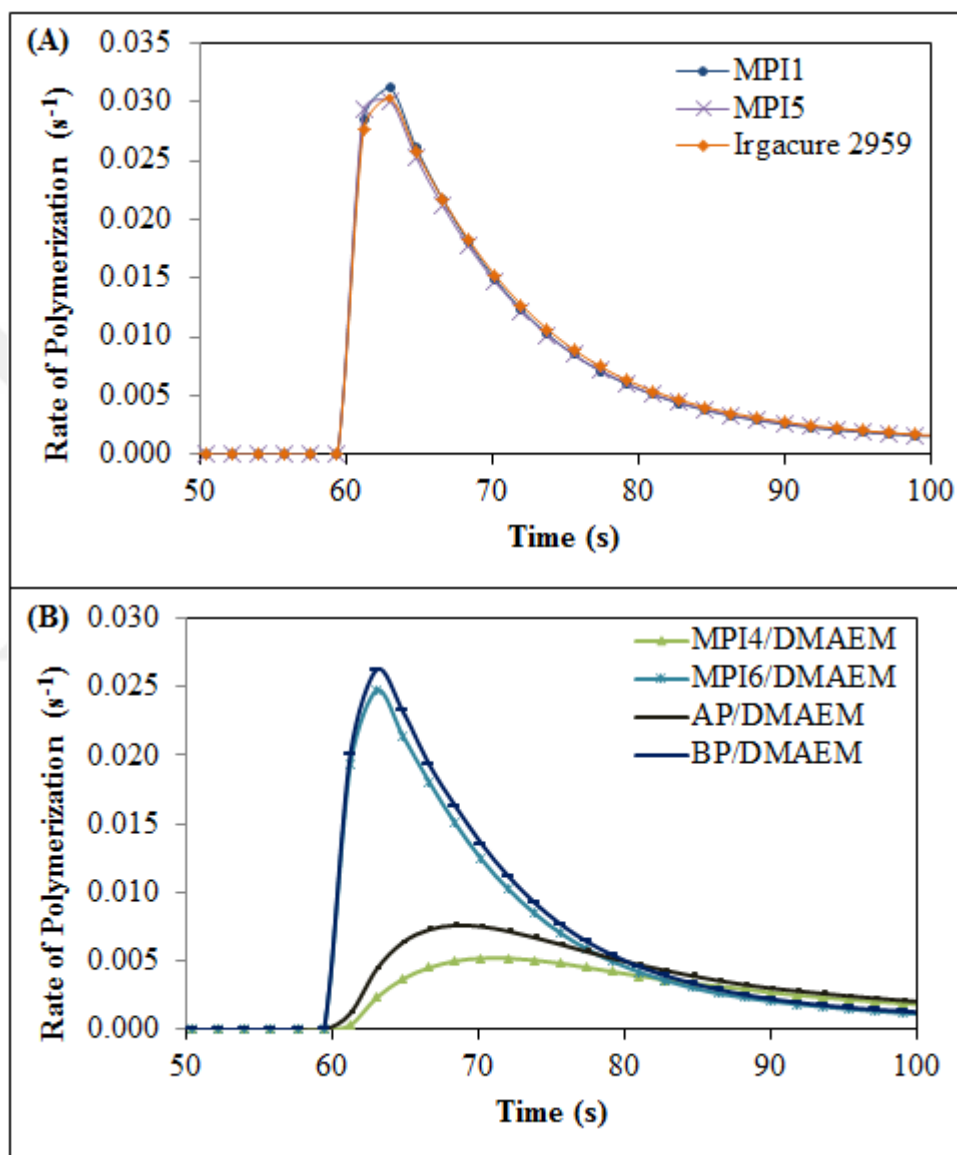


Figure 4.16. Rate-time plots for the photopolymerization of TMPTA under nitrogen initiated by (A) MPI1, MPI5 and Irgacure 2959 (PI concentration is 2 mol%); (B) MPI4/DMAEM, MPI6/DMAEM, BP/ DMAEM and AP/DMAEM (PI and DMAEM concentrations are 1 and 3 mol%).

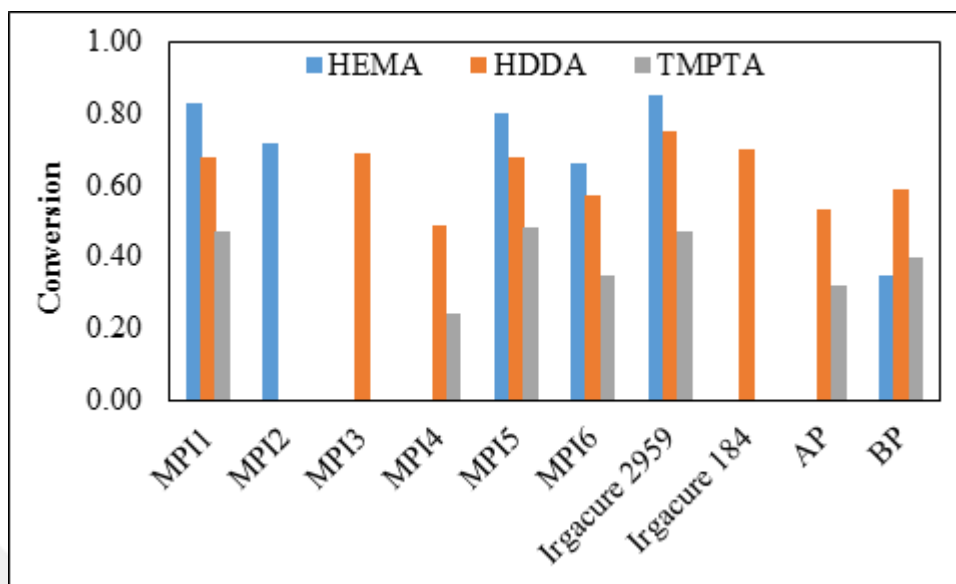


Figure 4.17. Conversion values of MPIs in photopolymerization of HDDA, HEMA and TMPTA.

#### 4.5.6. Migration Study

The migration stability of three of the synthesized MPIs (MPI1, MPI2 and MPI5) was investigated together with Irgacure 2959. The unreacted MPIs were extracted for 7 days from HDDA polymer samples using chloroform. The amount of extracted photoinitiators was determined using UV-vis spectroscopy. As shown in Figure 4.18, the amount of MPI1 and MPI2 extracted from the polymer sample was much less than that of Irgacure 2959. The mass fraction of MPI1, MPI2 and MPI5 was found to be 10, 6 and 11 times lower than Irgacure 2959. This result is due to participation of MPIs in both photoinitiation and photo-crosslinking reactions. Therefore, these novel MPIs can be used to decrease the toxicity of the cured film.

### 4.6. Conclusions

In this study, the synthesis and photochemical properties of six monomeric photoinitiators (MPI1-MPI6) based on BP, AP, Irgacure 184 and Irgacure 2959 attached to two different methacrylates (TBBr and IEM) are reported. The UV spectra of these derivatives were very similar to those of their commercial analogues except one

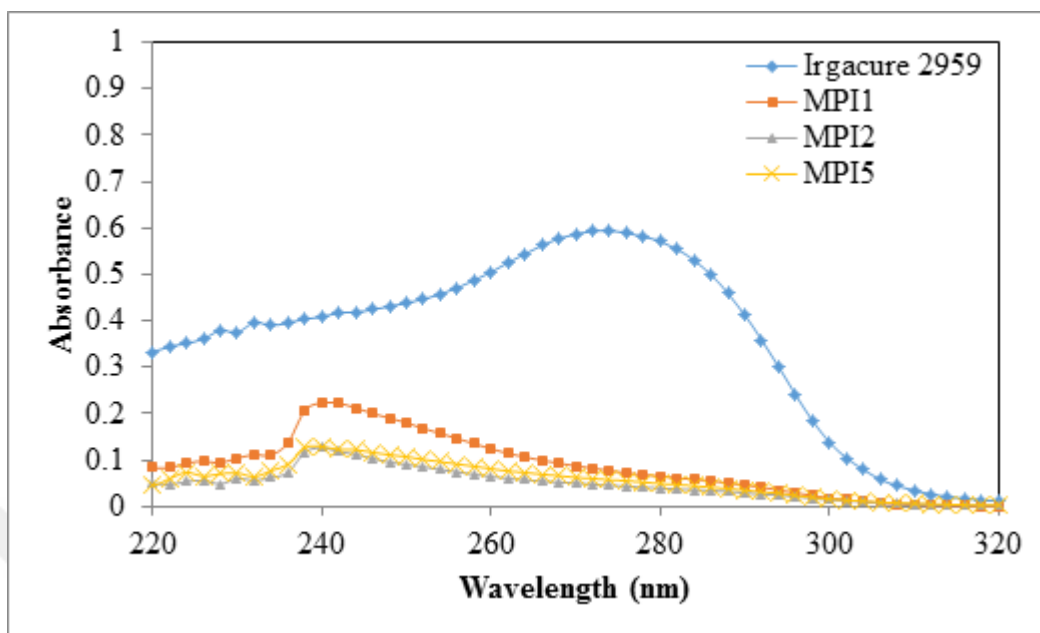


Figure 4.18. UV-vis absorption spectra of Irgacure 2959, MPI1, MPI2 and MPI5 extracted with chloroform from the polymer samples.

(MPI4). Molecular orbital (MO) calculations show that the lowest energy transition exhibits a  $\pi \rightarrow \pi^*$ . HOMO and LUMO are mainly localized on the fragments of the donor and acceptor moieties (benzene groups mostly, sometimes carbonyl group). The photopolymerization of HEMA, HDDA and TMPTA initiated by these photoinitiators and non-polymerizable commercial low molecular weight analogs was studied through photo-DSC. The effect of polymerizable group structure on photoinitiation efficiency was found to be minimal for fast polymerizing systems e.g. involving Type I MPIs; however for slower systems, e.g. monofunctional acrylates or those involving Type II MPIs the structure of the initiator makes a difference. MPIs based on Irgacure 2959, Irgacure 184 and BP with similar or increased photoinitiating activity compared to their commercial precursors appear to be promising photoinitiators. Also, their copolymerization ability decreases their migration in the photocured matrix.

## 5. RELATIONSHIP BETWEEN THE FREE RADICAL POLYMERIZATION RATES OF METHACRYLATES AND THE CHEMICAL PROPERTIES OF THEIR MONOMERIC RADICALS

Free radical polymerization (FRP) is one of the most favorable chemical reactions, because it can convert a wide variety of vinyl monomers into high molecular weight polymeric materials without extensive purification of commercially available monomers [50,51]. Although it has some limitations, like the poor control of molecular weight, polydispersity, end functionality, chain architecture, and composition, FRP is still subject to great interest in polymer chemistry.

Among the most common monomers in polymer industry which is also the subject of this study, are the acrylates and methacrylates, due to their high reactivity and excellent polymer properties. Photoinitiated polymerization of these monomers is currently being used for many applications such as textiles, adhesives, dental materials, biomaterials, coatings, polymeric membranes, microfluidic devices and stereolithography [52–55]. For these applications, some properties are desired like fast polymerization (e.g., for adhesives), hardness (e.g., for dental materials), and long-term chemical/mechanical stability (e.g., for coatings).

Understanding of both structure–property and structure–reactivity relationships is important for successful development of polymeric materials for any application. If the polymerization reaction is too slow or does not proceed to completion, the resulting polymer will lack the desired properties. (Meth)acrylates are good candidates for high performance materials in a wide variety of current and potential applications. Because of this feature of (meth)acrylates, extensive research is still being conducted to understand the relationship between the monomer structure and its reactivity and to develop monomers with enhanced reactivity. Several potential factors enhancing the reactivities of methacrylates such as hydrogen abstraction at the alpha position, molecular dipole,

hydrogen bonding, and  $\pi - \pi$  stacking have been proposed experimentally [56–63] and computationally [7, 64–67].

## 5.1. Introduction

Over the last decades, several factors leading to the improved reactivity of (meth)acrylates were hypothesized. Decker *et al.* [68] quantified the effect of the photoinitiator, the monomer functionality, and atmospheric oxygen on the polymerization rate of mono- and multiacrylic monomers, by using real-time infrared spectroscopy. In 1990, the same authors published their findings on the design of a new class of monoacrylates, containing cyclic carbonate, carbamate or oxazolidone groups, with the same high reactivity as some di- and triacrylates [69–71]. Later, Decker *et al.* [72] showed that the functional group introduced into the acrylic monomer unit has a drastic effect on both the reactivity and the physical characteristics of the photocrosslinked co-polymer with polyurethane-diacrylate. Experimental evaluations by Bowman *et al.* [58] showed that the combination of hydrogen bonding, hydrogen abstraction, and the electronic characteristics of the monomer leads to enhanced polymerization kinetics, i.e., monovinyl methacrylic monomers with reactivities that rival those of commonly used divinyl monomers.

Beckel *et al.* showed that increased acid concentration reduces the polymerization rate of (meth)acrylates [73]. The acrylate monomers showed a much more pronounced polymerization rate decrease with increasing acid concentration than their methacrylate counterparts, which was attributed to the difference in stability of the methacrylic versus acrylic propagating radical. The same authors indicated that the presence of secondary functionalities intramolecularly alters the monomer chemistry of acrylates, resulting in reduced activation energies of both Michael addition and photopolymerization reactions, and therefore in the higher reactivity of the acrylates characterized by the secondary functionalities [74]. Jansen and co-workers have claimed that for molecules with a high dipole moment, the more polar medium reduces the activation energy for propagation, leading to acceleration in the propagation reaction rate [56]. In 2011, Karahan *et al.* found that, for non-hydrogen bonded monomers, there exists

a correlation between the chemical shift differences of the double bond carbons, the calculated dipole moments, and the monomer reactivity [60]. The same group has investigated the propagation kinetics of  $\alpha$ -substituted acrylates derivatives with DFT calculations [75].

Successful correlations can support the understanding on the reactivity of monomers, and can facilitate to predict the outcome of chemical reactions and rationally design optimal reagents. Isik *et al.* have established a quantitative structure-activity relationship (QSAR), by using Multiple Regression Analysis (MRA) on the properties of 16 alkyl  $\alpha$ -hydroxymethacrylate (RHMA) derivatives with different functionalities [76]. Among the various descriptors considered, the ionization energy ( $IE$ ) and electron affinity ( $EA$ ) of the monomers, the resonance stabilization parameter ( $Res$ ) and the Mulliken atomic spin density ( $\rho_s$ ) of the monomeric radical, and, to a smaller extent, the atom-atom overlap weighed NAO bond order of the carbonyl double bond of the monomer unit were found to correlate with the experimental rates of photopolymerization, with the electron affinity of the monomer being the dominating factor. The inclusion of both polar ( $IE$  and  $EA$  of the monomer) and enthalpy effects, ( $Res$  and  $\rho_s$  of the monomeric radical) into the best-fit parameter set for the description of the polymerization rate is in agreement with what has been found in general for radical addition reactions. From literature, it is known that the rate of radical addition is often governed by polar effects and that in many cases this rate can be correlated with the electron affinity or the ionization potential of the monomers, depending on the nucleophilic or electrophilic character, respectively, of the attacking radical [77–82]. In addition, again depending on the electronic nature of the radical, enthalpy effects come into play: for moderately to weak electrophilic/nucleophilic radicals, the radical addition rate could be entirely dominated by enthalpy effects [82].

De Vleeschouwer *et al.* have already investigated with success the orientation of (nucleophilic) radical additions to electron-rich, -neutral, and -poor monosubstituted alkenes, through the use of only two simple but well-defined chemical concepts, i.e., radical stability [83] and the conceptual density functional theory based dual descriptor [84], which allows us to match electrophilic with nucleophilic regions [85].



In this study, the aim is to get insight into the effects that govern the polymerization rate of methacrylate monomers, by using merely two well-defined concepts in radical chemistry, i.e., radical stability and radical electrophilicity/nucleophilicity [83, 86–89] The rate of photopolymerization ( $R_p$ ) of 21 alkyl methacrylates has been correlated with the chemical properties of the monomeric radicals by making use of the enthalpic and polar effects of the radicals. Based on these two properties, a general non-linear expression has been derived by optimizing the radicals and evaluating their stability (*stab*) and polar effects via the radical electrophilicity ( $\omega$ ) with density functional theory.

## 5.2. Computational Details

The semi-empirical method PM3 [90,91] in the Spartan'10 program [92] was used for the conformational study of the monomers and their monomeric radicals. The geometries corresponding to the global minima on the PM3 potential energy surface of all monomeric radicals were further optimized at the B3LYP/6-31+G(d) level of theory [5,6,93] using the Gaussian09 software package [47] In addition, second order energy derivative calculations were performed to ensure that minimum energy structures were obtained.

The first chemical concept of interest in this study is radical electrophilicity. It is stated that radicals can be regarded as electrophilic or nucleophilic and that the nature of radicals is certainly of relevance in a variety of radical reactions [94–105]. In 2007, De Vleeschouwer and coworkers used the electrophilicity index, as introduced by Parr *et al.* [106], to construct electrophilicity scales of radicals important in organic chemistry [86, 87]. This scale is independent of the reaction partner and free from experimental or theoretical reaction data. The electrophilicity index is defined as: [106]

$$\omega = \frac{\mu^2}{2\eta} \approx \frac{(IE + EA)^2}{8(IE - EA)} \quad (5.1)$$

with  $\mu$  the electronic chemical potential,  $\eta$  the chemical hardness,  $IE$  the vertical ionization energy and  $EA$  the vertical electron affinity. The division between nucleophilic and electrophilic radicals is situated around 2 eV. This means that radicals with  $\omega < 2$  (eV) can be designated as nucleophilic and radicals with  $\omega > 2$  can be designated as electrophilic. Throughout this work, the quantities  $IE$  and  $EA$ , resulting in the electrophilicity index  $\omega$ , were calculated as an energy difference between the neutral radical system and its cationic or anionic counterpart, respectively, using the B3LYP/6-311+G(d,p) method.

An equally important chemical concept in this study is radical stability. In 2008, a model was presented that breaks down Bond Dissociation Enthalpies (BDEs) into parts that only incorporate properties of the individual radical fragments, that is radical electrophilicity  $\omega$ , radical stability  $stab$  and Pauling electronegativity of the radical center  $\chi$ : [83]

$$BDE(A - B) = \begin{cases} (stab_A + stab_B) + a\Delta\omega_A\Delta\omega_B, & \text{if } \Delta\chi_A < 0 \text{ and } \Delta\chi_B < 0 \\ (stab_A + stab_B) + a\Delta\omega_A\Delta\omega_B + b\Delta\chi_A\Delta\chi_B, & \text{otherwise} \end{cases} \quad (5.2)$$

with  $\Delta\omega = \omega - 2$  (eV) and  $\Delta\chi = \chi - 3$ , where 3 is the boundary between strongly and weakly electronegative radical centers. The parameters  $a$  and  $b$  were estimated to be equal to  $-12.69 \text{ kJ mol}^{-1} \text{ eV}^{-2}$  and  $-218.10 \text{ kJ mol}^{-1}$ , respectively. Note that a large value for the property  $stab$  means that we are dealing with an unstable radical, while a small value corresponds with a stable radical system. It is recommended to use an averaged stability value, i.e., the average of the stabilities obtained from the combination of radical B with the electrophilic fluorine atom, the neutral hydrogen atom and the nucleophilic hydroxymethyl radical (Equation 5.3). As such, the influence of different chemical environments is properly taken into account. The resulting scale reproduces several acknowledged stability sequences from literature, such as the effect

of increasing alkylation and delocalization.

$$stab_B = \frac{1}{3}(stab[F - B] + stab[H - B] + stab[CH_2OH - B]) \quad (5.3)$$

In addition, the BDE model is suitable to compute intrinsic stabilities for other (un-charged) intermediates like biradical and divalent systems [85]. The stabilities were calculated, using B3LYP/6-31+G(d) geometries and thermochemical enthalpy corrections, B3P86/6-311+G(d,p) energetics [107] for the bond dissociation enthalpies and B3LYP/6-311+G(d,p) energies for the electrophilicities. The *stab* values for the hydroxymethyl radical, the hydrogen atom and the fluorine atom were previously estimated to be 169.8, 235.7 and 181.0 kJ mol<sup>-1</sup>, respectively [89].

### 5.3. Experimental Methods

Photopolymerization reactivities of the various commercially available methacrylate monomers are being determined by photo-DSC. Monomers have been photopolymerized at room temperature using 2,2-dimethoxy-1,2-diphenyl-ethanone (Irgacure 651) as initiator and using an incident light intensity of 20 mW cm<sup>-2</sup> under nitrogen flow. Rates of polymerization  $R_p$  were calculated according to the formula:

$$R_p = \frac{(\frac{Q}{s})M}{n\Delta H_p m} \quad (5.4)$$

where  $Q/s$  is the heat flow per second,  $M$  the molar mass of the monomer,  $n$  the number of double bonds per monomer molecule,  $\Delta H_p$  the heat released per mole of double bonds reacted and  $m$  the mass of monomer in the sample. The theoretical value used for the heat of reaction ( $\Delta H_p$ ) is 13.1 kcal mol<sup>-1</sup> for methacrylate double bonds [108, 109].

## 5.4. Results and Discussions

In this study we have investigated the reactivity of 21 alkyl  $\alpha$ -hydroxymethacrylate (RHMA) derivatives. The general structure is depicted in Figure 5.1, where  $R_1$  is an ethyl or tertiary butyl group for monomers M1-M16 and a variety of groups for monomers M17-M21, and where  $R_2$  is a methyl group for monomers M17-M21 and a secondary functionality such as ether, ester, carbamate, and cyclic carbonate with a terminal functional group for monomers M1-M16. The complete list of monomers with corresponding structure is given in Table 5.2

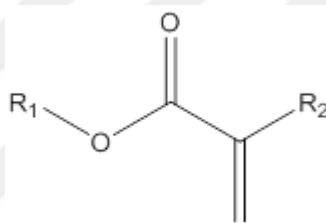


Figure 5.1. General structure of methacrylates.

The monomeric radicals were modeled as the products of a methyl radical attack to the unsubstituted carbon atom of the ethylenic double bond of the RHMA monomers, as depicted in Figure 5.3, and in accordance with a previous study [76].

In this study, a correlation between the polymerization kinetics of the RHMA monomers and the reactivity of their corresponding radicals,  $R$  is established. As mentioned earlier, two chemical concepts that are widely used to explain reactivity are radical electrophilicity or nucleophilicity, via the electrophilicity index  $\omega$  (Equation 5.1), and radical stability, via the property *stab* in Equation 5.2 and 5.3. The computed electrophilicity index and stability values (for the combination with the nucleophilic hydroxymethyl radical, the neutral hydrogen atom and electrophilic fluorine atom) are listed in Table 5.1.

When comparing the electrophilicity index values with the previously published radical electrophilicity scale, [83, 86] all radicals can be designated as weakly to moderately nucleophilic, [85] with R20 being the most and R13 the least nucleophilic.

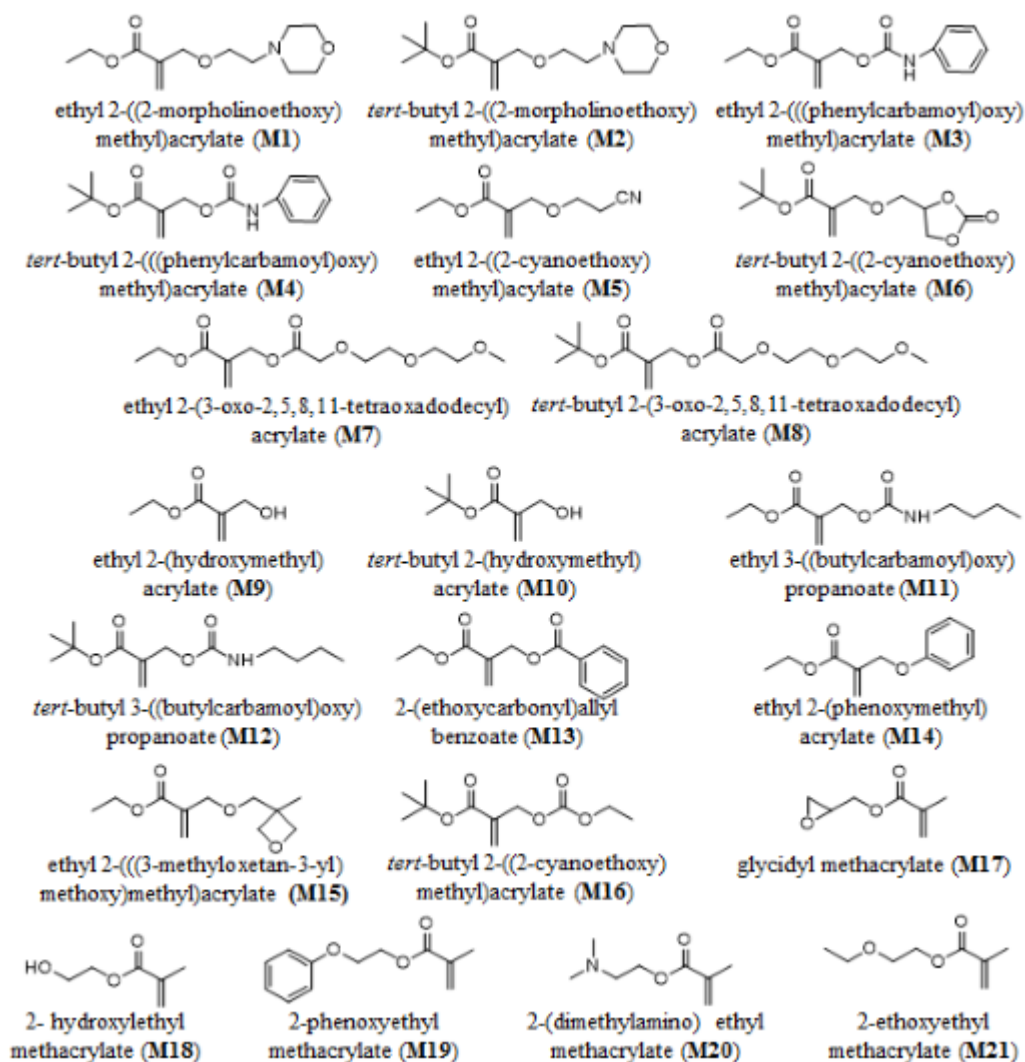


Figure 5.2. List of methacrylate monomers, investigated in this study.

Concerning the stability, all radicals are found to be relatively stable, comparable to the stability of benzyl radicals [83]. In Table 5.1 also stability difference values  $\Delta stab$ , relative to the most stable radical R18 are listed, to get a more clear idea about the variation in stabilities for this dataset.

In order to separate the polar (through  $\omega$ ) from the enthalpy (through  $\Delta stab$ ) effects, the monomeric radicals are divided into three series of similar radical stability (Table 5.2). The first series contains radicals with a  $\Delta stab$  value in the range of 0-4 kJ mol<sup>-1</sup> (R17, R18, R20, R21). The second series includes radicals with  $\Delta stab$  between 6 and 7.5 kJ mol<sup>-1</sup> (R7, R8, R9, R10, R11). The third series comprises radicals with

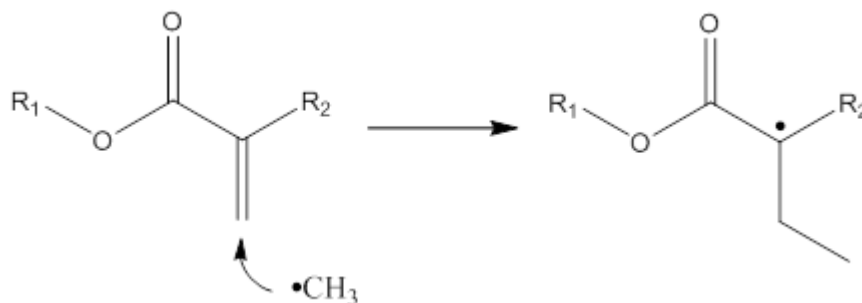


Figure 5.3. Formation of the monomeric radicals via methyl radical attack to the ethylenic double bond of the monomer.

a  $\Delta stab$  value within 9-12 kJ mol<sup>-1</sup> (R1, R2, R5, R6, R12, R15, R16). Remark that we have left out those radicals that have a pendant phenyl ring in their structure (R3, R4, R13, R14, R19), denoted as Series 4. It is shown that these radicals display a much higher reactivity than predicted. For each series a quadratic correlation is found between the electrophilicity index value  $\omega$  and the rate of polymerization of the corresponding monomer/radical set. The correlation equations are of the following type:

$$R_{p,pred} = a(\omega - \omega_0)^2 + b \quad (5.5)$$

where the coefficients  $a$  and  $b$  vary for each series, and where  $\omega_0$  is taken as a constant. The latter was estimated under the regression condition of minimal standard deviation  $\sigma$  between the experimental and the predicted rates of polymerization. The linear regression resulted in  $\omega_0 = 1.355$  eV, which is close to the smallest electrophilicity index value in the whole dataset, and  $\sigma = 0.000815$  with  $\sigma$  calculated as:

$$\sigma = \sqrt{\frac{1}{N-1} \sum_{i=1}^N (R_{p,pred,i} - R_{p,exp,i})^2} \quad (5.6)$$

and  $N = 16$ , the total number of radicals in the three series.

Table 5.1. Experimental rates of polymerization  $R_{p,exp}$  of the monomers (M1-M21) and the property values of the corresponding radicals (R1-R21): the electrophilicity index  $\omega$  in eV, the stability values *stab* based on the combination of R and CH<sub>2</sub>OH, H and F, the average stability values *stab<sub>av</sub>* (Equation 3), and the stability difference values  $\Delta stab$  relative to the most stable radical R18. All stability values are in kJ mol<sup>-1</sup>.

R	$\omega$	<i>stab</i> [R-H]	<i>stab</i> [R-F]	<i>stab</i> [R-CH <sub>2</sub> OH]	<i>stab<sub>av</sub></i>	$\Delta stab$	$R_{p,exp}$
R1	1.671	131.3	139.5	126.0	132.3	10.6	0.009
R2	1.465	135.4	134.9	126.6	132.3	10.6	0.003
R3	1.578	131.8	129.5	115.2	125.5	3.8	0.038
R4	1.579	134.2	135.3	117.1	128.9	7.2	0.022
R5	1.676	136.8	138.9	124.7	133.5	11.8	0.012
R6	1.604	136.8	138.6	125.5	133.6	11.9	0.007
R7	1.662	133.9	135.3	115.7	128.3	6.6	0.015
R8	1.598	134.9	135.7	115.4	128.7	7.0	0.008
R9	1.675	132.4	137.6	114.4	128.1	6.4	0.019
R10	1.649	132.8	138.9	114.9	128.9	7.2	0.015
R11	1.561	131.1	132.2	123.4	128.9	7.2	0.007
R12	1.518	133.9	134.0	126.9	131.6	9.9	0.005
R13	1.761	134.7	140.3	113.0	129.3	7.6	0.033
R14	1.611	137.3	136.9	126.7	133.6	11.9	0.024
R15	1.541	135.3	135.1	125.8	132.1	10.4	0.005
R16	1.564	133.9	133.3	125.0	130.7	9.0	0.006
R17	1.539	125.6	131.7	117.7	125.0	3.3	0.013
R18	1.660	124.0	131.5	109.6	121.7	0.0	0.032
R19	1.451	124.1	127.8	114.4	122.1	0.4	0.021
R20	1.373	125.3	128.8	115.7	123.3	1.6	0.002
R21	1.401	124.7	127.9	116.6	123.1	1.4	0.003

For each series of radicals, the predicted  $R_p$  values are computed from the linear correlation equations between the  $(\omega - \omega_0)^2$  values and the experimental  $R_p$  values. The exact data can be retrieved from Table 5.2. Within each of the series, very good  $R_p$  predictions are made, with deviations less or equal to 0.001 s<sup>-1</sup>. The excellent correlations between the electrophilicity index descriptors  $(\omega - \omega_0)^2$  and experimental rates of polymerization can also be seen in Figure 5.4, with correlation coefficients  $R^2$  of 0.9998, 0.9466 and 0.9199 for Series 1, 2 and 3, respectively. The monomeric radicals in Series 4 are clearly deviating from the corresponding correlation equations, with the exception of R13. The presence of the pendant phenyl group seems to averagely

increase the predicted rate of polymerization by a value of 0.0165 s<sup>-1</sup>. In literature, this enhanced reactivity has been attributed to the possibility of  $\pi - \pi$  stacking [60,61,110], which is not accounted for by our two reactivity descriptors. Finally, Figure 5.5 shows that the predicted, using the three separate equations, and the experimental rates of polymerization are highly correlated.

Table 5.2. The electrophilicity index descriptor  $(\omega - \omega_0)^2$  in eV<sup>2</sup>, the predicted rate of polymerization  $R_{p,pred1}$  (s<sup>-1</sup>) the difference  $\Delta R_p$  (s<sup>-1</sup>) with the experimental rate of polymerization  $R_{p,exp}$  (s<sup>-1</sup>) for Series 1-4, with  $a = 0.3209$  eV<sup>-2</sup> s<sup>-1</sup> and  $b = 0.0021$  s<sup>-1</sup>,  $a = 0.1971$  eV<sup>-2</sup> s<sup>-1</sup> and  $b = -0.0024$  s<sup>-1</sup>,  $a = 0.0805$  eV<sup>-2</sup> s<sup>-1</sup> and  $b = 0.0023$  s<sup>-1</sup>, for Series 1, 2, 3 of the monomeric radicals, respectively.

		$\Delta stab$	$\omega$	$(\omega - \omega_0)^2$	$R_{p,pred1}$	$R_{p,exp}$	$\Delta R_p$
Series 1	R20	1.6	1.373	0.001	0.002	0.002	0.000
	R21	1.4	1.401	0.002	0.003	0.003	0.000
	R17	3.3	1.539	0.034	0.013	0.013	0.000
	R18	0.0	1.660	0.093	0.032	0.032	0.000
	R11	7.2	1.561	0.043	0.006	0.007	-0.001
Series 2	R8	7.0	1.598	0.059	0.009	0.008	0.001
	R7	6.6	1.662	0.087	0.015	0.015	0.000
	R10	7.2	1.649	0.094	0.016	0.015	0.001
	R9	6.4	1.675	0.103	0.018	0.019	-0.001
Series 3	R2	10.6	1.465	0.012	0.003	0.003	0.000
	R12	9.9	1.518	0.027	0.004	0.005	-0.001
	R15	10.4	1.541	0.035	0.005	0.005	0.000
	R16	9.0	1.564	0.044	0.006	0.006	0.000
	R6	11.9	1.604	0.062	0.007	0.007	0.000
	R1	10.6	1.671	0.100	0.010	0.009	0.001
	R5	11.8	1.676	0.103	0.011	0.012	-0.001
Series 4	R19	10.6	1.451	0.009	0.005	0.021	-0.016
	R3	9.9	1.578	0.050	0.018	0.038	-0.020
	R4	10.4	1.579	0.050	0.008	0.022	-0.014
	R14	9.0	1.611	0.066	0.008	0.024	-0.016
	R13	11.9	1.761	0.165	0.030	0.033	-0.003

Next, we tried to find a general expression, linking both the radical stability and electrophilicity to the polymerization rate  $R_p$ . First of all, we notice that the intercepts of the correlation equation for Series 1 and 3 (parameter  $b$  in Equation 5.5) are practically the same, with values of 0.0021 and 0.0023 s<sup>-1</sup>, respectively. The



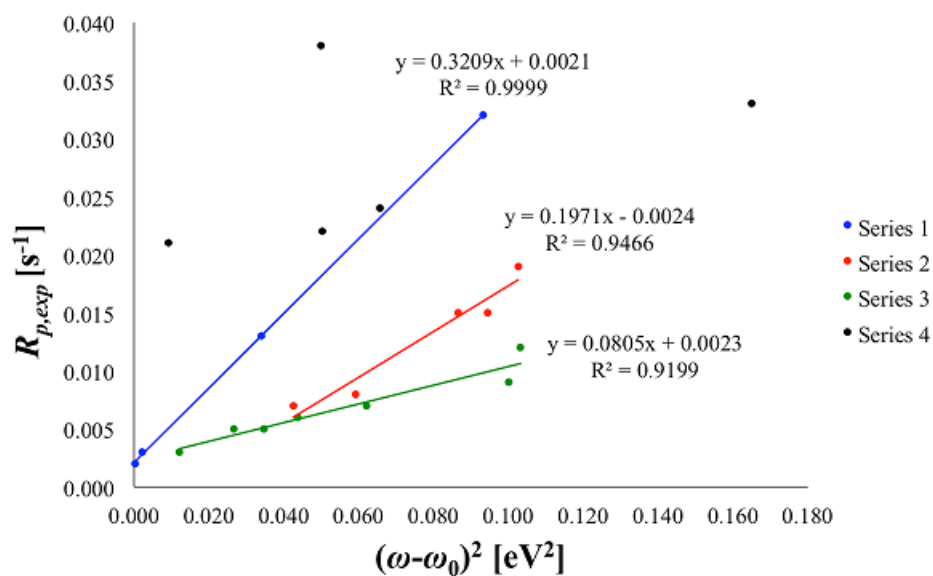


Figure 5.4. Correlation between the experimental rates of polymerization  $R_{p,exp}$  and the electrophilicity index descriptor  $(\omega - \omega_0)^2$  for Series 1-3.

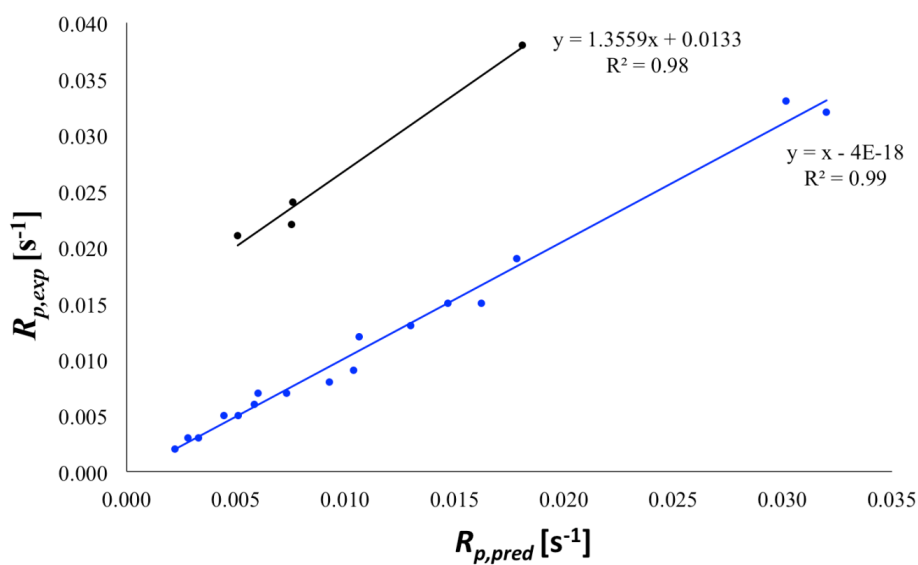


Figure 5.5. Correlation between the predicted and the experimental rates of polymerization, according to Table 5.2. Series 1-3 are in blue, and Series 4 is in black. R13 from Series 4 was included in the correlation given by the blue marks.

intercept of Series 2, however, has the opposite sign ( $b = -0.0024 \text{ s}^{-1}$ ). Concerning the slope, a reasonable correlation was found between parameter  $a$  (in  $\text{eV}^{-2} \text{ s}^{-1}$ ) and the average  $\Delta stab$  value of each series (Figure 5.6). Again, Series 2 is deviating slightly from the linear correlation. We expect the slope of the correlation equation of Series 2 to be somewhat lower than  $0.1971 \text{ eV}^{-2} \text{ s}^{-1}$ , which would in turn correspond with a higher value (than  $-0.0024 \text{ s}^{-1}$ ) for the intercept  $b$ . When the correlation equation in Figure 5.6 is combined with Equation 5.5, we get the following general expression for  $R_p$ :

$$R_p = a'(\Delta stab - \Delta stab_0)(\omega - \omega_0)^2 + b \quad (5.7)$$

with  $a' = (-40.82)^{-1} \text{ kJ}^{-1} \text{ mol eV}^{-2} \text{ s}^{-1}$ ,  $\Delta stab_0 = 14.7 \text{ kJ mol}^{-1}$ ,  $\omega_0 = 1.355 \text{ eV}$ , and  $b = 0.002 \text{ s}^{-1}$ . This expression indicates that a more stable monomeric radical (i.e., a small value for  $\Delta stab$ ) will result in a higher polymerization rate (for constant  $\omega$ ), while a more nucleophilic monomeric radical (i.e., a small value for  $\omega$ ) will result in a lower polymerization rate (for constant  $\Delta stab$ ). In addition, the higher is the stability of the radical, the more important are the polar effects (represented by the electrophilicity index). Remark that both quantities have boundaries: the correlation does not hold for radicals that are more than  $14.7 \text{ kJ mol}^{-1}$  less stable than R18, and more nucleophilic than  $1.355 \text{ eV}$  (approximately the value for R20). The resulting rates of polymerization for each of the monomers can be retrieved from Table 5.3.

It is also possible to re-estimate the parameters  $a'$ ,  $\Delta stab_0$ ,  $\omega_0$ , and  $b$  in Equation 5.7 using the properties and rates of polymerization of all radicals in Series 1-3. The multiple regression analysis resulted in the following equation:

$$R_p = -0.01399(\Delta stab - 15.60)(\omega - 1.295)^2 + 0.0005 \quad (5.8)$$

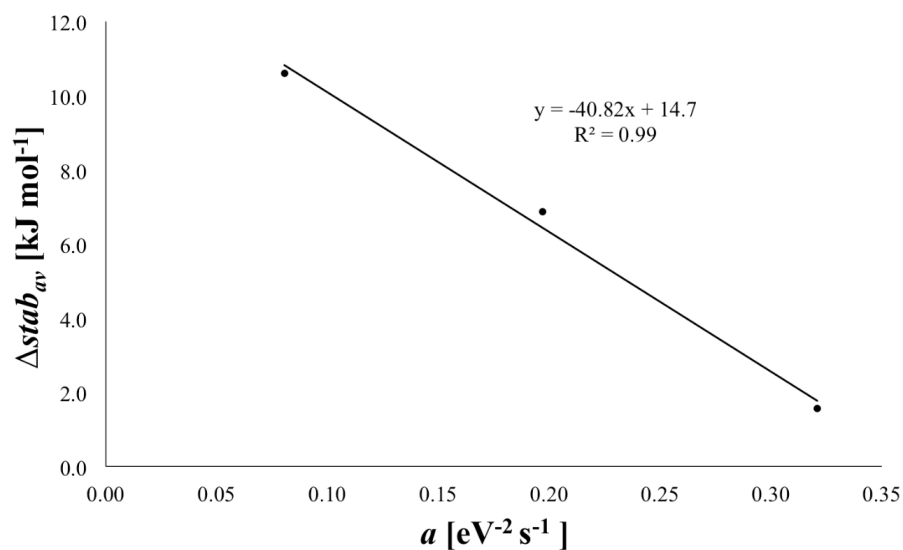


Figure 5.6. Correlation between the slopes of the correlation equations of Figure 5.3 and the average  $\Delta stab$  values for each of the corresponding Series 1-3.

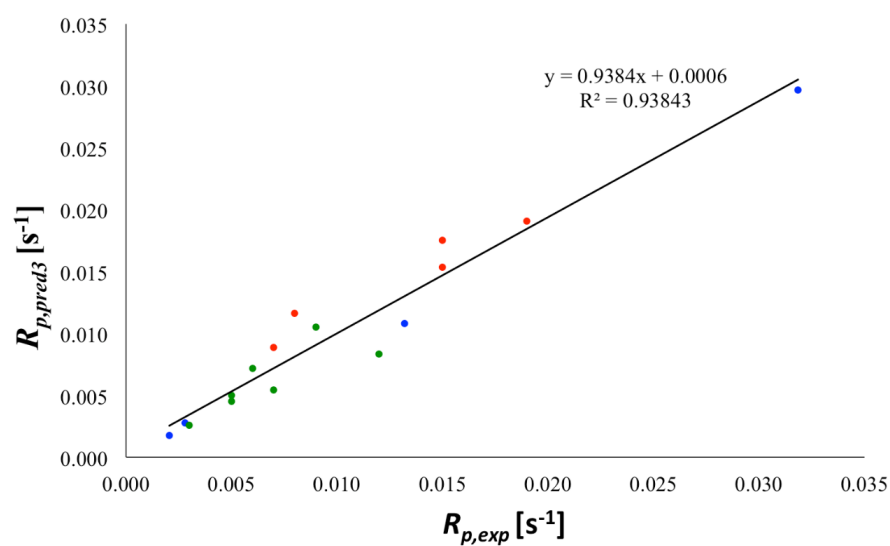


Figure 5.7. Comparison between the predicted (Equation 5.8) and the experimental rates of polymerization for the monomeric radicals of Series 1 (blue), Series 2 (red), and Series 3 (green).

Table 5.3. The predicted rates of polymerization  $R_{p,pred2}$  and  $R_{p,pred3}$  ( $s^{-1}$ ) resulting from Equation 5.7.

R	$R_{p,pred2}$	$R_{p,pred3}$	$R_{p,exp}$
R1	0.012	0.011	0.009
R2	0.003	0.003	0.003
R5	0.009	0.008	0.012
R6	0.006	0.005	0.007
R7	0.021	0.018	0.015
R8	0.013	0.012	0.008
R9	0.023	0.019	0.019
R10	0.018	0.015	0.015
R11	0.010	0.009	0.007
R12	0.005	0.005	0.005
R15	0.006	0.005	0.005
R16	0.008	0.007	0.006
R17	0.011	0.011	0.013
R18	0.035	0.030	0.032
R20	0.002	0.002	0.002
R21	0.003	0.003	0.003

The boundaries of this expression have broadened slightly compared to the previous one, while the intercept  $b$  is now very close to zero. The predicted  $R_p$  values are listed in Table 5.3 with parameters  $a' = -0.02450 \text{ kJ}^{-1} \text{ mol eV}^{-2} \text{ s}^{-1}$ ,  $\Delta stab_0 = 14.7 \text{ kJ mol}^{-1}$ ,  $\omega_0 = 1.355 \text{ eV}$ ,  $b = 0.002 \text{ s}^{-1}$ , and  $a' = -0.01399 \text{ kJ}^{-1} \text{ mol eV}^{-2} \text{ s}^{-1}$ ,  $\Delta stab_0 = 15.6 \text{ kJ mol}^{-1}$ ,  $\omega_0 = 1.295 \text{ eV}$ ,  $b = 0.0005 \text{ s}^{-1}$ , respectively, for the monomeric radicals of Series 1-3, and correlate well with the experimental rates is shown in Figure 5.7. The corresponding correlation coefficient  $R^2$  is found to be 0.9384, and, taken into account the number of predictors in Equation 5.8, a similar value of 0.9160 is obtained for the adjusted  $R^2$ , indicating that the expression in Equation 5.8 is not overspecified.

## 5.5. Conclusions

In this study, the polymerization rate of 21 methacrylate monomers was explained using solely chemical properties of the monomeric radicals. Both enthalpy effects, via the radical stability ( $stab$ ), and polar effect, via the radical electrophilicity ( $\omega$ ), seem to play a significant role in understanding the polymerization rate  $R_p$ . Increasing the stability or decreasing the nucleophilicity of the monomeric radical results in a higher

polymerization rate. Furthermore, it is seen that the influence of the polar effects becomes larger for more stable radicals. Based on those two properties, a general non-linear expression were derived which performs quite well in predicting  $R_p$  for 16 of the 21 methacrylates in our set, with an  $R^2$  value of 0.9384 and an adjusted  $R^2$  value of 0.9160. However, this expression probably does not hold for too unstable and/or too nucleophilic radicals. In addition, the monomers containing a pendant phenyl group were experimentally found to have a higher polymerization rate than predicted. In these cases, also  $\pi - \pi$  stacking plays an important role, which was not accounted for by the expression.

## 6. SYNTHESIS AND EVALUATION OF NOVEL CARBOXYLIC ACID FUNCTIONALIZED METHACRYLATES FOR HYDROGELS IN BIOMEDICAL APPLICATIONS

Hydrogels, three-dimensional, hydrophilic and cross-linked networks, are one of the important biomaterial classes in biotechnology and medicine because their excellent biocompatibilities. They were the first biomaterials designed for use in the human body [111]. The biocompatibility is promoted by the high water content of hydrogels and the physiochemical similarity of hydrogels to the native extracellular matrix, both compositionally and mechanically [112]. The advantageous properties of hydrogels, namely their adjustable chemical and physical structures, good mechanical properties, high water content and, as mentioned, biocompatibilities make them useful in tissue engineering, drug delivery, biomedical implants and biotechnology. The design and preparation of hydrogels have a great interest in biomedical engineering and pharmaceutical applications [113].

Hydrogels are generally prepared from hydrophilic polymers that are crosslinked by either physical crosslinking (e.g. hydrogen bonding, hydrophobic interactions, aggregation, self-assembly) or chemical crosslinking (by various crosslinkers). By free radical polymerization (FRP) of water-soluble or hydrophilic monomers, synthetic hydrogels are prepared in water with the use of difunctional or multifunctional crosslinkers. Some types of hydrogels can be prepared in vitro and in vivo by photopolymerization using photoinitiators under visible or UV light [114].

Photopolymerization makes in situ hydrogel preparation practical. The choice of photoinitiators and monomers (or macromers) are important (as discussed previously in Part 4). Photoinitiators that will be used in hydrogel synthesis should be selected according to their biocompatibility, solubility in water, cytotoxicity and stability [115,116]. In tissue engineering, photopolymerized hydrogels have been used as

tissue barriers, drug delivery systems, cell encapsulators and scaffold materials.

### 6.1. Introduction

Hydrogels for tissue engineering are generally formed from macromolecular hydrogel precursors, e.g. water soluble polymers with two or more reactive groups. PEG acrylate derivatives and PEG methacrylate derivatives, polyvinyl alcohol derivatives are some of examples for macromolecular hydrogel precursors (Figure 6.1). The permeability and mechanical properties of hydrogels depend on the length of the PEG and macromer concentration in the solution [114].

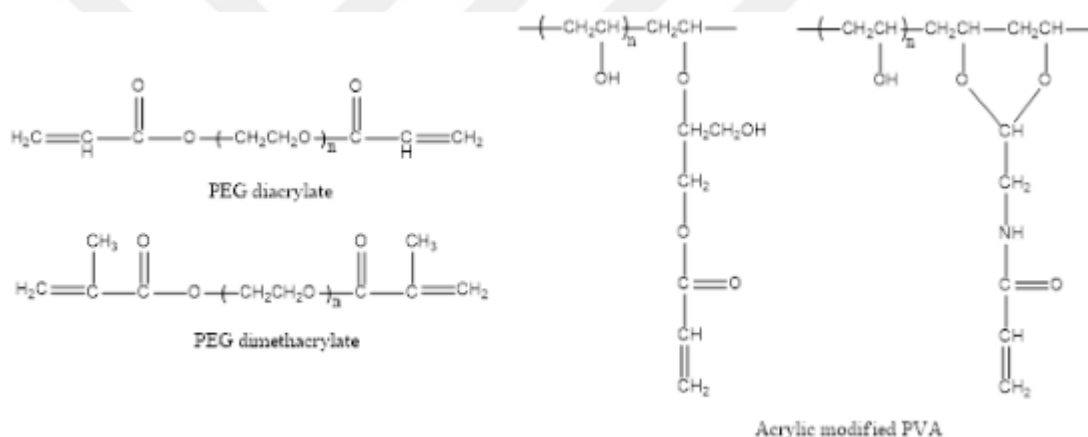


Figure 6.1. Chemical structures of materials that can be photopolymerized to create crosslinked hydrogel networks.

Strong adhesion between the organic and inorganic materials can be achieved for hydrogels functionalized with carboxylate ligands. Figure 6.2 indicates natural bone synthesis with synthetic polymers functionalized to mimic the mineral-nucleating proteins in bone. Bertozzi et. al [117] developed polymethacrylamide and polymethacrylate hydrogels functionalized with anionic groups similar to glutamate-, aspartate-, and phosphoserine-rich bone proteins and used them to form templates for the formation of hydroxyapatite.

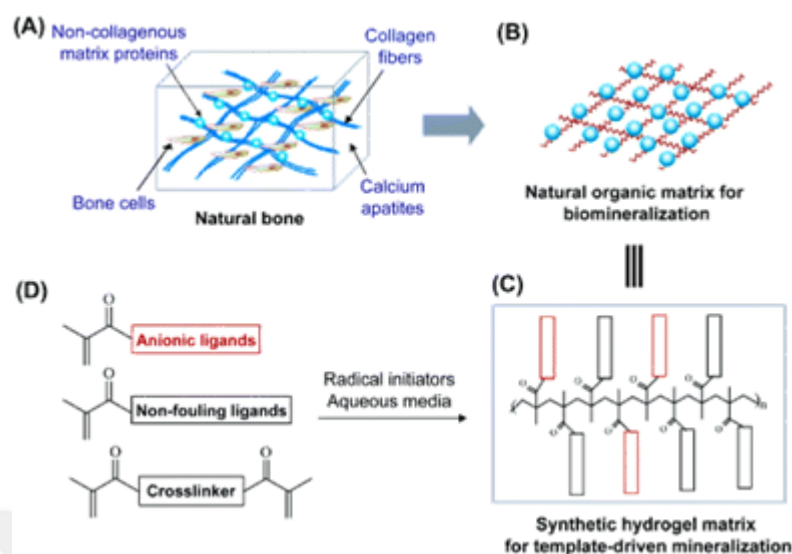


Figure 6.2. Natural bone synthesis with synthetic polymers.

In order to improve mechanical properties of hydrogels, interpenetrating networks also have been used [118]. Frank et. al [119] formed the IPNs by synthesis of a crosslinked poly(acrylic acid) (PAA) network within an end-linked poly(ethylene glycol) (PEG) macromonomer network. The IPNs might be useful as replacement materials for the cornea, cartilage, and other load-bearing anatomical structures.

The equilibrium swelling degree of hydrogels depends on the cross-link and charge densities of the polymer network as well as on the cross-linked polymer concentration after the gel preparation. In swelling mediated by external stimuli (e.g. pH, temperature, ionic strength, light), hydrogels may show continuous or discontinuous changes. Generally, stimuli responsive hydrogels are (meth)acrylate derivatives and their copolymers [120]. While both natural and synthetic polymers can be used for the production of hydrogels, those derived from the natural ones are best for pH-sensitive controlled release systems because of swelling properties and network structure that can encompass the target drugs [121]. They are also environmentally compatible, and safe for human use.

Our purpose in this chapter is to synthesize new hydrogels containing carboxylic acid groups with improved rates of mineralization to be used as tissue scaffolds. It is



suggested that the choice of the polymeric backbone might also affect the activity and there are no alkyl  $\alpha$ -hydroxymethacrylate (RHMA)-based hydrogels reported in the literature.

## 6.2. Materials and Characterization

### 6.2.1. Materials

*tert*-Butyl  $\alpha$ -bromomethacrylate (TBBr) and *tert*-butyl  $\alpha$ -hydroxymethacrylate (TBHMA) were synthesized according to the literature procedures [44, 45]. Poly(ethylene) glycol (PEG) ( $M_n=400, 600$ ), triethyl amine (TEA), trifluoroacetic acid (TFA), 2-hydroxyethyl methacrylate (HEMA), 2,2-dimethoxy-2-phenylacetophenone (DMPA), 2-hydroxy-4'-(2-hydroxyethoxy)-2-methylpropiophenone (Irgacure2959), poly(ethylene glycol) diacrylate (PEGDA) ( $M_n=575$ ) and all other reagents and solvents were obtained from Aldrich and used as received. Dichloromethane was dried over activated molecular sieves.

### 6.2.2. Characterization

Monomer characterization involved  $^1\text{H}$  spectroscopy (Varian Gemini 400 MHz) and FTIR spectroscopy (T 380). Combi Flash Companion Teledyne ISCO Flash Chromatography with C18 reverse-phase silica gel as a stationary phase was used for purification of monomers. The presence of calcium in mineralized hydrogels was determined by EDX (Bruker X flash 5010 123 eV).

## 6.3. Synthesis of Monomers

To synthesize monomers 1 and 2, first their *tert*-butyl ester derivatives (1a and 2a) were synthesized by nucleophilic substitution reaction of PEG 400 and PEG 600 respectively with *tert*-butyl  $\alpha$ -bromomethacrylate (TBBr) under basic conditions. To an ice-cold solution of the PEG (5 mmol) and TEA (20 mmol) in THF (3.3 mL for PEG 600 and 5 mL for PEG 400) under nitrogen, TBBr (10 mmol) was added dropwise. The

solution was stirred at 60°C for 24 h under nitrogen. Then the solution was diluted with 20 mL CH<sub>2</sub>Cl<sub>2</sub> and extracted with saturated NaCl solution (3 x 5 mL). The organic layer was dried over anhydrous sodium sulfate, filtered and evaporated under reduced pressure to give monomers 1a or 2a as yellowish viscous liquids. To monomer 1a or 2a (1 mmol) in an ice bath, TFA (7.02 mmol) was added under nitrogen. The solution was stirred at room temperature for 24 h. After removal of TFA, the residue was purified by reverse-phase flash chromatography on C18 using water:acetonitrile solvent pair. The desired carboxylic acid functionalized monomers (1 or 2) were obtained as viscous colorless liquids after lyophilization of the eluted solutions.

1a: <sup>1</sup>H NMR (400 MHz, CDCl<sub>3</sub>, δ): 1.41 (s, 18H, CCH<sub>3</sub>), 3.59 (m, 20H, CH<sub>2</sub>CH<sub>2</sub>O), 4.14 (s, 4H, OCH<sub>2</sub>C=CH<sub>2</sub>), 5.77, 6.11 (s, 4H, CH<sub>2</sub>=C) ppm. FTIR (ATR, cm<sup>-1</sup>): 2871 (C-H), 1705 (C=O), 1640 (C=C), 1099 (C-O).

1: <sup>1</sup>H NMR (400 MHz, D<sub>2</sub>O, δ): 3.55 (m, 20H, CH<sub>2</sub>CH<sub>2</sub>O), 4.13 (s, 4H, OCH<sub>2</sub>C=CH<sub>2</sub>), 5.86, 6.25 (s, 4H, CH<sub>2</sub>=C) ppm. FTIR (ATR, cm<sup>-1</sup>): 2870 (C-H), 1710 (C=O), 1640 (C=C), 1160 (C-O).

2a: <sup>1</sup>H NMR (400 MHz, CDCl<sub>3</sub>, δ): 1.48 (s, 18H, CCH<sub>3</sub>), 3.64 (m, 40H, CH<sub>2</sub>CH<sub>2</sub>O), 4.20 (s, 4H, OCH<sub>2</sub>C=CH<sub>2</sub>), 5.78, 6.17 (s, 4H, CH<sub>2</sub>=C) ppm. FTIR (ATR, cm<sup>-1</sup>): 2866 (C-H), 1710 (C=O), 1639 (C=C), 1096 (C-O).

2: <sup>1</sup>H NMR (400 MHz, D<sub>2</sub>O, δ): 3.71 (m, 20H, CH<sub>2</sub>CH<sub>2</sub>O), 4.30 (s, 4H, OCH<sub>2</sub>C=CH<sub>2</sub>), 5.99, 6.44 (s, 4H, CH<sub>2</sub>=C) ppm. FTIR (ATR, cm<sup>-1</sup>): 2870 (C-H), 1705 (C=O), 1637 (C=C), 1088 (C-O).

#### 6.4. Synthesis of Hydrogels

Monomers 1 or 2 (8 or 15 wt%), PEGDA (42 or 35 wt%) and HEMA (50 wt%) were dissolved in phosphate-buffered saline (PBS, pH=7.38) (20 wt%) to form precursor solutions of hydrogels H1-H4 (Table 6.1). Irgacure 2959 was added (2 wt%) to the mixture of monomers as a photoinitiator. The precursor solution was then poured

into teflon molds and subjected to UV light for 30 minutes. A blank hydrogel H0 that does not contain any carboxylic acid-functionalized monomer was also prepared from PEGDA (50 wt%) and HEMA (50 wt%) under the same conditions with other hydrogels.

#### 6.4.1. Gelation Percentage

The dry gel samples were weighed ( $W_i$ ) before soaking into distilled water to remove unreacted monomers. The swollen samples were dried in vacuum oven until constant weight is obtained and weighed ( $W_d$ ) again. The percent gelation was calculated using the following formula;

$$Gelation(\%) = \frac{W_d}{W_i} \cdot 100 \quad (6.1)$$

#### 6.4.2. Equilibrium Swelling Ratio (ESR)

Swelling studies were conducted by immersing a dry hydrogel sample into water at room temperature. The hydrogel samples were removed at predetermined time intervals, blotted on filter paper, and the swollen weight was measured. The increase in the weight of hydrogel sample was recorded as a function of time until equilibration was reached. The equilibrium swelling ratio (ESR) was calculated using the following equation:

$$ESR(\%) = \frac{W_s - W_d}{W_d} \cdot 100 \quad (6.2)$$

where  $W_s$  and  $W_d$  are the weights of the swollen and of dry gel, respectively.

### 6.4.3. Contact Angle Measurements

A sessile drop method (DSA 10, KRÜSS GmbH) was used to measure a contact angle ( $\theta$ ) of a 3–5  $\mu\text{L}$  distilled water drop, which was applied to the surface by means of syringes at room temperature and its image was captured by a camera. For each sample at least three measurements were made and the average was taken.

### 6.4.4. Mineralization of Hydrogels

The mineralization abilities of carboxylic acid containing hydrogels were evaluated by immersing them into 40 mM  $\text{Ca}^{2+}$  /24 mM  $\text{HPO}_4^{2-}$  metastable solution for 30 min and then immersing into SBF for 24 h. As a control, hydrogels were immersed into ultrapure water for 72 h.

Simulated body fluid (SBF) was prepared with literature procedures by Koç University [122]. 1L of buffer solution with pH 7.4 containing 142 mM  $\text{Na}^+$ , 5 mM  $\text{K}^+$ , 1.5 mM  $\text{Mg}^{2+}$ , 2.5 mM  $\text{Ca}^{2+}$ , 147.8 mM  $\text{Cl}^-$ , 4.2 mM  $\text{HCO}_3^-$ , 1 mM  $\text{HPO}_4^{2-}$ , and 0.5 mM  $\text{SO}_4^{2-}$  was prepared in ultrapure water. 40 mM  $\text{Ca}^{2+}$  /24 mM  $\text{HPO}_4^{2-}$  solution was prepared as described by Phadke *et al.* [123]. In 500 mL ultrapure water, 2.74 g of  $\text{K}_2\text{HPO}_4 \cdot 3\text{H}_2\text{O}$  and 2.22 g  $\text{CaCl}_2$  were dissolved. Then, 6 N HCl was added until disappearance of turbidity. To this solution, 1 M Tris-HCl (pH 7.5) was added in order to increase pH to 5.2 before using.

Morphological properties of the hydrogels before and after mineralization were characterized by SEM analysis. The samples were lyophilized and sputter-coated with Au prior to analysis. The images were obtained using Zeiss Ultra Plus FE-SEM. The presence of calcium in mineralized hydrogels was determined by using EDX.

### 6.4.5. Measurement of $\text{Ca}^{2+}$ Content

As a quantitative analysis of mineralization,  $\text{Ca}^{2+}$  content was measured according to a literature procedure [123]. Mineralized hydrogel samples were lyophilized, then

homogenized in 0.5 mL of 0.5 N HCl and mechanical force applied for complete disruption. The  $\text{Ca}^{2+}$  concentration in the solution was measured using spectrophotometric analysis. Cresolphthalein complexone and Calcium Reagent set were used to determine  $\text{Ca}^{2+}$  content.  $\text{Ca}^{2+}$  content (in  $\mu\text{g}$ ) were normalized with the dry weight of sample (in mg).

## 6.5. Results and Discussion

### 6.5.1. Synthesis of Monomers

Two carboxylic acid-containing difunctional monomers (1 and 2) which are derivatives of TBHMA were synthesized to be used as crosslinkers for biomedical applications such as tissue engineering scaffolds. The monomers contain PEG in their structure which was chosen for its favorable properties such as water solubility, biocompatibility, nontoxicity, and nonimmunogenicity. The carboxylic acid groups serve dual functions: Firstly they impart pH sensitivity to the hydrogels, as secondly, due to their affinity towards  $\text{Ca}^{2+}$  ions they are expected to induce mineralization of the hydrogels made from these crosslinkers.

Monomers 1 and 2 were synthesized in two steps (Figure 6.3). Nucleophilic substitution reaction of PEG 400 or PEG 600 with TBBBr under basic conditions gave ether derivatives which were then converted to carboxylic acid derivatives by cleavage of *tert*-butyl groups using TFA. The monomers were obtained as viscous colorless liquids with the yields of 92 and 84 % after column chromatography. The expected structures of monomers were confirmed by  $^1\text{H}$  NMR, and FTIR spectroscopies (Figure 6.4, 6.5 and 6.6). FTIR spectrum of the monomers showed characteristic C=O and C=C peaks at around 1710 and 1640  $\text{cm}^{-1}$ . Examination of the  $^1\text{H}$  NMR spectra of both monomers revealed the characteristic peak for  $\text{CH}_2$  attached to the double bond at around 4.2 ppm.

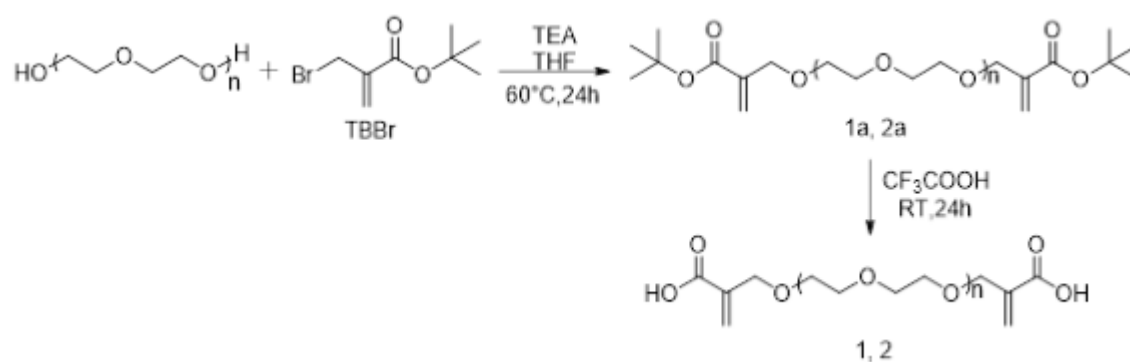


Figure 6.3. Synthesis of carboxylic acid-functionalized monomers 1 and 2.

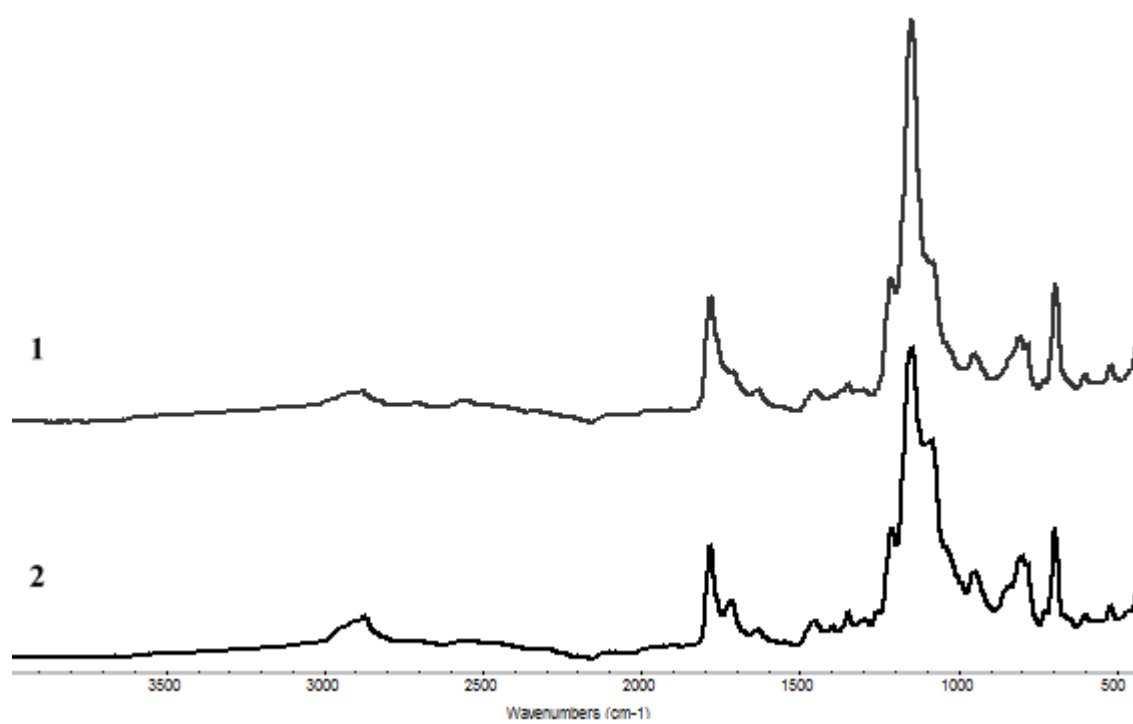


Figure 6.4. FTIR spectra of monomers 1 and 2.

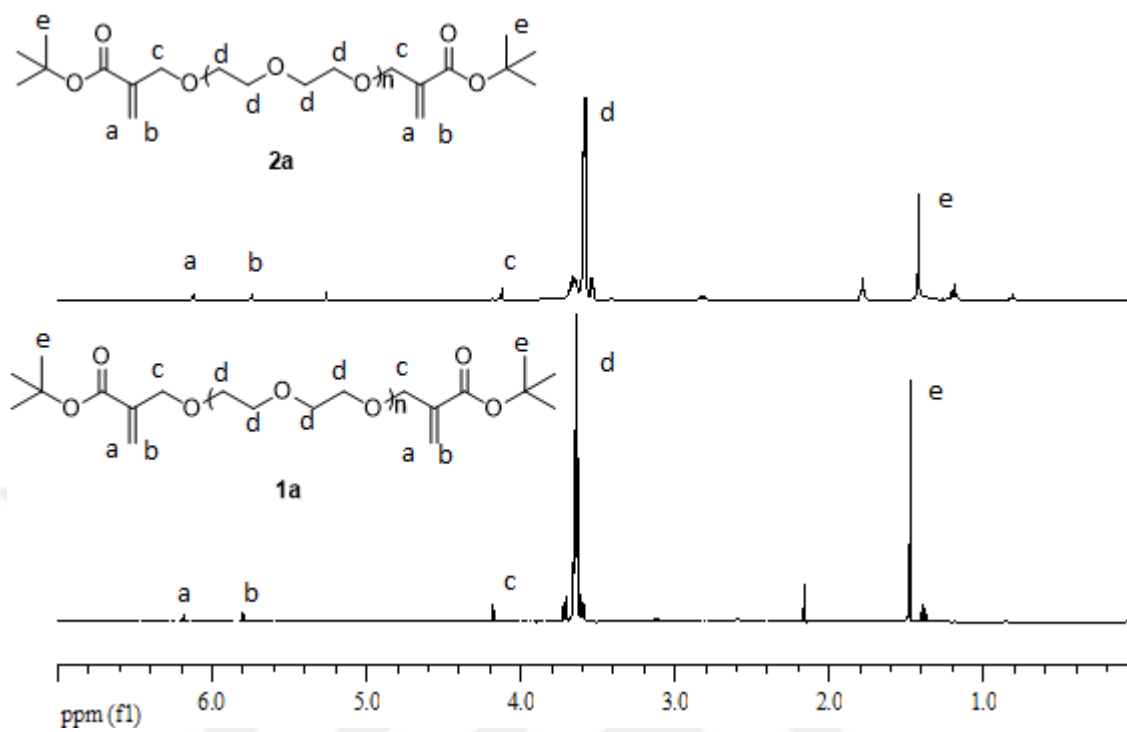


Figure 6.5.  $^1\text{H}$  NMR spectra of monomers 1a and 2a.

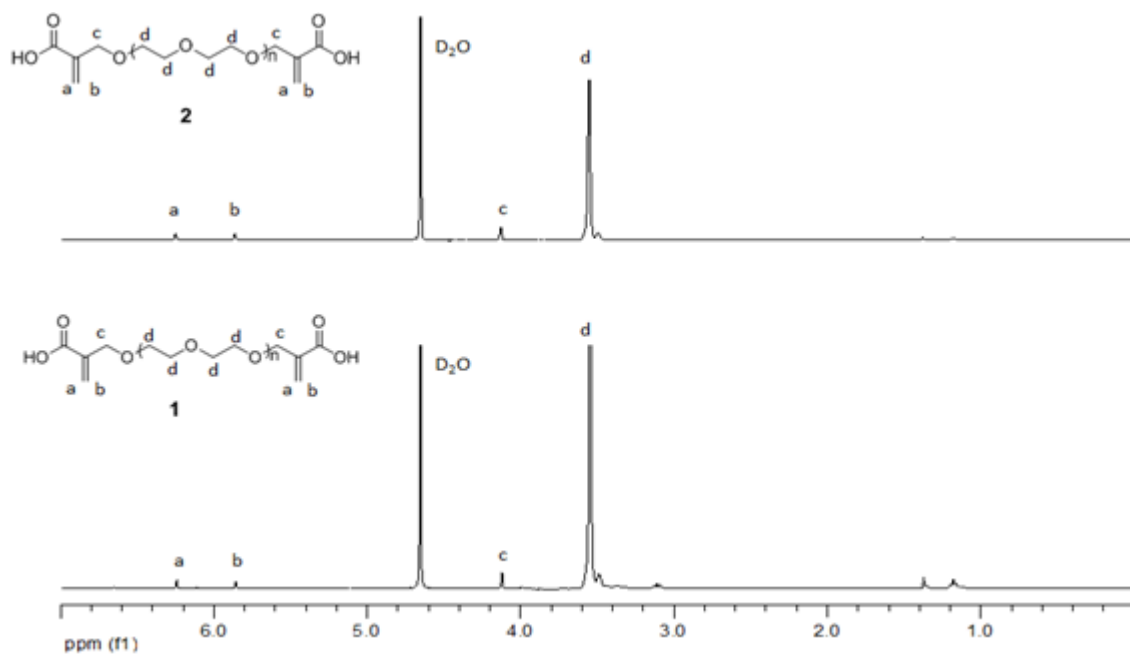


Figure 6.6.  $^1\text{H}$  NMR spectra of monomers 1 and 2.

### 6.5.2. Photopolymerization

The reactivities of the synthesized monomers 1 and 2 were investigated by photopolymerization using photodifferential scanning calorimetry (photo-DSC). Formulations consisting of PEGDA/1/HEMA or PEGDA/2/HEMA (35/15/50 wt%) were prepared and photopolymerized using DMPA (2 mol%). PEGDA/HEMA (50/50 wt%) formulation was used as blank. Figure 6.7 shows photopolymerization results such as maximum rate of polymerization ( $R_{pmax}$ ), time to reach maximum polymerization rate ( $t_{max}$ ) and conversion (%). The  $t_{max}$  value of the blank formulation (88.2 s) is lower than the carboxylic acid-containing formulations (90 s for 1 and 93.6 s for 2).  $R_{pmax}$  values were found to be 0.0243, 0.0152 and 0.0100  $s^{-1}$  for blank, 1 and 2, respectively. Because acrylates are more reactive than the corresponding methacrylates, replacement of PEGDA with monomer 1 or 2 caused a decrease in  $R_{pmax}$ . The higher  $R_{pmax}$  of monomer 1 containing formulation (0.0152  $s^{-1}$ ) than that of monomer 2 containing one (0.0100  $s^{-1}$ ) is due to its higher double concentration. The blank formulation has higher conversion (55.6 %) than those of the 1 and 2 incorporated ones. The acid groups of 1 and 2 causes higher intermolecular forces, which decrease the flexibility of the system and cause reduction in conversion.

### 6.5.3. Synthesis and Characterization of Hydrogels

The crosslinkers 1 and 2 together with PEGDA were incorporated into HEMA by using 2 wt% Irgacure 2959 as photoinitiator, to form the hydrogels H1-H4, with percent gelation values between 90% and 96% (Table 6.1). PEGDA was used as only crosslinker by 50 wt% to make hydrogels H0 as a control that do not have any acid groups.



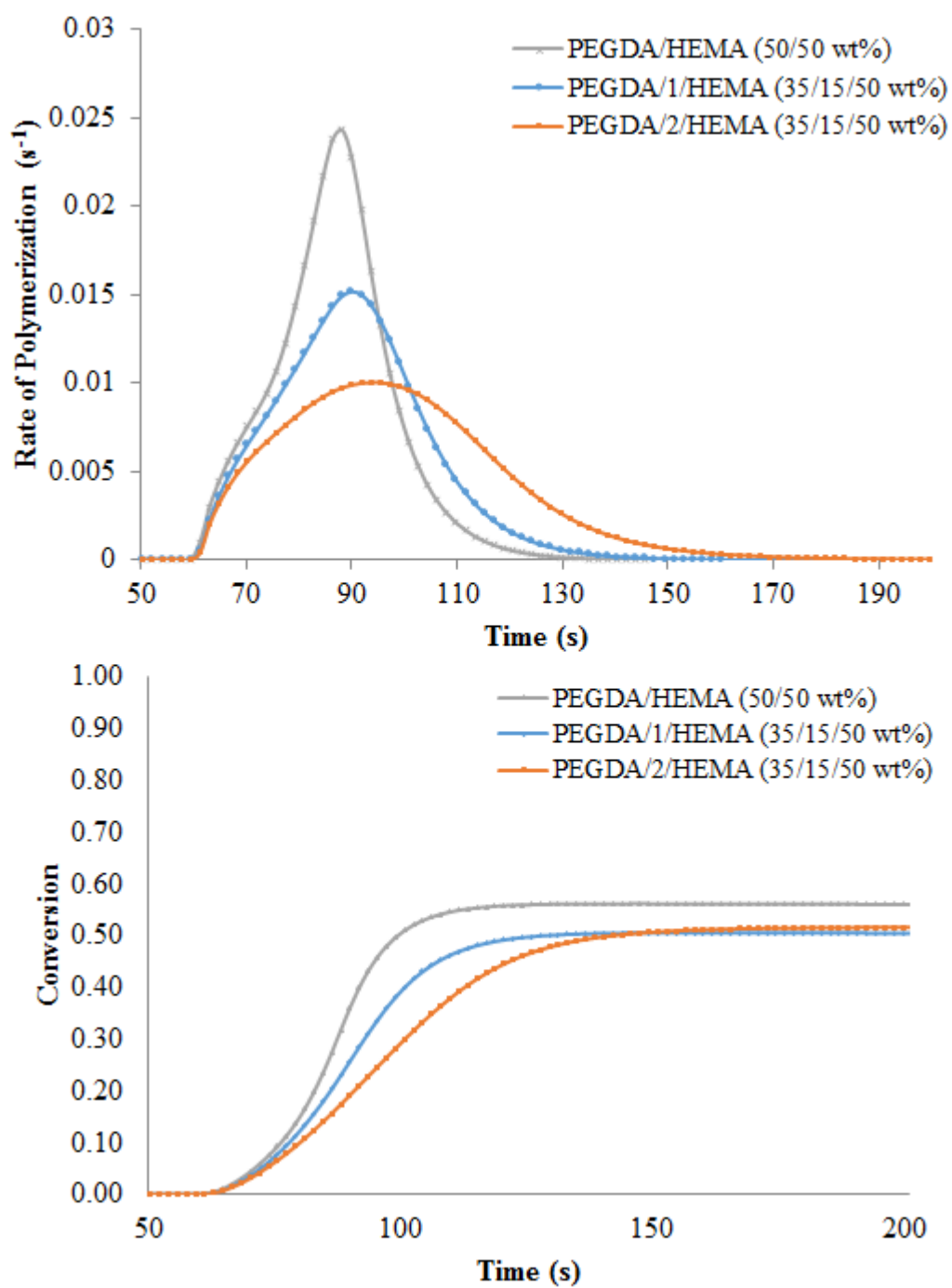


Figure 6.7. Rate-time and conversion-time plots for copolymerizations of 1 and 2 with PEGDA and HEMA at 40 °C using DMPA.

Table 6.1. Compositions of the synthesized hydrogels (H0-H4).

Hydrogel	Incorporated Monomer (wt%)	PEGDA (wt%)	HEMA (wt%)	PBS (wt%) (pH = 7.38)	Gelation (%)	ESR (%)
H0	-	50	50	20	96	43
H1	1 (8)	42	50	20	-	44
H2	1 (15)	35	50	20	90	52
H3	2 (8)	42	50	20	90	59
H4	2 (15)	35	50	20	92	94

6.5.3.1. Swelling Properties. We believe that the swelling amount is influenced by two factors: the amount of hydrophilic carboxylic acid groups, and the space inside the hydrogel matrix, determined by the distance between the double bonds. Replacement of PEGDA's PEG chain by that of monomer 1 (molecular weight of 1: 566 g/mol) does not change its length appreciably, making that factor more or less irrelevant for H1 and H2. At 8 wt% replacement, the carboxylic acid groups cannot make a difference either, leading to H1's ESR to be the same as that of H0. However at 15 wt%, the hydrophilicities of carboxylic acid groups start to work synergistically, and so give higher ESR. The PEG chain of monomer 2 (molecular weight of 2: 766 g/mol) is longer, so in its replacement, both factors contribute to increased ESR compared to H0, even at 8 wt%, it is higher than 15 wt% of monomer 1 (despite 8 wt% of 2 corresponding to lower mol% than 8 wt% of 1). As expected, the ESR increase is higher for H4, with 15wt% of monomer 2. Swelling studies were also conducted at three different pHs – 3.2, 7.4 and 9.2 for H2, to see the swelling response in acidic, neutral and basic media (Figure 6.8). Swelling ratios were determined for small time intervals-each 20 min in 3 hours and then the data were taken for longer intervals until constant weight is obtained. The ESR values for H2 were increased as pH increased. In basic medium, H4 which contains pendant two carboxylic acid groups, showed 82% swelling. The degree of swelling at pH 9 was observed to be higher which is resulting from the deprotonation of the acids generating negative charges on the carboxylates

which repel each other and expand the hydrogel.

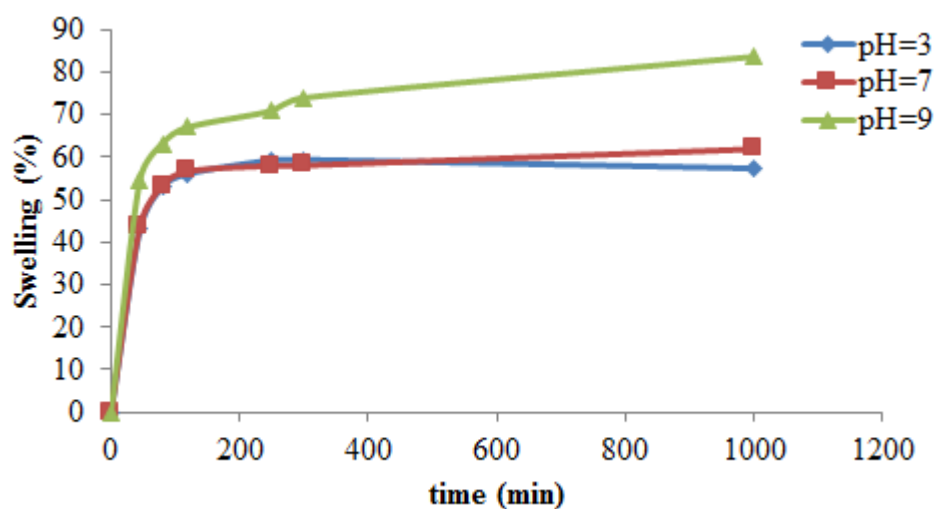


Figure 6.8. pH response of the hydrogel composition “H2” (15% monomer 1 incorporation).

6.5.3.2. Contact Angle Measurements. Hydrophilicity characters of the hydrogels were measured by contact angle measurements. The contact angle was defined as the angle formed between the surface of a solid and the line tangent to the droplet radius from the point of contact with the solid [124]. The contact angle of water on hydrogels H2 and H4 were tested and the results with the related images are given in Figure 6.9. Higher contact angle value is both related with low surface energy and roughness [125]. Contact angle of water on H2 is the lower than H4 showing its higher hydrophilicity. It is claimed that a polymer surface with a water contact angle of  $70^\circ$  gives the most suitable surface for cell adhesion [126]. H4 has a contact angle  $86.5^\circ$ , close to  $70^\circ$ , and its cell adhesion property can be improved by little modifications in synthesis of hydrogels.

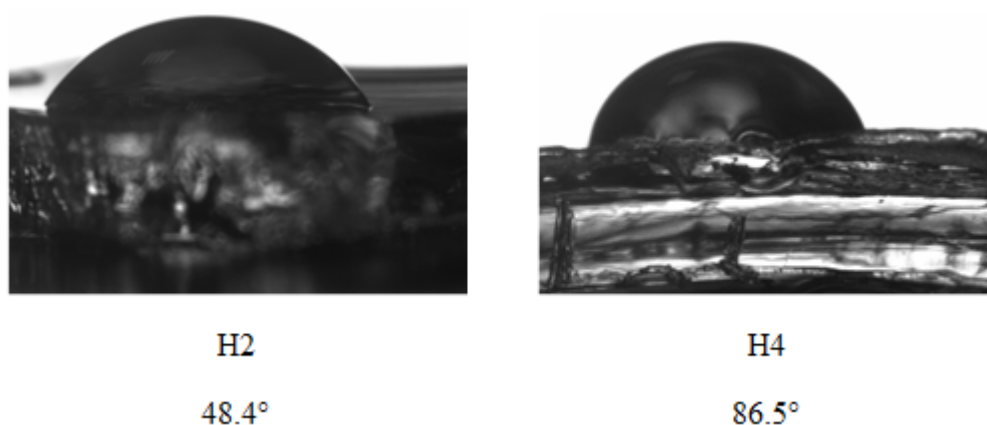


Figure 6.9. Images and angles taken from contact angle measurements.

6.5.3.3. Mineralization of Hydrogels. The mineralization abilities of carboxylic acid containing hydrogels were evaluated by immersing them into 40 mM  $\text{Ca}^{2+}$  /24 mM  $\text{HPO}_4^{2-}$  metastable solution for 30 min and then immersing into SBF for 24 h. As a control, hydrogels were immersed into ultrapure water for 72 h.

Morphological properties of the hydrogels (H2 and H4) before and after mineralization were characterized by SEM-EDS analysis and calcium determination was made by using EDX (Figure 6.10 and 6.11). Before mineralization hydrogels showed porous surface and after mineralization the surface was plated with a little mineral deposits. The calcium in the hydrogel surface was verified by EDX analysis. As a quantitative analysis of mineralization,  $\text{Ca}^{2+}$  content was measured by spectrophotometric analysis according to a literature procedure [123] and the results were shown in Figure 6.12. Hydrogel H0 does not show any Ca presence at all which shows that the acid groups in the hydrogels promotes mineralization. H2 exhibited highest  $\text{Ca}^{2+}$  content ( $1.9 \mu\text{g Ca/mg dry gel}$ ) followed by H4 ( $1.1 \mu\text{g Ca/mg dry gel}$ ). Because H2 contains more acidic groups in the formulation than it is in H4 its mineralization capacity is slightly higher than H4.

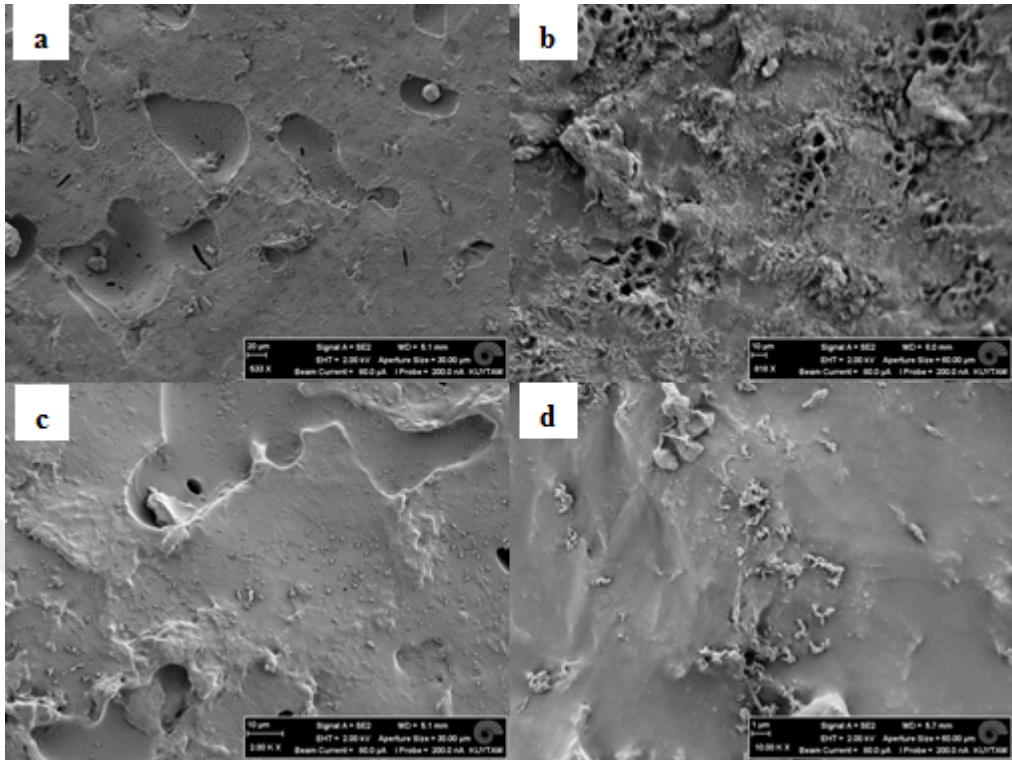


Figure 6.10. SEM images of hydrogels (a) H2, (b) H4, (c) mineralized H2, and (d) mineralized H4.

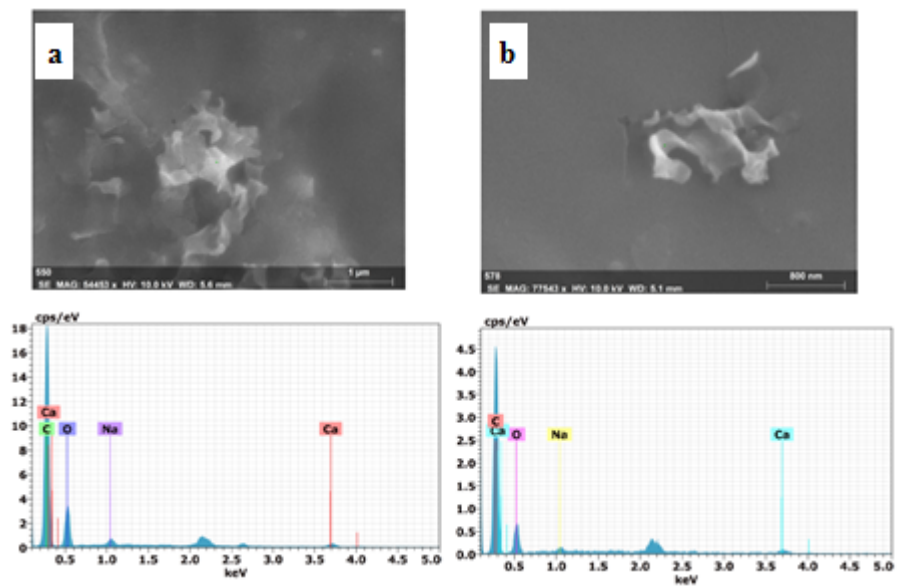


Figure 6.11. SEM images and EDX spectra of (a) mineralized H2 and (b) mineralized H4.

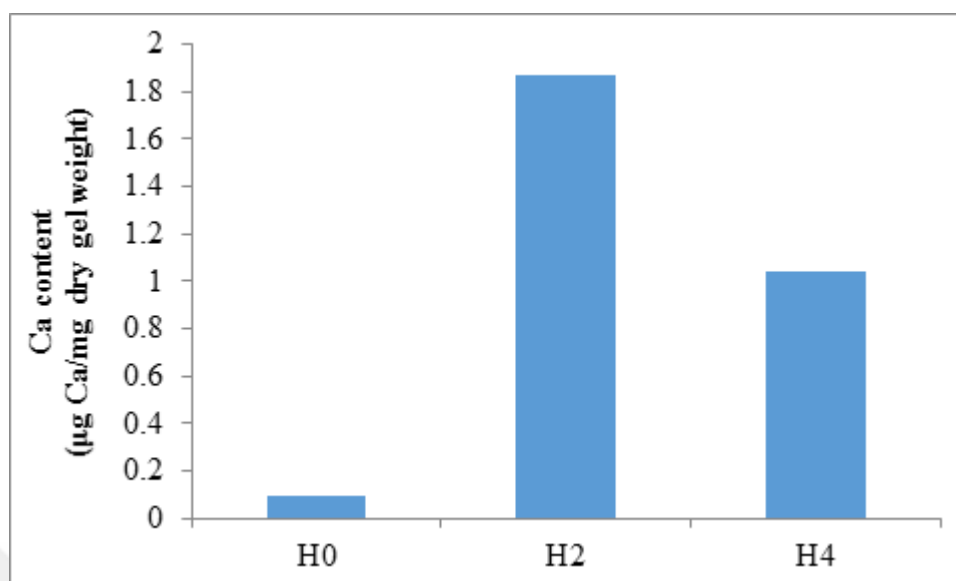


Figure 6.12.  $\text{Ca}^{2+}$  deposition assay measured as the total  $\text{Ca}^{2+}$  content in the mineralized hydrogels.

## 6.6. Conclusion

In this study, the syntheses of two novel carboxylic acid functionalized PEG monomers (1 and 2) were reported. These monomers were used for fabrication of hydrogel scaffolds (H1-H4) by copolymerization with HEMA and PEGDA. The polymerization efficiencies of the synthesized monomers were investigated by photo-DSC. The photopolymerization results indicated that monomers 1 and 2 were copolymerizable efficiently with PEGDA:HEMA mixtures. However, replacement of PEGDA with monomer 1 or 2 decreased the rates due to their dimethacrylate structures compared to that of diacrylate in PEGDA, without a significant change in the conversions. The hydrogels were evaluated by their swelling properties both in water and at different pH environments. It was observed that both the amount of hydrophilic carboxylic acid groups, and the distance between the double bonds affect the degree of swelling. The hydrogels containing 15 wt% of monomer 2 (H4) showed the highest degree of swelling (94%) in water compared to the blank hydrogel (43%) with no acid monomer. The highest hydrophilicity of H2 was also verified by the contact angle measurements, with a value of 48.4 compared to 86.5 for H4. H2 and H4 showed little mineralization after

immersing them into 40 mM  $\text{Ca}^{2+}$  /24 mM  $\text{HPO}_4^{2-}$  metastable solution. Mineralization of H2 is slightly higher than H4, because the former has higher acid concentration than the latter.



## 7. ORIGINS OF EXO-STEREOSELECTIVITY OF NORBORNENE IN HETERO DIELS-ALDER REACTIONS

Cycloadditions are the most widely used reactions in organic synthesis because of their widespread applications and value in synthesis. Significant one among them is the Diels-Alder reaction by its advantage for versatility and the control of stereochemistry. The Diels-Alder cycloaddition is widely used to build up a six-membered ring with up to four contiguous stereogenic centers, in a regio- and stereo-controlled way. In a classical Diels-Alder reaction, a conjugated diene and a dienophile, which has at least one double bond, forms a six membered cycloadduct (Figure 7.1). The Diels-Alder reaction can be both intermolecular and intramolecular. Even though it is carried out easily at ambient temperatures or slightly elevated temperature, there are also examples for catalyzed and/or high pressure Diels-Alder reactions in the literature.

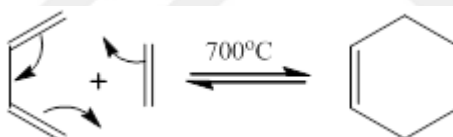


Figure 7.1. Parent system of the Diels-Alder reaction

The nature of the diene and the dienophile plays an important role in the stereoselectivity of the reaction because their electronic effects also influence the rate of cycloaddition. The rate of Diels-Alder reaction is determined mainly by extent of interaction between highest occupied molecular orbital (HOMO) of one component and lowest unoccupied molecular orbital (LUMO) of the other. The smaller the energy separation between the HOMO and the LUMO, results in more readily driven reaction. In normal electron-demand Diels-Alder reactions, where HOMO of diene and LUMO of dienophile interacts, a diene with an electron donating group (e.g. alkyl, alkoxy) accelerates the reaction by lowering the energy of its LUMO, with a dienophile bearing an electron attracting group (e.g. CO, CN) [127]. However, in inverse electron-demand Diels-Alder reactions, where LUMO of diene and HOMO of dienophile reacts, electron-withdrawing substituents on diene accelerate the cycloaddition with the dienophiles



that have electron-donating substituents [128]. In short, as shown in Figure 7.2, donor substituents (D) increase energy of HOMO and LUMO while acceptor substituents (A) lower the energies of the frontier orbitals. The strength of the interaction increases with reducing energy difference  $\delta E_{HOMO-LUMO}$ .

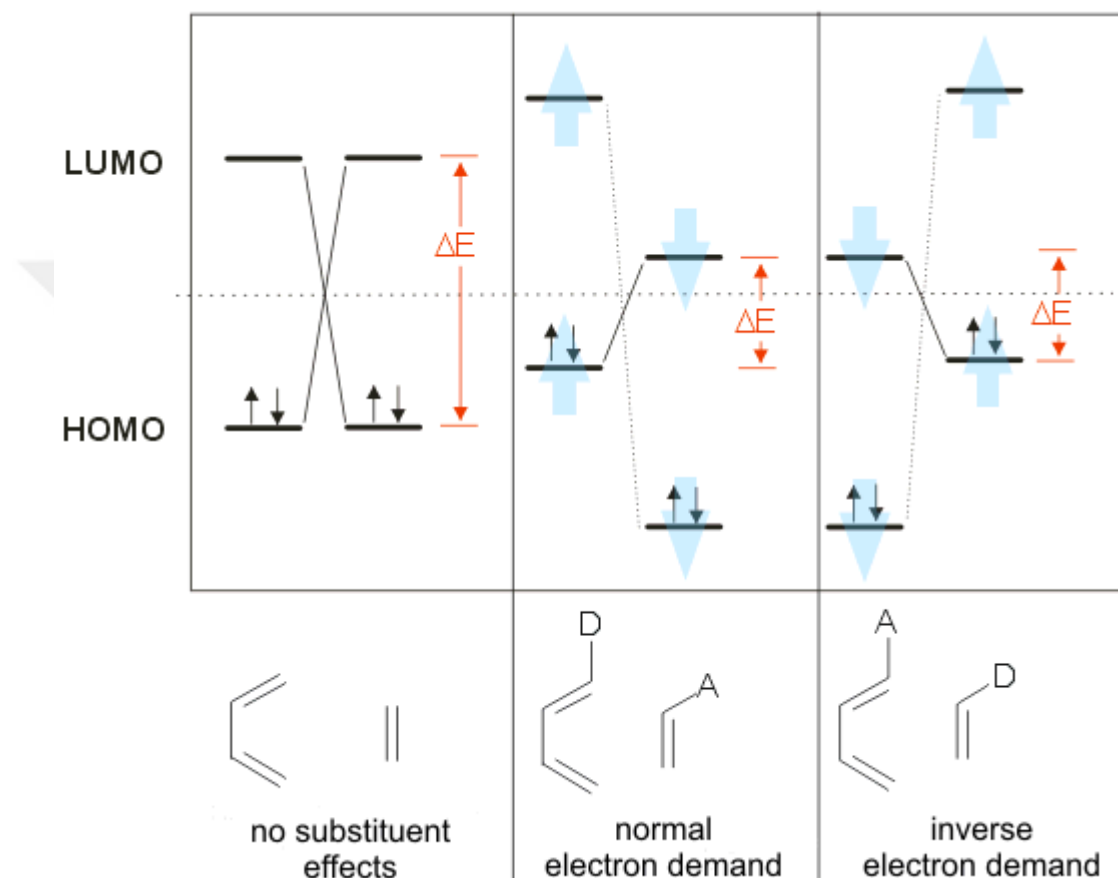


Figure 7.2. Molecular orbital representation of Diels-Alder reactions with normal and inverse electron demand.

For a substituted dienophile, there are two possible stereochemical orientations with respect to the diene, endo and exo. In the endo transition state, the reference substituent on the dienophile is oriented toward the orbitals of the diene. In the exo transition state, the substituent is oriented away from the system. (Figure 7.3)

A wide range of dienes take part in the Diels-Alder reactions being open chain and cyclic dienes. Cyclic dienes are generally more reactive than the open chain ones [129]. Heterodienes, which contains one or more hetero-atoms are also much used in synthesis. Heterosubstituents on the diene have a controlling effect on the regioselectivity of the

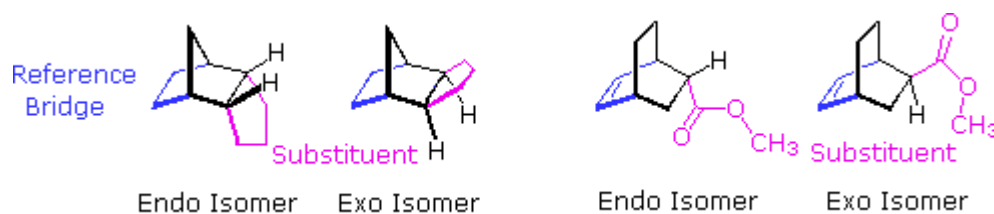


Figure 7.3. Examples for exo and endo stereoisomers in Diels-Alder reaction.

cycloaddition reactions and formation of heterocyclic-six-membered rings [130].

## 7.1. Introduction

The Diels-Alder reaction plays an important role in organic synthesis. The enantioselectivity of the Diels-Alder reaction has been controlled by a variety of chiral catalysts or chiral auxiliaries, however the control of exo/endo selectivity has been found to be more difficult [131–135]. Recently, some of us have used an inverse-electron demand hetero Diels-Alder reaction of norbornene with thiazolidine scaffold containing thiadienes. This synthesis was the first reaction to achieve an absolute *exo*-selectivity of a norbornene ring in an inverse-electron demand hetero Diels Alder reaction [136]. The synthesis of the heterodienes was done by a sequential conversion of the corresponding thiazolidine-4-ones [137] (1) using Lawesson's reagent (LR) to 2-arylimino-3-aryl-thiazolidine-4-thiones (2) and into 5-benzylidene-2-arylimino-3-aryl-thiazolidine-4-thiones (3) by reaction with benzaldehyde (Figure 7.4) [136]. 5-Benzylidene-2-arylimino-3-aryl-thiazolidine-4-thione (3) is a derivative of thiazolidine which belongs to an important group of heterocyclic compounds containing sulfur and nitrogen in a five member ring. The latter nucleus is also known as the wonder nucleus because it gives out different derivatives with all different types of biological activities [138]. The thiazolidinone nucleus having a diverse biological potential, has drawn the attention of chemists and pharmacologists. The anticancer and anti HIV activities are the most encouraging results for the pharmacists. Also the research in anticonvulsant, FSH agonistic and CFTR inhibitory activity has given positive results [139]. Methods for labeling biomolecules with fluorescent dyes and affinity tags have become indispensable tools in the modern life sciences. Strategies that allow site-specific post

synthetic coupling of molecules under mild conditions are sought [140]; and in this respect cycloaddition reactions have recently gained considerable importance [141–146]. Among others Jaschke and coworkers have used cycloadditions as tools for labeling and modifying biomolecules [146–148] and have established inverse-electron-demand Diels-Alder reactions as tools for the covalent and irreversible derivatization of various molecules, such as peptides and small-molecule drugs [149–154]. In a recent study, norbornene moieties are introduced as dienophiles into oligonucleotides during solid-phase synthesis, and the deprotected oligomers are then conjugated with water-stable tetrazinedienes [155].

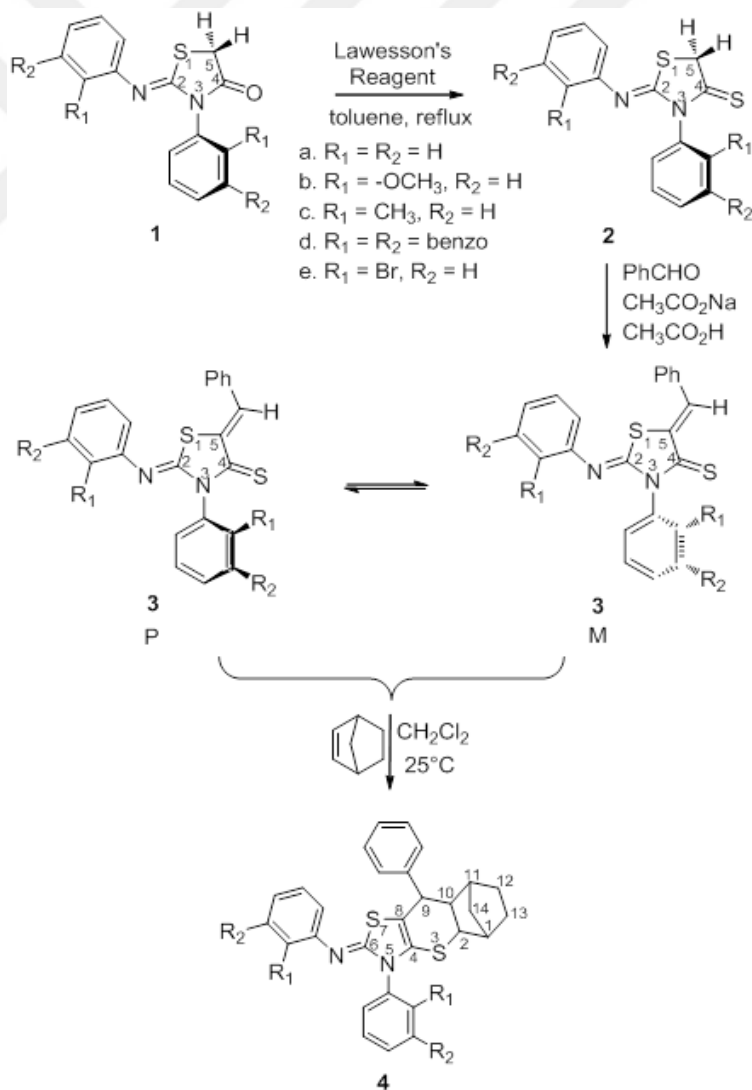


Figure 7.4. Synthesis of 2, 3 and 4.

Atropisomerism on the other hand, is a stereochemical phenomenon which may have important implications in medicinal [156] and biochemical [157] fields. If within a molecule the activation barrier for rotation around a single bond amounts to 23 kcal/mole at ambient temperature the conformers become stable enough to be isolable and they are then termed as atropisomers [158].

Exo selectivity of norbornene and its high reactivity in Diels-Alder reaction has great interest in organic chemistry [159]. The origins of this selectivity have been studied by several groups [160–162]. In the study of Dogan *et al.* atropisomeric 5-benzylidene-2-arylimino-3-aryl-thiazolidine-4-thiones (**3**) were used as heterodienes in the inverse electron-demand hetero Diels-Alder cycloadditions with norbornene as a dienophile at 25 °C (Figure 7.4). The reactions with norbornene were found to proceed with 100% *exo*-selectivity as determined by NMR experiments [136]. It is the purpose of this study to elucidate the origins of the stereoselectivity of the hetero Diels-Alder cycloaddition by using quantum chemical computational tools.

In this study the *exo* selectivity in the hetero Diels-Alder reaction of atropisomeric 5-benzylidene-2-arylimino-3-aryl-thiazolidine-4-thiones with norbornene has been investigated with computational tools. Taking into account the *M/P* chiral character of the *o*-methoxyphenyl substituted heterodienes in addition to the *exo/endo* selectivity, 8 different transition structures have been located. Based on the direction of approach of the diene and the dienophile for each plausible path it is found that *endo* products are not preferred because of the large distortion of norbornene and the rather eclipsed conformations of these transition state structures. Computational results are consistent with the experimental *exo/endo* selectivity. The computational methodology (M06-2X/6-31+G(d)//B3LYP/6-31+G(d)) has been justified by comparison of the experimental rotational barriers with the calculated ones for selected compounds.

## 7.2. Computational Methodology

All computations were carried out with the Gaussian 09 series of programs [47]. The stationary points were located using the B3LYP/6-31+G(d) [2, 5, 6, 163, 164], M06-

2X/6-31+G(d) [7] methodologies. All stationary points have been characterized by a frequency analysis from which thermal corrections have also been obtained. Local minima and first order saddle points were identified by the number of imaginary vibrational frequencies. Intrinsic reaction coordinate (IRC) [165] calculations were performed on the transition state structures to determine the connectivity of the transition state structure to the corresponding product and reactant. Conformational searches for the structures corresponding to reactants, transition states and products have been carried out with the methodologies used. Charge analysis was carried out by using full natural population analysis (NPA) [166].

B3LYP is found to be poor in computing  $\pi$  -  $\sigma$  energy changes; it underestimates the exothermicity of Diels-Alder reactions [167] and the intermolecular hydrogen bonding interactions [168]. In Diels-Alder reactions, M06-2X, is known to yield more exothermic reactions than predicted by B3LYP [167]. Even though both methodologies have been used in this study, M06-2X seems to reproduce better the experimental findings when applied to the geometries optimized with B3LYP.

Solvent calculations were carried out with the Integral Equation Formalism Polarizable Continuum Model (IEFPCM) [14, 15]. Dichloromethane ( $\epsilon=8.93$ ) has been used for compound 4 and toluene ( $\epsilon=2.37$ ) has been used to evaluate the rotational barriers of 1b and 2b. We used the ideal gas approximation and assumed  $T = 298.15$  K and 1 atm (gas phase) or 1 M (solution). The computation of free energies of activation in solution was done according to typical procedures based on thermodynamic cycles. Accordingly, solvation free energies include a correction to account for a change in the reference state (This change is  $RT \ln(24.5)$  which corresponds to  $1.89 \text{ kcal mol}^{-1}$  at  $298.15$  K) [169, 170]. The population of the different conformations was calculated by taking into account the Gibbs Free energies using the Boltzmann distribution under the experimental conditions.

Decomposition of the activation energy ( $\Delta E^\ddagger$ ) into distortion energy and interaction energy yields valuable insight into the difference between the activation energies of the *endo* and *exo* pathways [2, 5–7, 163, 164]. The distortion energy ( $\Delta E_{dist}^\ddagger$ ) is the

energy required to distort the reactants into the geometry they have in the transition states and interaction energy ( $\Delta E_{int}^\ddagger$ ) is a negative value which indicates favorable interaction between the reactants. The activation barrier is the sum of these two terms,  $\Delta E^\ddagger = \Delta E_{dist}^\ddagger + \Delta E_{int}^\ddagger$ .

### 7.3. Results and Discussion

The thionation reaction of 2-arylimino-3-aryl-thiazolidine-4-one with Lawesson's reagent gave the corresponding thiazolidine-4-thione (Figure 7.4). Compound 2 was converted into the corresponding 5-benzylidene-2-arylimino-3-aryl-thiazolidine-4-thione (3) by reaction with benzaldehyde (Figure 7.4). In compounds 1-4, if  $R_1 \neq H$  the rotation about the  $N(sp^2)-C_{aryl}$  bond is sterically restricted due to the presence of the exocyclic groups bonded to C4 or the arylimino group on the heterocyclic ring and the partial rotation about this bond gives rise to M and P enantiomers [136]. In inverse electron demand Diels-Alder reaction unlike the normal Diels-Alder, the cycloaddition takes place between an electron rich dienophile and an electron poor diene. Norbornene being an electron rich alkene is ideally suited for such a reaction. The reactivity and *exo*-selectivity of norbornene in cycloadditions has been of mechanistic interest and has led to useful chemistry involving norbornenes [159, 171]. Huisgen and co-workers have observed the high reactivity of norbornene and its derivatives [172–175]. Houk *et al.* have recently investigated the transition states for 1,3-dipolar cycloadditions to a number of norbornenes and to simple alkenes [176], and reviewed the torsional control of stereoselectivities in electrophilic additions and cycloadditions to alkenes including norbornenes [177]. When, the hetero Diels-Alder reaction of the *ortho*-unsubstituted compound 3a with norbornene takes place, a racemic mixture of two enantiomeric rings is produced. The addition can follow in principle four different pathways (Figure 7.5) to produce two diastereomeric pairs. The fact that only one racemic pair is experimentally obtained *exo* selectively points to the up-*exo* and down-*exo* approaches of the norbornene ring to the heterodiene (Figure 7.5). In this study the inverse electron-demand hetero Diels-Alder reaction of compound 3b with norbornene is investigated in order to explain the stereoselectivity found by Dogan *et al.*

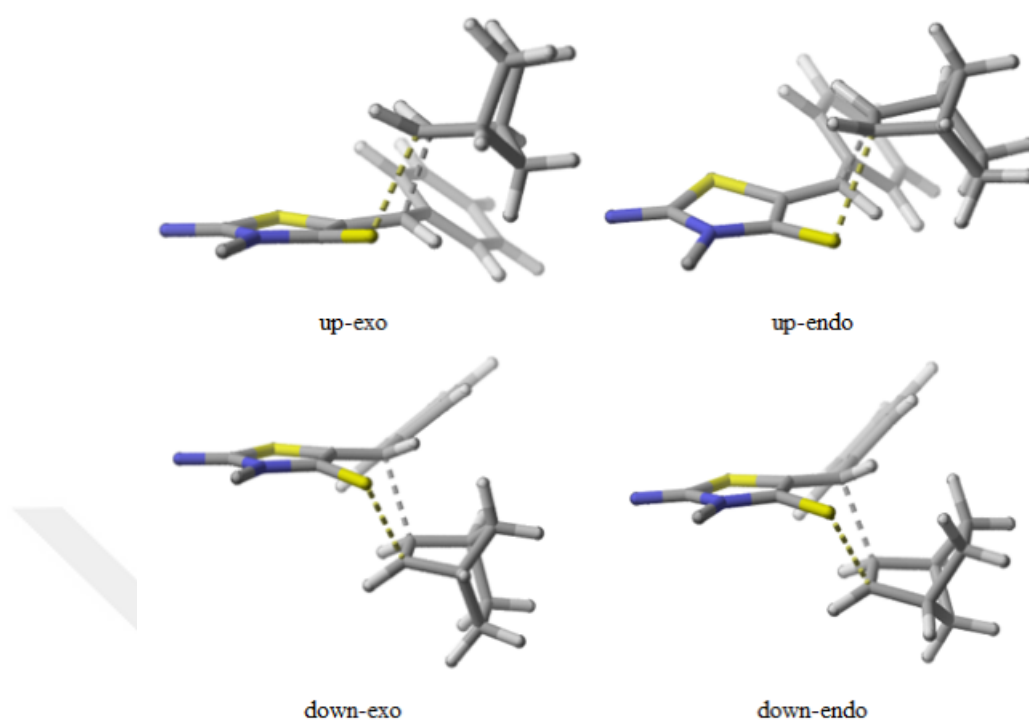


Figure 7.5. The inverse-electron demand Diels-Alder reaction of 5-benzylidene-3-phenyl-2-phenyliminothiazolidine-4-thione (3a) with norbornene yielding endo and exo products.

### 7.3.1. Rotational Barriers of 1b and 2b

Compounds 1b and 2b exist as racemates of interconvertible enantiomers M and P. Experimentally, barriers to rotation about the N3(sp<sup>2</sup>)-C<sub>aryl</sub> bond have been determined by thermal racemization of the micropreparatively separated enantiomers. The activation barrier of the compound 1b had been determined as 23.4 kcal/mol in ethanol [137]. It is known that solvents used during the thermal racemization process may change the barrier significantly [178, 179]. In order to be able to compare the activation barrier of 1b with that of 2b which has been determined as 27.2 kcal/mol in toluene, the barrier of 1b in this study has been determined also in toluene after a micropreparative separation on the Chiralpak IA column by enantiospecific HPLC, and found as 22.7 kcal/mol. The result is in accordance with the previous finding that the nonpolar solvents decrease the rate of interconversion of the enantiomers of axially chiral nonbiaryl atropisomers [178]. Thus, a benchmark study has been carried out first in order to test the methodologies. During racemization via rotation around

the pivot N3(sp<sup>2</sup>)-C<sub>aryl</sub> bond, 1b and 2b may in principle pass through two different planar transition states; the methoxy group passing N or the methoxy group passing S/O. Rotations from both sites-N and S/O have been evaluated and the results are summarized in Table 7.1.

Table 7.1. Rotational barriers (kcal/mol) of 1b and 2b around the N3-C<sub>aryl</sub> bond. Toluene is used as a solvent at T=333K.

	exp	M06-2X/6-31+G(d)/ B3LYP/6-31+G(d) $\Delta G_s^\ddagger$	M06-2X/ 6-31+G(d) $\Delta G_s^\ddagger$
TS-rot-1b-O	22.7	25.1	24.2
TS-rot-1b-N		25.4	25.7
TS-rot-2b-S	27.2	31.5	30.7
TS-rot-2b-N		29.9	29.6

All the methodologies used reproduce qualitatively quite well the experimental trend (Table 7.1), the discussion that follows will be carried out with M06-2X/6-31+G(d)//B3LYP/6-31+G(d) in toluene. The activation barriers for TS-rot-1b-N and TS-rot-1b-O are very close to each other indicating that rotation at room temperature can take place from both sides (1/1.7). TS-rot-1b-O is favored over TS-rot-1b-N due to favorable O-CH<sub>3</sub>...O interactions in the former. Also note that in TS-rot-1b-N the proximity of the phenyl and methoxy is not in favor of its stability. On the other hand, due to the repulsion of the oxygen atoms, the oxazolidine ring is more distorted in TS-rot-1b-O ( $\theta_{S-C-C-O}$ :152.8°) as compared to TS-rot-1b-N ( $\theta_{S-C-C-O}$ :176.8°) and 1b ( $\theta_{S-C-C-O}$ : -178.9°).

TS-rot-2b-S has a larger activation barrier difference than TS-rot-1b-O, (31.5 vs 25.1 kcal/mol), this difference stems from the replacement of O by S rendering the rotation about the N3(sp<sup>2</sup>)-C<sub>aryl</sub> bond more hindered. The rotation of the ring via N (TS-rot-2b-N) is favored over its rotation via S (TS-rot-2b-S). The charge analysis has shown that in TS-rot-2b-N there is a repulsion between N and O, whereas TS-rot-2b-S has two stabilizing interactions, one between N and H (benzene) and a weaker one



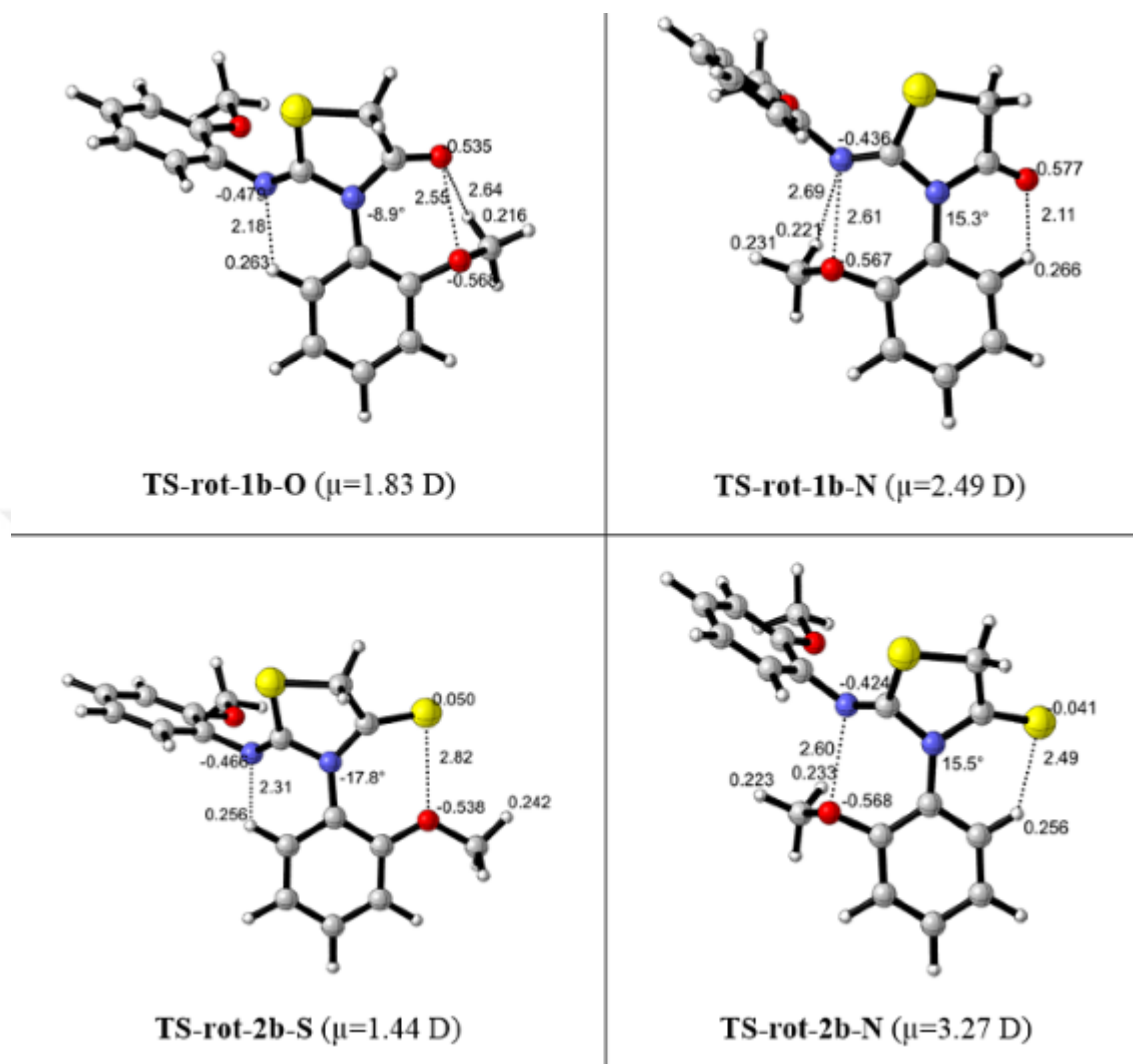


Figure 7.6. Rotational transition state structures with NPA charges and dipole moments ( $\mu$ ) for 1b and 2b in toluene (M06-2X/6-31+G(d)//B3LYP /6-31+G(d)).

between O and S, nevertheless the 5-membered ring in TS-rot-2b-S ( $\theta_{S-C-C-S}$ :140.8°) is more distorted than the one in in TS-rot-2b-N ( $\theta_{S-C-C-S}$ :170.4°) as compared to the one in 2b ( $\theta_{S-C-C-S}$ : -179.0°), also the solvent stabilizes further the more polar transition structure TS-rot-2b-N.

### 7.3.2. Hetero Diels-Alder Reactions of 3b with Norbornene

The reactivity and exo-selectivity of norbornene in cycloadditions has been of mechanistic interest and has led to useful chemistry involving norbornenes [159, 171]. Huisgen and co-workers have observed the high reactivity of norbornene and its deriva-

tives [172–175]. Houk *et al.* have recently investigated the transition states for 1,3-dipolar cycloadditions to a number of norbornenes and to simple alkenes [176].

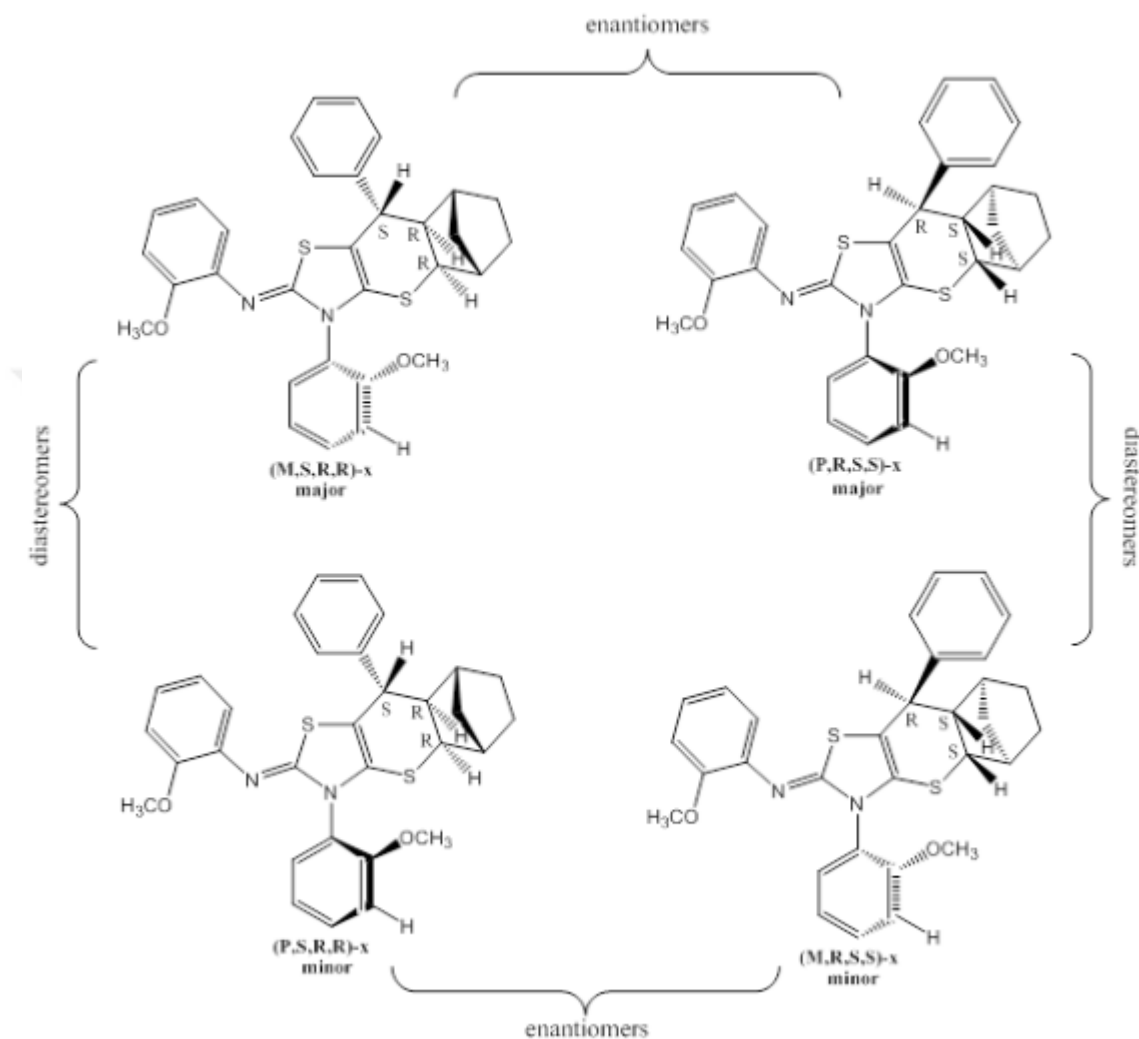


Figure 7.7. Experimental results for the adduct.

In the reaction of 3b and norbornene, the addition of norbornene to compound 3b can take place via 8 different transition structures based on the nature of the chiral centers 2,9 and 10 (Figure 7.1- 7.2). Note that C2 and C10 must have the same chirality so that for example the configuration S,R,S can not take place. The following combinations have been considered as plausible transition structures: M,S,R,R (its enantiomer P,R,S,S); P,S,R,R (its enantiomer M,R,S,S); P,S,S,S (its enantiomer M,R,R,R); M,S,S,S (its enantiomer P,R,R,R). In each of the four different cases (M,S,R,R; P,S,R,R; P,S,S,S; M,S,S,S) the orientation of norbornene can be exo (x) or endo (n).

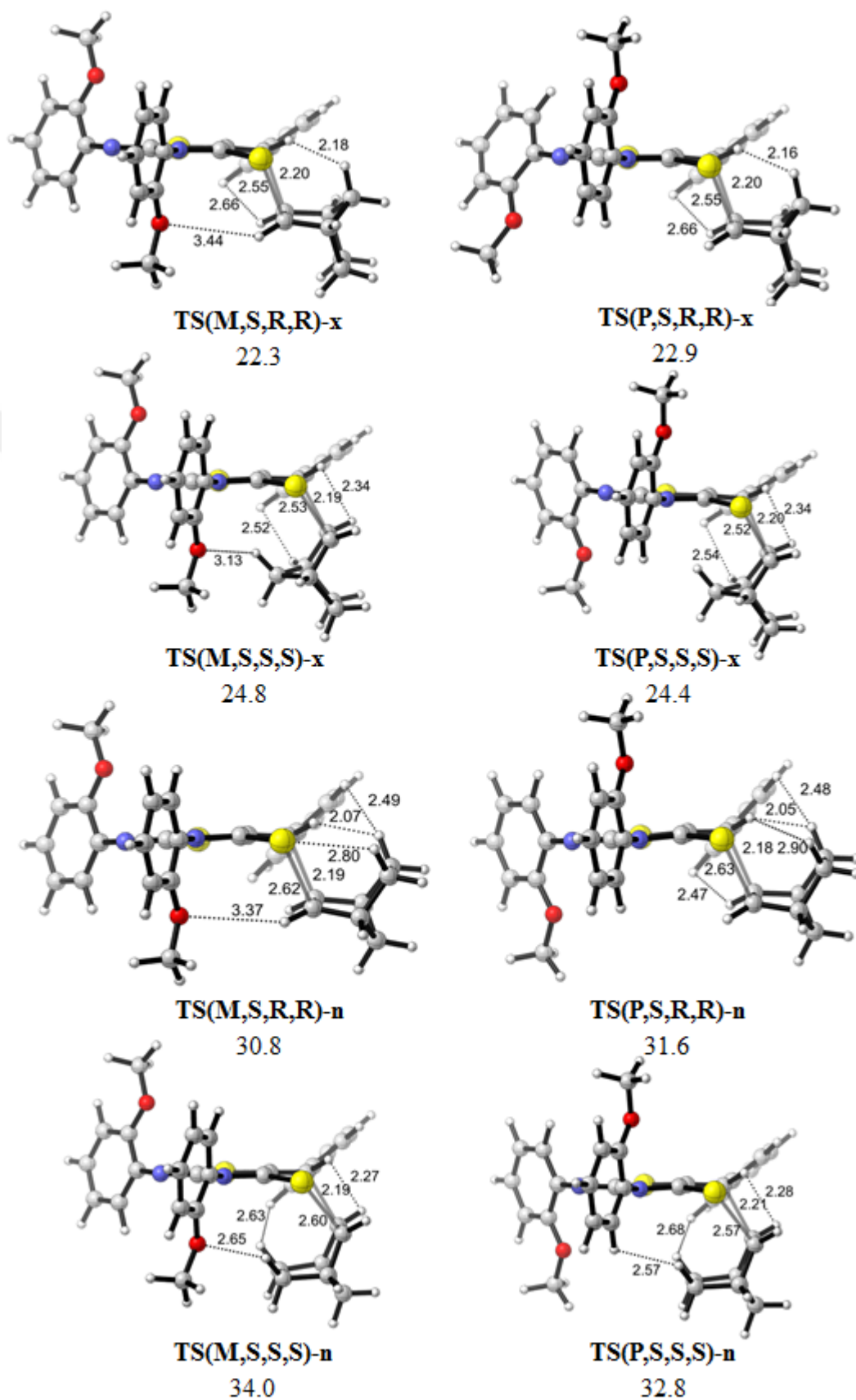


Figure 7.8. Transition structures for the reaction between 3b and norbornene.

Table 7.2. Activation energies ( $\Delta G^\ddagger = G(\text{TS}) - G(3b) - G(\text{norbornene})$ ), reaction energies ( $\Delta G_{rxn} = G(\text{Product}) - G(3b) - G(\text{norbornene})$ ), dihedral angles and distortion-interaction energies for the transition states.  
(M06-2X/6-31+G(d)//B3LYP/6-31+G(d) in  $\text{CH}_2\text{Cl}_2$ )

Structures	$\Delta G^\ddagger$	$\Delta H^\ddagger$	$\Delta G_{rxn}$	$\theta_1(^{\circ})$	$\theta_2(^{\circ})$	$\theta_{twist(^{\circ})}$	$\Delta E^\ddagger$	$\Delta E_{d}^{\ddagger, thione}$	$\Delta E_{d}^{\ddagger, norbornene}$	$\Delta E_{d}^{\ddagger, total}$	$\Delta E_q^{\ddagger}$
TS(M,S,R,R)-x	22.3	20.5	-15.3	143	-148.4	-176.1	9.6	11.5	9.3	20.8	-11.3
TS(P,S,R,R)-x	22.9	20.5	-15.5	143.1	-148	-176.1	10.2	11.9	9.4	21.3	-11.1
TS(M,S,S,S)-x	24.8	23	-11.8	146.1	-140.9	-179.8	11	12.4	10.8	23.2	-12.2
TS(P,S,S,S)-x	24.4	22.7	-11.3	146.2	-140.6	-179.8	10.9	12.1	10.9	23	-12.1
TS(M,S,R,R)-n	30.8	29.2	-13.2	-150.5	140.4	115.7	18.5	12	17.7	29.7	-11.2
TS(P,S,R,R)-n	31.6	23.8	-13.7	-150.4	140.6	115.6	19	12.3	17.7	30	-10.9
TS(M,S,S,S)-n	34	32.4	-12	-137.7	147.4	102	20.5	13.2	20.2	33.4	-13
TS(P,S,S,S)-n	32.8	31.8	-11.9	-137.9	147	102.3	19.6	12.6	20.2	32.8	-13.1

The transition structures corresponding to the addition of norbornene to 5-benzylidene-2-arylimino-3-aryl-thiazolidine-4-thiones (3b) via these alternatives are depicted in Figure 7.8, the energetics related to their formation are reported in Table 7.2, whereas the experimental results are given in Figure 7.7. The reactions are concerted, bond formation is synchronous, i.e. forming C-C and C-S bonds are approximately 40% of their values in the products furthermore forming bond distances do not vary significantly ( $2.18 \text{ \AA} < \text{C}\dots\text{C} < 2.21 \text{ \AA}$  and  $2.52 \text{ \AA} < \text{C}\dots\text{S} < 2.63 \text{ \AA}$ ). The distortion of norbornene in the transition structures has been taken into account by comparing the structure of norbornene prior to the cycloaddition to the one in the transition structures. The change in the dihedral angles  $\theta_1$ ,  $\theta_2$  and  $\theta_{twist}$  along the reaction have been monitored.  $\theta_1$  (C2-C1-C3-C7) is indicated by the green atoms,  $\theta_2$  (C4-C3-C1-C8) is shown with the yellow line,  $\theta_{twist}$  is the dihedral of the atoms C13-C4-C3-C7 (Figure 7.9). These dihedrals in the optimized norbornene are  $\theta_1 = 172.8^\circ$ ,  $\theta_2 = -172.8^\circ$  and  $\theta_{twist} = 153.7^\circ$ .

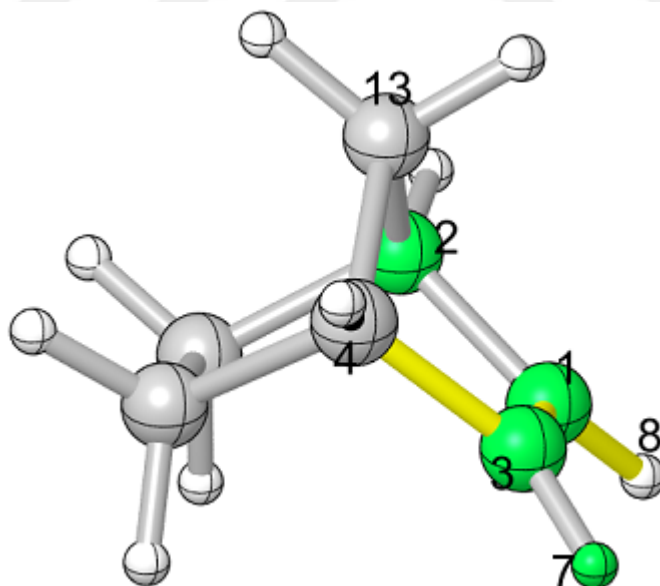


Figure 7.9. Optimized structure for norbornene in  $\text{CH}_2\text{Cl}_2$  (M06-2X/6-31+G(d)//B3LYP/6-31+G(d))

Among these structures M/P-S,R,R-n and M/P-S,S,S-n have very high activation barriers as expected because of steric hindrance in the *endo* transition structures.

Figure 7.10 shows Newman projections of  $\text{TS}(\text{M},\text{S},\text{R},\text{R})\text{-x}$  and  $\text{TS}(\text{M},\text{S},\text{R},\text{R})\text{-n}$  where the former is in the almost staggered conformation and in the latter the forming bonds are eclipsing with the vicinal HCCH bonds of the norbornene. The transition state structures for the exo approach shows a staggered conformation of the partially formed C-S and C-C bonds with respect to the C-C and C-H bonds to the bridgehead carbons (dihedral angles  $83.8^\circ$  and  $-43.9^\circ$ ). For the endo approach on the other hand, the conformation is rather eclipsed (dihedral angles  $52.2^\circ$  and  $-78.6^\circ$ ), as has been found before for several 1,3-dipolar cycloaddition reactions [176]. This makes the exo approach more favorable by 8.5 kcal/mol compared to the endo approach and constitutes the major contribution to the exo selectivity issue also in the hetero Diels-Alder reactions.  $\text{TS}(\text{M},\text{S},\text{R},\text{R})\text{-x}$  yields highly endothermic product ( $\Delta G_{rxn} = -15.3$  kcal/mol) and is the most favorable. Both  $\text{TS}(\text{M},\text{S},\text{R},\text{R})\text{-x}$  and  $\text{TS}(\text{M},\text{S},\text{S},\text{S})\text{-x}$  are well stabilized by long range  $\text{H}_3\text{C}\cdots\text{H-C}$  (norbornene) favorable interactions ( $3.44\text{\AA}$  and  $3.13\text{\AA}$  respectively), these are missing in the other transition structures. Note that the dihedral angles of norbornene  $\theta_1$ ,  $\theta_2$  and  $\theta_{twist}$  are the least distorted in  $\text{TS}(\text{M},\text{S},\text{R},\text{R})\text{-x}$  and  $\text{TS}(\text{P},\text{S},\text{R},\text{R})\text{-x}$  as compared to the naked norbornene. Furthermore these 2 transition structures yield the most stable products. The energy profile of 3b yielding 4b via the transition structure  $\text{TS}(\text{M},\text{S},\text{R},\text{R})\text{-x}$  is displayed in Figure 7.11.

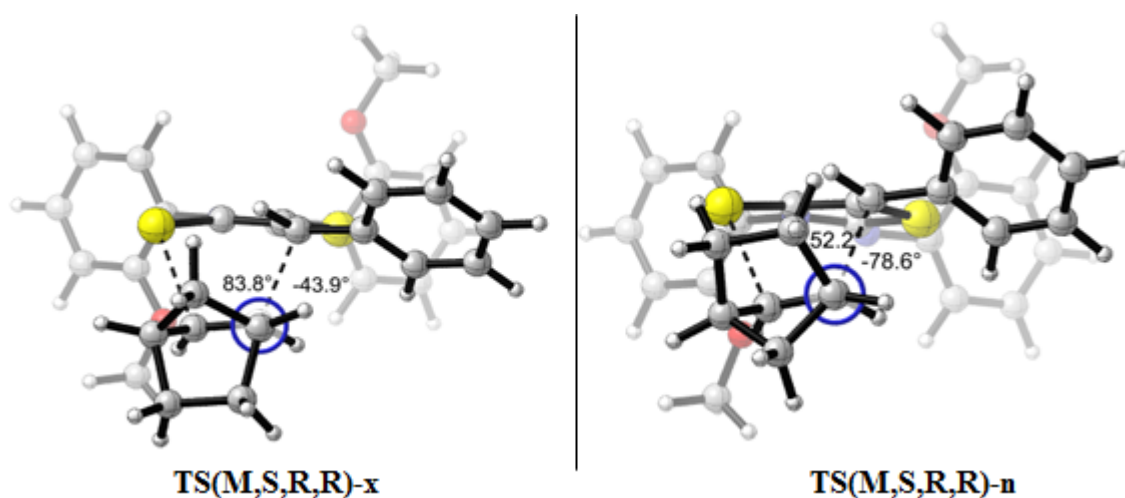


Figure 7.10. Newman projections for the cycloadditions of norbornene to thione with exo and endo faces (M06-2X/6-31+G(d)//B3LYP/6-31+G(d) in  $\text{CH}_2\text{Cl}_2$ ).

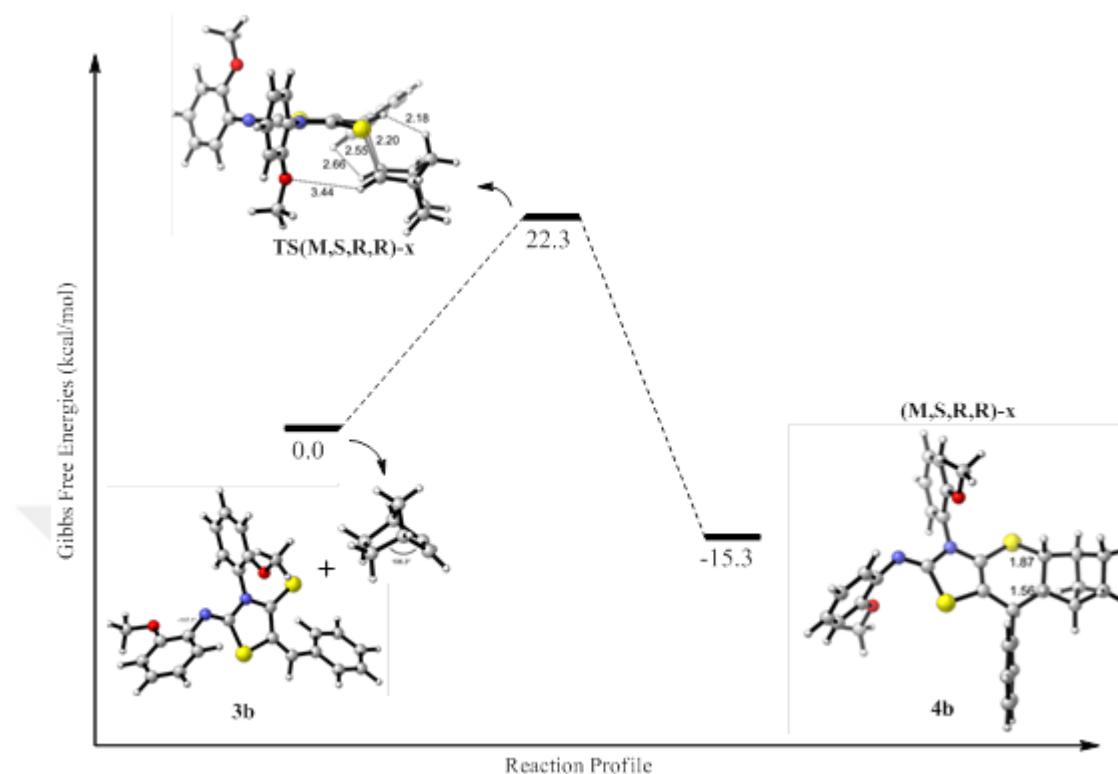


Figure 7.11. Reaction profile for the reaction 3b with norbornene resulting in 4b (M06-2X/6-31+G(d)// B3LYP/6-31+G(d)).

In order to have a deeper insight for the transition structures, the distortion-interaction model [180–186] has been utilized (Table 7.2). The distortion/interaction model which is an approach to dissect the activation barriers into distortion energy and interaction energy has been used by our group in various cases [187–189]. Unlike the interaction energies ( $\Delta E_{int}^\ddagger$ ) (10.9–13.1 kcal/mol), activation barriers ( $\Delta E^\ddagger$ ) and distortion energies ( $\Delta E_d^\ddagger$ ) are in a large range ( $9.6 < \Delta E^\ddagger < 20.5$  and  $20.8 < \Delta E_d^\ddagger < 33.4$  kcal/mol) which shows that the activation energy is governed mainly by the distortion energy. The distortion of norbornene comprises  $\sim 45\%$  of the total distortion energy in the exo transition structures while it makes up  $\sim 60\%$  of the total distortion energy in the endo transition structures. This portion of the distortion energy is the energy required to distort norbornene from its equilibrium structure, indicating that for the endo transition structures norbornene is 1.5 fold more distorted than the thione moiety while for the exo transition structures the two moieties are almost equally distorted. Figure 6 shows a strong correlation ( $R^2=0.98$ ) between activation energies and reactant

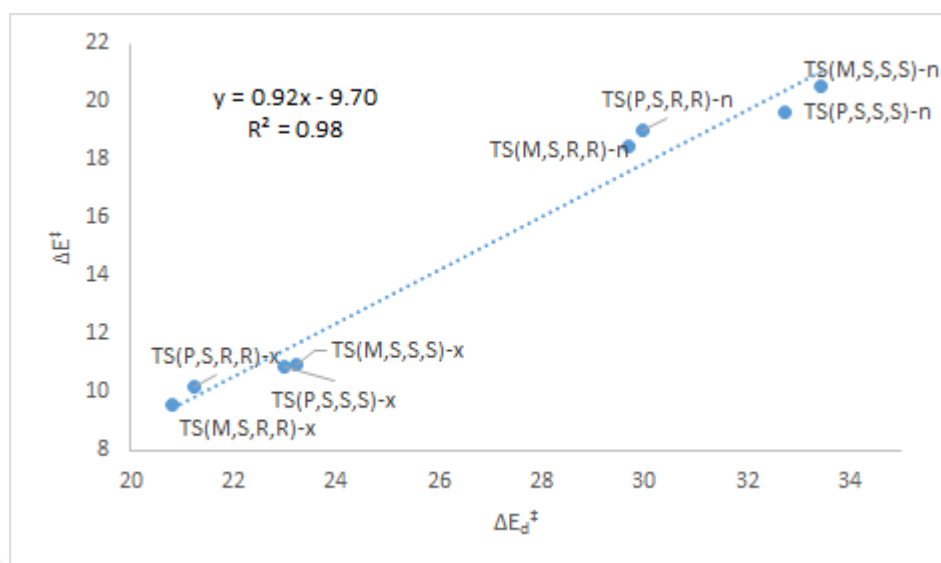


Figure 7.12. Plot of activation energies versus distortion energies of the reactions of thione derivatives and norbornene calculated by M06-2X/6-31+G(d)//B3LYP/6-31+G(d). Values in kcal/mol.

distortion energies. The large distortion is mostly associated with bending of C-H bonds out of plane in norbornene. Comparison of the dihedral angle,  $\theta_{twist}$  of norbornene ( $153.7^\circ$ ) shows that TS(M,S,R,R)-x and TS(P,S,R,R)-x are less distorted ( $-176.1^\circ$ ) as compared to TS(M,S,S,S)-n and TS(P,S,S,S)-n ( $102^\circ$ ). On the other hand TS(M,S,S,S)-n and TS(P,S,S,S)-n have slightly higher interaction energies than TS(M,S,R,R)-x due to the presence of strong H-bonds ( $2.65 \text{ \AA}$  and  $2.57 \text{ \AA}$  in the former, as compared to  $3.44 \text{ \AA}$  in the latter). The Gibbs free energy activation barriers of TS(P,S,R,R)-x and TS(M,S,R,R)-x are close to each other, the Boltzmann distribution ratio has been found as 1:2.9 which is in harmony with the experimental results (1:2).

### 7.3.3. Rotational Barrier of the Hetero Diels-Alder Adduct (4b)

The reaction of 5-benzylidene-2-arylimino-3-aryl-thiazolidine-4-thione (3b) with norbornene yields mainly 4b (M,S,R,R)-x, the latter can be converted to its diastereomer (P,S,R,R)-x if the rotational barrier between the two can be overcome at room temperature. The Gibbs Free energy profile of the interconversion of 4b has shown the rotation via S (TS-4b-rot-S) to be favored by almost 5 kcal/mol over the rotation via N (TS-4b-rot-N) (Figure 7.13). This selectivity can be attributed to the charge distri-



bution in the thiazolidine ring: in TS-4b-rot-S two stabilizing interactions are available between S(0.298)—O(-0.547) and N(-0.486)—H(0.269) whereas in TS-4b-rot-N there is a repulsive interaction between the same eclipsing centers (S(0.268)—H(0.242) and N(-0.441)—O(-0.530)). The distortion orientation of the thiazolidine ring has been followed by observing the S-C-C-S angle which is 158.9 in TS-4b-rot-N, 152.6 in TS-4b-rot-S and 179.6 in 4b. Overall, the magnitude of the activation barrier of this rotation (20.6 kcal/mol) indicates that the conversion of (M,S,R,R)-x to (P,S,R,R)-x is feasible and thus 4b is *not* atropisomeric at room temperature, in harmony with experimental findings [136].

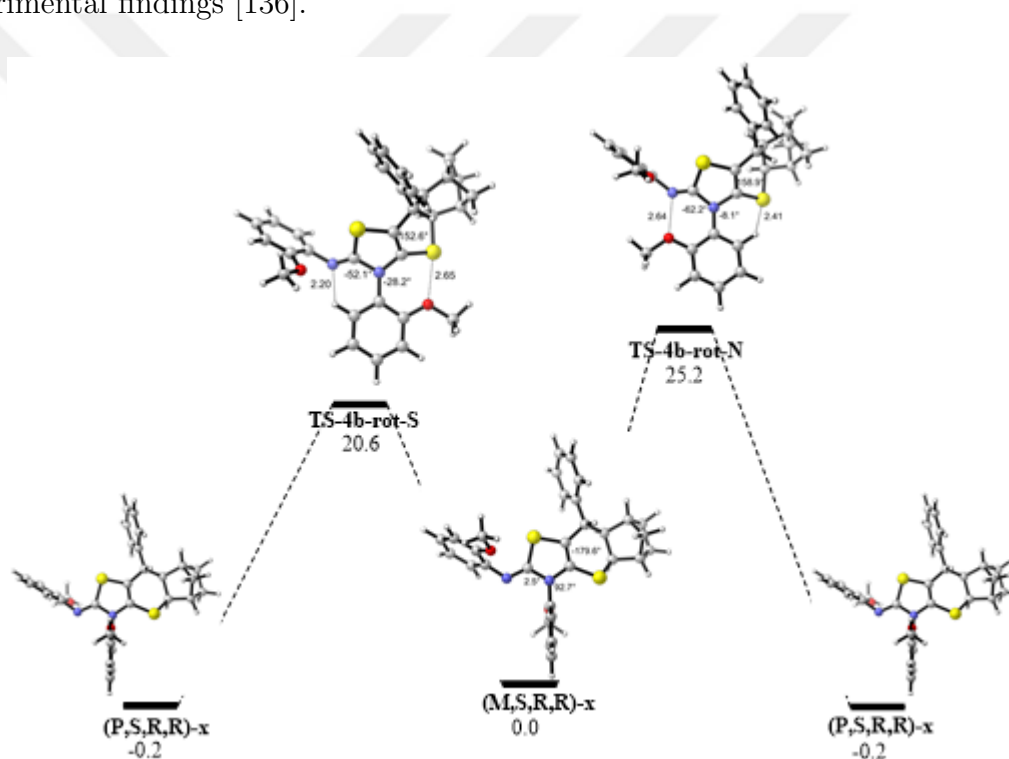


Figure 7.13. Gibbs Free Energy profile (kcal/mol) for the interconversion of (M,S,R,R)-x to (P,S,R,R)-x in CH<sub>2</sub>Cl<sub>2</sub> at room temperature (M06-2X/6-31+G(d)//B3LYP/6-31+G(d)).

#### 7.4. Conclusion

In this work, the exo selectivity of norbornene in the inverse-electron demand Diels-Alder reaction with atropisomeric 5-benzylidene-3-(2-methoxyphenyl)-2-((2-methoxyphenyl)imino)thiazolidine-4-thione (3b) is demonstrated computationally. Further-

more the rotational activation barriers of the thione precursors have been evaluated and this has shown that 1b and 2b can rotate from both sides (O/N and S/N respectively). The adduct 4b although has been found to be nonatropisomeric at room temperature, the internal bond rotation was slow enough on the NMR time scale to make the minor and the major diastereomers distinguishable. The inverse electron demand Diels-Alder reaction has been investigated for each plausible type of approach of norbornene to thione and it is found that endo products are not preferred because of the large distortion of norbornene and the higher torsional strain present in these structures. Among the exo transition states, TS(M,S,R,R)-x is the most stable one because of the least steric hindrance and favorable intramolecular interactions. The calculated population of TS(P,S,R,R)-x and TS(M,S,R,R)-x reflects the experimental findings (1:2). Overall, in the hetero Diels-Alder reaction, the powerful effect of distortion of norbornene, the steric effect of the quasi-eclipsing forming bonds in the endo transition structures have been demonstrated successfully and the origins of the exo selectivity of norbornene have been highlighted with the M06-2X/6-31+G(d)//B3LYP/6-31+G(d) methodology.

## 8. ASSESSMENT OF THE DEGRADATION MECHANISM AND TOXICITY OF DICLOFENAC AND ITS BYPRODUCTS

Diclofenac (DCF) is a common non-steroidal anti-inflammatory drug used all over the world [190]. It is used to reduce inflammation and relieve pain diseases such as arthritis or acute injury. The name diclofenac is derived from its chemical name, 2-(2,6-dichloroanilino)phenylacetic acid. (Figure 8.1) Because of its persistent occurrence in fresh water environments owing to poor degradation in sewage treatment and its potential toxicity towards several aquatic organisms (e.g. fish and mussels), diclofenac is an emerging contaminant [147,191]. DCF is found in groundwater sources as a result of leaching through landfills ( $0.001\text{--}28.4 \mu\text{gL}^{-1}$  in surface and  $0.59 \mu\text{gL}^{-1}$  in groundwater) [192–194]. Although the short-term human health risks at these concentration levels is low, long-term effects are highly anticipated based on severe health effects in fish [195,196].

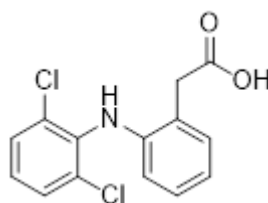


Figure 8.1. Structure of DCF (2-(2,6-dichloroanilino)phenylacetic acid)

Elimination of compounds in water by “Advanced Oxidation Processes” (AOPs) is a promising “green technology” owing to their effectiveness in the in-situ generation of reactive hydroxyl radicals ( $\cdot\text{OH}$ ) [197]. However, AOPs are energy intensive and therefore rarely used in large-scale water treatment. In any case, monitoring of the intermediate products and their relative toxicity are of utmost significance to assess the environmental safety and the efficiency of the applied process. Amongst a wide variety of AOPs (e.g. UV/ $\text{H}_2\text{O}_2$ ,  $\text{O}_3$ ,  $\text{O}_3/\text{UV}$ , UV/Fenton, UV/ $\text{TiO}_2$ ), ultrasonic irradiation (US) has lately received particular interest not only due to the uniqueness

of  $\cdot\text{OH}$  formation by thermal fragmentation of water molecules during implosion of cavitation bubbles, but also by additional benefits such as enhancement of mass transfer and chemical reaction rates, cleaning of solid surfaces and improving of catalytic activities [198].

### 8.1. Introduction

Diclofenac, (2-[2',6'-dichlorophenyl]amino] phenylacetic acid) (DCF) (Figure 8.1) is widely used as a non-steroidal anti-inflammatory drug and pain-relieving analgesic in humans and domestic animals. Owing to the fact that DCF exhibits low biodegradability and is readily excreted with urine, it is frequently detected in sewage treatment plant effluents and fresh water resources with moderate levels of aquatic toxicity [199]. Hence, DCF has been classified as an 'emerging water pollutant' due to its potential for long-term unpredictable health effects in humans. As such, a lot of research has been lately devoted to the degradation of the parent compound and its metabolites in water and advanced oxidation processes (AOPs) have been demonstrated to be viable solutions to the problem [200–202]. AOPs are based on the in-situ production of hydroxyl radicals ( $\cdot\text{OH}$ ) and reactive oxygen species (ROS) in water upon irradiation of the sample by UV light, ultrasound, electromagnetic radiation, and/or the addition of ozone or a semiconductor. The advantages of  $\cdot\text{OH}$  and ROS are that they are non-selective and highly reactive with a large range of organic compounds.

Reaction mechanisms for the decomposition of DCF by  $\cdot\text{OH}$ -mediated oxidation have been proposed [202–206], but need to be further explored. The results of previous studies show that the most common degradation intermediates are hydroxylated compounds as depicted in Figure 8.2, and compounds that form upon cleavage of the C-N bond, such as dichloroaniline, dichlorophenol, 2-indolinone. Subsequent oxidative ring cleavage was found to lead to carboxylic acid fragments via classic degradation pathways [204,206]. Further reaction of dichloroaniline with  $\cdot\text{OH}$  was found to produce 4-amino-3,5-dichlorophenol, 2,6-dichloro-p-hydroquinone and dichlorobenzene [204]. In addition, a cyclic intermediate (1-(2,6-dichlorophenyl)-indolin-2-one) has been detected by some researchers at highly acidic conditions [207]. The production of chloroanilines

such as N-(2,6-dichlorophenyl)-2-aminotoluene has been reported as part of the reduction pathway during the degradation of chlorobenzene [208, 209]. Final products such as oxalic acid, ammonium, nitric acid and hydrochloric acid were attributed to the mineralization process via complete cleavage of the NH-bridge [210]. Some of the above mentioned byproducts are displayed in Figure 8.2. More recently, it has been demonstrated that during  $\cdot\text{OH}$ -mediated oxidation, the toxicity of a DCF sample follows an up and down pattern during the early stages of the reaction, but stabilizes to a non-toxic level at extended reaction times [211].

The present work aims to propose the initial reactions of diclofenac with  $\cdot\text{OH}$  to elucidate the mechanism of subsequent reactions that yield the most common degradation byproducts reported in the literature. The study also encompasses estimation of acute toxicities of the intermediates to assess the potential risk of the parent compound and its oxidation byproducts in the aquatic environment.

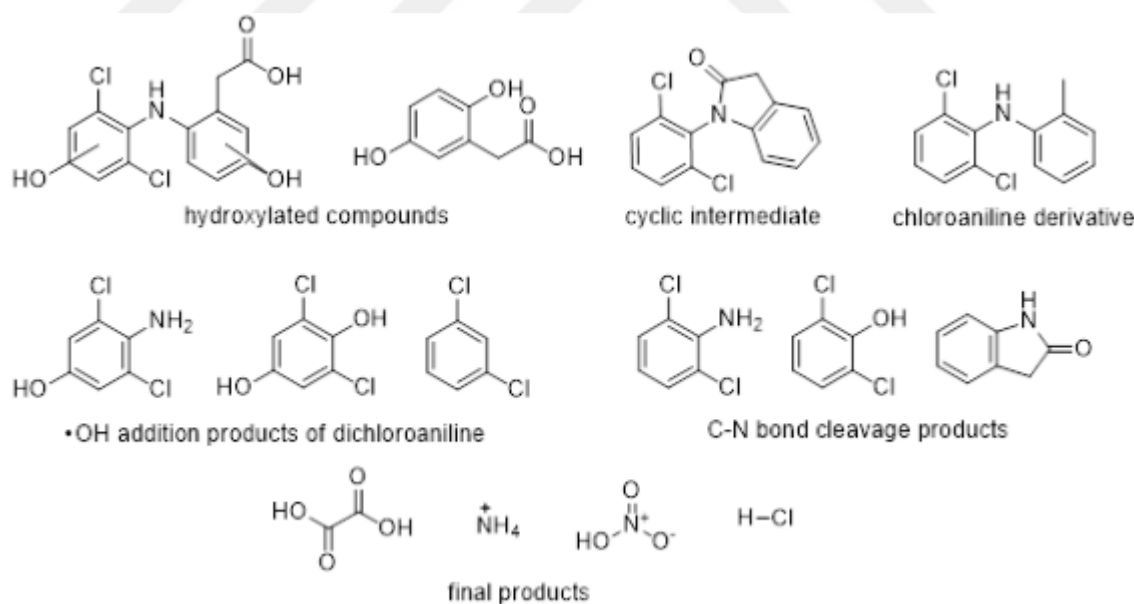


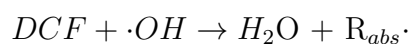
Figure 8.2. Molecular structures of some of the common degradation byproducts of diclofenac

## 8.2. Computational Methodology

### 8.2.1. Quantum Chemical Calculations

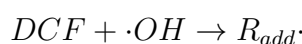
All computations were carried out with the Gaussian 09 program package [47]. The stationary points were located using the B3LYP/6-31+G(d) methodology [2, 5, 6, 163, 164] and characterized by frequency analysis, from which thermal corrections were obtained at 298K. Local minima and first order saddle points were identified by the number of imaginary vibrational frequencies. Intrinsic reaction coordinate (IRC) [165, 212] calculations were performed on the transition state structures to determine the connectivity of the transition state structure to the corresponding product and reactant. Conformational searches for the structures corresponding to reactants, transition states and products were carried out with the same methodology. Energies were further refined with the MPWB1K/6-311+G(3df,2p) level of theory [213]. The effect of the solvent environment was taken into account utilizing the Integral Equation Formalism Polarizable Continuum Model (IEFPCM) [14, 15], where water ( $\epsilon = 78.36$ ) was used as solvent. The stability of the radicals generated as a result of H-abstraction and OH-addition were calculated using Equation 8.1 and Equation 8.2 [214, 215] as:

*H – abstraction*



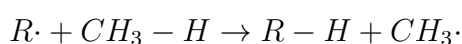
$$\Delta G_{rxn} = G(H_2O) + G(R_{abs}\cdot) - G(DCF) - G(\cdot OH) \quad (8.1)$$

*OH – abstraction*



$$\Delta G_{rxn} = G(R_{add\cdot}) + G(DCF) - G(\cdot OH) \quad (8.2)$$

The standard radical stabilization energies (RSE) of the generated radicals were also calculated using Equation 8.3 [216, 217], where  $\Delta H$  is the enthalpy change of the following isodesmic reaction and  $R\cdot$  is a carbon centered radical:



$$\Delta H_{298}^0 = \Delta_f H_{298}^0(\cdot CH_3) + \Delta_f H_{298}^0(R - H) - \Delta_f H_{298}^0(CH_3 - H) - \Delta_f H_{298}^0(R\cdot) \quad (8.3)$$

Note that when RSE is a positive number,  $R\cdot$  is supposed to be more stable than  $\cdot CH_3$  and if it is negative, it is less stable. The Gibbs free energies of the reactions were calculated by Eq. (4)

$$\Delta G_{rxn} = G(fragment(1)) + G(fragment(2)) - G(DCF) \quad (8.4)$$

The Gibbs free energies of the fragments are utilized in order to find the most possible fragmentation sites on DCF/DCF-.

### 8.2.2. Toxicity Assessment

The acute toxicity of DCF and its oxidation byproducts to green algae, daphnia and fish were estimated in terms of  $EC_{50}$  and  $LC_{50}$  using the ECOSAR software [218].

### 8.3. Results and Discussion

#### 8.3.1. Initial Reactions of Diclofenac with $\cdot\text{OH}$

Diclofenac has two aromatic rings connected with an amine group. The previous experimental work of some of the authors show that during degradation, the solution pH decreases from 6.50 to 5.23 in 30 min and even lower as the degradation proceeds, indicating the formation of acidic intermediates [211]. Because the medium is changing from a neutral to an acidic environment, the degradation of DCF is modeled in both its anionic and neutral forms ( $\text{pK}_a$  of diclofenac is 4.1-4.5 [219]); their best conformers are depicted in Figure 8.3. In both forms, there are strong intramolecular H-bonding interactions between the carboxylic oxygen and the amine hydrogen. As expected, these interactions are stronger in the anionic form (1.86 Å) than in the neutral form (2.08 Å) as a result of the excess negative charge on the oxygens in DCF<sup>-</sup>. Both ring systems in DCF (DCF<sup>-</sup>) are slightly twisted away from each other with a dihedral of  $-161.8^\circ$  ( $164.3^\circ$ ) to avoid steric clashes, as seen in Figure 8.3.

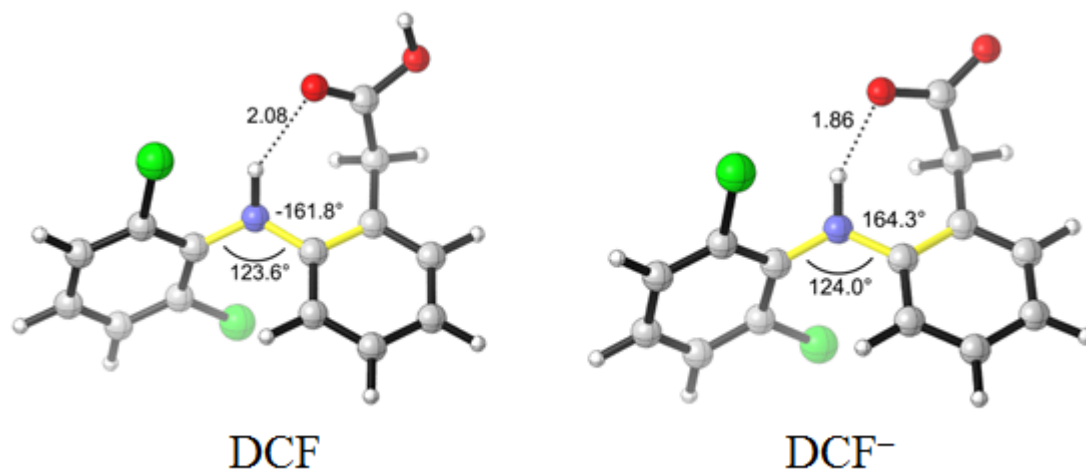


Figure 8.3. Optimized structures of diclofenac in neutral (DCF) and anionic forms (DCF<sup>-</sup>) (B3LYP/6-31+G(d) in water).

AOPs produce highly reactive hydroxyl radicals ( $\cdot\text{OH}$ ), which are the main oxidants in the degradation processes [220, 221]. In aqueous medium,  $\cdot\text{OH}$  radicals can



either add to diclofenac or abstract a hydrogen from it to give either addition or abstraction intermediates, respectively. In Figures 8.4 and 8.5, the reaction sites of DCF are labeled with numbers (1-7) and letters (a, b) in order to characterize their reactivities upon H-abstraction and OH-addition reactions.  $\cdot\text{OH}$  can abstract a hydrogen from the aromatic (1-6) or benzylic positions (7), leading to the formation of a radical carbon center on the DCF molecule and the elimination of water (Figure 8.4).

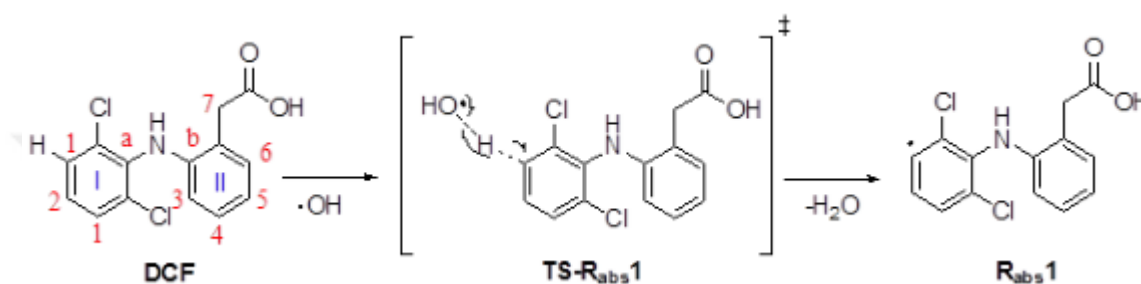


Figure 8.4. H-abstraction by OH from DCF, generating radical intermediate ( $R_{abs}$ ).

Table 8.1. Activation Gibbs free energies ( $\Delta G^\ddagger$ ), activation enthalpies ( $\Delta H^\ddagger$ ), reaction Gibbs free energies ( $\Delta G_{rxn}$ ), reaction enthalpies ( $\Delta H_{rxn}$ ) for the  $R_{abs}$  intermediates calculated from Equation 8.2 and RSE values calculated from Equation 8.3 (MPWB1K/6-311+G(3df,2p) //B3LYP/6-31+G(d), kcal mol<sup>-1</sup>). Values in parentheses have been calculated with B3LYP/6-31+G(d) in water.

	DCF					DCF <sup>-</sup>				
	$\Delta H_{rxn}$	$\Delta G_{rxn}$	$\Delta H^\ddagger$	$\Delta G^\ddagger$	RSE	$\Delta H_{rxn}$	$\Delta G_{rxn}$	$\Delta H^\ddagger$	$\Delta G^\ddagger$	RSE
$R_{abs1}$	-5.2 (-1.7)	-6.4 (-2.8)	3.1 -3.9	11.6 -12.4	-8.6 (-8.6)	-5.8 (-2.1)	-7.2 (-3.6)	2.9 -2.8	10.9 -10.9	-8.2 (-8.2)
$R_{abs2}$	-5.5 (-1.8)	-6.4 (-2.7)	3.4 -2.1	10.6 -11.9	-8.5 (-8.4)	-5.7 (-2.0)	-7.0 (-3.3)	1.9 -3.1	10.0 -11.2	-8.1 (-8.4)
$R_{abs3}$	-6.4 (-3.0)	-7.3 (-4.0)	3.7 -2.1	10.8 -12.5	-7.5 (-7.3)	-7.0 (-3.6)	-8.5 (-5.1)	1.4 -2.8	9.5 -10.9	-6.9 (-6.8)
$R_{abs4}$	-7.2 (-3.4)	-8.3 (-4.5)	1.3 -0.6	8.5 -9.2	6.7 (-6.9)	-7.6 (-3.8)	-8.7 (-4.9)	-0.2 -0.2	7.9 -8.3	-6.3 (-6.6)
$R_{abs5}$	-6.2 (-2.4)	-7.1 (-3.3)	2.0 -1.1	9.0 -10.0	7.7 (-8.0)	-6.6 (-2.8)	-7.7 (-3.9)	0.3 -1.0	8.5 -9.2	-7.3 (-7.5)
$R_{abs6}$	-7.2 (-3.5)	-8.3 (-4.6)	0.6 (-0.1)	10.2 -10.9	-6.6 (-6.8)	-7.9 (-4.2)	-9.0 (-5.3)	-3.4 (-1.4)	6.7 -8.7	-5.9 (-6.2)
$R_{abs7}$	-36.3 (-34.4)	-36.6 (-34.7)	-8.7 (-6.1)	3.7 -1.1	22.4 -24.1	-30.4 (-27.4)	-34.9 (-32.4)	-7.0 (-6.7)	2.7 -3.0	16.5 -17.0

Relative stabilities of the free radicals formed via H-abstraction ( $R_{abs}$ ) during oxidation of diclofenac are summarized in Table 8.1. The most stable radical is the one corresponding to  $R_{abs}7$ , which is almost  $30 \text{ kcal mol}^{-1}$  more stable than those on the benzene rings. H-abstraction from the benzylic position is found to be more favorable -both thermodynamically and kinetically- when compared to H-abstraction from the rings, this is expected based on the stabilization generated by conjugation of the benzylic radical in the former case. The preference of H-abstraction from benzylic carbon over aromatic carbons is also reported by Sehested *et al.* [222]. Radicals on the ring are thermodynamically less favored than  $R_{abs}7$ , however their generation is still kinetically feasible in terms of their activation barriers ( $\Delta G^\ddagger \sim 10 \text{ kcal mol}^{-1}$  vs  $\sim 3 \text{ kcal mol}^{-1}$ ). Radicals on the second ring are more stable (RSE  $\sim -8 \text{ kcal mol}^{-1}$ ) than those on the first ring (RSE  $\sim -6 \text{ kcal mol}^{-1}$ ). When the two forms of diclofenac are compared, it is observed that DCF<sup>-</sup> is more prone to H-abstraction than DCF with slightly lower activation barriers and higher exergonicity. In aqueous medium,  $\cdot\text{OH}$  can readily add to aromatic molecules producing hydroxycyclohexadienyl type radicals [223]. Hence,  $\cdot\text{OH}$  could add to DCF forming  $R_{add}$  intermediates as shown in Figure 8.5. As opposed to H-abstraction, there are two additional reactive sites (a and b) for hydroxyl radical addition.

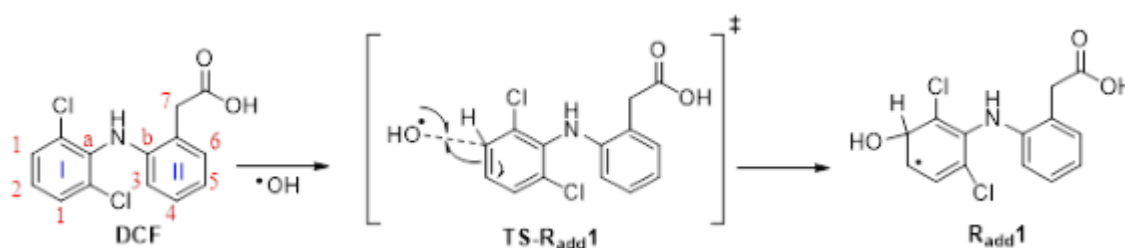


Figure 8.5. OH-addition of  $\cdot\text{OH}$  to DCF, generating radical intermediate ( $R_{add}$ ).

The stabilities of the  $R_{add}$  intermediates (arenium radicals) as calculated by Equation 8.2 are listed in Table 8.2 for DCF and DCF<sup>-</sup>. Unlike the H-abstraction route, the radicals formed on the first ring are more exergonic than those on the second ring, but have slightly higher activation barriers. The addition of  $\cdot\text{OH}$  to positions a and b is slightly less favorable than addition to the rings and the reaction is not likely since

re-aromatization is not probable. However, those intermediates could lead to C-N bond cleavage and fragmentation [224]. Furthermore, similar to the H-abstraction route, we found that OH-addition to the anionic form of diclofenac is thermodynamically and kinetically more favorable than the neutral one. The complete reaction profiles for these two reactions are presented in Figures 8.6 and 8.7.

Table 8.2. Activation Gibbs free energies ( $\Delta G^\ddagger$ ), activation enthalpies ( $\Delta H^\ddagger$ ), reaction Gibbs free energies ( $\Delta G_{rxn}$ ), reaction enthalpies ( $\Delta H_{rxn}$ ) for the  $R_{add}$  intermediates calculated from Equation 8.2 and RSE values calculated from Equation 8.3 (MPWB1K/6-311+G(3df,2p) //B3LYP/6-31+G(d), kcal mol<sup>-1</sup>). Values in parentheses have been calculated with B3LYP/6-31+G(d) in water.

	DCF					DCF <sup>-</sup>				
	$\Delta H_{rxn}$	$\Delta G_{rxn}$	$\Delta H^\ddagger$	$\Delta G^\ddagger$	RSE	$\Delta H_{rxn}$	$\Delta G_{rxn}$	$\Delta H^\ddagger$	$\Delta G^\ddagger$	RSE
$R_{add1}$	-17.2 (-14.3)	-7.9 (-5.0)	-0.2 (-0.6)	9.1 -8.6	27.8 -25.8	-18.4 (-15.4)	-8.7 (-5.7)	-2.0 (-2.6)	7.2 -6.6	27.5 -25.5
$R_{add2}$	-18.3 (-15.7)	-8.4 (-5.7)	-1.8 (-2.9)	7.4 -6.2	30.4 -30.0	-20.1 (-17.)	-10.1 (-7.4)	* *	* *	31.8 -31.4
$R_{add3}$	-17.2 (-14.3)	-7.5 (-4.6)	-3.2 (-4.3)	6.7 -5.5	31.2 -31.2	-19.0 (-16.0)	-8.7 (-5.8)	-5.2 (-6.3)	4.3 -3.2	32.0 -32.2
$R_{add4}$	-15.1 (-12.8)	-5.6 (-3.3)	-1.0 (-2.2)	8.4 -7.2	28.5 -29.0	-17.2 (-14.9)	-7.8 (-5.5)	-2.9 (-4.4)	5.7 -4.1	30.1 -29.9
$R_{add5}$	-17.6 (-15.3)	-8.0 (-5.7)	* *	* *	32.7 -32.7	-19.7 (-17.4)	-9.9 (-7.7)	* *	* *	33.7 -33.8
$R_{add6}$	-15.8 (-13.2)	-5.7 (-3.1)	-2.0 (-2.9)	7.4 -6.5	29.5 -29.2	-18.9 (-15.7)	-8.7 (-5.5)	-2.5 (-3.6)	6.3 -5.2	30.0 -29.8
$R_{adda}$	-14.7 (-11.7)	-4.6 (-1.6)	1.9 -2.4	14.2 -14.8	30.4 -30.4	-14.9 (-12.0)	-4.9 (-1.9)	-0.1 (-0.4)	9.3 -9.0	31.6 -31.7
$R_{addb}$	-14.0 (-11.0)	-3.3 (-0.3)	-0.6 (-0.3)	9.7 -10.0	29.4 -30.1	-17.1 (-14.0)	-6.6 (-3.4)	-0.7 (-0.8)	9.3 -9.2	30.9 -31.3

\*Transition states could not be located.

The reactivity of DCF and DCF<sup>-</sup> show the same trends, nonetheless with lower energy barriers and higher exergonicities for DCF<sup>-</sup>. It is known that OH-addition to benzene ring is kinetically more favored than H-abstraction from the ring carbons [225]. Similarly, based on RSE results one can see that OH-addition radicals are more stable than  $\cdot\text{CH}_3$ , note also that the radicals generated by H-abstraction on the ring carbons are less stable than the ones formed by OH-addition.

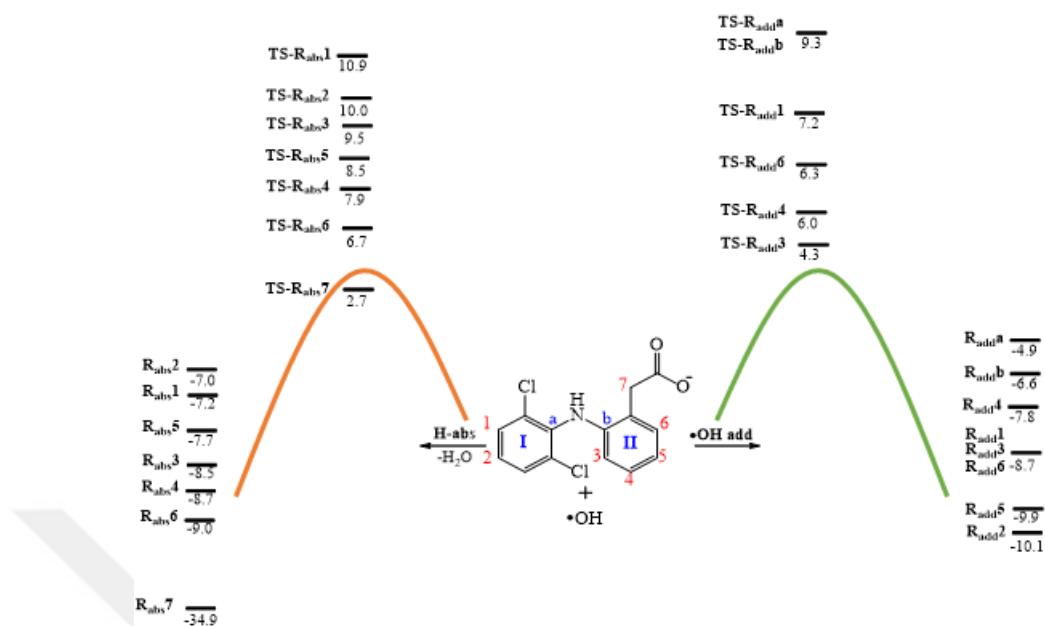


Figure 8.6. Gibbs free energies of the reaction ( $\Delta G_{rxn}$ ) of  $\cdot\text{OH}$  with  $\text{DCF}^-$  to give H-abstraction intermediates ( $R_{abs}$ ) on the left (red path) and OH-addition intermediates ( $R_{add}$ ) on the right (orange path).

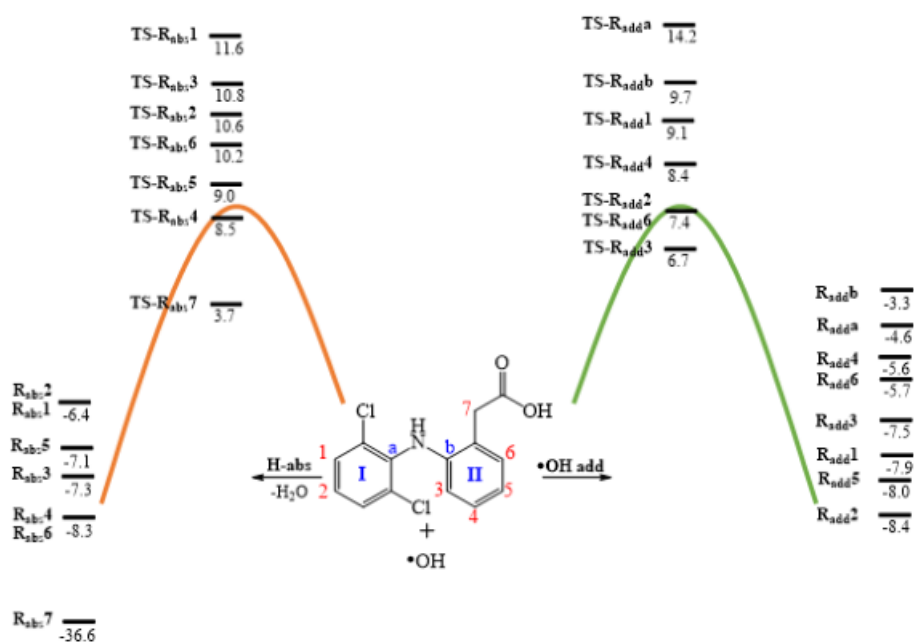


Figure 8.7. Gibbs free energies of the reaction of  $\cdot\text{OH}$  with  $\text{DCF}$  to give H-abstraction intermediates ( $R_{abs}$ ) on the left (orange path) and OH-addition intermediates ( $R_{add}$ ) on the right (green path).

When the whole reaction path is examined (Figure 8.6 for DCF<sup>-</sup> and Figure 8.7 for DCF), the major H-abstraction intermediate is found to be Rabs7 and this may lead to the fragmentation of DCF/DCF<sup>-</sup>. R<sub>add</sub>2 and R<sub>add</sub>3 are the most easily formed radicals among others.

### 8.3.2. Fragmentation of DCF/DCF<sup>-</sup>

The fragmentation of DCF/DCF<sup>-</sup> is modeled in order to understand the most probable degradation paths and be able to predict the possible fates of the generated radical intermediates. All fragments are optimized and their reaction energies are calculated with Equation 8.4 (Table 8.3). The fragmentation energies are arranged in an increasing order. Based on Hammond's postulate ring cleavages from either side of the nitrogen (entries 2 and 3) seem to be as easy as decarboxylation (entry 1). The rupture of the C-Cl bond (entries 4 and 6) is almost equally difficult in both cases (Cl (1) and Cl (2)). On the other hand, the losses of OH (entry 7) in the neutral form and O in the anionic form are more endergonic than the others; decarboxylation is less endergonic for DCF<sup>-</sup> (50.6 kcal mol<sup>-1</sup>) than for DCF (66.2 kcal mol<sup>-1</sup>).

Table 8.3. Reaction Gibbs free energies ( $\Delta G_{rxn}$ ) for the fragments of DCF/DCF<sup>-</sup> calculated with Equation 8.4 (MPWB1K/6-311+G(3df,2p)//B3LYP/6-31+G(d), kcal mol<sup>-1</sup>). Values in parentheses have been calculated with B3LYP/6-31+G(d) in water.

entry	fragments	DCF	DCF <sup>-</sup>
1	COOH <sup>-</sup>	66.2 -60.7	50.6 -45.0
2	Ring II (C-N cleavage)	71.0 -61.0	73.0 -62.9
3	Ring I (C-N cleavage)	74.5 -63.6	74.3 -63.4
4	Cl (2)	84.2 -73.8	83.3 -73.1
5	CH <sub>2</sub> COOH/CH <sub>2</sub> COO <sup>-</sup>	82.6 -74.7	85.6 -77.4
6	Cl (1)	87.9 -77.5	87.2 -77.0
7	OH/O <sup>-</sup>	97.4 -90.7	121.7 -113.4

### 8.3.3. Analysis of the Degradation Byproducts

Following the generation of radicals through H-abstraction and OH-addition, subsequent reactions are examined to understand the formation of the mostly encountered degradation byproducts of DCF, namely P1-P9 (Figure 8.8). The degradation mechanisms that follow are based on the outcomes of section 8.3.1. Hydroxylated derivatives lead to the degradation byproducts, P5 [203, 204, 226], P6 [204, 206], P7 and P8 [203, 204, 206, 226–228], H-abstraction intermediate  $R_{abs}3$  gives P4 [205, 229–233]; decarboxylated fragment of DCF results in P3 [228] by ring closure; ring cleavage fragmentation produces P1 [203, 204, 206, 227, 228, 234, 235], P5, P6 and P9 [204, 206]; the rearrangement gives cyclization product P2 [204, 234]. The mechanisms and the reaction energies of each of these products (P1-P9 except P2) for  $DCF^-$  are examined and displayed in Figure 8.8. The detailed reaction mechanisms and the reaction profiles are reported in Figures 8.9-8.28.

Subsequent degradation mechanism of DCF involves  $\cdot OH$  almost in every step because it is well known that high  $\cdot OH$  concentrations are produced under extreme conditions in advanced oxidation processes (AOP) [236–239]. Despite the high concentration of  $\cdot OH$ , P2 and P3 are formed presumably by rearrangement of DCF before the attack of  $\cdot OH$  (Figure 8.8-I). P2 is the result of an intramolecular cyclization leading to water loss (Figure 8.9). Even though the activation barrier for P2 formation is very high ( $\Delta G^\ddagger = 47.0$  kcal/mol), its overall formation is exergonic ( $\Delta G_{rxn} = -12.7$  kcal/mol). Moreover, this product has been experimentally observed in several studies, mostly at the early stages of the experiments, and is proposed to form under decreasing pH [204].

The mechanism suggested for the formation of P2 starts with cyclization and is followed by water elimination. A cyclic tetrahedral gemdiol intermediate would form by attack of nitrogen to the carbonyl carbon, and then the intermediate loses a water molecule aided by the solvent, yielding the amide P2. This mechanism has been proposed for DCF and not for  $DCF^-$ , it is expected to take place at the initial stages of the AOP process.

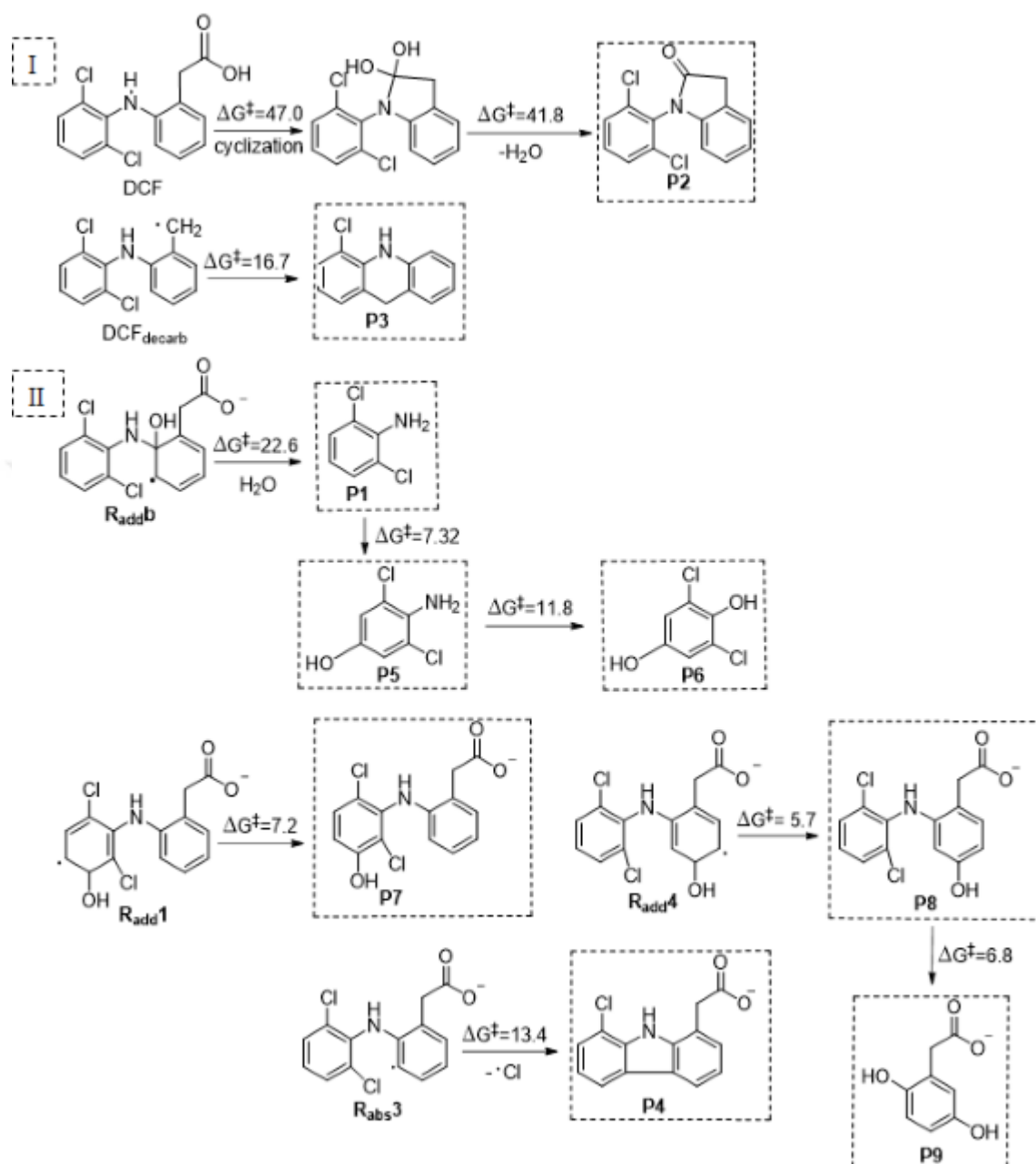


Figure 8.8. Schematic representation of the generation of degradation byproducts by (I) rearrangement and (II) in the presence of  $\bullet\text{OH}$  using DCF<sup>-</sup> (except for P2 where DCF has been utilized) Gibbs free energies are given in kcal/mol.

Another degradation byproduct that forms without  $\bullet\text{OH}$  in its subsequent degradation mechanism, is P3 (Figure 8.10). The decarboxylation of DCF/DCF<sup>-</sup> is relatively facile as shown in section 8.3.2. After decarboxylation, DCF<sub>decarb</sub> is formed; the exocyclic methylene radical attacks the chlorinated carbon, ejecting a  $\text{Cl}^\cdot$  and yielding

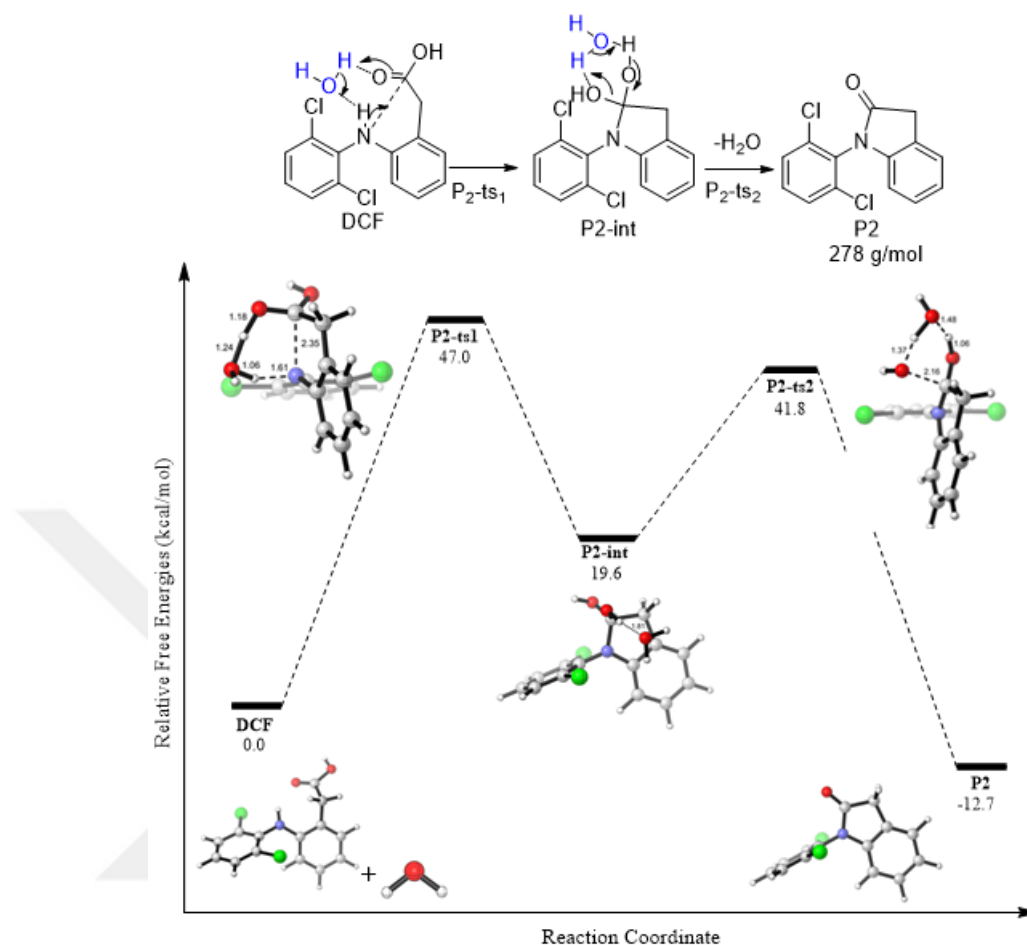


Figure 8.9. Degradation mechanism and reaction profile yielding P2 starting from DCF. Gibbs free energies are given in kcal/mol.

P3. The barrier for this reaction is feasible ( $\Delta G^\ddagger = 16.7$  kcal/mol) and the reaction is highly exergonic ( $\Delta G_{rxn} = -32.2$  kcal/mol) due to the formation of the stable cyclic byproduct, P3 (Figure 8.10).

Besides P2 and P3, there is another cyclic degradation byproduct P4, which is also encountered frequently in the degradation experiments of DCF. P4 is produced in two steps, in the first step a radical center is generated by a H-abstraction from position 3 (on ring II), in the second step,  $R_{abs3}$  attacks the chlorinated carbon to form a 5-membered cyclic product with Cl, similar to the formation of P3 where a 6-membered ring was formed. The barrier to form P4 from  $R_{abs3}$  is 13.4 kcal/mol with very high exergonicity ( $\Delta G_{rxn} = -45.3$  kcal/mol) (Figure 8.11).



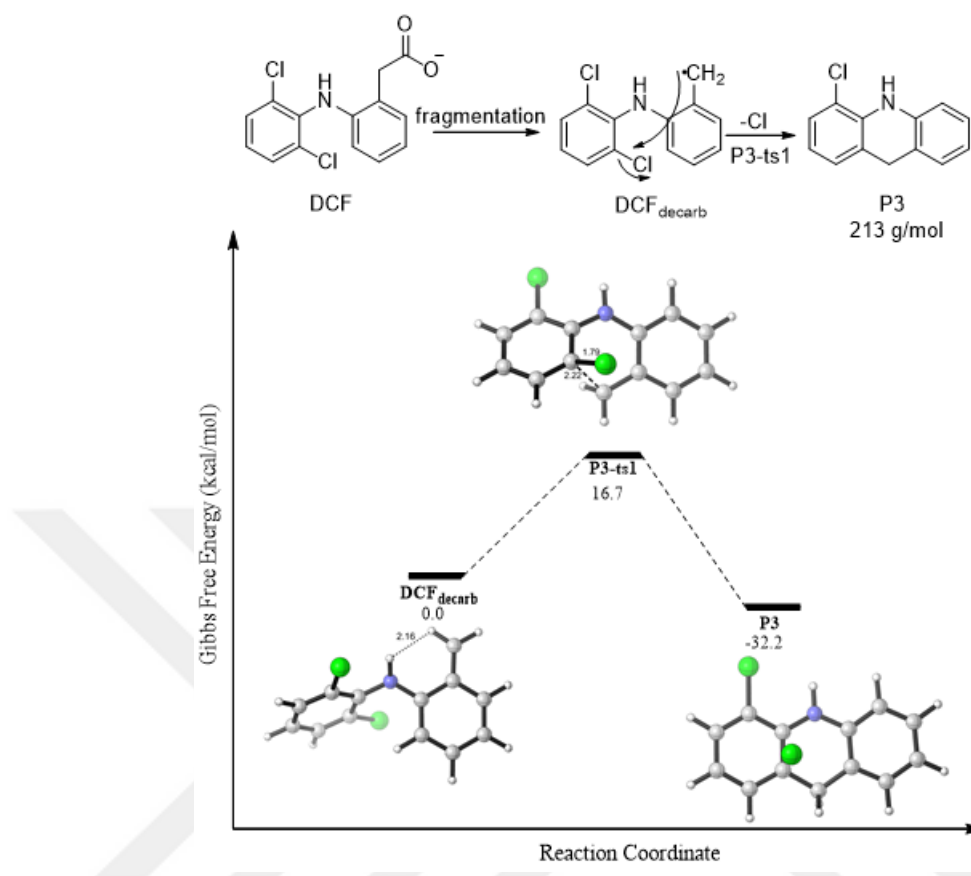


Figure 8.10. Degradation mechanism and reaction profile yielding P3 starting from decarboxylated DCF. Gibbs free energies are given in kcal/mol.

P1 was found experimentally to be formed at early stages of the reaction furthermore it is the precursor of the subsequent oxidative products e.g. P5 and P6 [211]. The C-N bond cleavage in DCF is a very common fragmentation site [203,204,206]. P1 is the first byproduct that forms upon cleavage of the bond between C of ring II and N (Figure 8.12). This cleavage is initiated with  $\cdot\text{OH}$  addition to position a (formation of  $R_{adda}$  with 9.3 kcal/mol) and disruption of the aromaticity of ring II (22.6 kcal/mol) (Figure 8.12). After formation of  $R_{addb}$ , the C-N bond is broken down with a proton transfer from O-H to N-H giving two products ( $\Delta G_{rxn} = -36.9$ ). This step requires 22.6 kcal/mol energy for the anionic form. The same transition state cannot be located for neutral form of diclofenac. The final products are P1 and a radical. These first cleavage products of P1 (Figure 8.12) give other degradation byproducts (P5 and P6) by further reacting with  $\cdot\text{OH}$ .  $\cdot\text{OH}$  addition to P1 produces an arenium radical on the ring and this radical captures another  $\cdot\text{OH}$  resulting in a diol with broken aromaticity in the ring (Figure 8.13). In order to rearomatize, a water molecule is lost and hydrox-

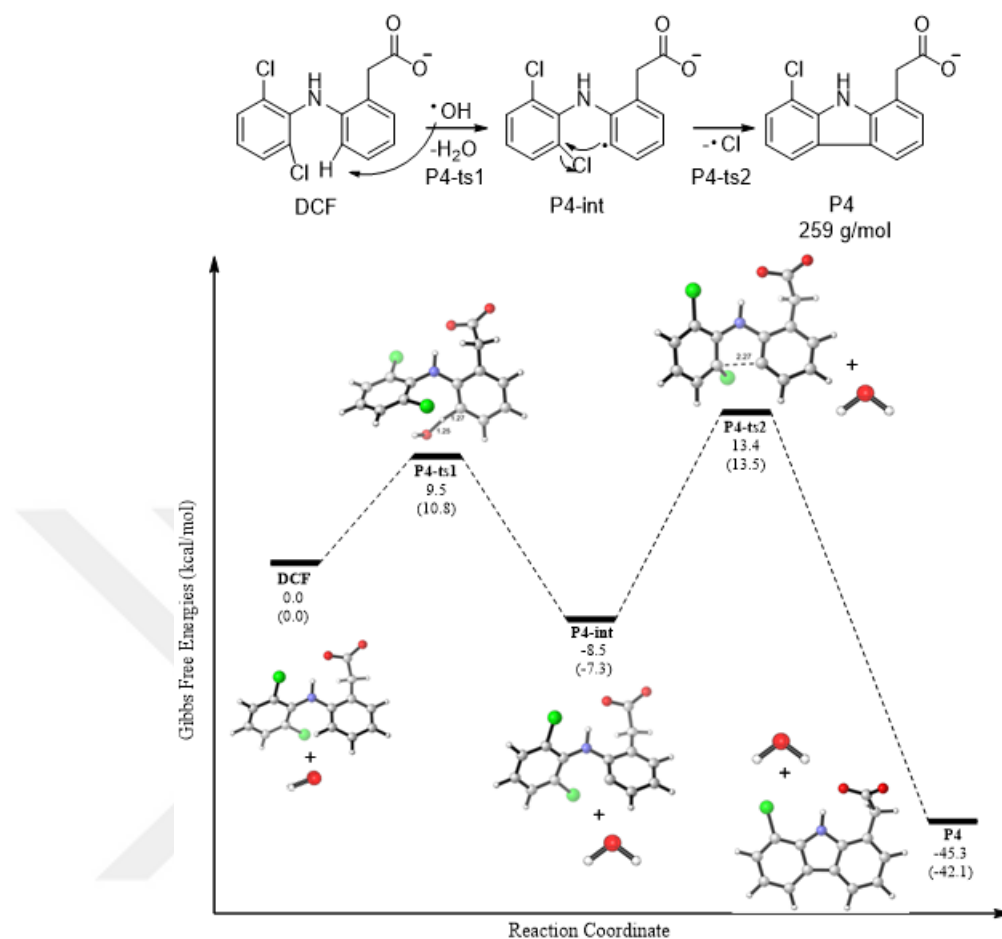


Figure 8.11. Reaction profile of the degradation product P4 starting from  $\text{DCF}^-$  and DCF in parenthesis. Gibbs free energies are given in kcal/mol.

ylated aniline is generated, which is found experimentally as one of the degradation byproducts of diclofenac, P5 with very high exergonicity (-105.9 kcal/mol relative to P1, Figure 8.13). Another attack of an  $\cdot\text{OH}$  to P5 results in substitution of OH with  $\text{NH}_2$  to give P6.  $\cdot\text{OH}$  attacks to the carbon where  $\text{NH}_2$  is attached and forms easily (4.5 kcal/mol) an arenium radical on the ring (Figure 8.14), the latter rearomatizes as the  $\text{NH}_2$  radical leaves (11.8 kcal/mol). P6 is found to be 6.7 kcal/mol more stable than P5 (Figure 8.14).

P7 and P8 are classified among the main degradation byproducts of DCF/ $\text{DCF}^-$ . (Figures 8.15 and 8.16  $\cdot\text{OH}$  adds to the ring ( $\Delta G^\ddagger = 7.2$  kcal/mol for P7 and  $\Delta G^\ddagger = 5.7$  kcal/mol for P8) forming arenium radical which is followed by a barrierless  $\cdot\text{OH}$ -addition. The latter intermediate is expected to lose a water and yield the final product

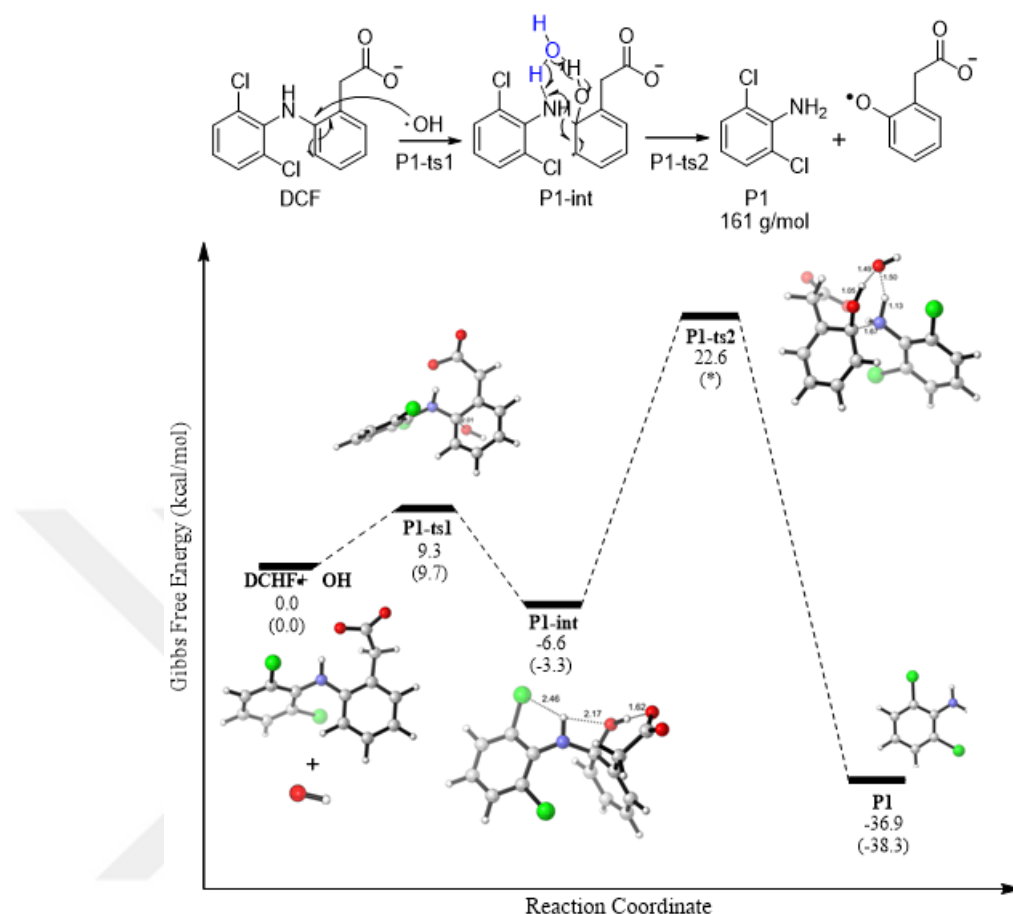


Figure 8.12. Degradation mechanism and reaction profile yielding P1 starting from DCF- and DCF in parenthesis. Gibbs free energies are given in kcal/mol. (\*Transition state could not be located.)

in an exergonic path ( $\Delta G_{rxn} = -108.4$  kcal/mol for P7 and  $\Delta G_{rxn} = -108.5$  kcal/mol for P8). Another OH-addition to position b in P8 results in C-N bond breakage and formation of P9 ( $\Delta G_{rxn} = -33.6$  kcal/mol). The mechanism is similar to formation of P1 but with a lower activation barrier ( $\Delta G^\ddagger = 6.8$  kcal/mol). (Figure 8.17)

In light of the experimental progression of the pH mentioned earlier (decrease from 6.50 to 5.23 in 30 min), in the late stages of the reaction when neutral DCF is the prevalent form, it is likely that energy demanding processes e.g. fragmentation and cyclization rates will increase. At the beginning of the AOP when pH is close to neutral and DCF<sup>-</sup> is predominant, H-abstraction and OH-addition are more likely to occur, leading to subsequent degradation reactions yielding byproducts P1, P4-P9.

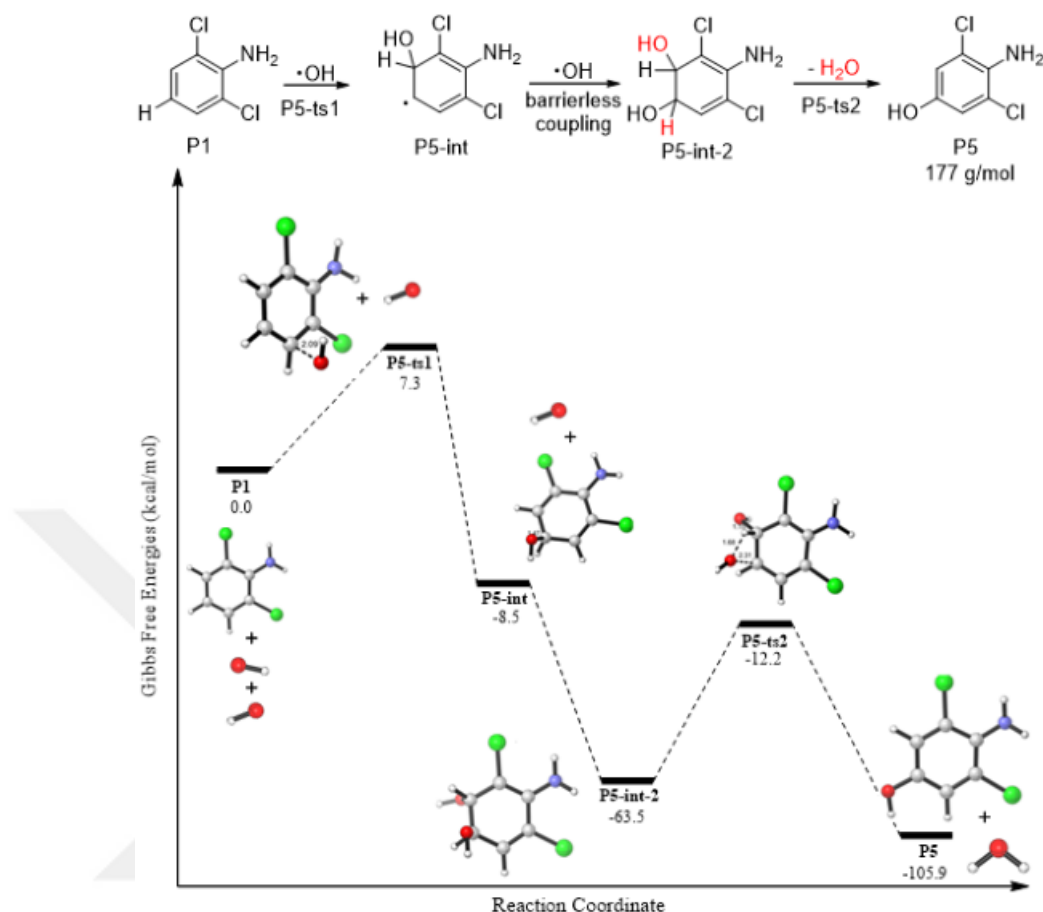


Figure 8.13. Degradation mechanism and reaction profile yielding P5 starting from P1. Gibbs free energies are given in kcal/mol.

### 8.3.4. Toxicity

The acute and chronic toxicity of diclofenac and its byproducts to aquatic organisms was predicted using the ECOSAR software at three trophic levels (green algae, daphnia, and fish). The octanol–water partitioning coefficient ( $\log K_{ow}$ ) was predicted as 4.02 for diclofenac, and the value is in good agreement with the experimental finding, 4.51 [240]. As such, DCF is potentially toxic to aquatic organisms based on the literature classifying chemicals as toxic with  $\log K_{ow} < 6.0$  [241,242]. The toxicity classification based on ranges of  $LC_{50}$  and  $EC_{50}$  (Table 8.4) was used to rationalize the acute toxicity of DCF and its byproducts (Table 8.5). The estimated value of  $EC_{50}$  (41.41) is slightly higher than that found experimentally (33.26) [211].  $LC_{50}$  of diclofenac for daphnia and fish was found as 25.75 and 37.66  $\text{mg L}^{-1}$ , respectively. The finding is in agreement with the European Union criteria [243] (Table 8.4), which classify diclofenac

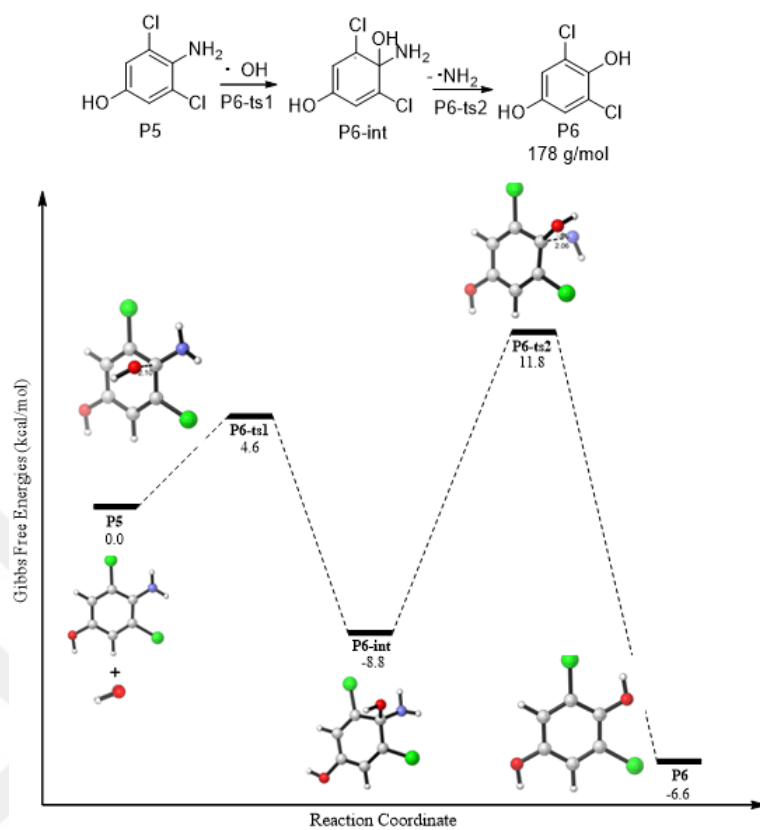


Figure 8.14. Degradation mechanism and reaction profile yielding P6 starting from P5. Gibbs free energies are given in kcal/mol.

as a harmful compound for the aquatic environment at all three trophic levels.

Table 8.4. Toxicity classification according to the Globally Harmonized System (GHS) of Classification and Labelling of Chemical

Toxicity range (mg/L)	Class
$LC_{50}/EC_{50} \leq 1$	Very toxic
$1 < LC_{50}/EC_{50} \leq 10$	Toxic
$10 < LC_{50}/EC_{50} \leq 100$	Harmful
$LC_{50}/EC_{50} > 100$	Not harmful

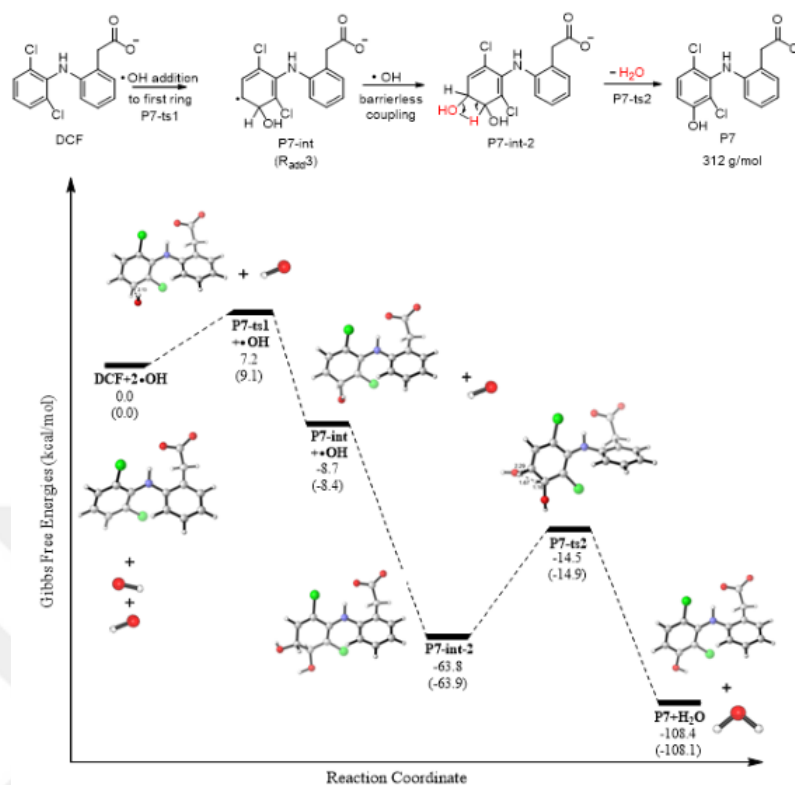


Figure 8.15. Degradation mechanism and reaction profile yielding P7 starting from DCF- and DCF in parenthesis. Gibbs free energies are given in kcal/mol.

Table 8.5. Toxicity values of DCF/ DCF<sup>-</sup> and its degradation byproducts P1-P9 to aquatic organisms (mg L<sup>-1</sup>) using ECOSAR.

	Green Algae	Daphnid	Fish
	EC <sub>50</sub>	LC <sub>50</sub>	LC <sub>50</sub>
DCF/DCF <sup>-</sup>	41.41	25.75	37.66
P1	1.51	1.15	12.87
P2	0.54	8.87	13.42
P3	3.25	2.06	3.03
P4	101.44	80.68	125.20
P5	2.62	1.29	53.61
P6	2.92	42.53	6.17
P7	142.67	34.80	68.21
P8	142.67	34.80	68.21
P9	116.11	10608.00	736.39

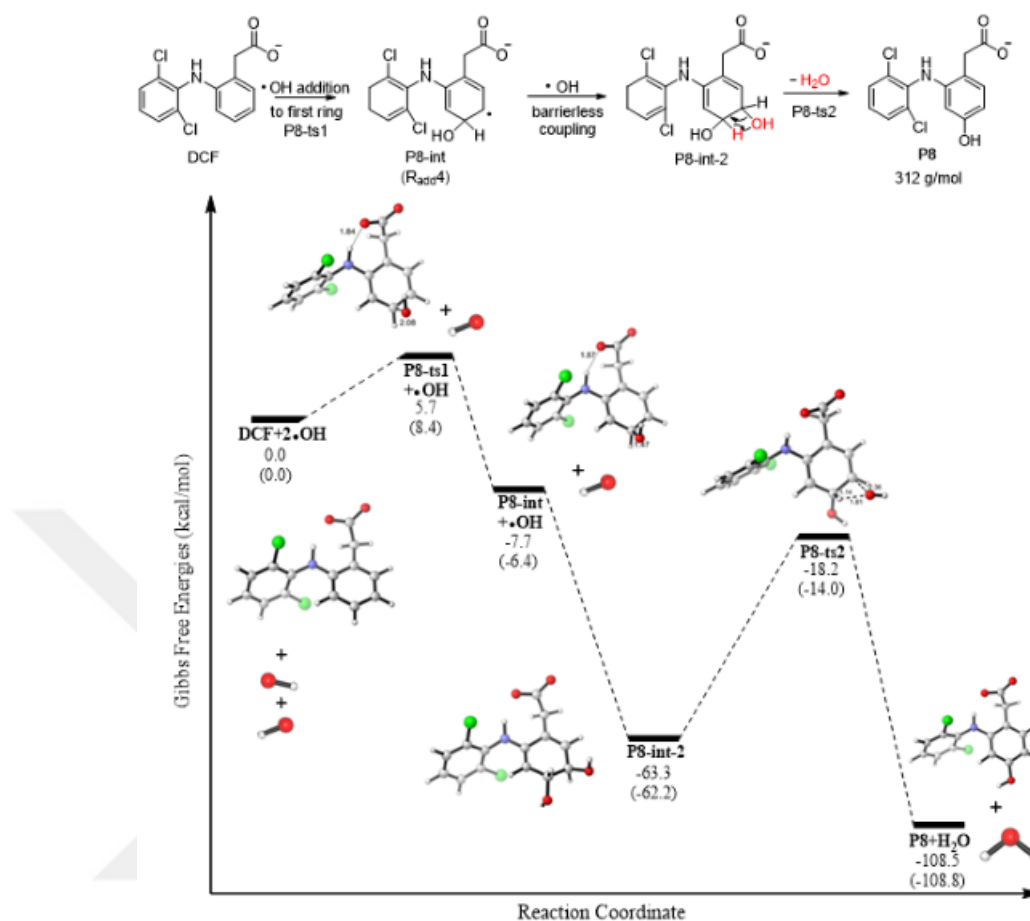


Figure 8.16. Degradation mechanism and reaction profile yielding P8 starting from  $\text{DCF}^-$  and DCF in parenthesis. Gibbs free energies are given in kcal/mol.

The aquatic toxicities upon degradation of diclofenac were tracked for three trophic levels (Table 8.5). As  $\cdot\text{OH}$  mediated degradation proceeds, toxicities fluctuate between harmful and toxic levels. Aquatic toxicities seem to be dependent on the presence of chlorine: P9, the only byproduct that is classified as not harmful for all three organisms, is free of chlorine. P4, P7 and P8, which possess an acidic group, are also classified as not harmful for green algae. The toxicities of P1, P2, P3, P5 and P6 are higher than DCF/ $\text{DCF}^-$  in regard to all three organisms. However, P5 is less toxic to fish ( $\text{LC}_{50} = 53.61 \text{ mg/L}$ ) and P6 is less toxic to daphnid ( $\text{LC}_{50} = 42.53 \text{ mg/L}$ ). Overall, the assessment of  $\text{EC}_{50}$  and  $\text{LC}_{50}$  shows that DCF and most of its oxidation byproducts are harmful for aquatic organisms.

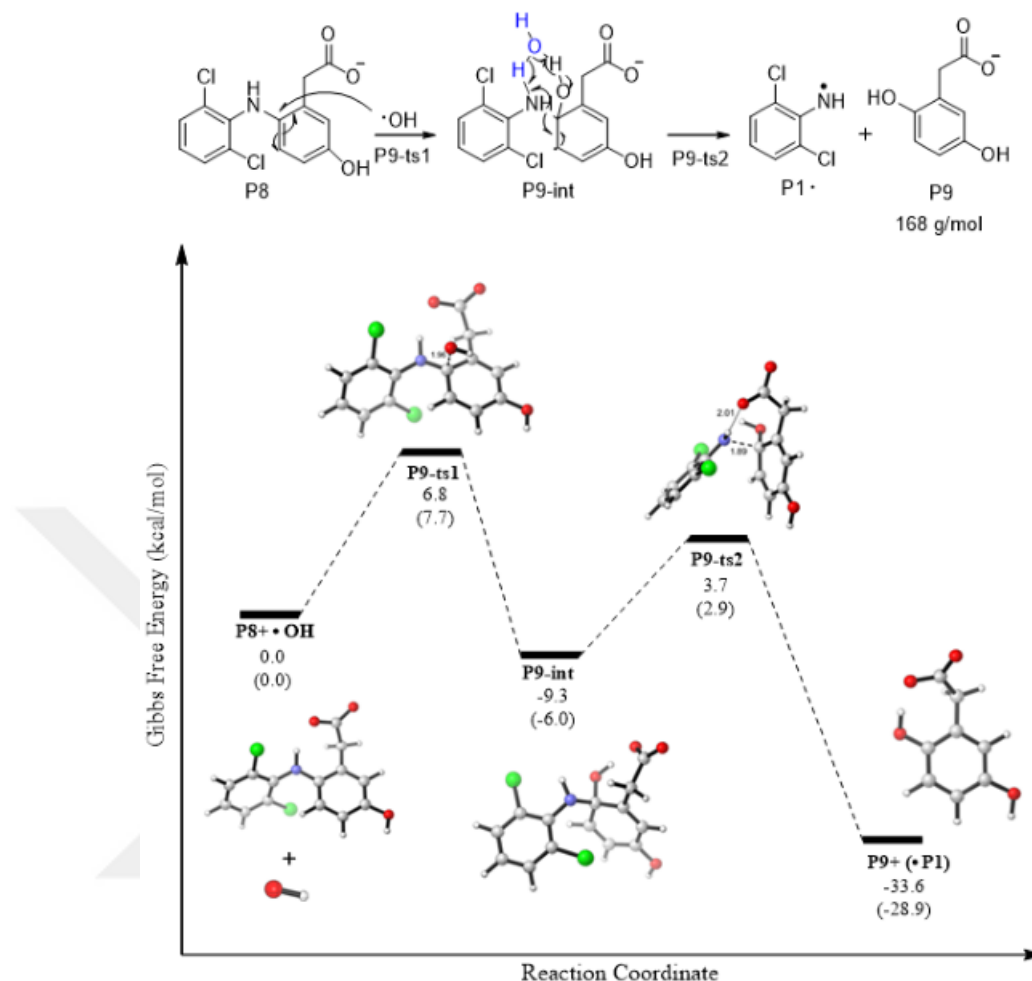


Figure 8.17. Degradation mechanism and reaction profile yielding P9 starting from P8 (neutral form is shown in parenthesis). Gibbs free energies are given in kcal/mol.

#### 8.4. Conclusions

The goal of this study was to computationally investigate the  $\cdot\text{OH}$  mediated degradation mechanisms of an emerging water pollutant, diclofenac (DCF/DCF<sup>-</sup>). The degradation by OH<sup>-</sup> addition and H-abstraction occurs almost readily. The methylene hydrogens are more readily abstractable than the others; this may lead to the decarboxylation of the ring. The radical stabilization energies of the arenium radicals are higher than those of the radicals formed by H-abstraction, indicating their longer lifetime. The byproducts (P1-P9) have been encountered experimentally during the degradation of (DCF/DCF<sup>-</sup>) by AOPs; this study sheds light on their formation. As reported by Ziylan et. al. [211] who have used LC/MS/MS to characterize the intermediates, P5, P6 and P9 form at a later stage from their precursors, P1 and P8. P1,



P7 and P8 are the most readily formed byproducts as pointed out by previous AOP studies. DCF is classified as “harmful” with ECOSAR. The  $EC_{50}$  values of some of the byproducts (P4, P7, P8, and P9) are found to be higher than those of DCF/DCF-, their presence in the environment is safer than that of the parent compound. This study is the first to provide a detailed mechanistic account of the degradation of diclofenac in aqueous medium.



## 9. COMPUTATIONAL INVESTIGATION OF DISPROPORTIONATIVE CONDENSATION REACTIONS OF INDOLES WITH CYCLIC KETONES

The chemistry of indole (benzo[b]pyrrole) is one of the most important field in the heterocyclic chemistry. The main reason for this growing interest towards indole is being the basis of many biologically active compounds such as pharmaceuticals, agrochemicals and alkaloids. The indole ring appears in many natural products such as indole alkaloids [244, 245], fungal metabolites [246] and marine natural products [247]. The importance of indole led to development of various bioactive compounds such as antimicrobial, antiviral, insecticidal, analgesic, anti-inflammatory, antidepressant, anticancer etc. [248–250].

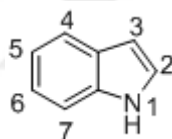


Figure 9.1. Structure of indole.

Indole is classified as a  $\pi$ -excessive aromatic compound and isoelectronic with naphthalene (Figure 9.1). The aromaticity of the molecule is the principle reason of several synthetic methods. Indole is a very weak base; the conjugate acid has a  $pK_a = -2.4$  [251].

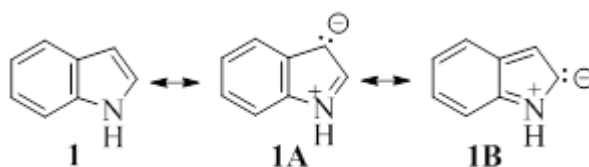


Figure 9.2. Resonance structures of indole.

Generally in electrophilic substitution reactions, indole reacts more slowly than pyrrole and faster than benzo[b]furan. In indoles, contrarily to pyrrole, substitution of the H-atom occurs mainly at position C3 with the contribution of resonance structure 1A (Figure 9.2). Electrophilic attack to the C3 results in a low energy iminium structure of the  $\sigma$ -complex, but attack on C2 gives a high energy orthoquinonoid iminium structure (Figure 9.3). Also, various molecular orbital calculations indicate the highest electron density and the highest concentration of the HOMO is located at C3 [252,253]. Position C3 is found to be  $10^{13}$  more reactive than benzene to electrophilic attack [254]. If the position C3 already occupied with a substituent, attack usually takes place on C2 and then on C6.  $pK_a$  of N1 in indole is found to be 16.7 in water [251], showing weakly acidic character. On the other hand, N1 is the most nucleophilic site in the anion of the molecule and usually participates base catalyzed reactions like alkylation, acylation etc.

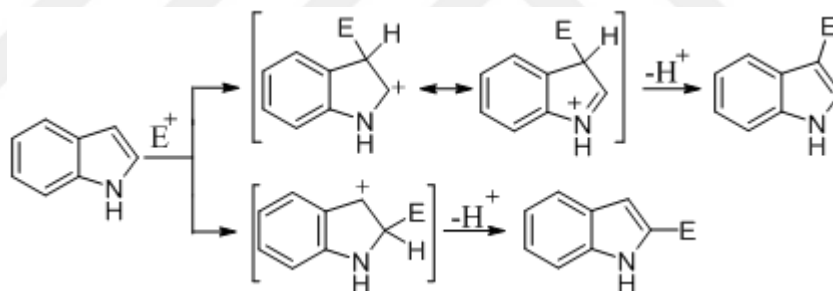


Figure 9.3. Electrophilic attack to C3 and C2 positions.

## 9.1. Introduction

Bisindole derivatives incorporating five or six-membered heterocycles bridging two identical indole substituents are common scaffolds in many pharmaceutically interesting natural products such as nortopsentins [255, 256]. The bis(indolyl)imidazole alkaloid nortopsentin A and its analogues demonstrate in vitro cytotoxicity against P388 cells however, nortopsentin A has been found to have antiplasmodial activity [257, 258]. The indole alkaloid yuehchukene containing indole as both fused and substituent is reported to possess strong anti-implantation activity in rats [259]. Recently, scalaridine A, a symmetrical bisindole alkaloid with pyridine linker from the marine sponge, was

isolated and evaluated, the cytotoxic activity against a human leukemia cell line, and its short synthesis were reported [260–262]. It is well known that the bis-indole structure is a requirement for cytotoxicity [263]. However, a new type of Pt(II) complexes of 2,6-bis(2'-indolyl)pyridine have been synthesized and demonstrated to be promising phosphorescent emitters in electroluminescent devices [264]. Bisindole (1,3-di(1H-indol-3-yl)benzene) was synthesized within a novel class of indole analogs to optimize anticancer actions of indole-3-carbinole derivatives (Figure 9.4) [265].

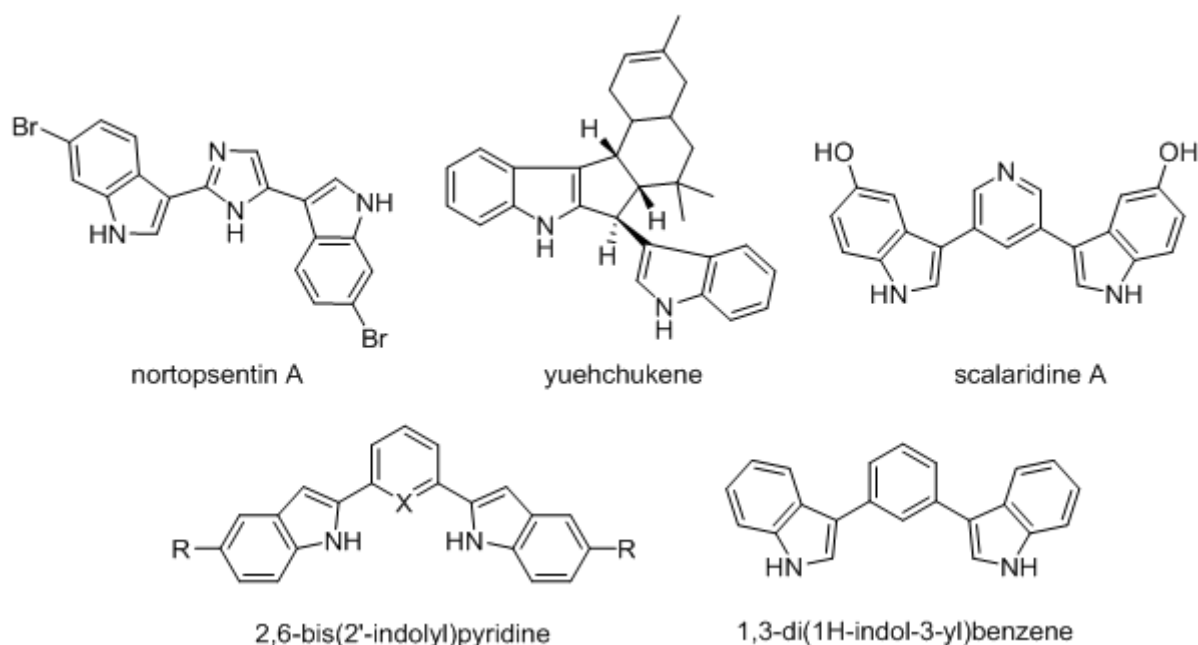


Figure 9.4. Representatives of some indole alkaloids and synthesized indoles.

It is not surprising that the design of substituted indoles has been a major focus and a challenging fundamental target of research for generations. Among the indole derivatives, there is no doubt that the synthesis of the 3-substituted indoles has been the most extensively studied due to the nature of these compounds [266,267]. The reactions of indoles with aldehydes or ketones as electrophiles has also been reported however less than the Michael addition [268]. In the condensation reaction, a vinylogous iminium or azafulvenium ion may serve as the electrophile to mainly three type of reactions (Figure 9.5). The reaction of indole with aldehydes or ketones using  $\text{Et}_3\text{SiH}$  and  $\text{H}_2$  as reducing agents results in the formation of C3-substituted indoles via a reductive alkylation procedure (Figure 9.5, Path A) [269,270]. The most characteristic reactivity for the

azafulvenium ion is the condensation of indole with aldehydes or ketones under both Lewis and Brønsted acidic conditions to yield bis(indolyl)methanes which represent the structurally important class of bioactive metabolites (Figure 9.5, Path B) [271–273]. Furthermore, the condensation between indole and carbonyl compounds to 3-vinylindole is followed by cycloaddition to form carbazole derivatives (Figure 9.5, Path B) [267,274–276].

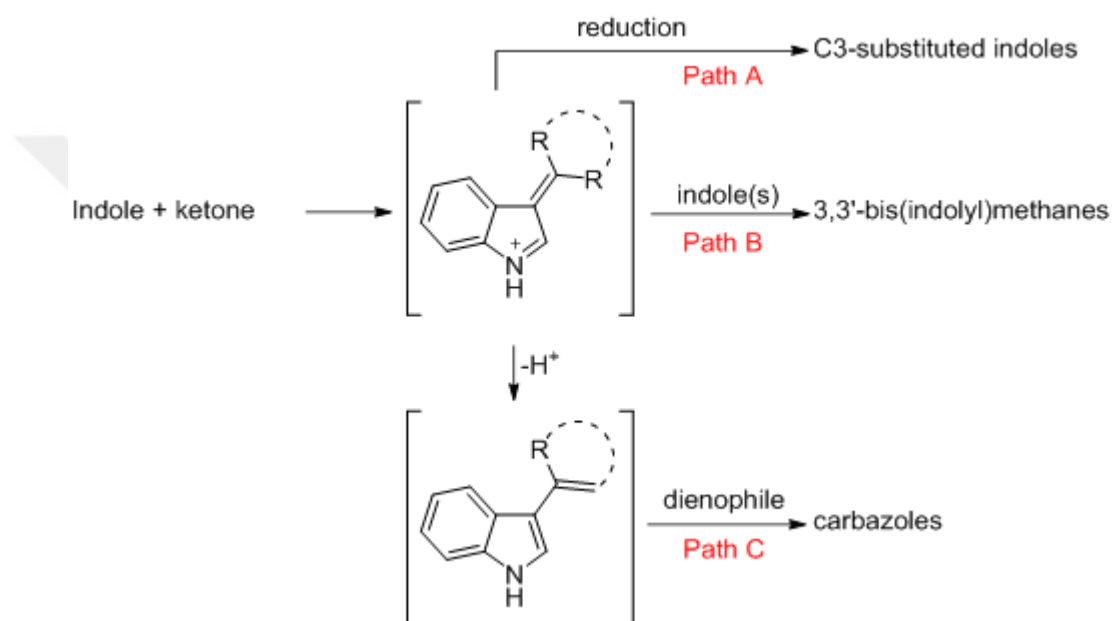


Figure 9.5. Vinylogous iminium or azafulvenium type reactivity of indole.

A disproportionation (or dismutation) reaction is a redox type reaction where a species is simultaneously both reduced and oxidized to give two different products. Organic disproportionation reactions often involve the transfer of electrons in the form of a hydride ion from one substance to another and are completed with the transfer of a proton. The Kornblum–DeLaMare rearrangement [277–279], the Meerwein–Ponndorf–Verley/Oppenauer reduction/oxidation [280,281], the catalytic disproportionation of toluene, the Tishchenko reaction, and the Cannizzaro reaction are the most prominent organic disproportionation reactions. Note that a study on the C3-alkylation of indoles by primary and secondary alcohols, that takes place via a disproportionative condensation reaction has been reported [282,283]. Recently the alkylation of indole and pyrrole alkylation with inactivated secondary alcohols has

been achieved in the presence of 2-methoxyacetophenone as an initiator and TfOH as an appropriate Brønsted acid catalyst [283]. Recently, a palladium-catalyzed direct approach to 3-arylindoles from indoles with cyclohexanones as aryl sources in one pot were realized via an alkylation followed by dehydrogenation sequence using molecular oxygen as the hydrogen acceptor [284]. Nevertheless, C3-cycloalkylated indoles could be synthesized through a sulfonyl-functionalized Brønsted acid ionic liquid. The aforementioned catalyzed reductive Friedel–Crafts alkylation of indoles and cyclic ketones proceeds by an external reducing agent in a likely radical way [285].

## 9.2. Computational Details

All computations were carried out with the Gaussian 09 program package [47]. The stationary points were located using the B3LYP/6-31+G(d) methodology and characterized by a frequency analysis, from which thermal corrections were obtained at 298.15K [2, 5, 6, 163, 164]. Local minima and first order saddle points were identified by the number of imaginary vibrational frequencies. Intrinsic reaction coordinate (IRC) calculations were performed on the transition state structures to determine the connectivity of the transition state structure to the corresponding product and reactant [165]. Conformational searches for the structures corresponding to reactants, transition states and products were carried out with the same methodology. Energies were further refined with the M06-2X/6-31+G(d,p) level of theory. This functional is recommended for thermochemistry, kinetics, and noncovalent interactions [7]. The effect of the solvent environment was taken into account utilizing the Integral Equation Formalism Polarizable Continuum Model (IEFPCM), where cyclohexanone ( $\epsilon = 18.2$ ) was used as solvent [14, 15].

## 9.3. Experimental Results

Recently, Saraçoğlu and coworkers have conducted bismuth nitrate-promoted disproportionative condensation of indoles with cyclohexanone and synthesized C3-cyclohexyl substituted indoles and 1,3-di(<sup>1</sup>H-indol-3-yl)benzene derivatives (Figure 9.6). Compound 26 unexpectedly gives Diels-Alder products after formation of dienophile

by H-shift.

In order to enlighten the plausible reaction mechanisms and explain the selectivities in the reactions in Figure 9.6 and also model Diels-Alder product formations, DFT calculations have been done by using M06-2X/6-31+G(d,p) methodology.

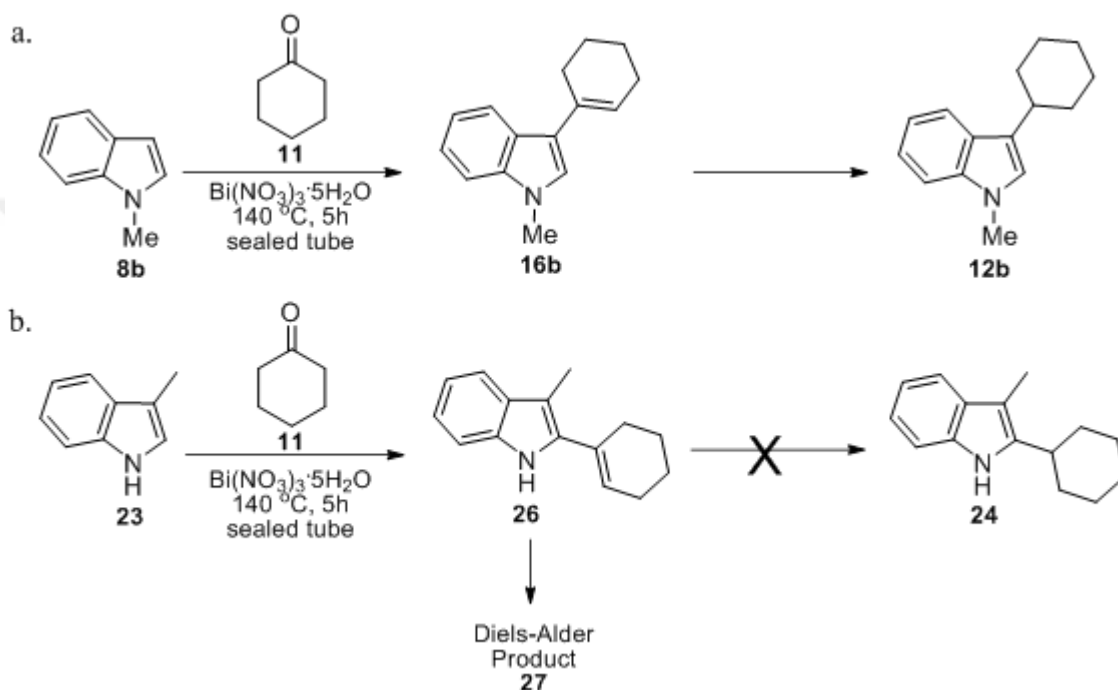


Figure 9.6. Reactions carried out by Saraçoğlu group.

#### 9.4. Results and Discussion

Bronsted acid catalyzed reactions of indoles show enhanced reactivity at C3 position. If C3 position of indole is occupied, C2 becomes prone to electrophilic attack. The study of Saraçoğlu group showed that electrophilic substitution at C3 position of N-methyl indole takes place under solvent free environment at 140°C in 5 hours. However, when 3-methyl indole is used instead of N-methyl indole, C2 substitution product (24) cannot be observed and the reaction results with a Diels-Alder product formation.

Figure 9.7 shows the reaction profile for the addition of N-methylindole (8b) to cyclohexanone (11). The reaction proceeds by the attack of the electron rich center (C2/C3) of N-methylindole (8b) to the carbonyl carbon of cyclohexanone. The presence of  $\text{Bi}^{3+}$  facilitates the reaction by surrounding the carbonyl oxygen and renders the carbonyl carbon more prone to be attacked by the nucleophile. In this study, the effect of the Lewis acid ( $\text{Bi}^{3+}$ ) has been mimicked by  $\text{H}^+$ . Note that the reaction path which proceeds with the attack of C3 is lower in energy than the one with C2, and indeed it is the path via C3 that leads to the experimentally observed condensation product 12b. It is the absence of a steric hindrance rather than the difference in the electronic charge distributions on these centers (C2:-0.105, C3:0.000) that lead to the condensation via C3. The rate determining step in the synthesis of 16b is the formation of the inter-cyclic double bond. The Gibbs free energy barrier (24.2 kcal/mol) is attainable at room temperature and the reaction is exergonic by 16.7 kcal/mol. The reaction via C3 rather than C2 can be attributed to the steric effect between the methyl group on N and the vicinal cyclohexanone in the case of C2 (Figure 9.7).

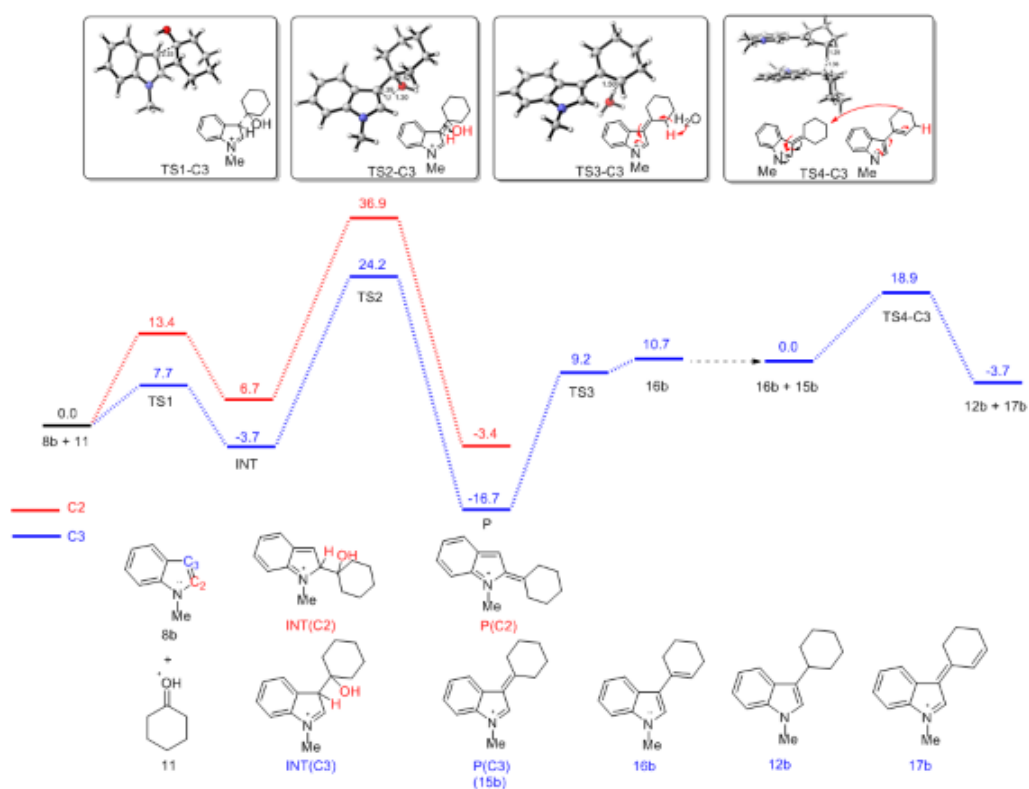


Figure 9.7. Gibbs Free energy profile for the formation of 12b (M06-2X/6-31+G(d,p) in cyclohexanone).



The same type of modeling was carried out for the reaction of 3-methylindole (23) with cyclohexanone (11) to recover compound 26 (Figure 9.8). Note that compounds 16b and 26 differ from each other in the location of the cyclohexene ring which is at positions C3 and C2 in compounds 16b and 26 respectively. The attack of C2 and N to the carbonyl C was monitored, the rate limiting barrier is the one for the formation of the exocyclic double bond in both cases. Attack of C2 is preferred over the attack of N by almost 16 kcal/mol justifying the reaction path via addition to C2 (Figure 9.8).

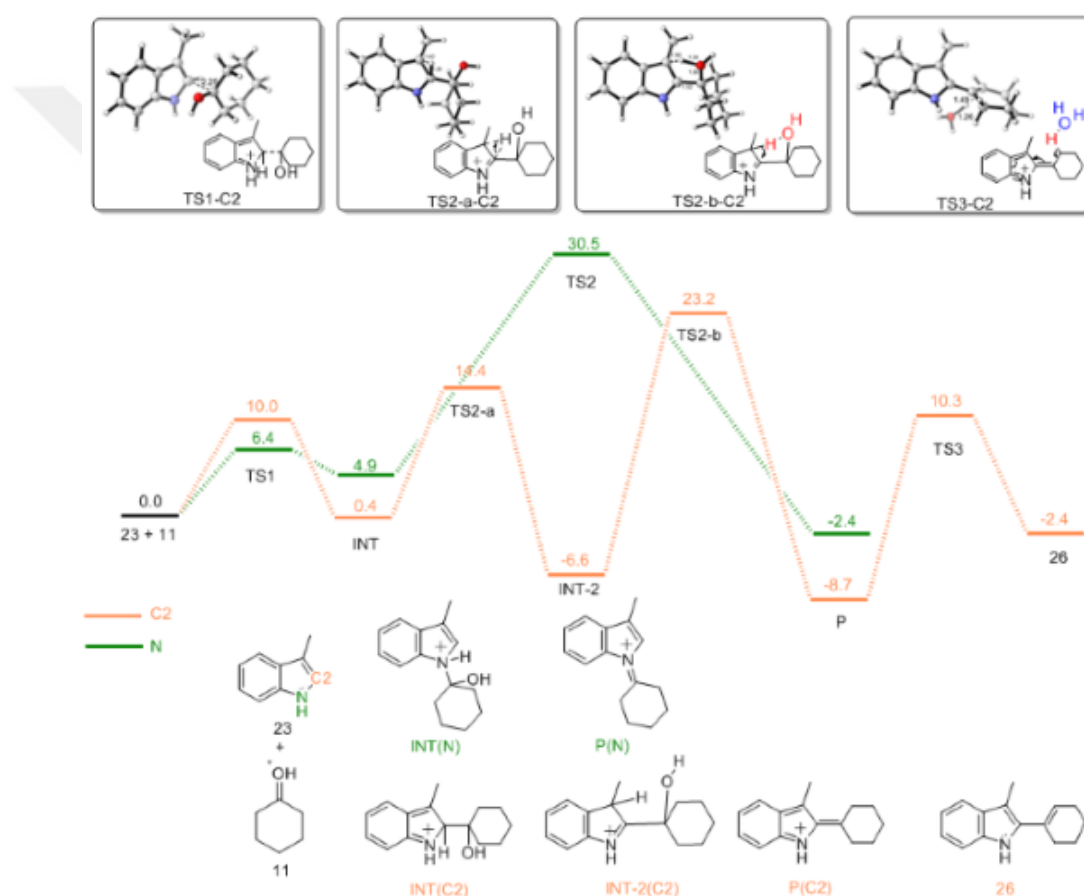


Figure 9.8. Gibbs Free energy profile for the formation of 26 (M06-2X/6-31+ G(d,p) in cyclohexanone).

Suggested mechanism for the unusual architecture of the polycyclic compound 27 (Diels-Alder product) is shown in Figure 9.9 and 9.10. This transformation is suggested to start with the direct dehydrative coupling of 23 with 11 to give 2-alkenylated indole 26 (Figure 9.9). A sequential sigmatropic hydrogen shift of the condensation product 26 yields an unusual formation of azafulvene intermediate 29. Basically, under thermal conditions, the azafulvene 29 and 26 undergo a subsequent intermolecular Diels-Alder

reaction to readily furnish 27 (Figure 9.10). Actually, this reaction can produce four possible hetero-Diels-Alder products (27, 31-33) as the exo and the endo adducts.

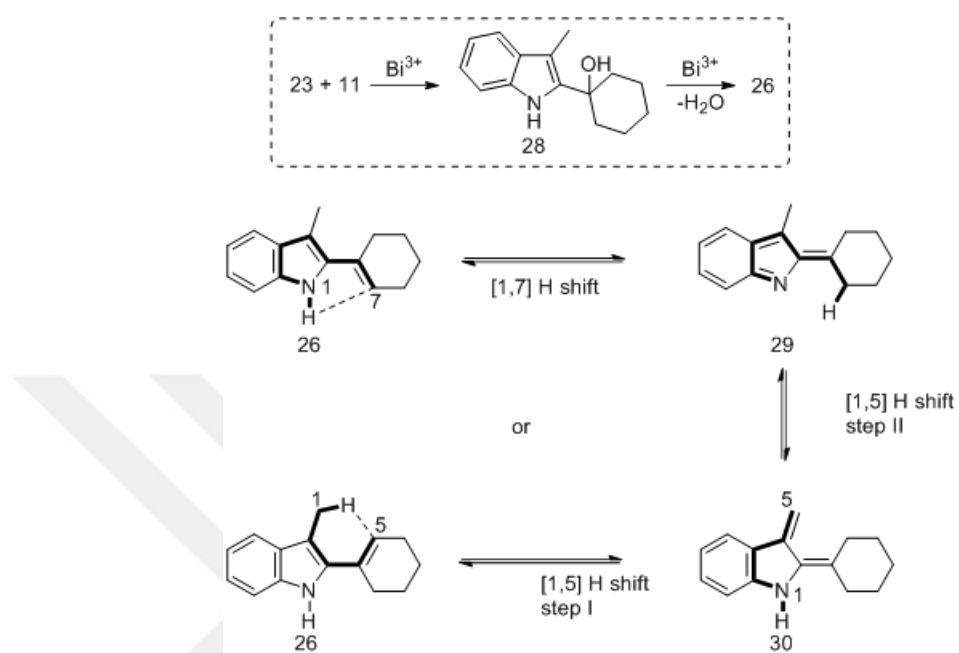


Figure 9.9. The formation mechanism of 26 from 23 and 11. Possible H shifts.

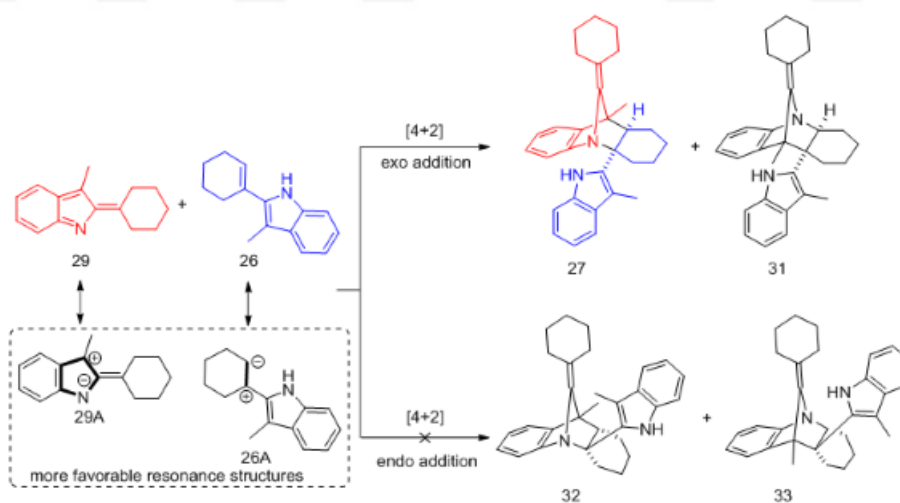


Figure 9.10. Possible cycloadduct structures for the Diels-Alder reaction of 26 and 29.

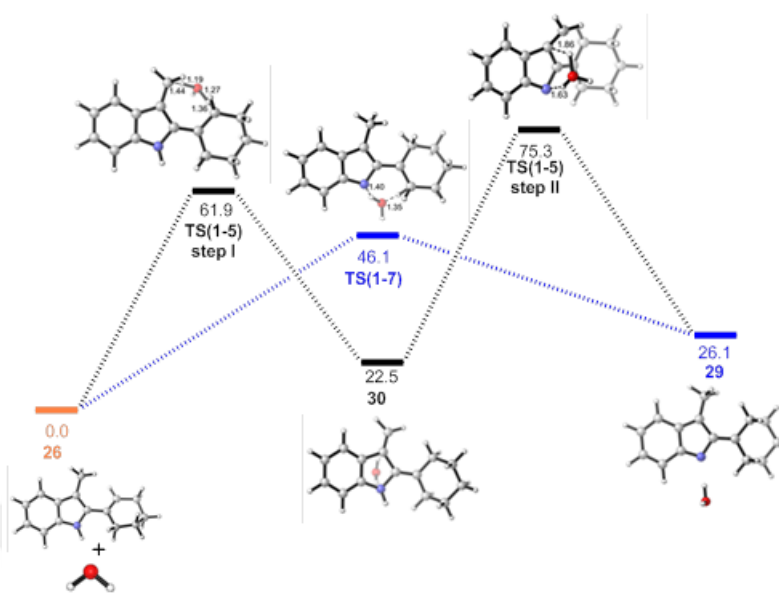


Figure 9.11. Gibbs Free Energy profile for [1,5] and [1,7] H-shift.

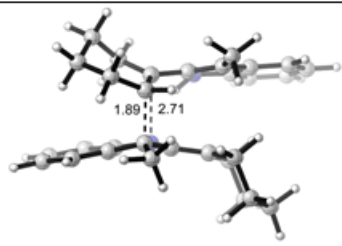
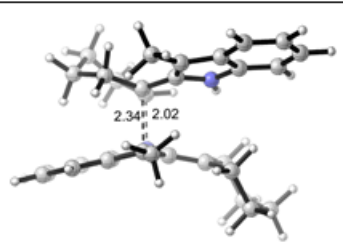
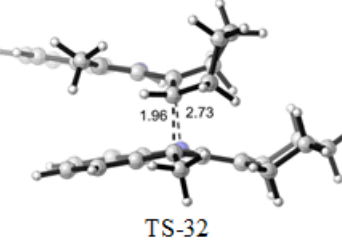
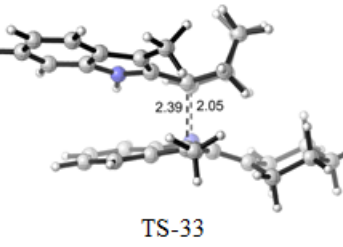
	[1.6]-addition	[1.5]-addition
[4+2] exo addition	 TS-27 $\Delta G^\ddagger = 28.0$ $\Delta H^\ddagger = 10.5$ $\Delta G_{\text{rxn}} = 2.8$ $\Delta H_{\text{rxn}} = -15.4$	 TS-31 $\Delta G^\ddagger = 38.5$ $\Delta H^\ddagger = 21.4$ $\Delta G_{\text{rxn}} = 5.8$ $\Delta H_{\text{rxn}} = -12.6$
[4+2] endo addition	 TS-32 $\Delta G^\ddagger = 31.5$ $\Delta H^\ddagger = 14.3$ $\Delta G_{\text{rxn}} = 1.9$ $\Delta H_{\text{rxn}} = -14.8$	 TS-33 $\Delta G^\ddagger = 37.1$ $\Delta H^\ddagger = 20.7$ $\Delta G_{\text{rxn}} = 3.6$ $\Delta H_{\text{rxn}} = -14.4$

Figure 9.12. Transition state structures of Diels-Alder reaction between 26 and 29 with 1,5- and 1,6-addition. Activation free energies, activation enthalpies, reaction energies and reaction enthalpies are given in kcal/mol.

The formation of the Diels-Alder adducts can only be explained with the attack of 26 to 29 (Figure 9.10). 29 can be formed from 26 via a single step ([1,7]H shift) or stepwise ([1,5]H shift). Both paths have been modeled and transition states have been located, a concerted single step reaction where the proton shifts directly from N to C7 is preferred over the stepwise mechanism (Figure 9.11). In this case, the Gibbs free energy of activation is still very high and barely reachable at room temperature however in a sealed tube provided that a small amount of 29 forms the Diels-Alder reaction is triggered by its formation. Also, note that even a small amount of 29 is enough to initiate the Diels-Alder reaction displayed in Figure 9.12. The 1,6-addition is favored over the 1,5 possibly due to steric reasons, the exo transition structure is preferred over the endo-structure as expected.

## 9.5. Conclusions

In this study, the reactions of two indoles, N-methyl indole and 3-methyl indole with cyclohexanone were investigated. N-methyl indole gives C3 substitution product as both thermodynamically and kinetically favored over C2 position. In 3-methyl indole, because C3 position is occupied, C2 substitution competes with N substitution. However, N-substitution is not favored because of higher activation barrier and smaller exothermicity. Another important experimental finding was Diels-Alder product formation which have been modeled. Diels-Alder product formation has started with [1,7] H-shift of substitution intermediate which behaves as diene and gives DA reaction with intermediate-dienophile.

## 10. CONCLUDING REMARKS

This dissertation focuses on the investigation of various molecules with biological activity in terms of their synthesis, characterization, assessment of reaction mechanisms and calculation of thermodynamic properties by the means of experimental and computational tools. These molecules can be classified into two, the ones with methacrylate functionality and the ones with pharmaceutical potential. The first three chapters studies the methacrylates and their derivatives because of their importance in polymer chemistry as well as biomedical applications. On the other hand, the last three chapters include theoretical studies on the synthesis or degradation mechanisms of several molecules that show pharmaceutical activity being a drug or its precursor.

Methacrylate functionalized monomers were synthesized for their different applicabilities like, their photoinitiating abilities in light induced photopolymerization reactions, their incorporation into hydrogels to be used in biomedical applications and also establishment of structure-reactivity relationships for free radical polymerization reactions.

The analyses of photochemical properties of the synthesized six novel monomeric photoinitiators (MPI) based on commercially available ones (BP, AP, Irgacure 184 and Irgacure 2959) that attached to methacrylates (TBBr and IEM) showed similar or increased results than their commercial precursors. The effect of polymerizable group, either TBBr or IEM, on photoinitiation efficiency depends on being Type I or Type II photoinitiators. Also, in identification of the light absorption properties of the MPIs, molecular orbital calculations (TD-DFT) gave applicable results. HOMO to LUMO charge transfer transition with a  $\pi$  to  $\pi^*$  character leads an excellent photoinitiation character. The analyses of the photoinitiating abilities of the MPIs and comparison of them with their precursors indicate that they appear to be promising photoinitiators.

A relationship between the free radical polymerization rates of 21 methacrylate monomers and the chemical properties of their monomeric radicals were built by deriva-

tion of a non-linear expression. The resulting equation showed that polymerization rate increases as radical stability (stab) increases or nucleophilicity of the monomeric radical decreases. Construction of such a relationship is important with regard to get a foresight and make improvements on novel methacrylate derivatives.

As a last study on methacrylates and its derivatives, hydrogel scaffolds were prepared from synthesized novel carboxylic acid-functionalized monomers. These hydrogels showed average hydrophilicity and swelling ratio. In basic media, increased swelling has been observed due to charged pendant acidic groups which causes improvement in mineralization of the hydrogels.

As a continuation to the molecules with biological activity, the ones with pharmaceutical capacity have been investigated computationally in order to have an insight into their molecular and mechanistic properties. For these purpose the reactions of three different molecules have been analyzed, thiazolidinones, diclofenac and indoles.

The calculations on the inverse-electron demand Diels-Alder reactions of norbornenes with thiones to give thiazolidinones demonstrated that, the exo selectivity of norbornene originates from large distortion of norbornene and higher torsional strain of endo product in transition states. Modeling each plausible structure in the Diels-Alder reaction helped to demonstrated the powerful effect of distortion of norbornene and the steric effect of the quasi-eclipsing forming bonds in the endo transition structures, successfully.

The degradation of an anti-inflammatory drug diclofenac (DCF) in aquatic environment has been modelled in order to describe the reaction mechanisms and toxicity progress during the reaction. It is confirmed that hydroxyl radical mediated degradation starts with an OH-addition or a H-abstraction from any possible site of the molecule. Subsequent reactions to the OH-addition and H-abstraction intermediates have been modeled and degradation mechanisms of possible byproducts have been disclosed. Toxicity studies classified DCF as 'harmful'. Its byproducts -except highly chlorinated ones- were found to be slightly less toxic than DCF. Being the first com-

prehensive theoretical study on the degradation of diclofenac, the results provide a detailed mechanistic account of the degradation of diclofenac in aqueous medium.

In the last chapter, indoles have been the subject of the study because of their distinctive reactivity in organic reactions and also being the basis of the many biologically active molecules. The reactions of N-methyl indole and 3-methyl indole with cyclohexanone were modeled in order to reveal the origins of the regioselectivities. N-methyl indole gives C3 substitution as the only product; however 3-methyl indole results in C2 substitution because of C3 site being occupied. Subsequent Diels-Alder reactions of 3-methyl indole derivative has been modeled and verified theoretically as well.

Consequently, this dissertation has focused on the clarification of the several concerns such as reaction mechanisms and their feasibilities, novel monomer syntheses and their applicabilities, and also developing an expression for structure-reactivity relationship. In order to fulfill the objectives, experimental and quantum mechanical methods have been employed.

## 11. FUTURE WORK SUGGESTIONS

The topics covered in this dissertation have a potential to be studied in order to shed light to further issues. The synthesis of novel polymerizable photoinitiators has a growing interest because of its advantages both environmentally and experimentally. For this purpose, new monomeric and polymeric photoinitiators can be developed. Also the monomeric photoinitiators that were utilized in this thesis could be polymerized and evaluated in terms of their photoinitiating efficiencies.

Predicting the polymerization rate of a monomer before its synthesis is very important in terms of time-saving and cost. In this regard, structure-reactivity relationship could be extended for larger groups of monomers by using different chemical descriptors such as Mulliken atomic charges, molecular polarizability and energies of the frontier molecular orbitals.

Optimizing the formulations of hydrogels is important for their usage in biomedical applications. Hydrogels with good mechanical strength, high swelling ratio, rapid respond to pH changes and high mineralization capability, are considered as advantageous for drug delivery. In order to develop the proper hydrogels, formulations will be improved by changing the ratio of the constituents.

Investigation and synthesis of the heterocompounds that show pharmaceutical activity, have a growing interest. A mechanistic view to the reactions and their stereo- and regioselectivities is important in order to have a deeper understanding to the reaction at a molecular level. For these purposes, the synthesis and selectivities of the reactions of thiohydantoin will be investigated theoretically.



## REFERENCES

1. Parr, R. G. and W. Yang, *Density-Functional Theory of Atoms and Molecules*, Oxford University Press, New York, 1989.
2. Becke, A. D., “A New Mixing of Hartree–Fock and Local Density-Functional Theories”, *The Journal of Chemical Physics*, Vol. 98, No. 2, pp. 1372–1377, 1993.
3. Becke, A. D., “Density-Functional Exchange-Energy Approximation with Correct Asymptotic-Behaviour”, *Physical Review A*, Vol. 38, pp. 3098–3100, 1988.
4. Lewars, E., *Computational Chemistry: Introduction to the Theory and Applications of Molecular and Quantum Mechanics*, Kluwer Academic Publishers, Canada, 2003.
5. Lee, C., W. Yang and R. G. Parr, “Development of the Colle-Salvetti Correlation-Energy Formula into a Functional of the Electron Density”, *Physical Review B*, Vol. 37, No. 2, p. 785, 1988.
6. Becke, A. D., “Density-Functional Thermochemistry. III. The Role of Exact Exchange”, *The Journal of Chemical Physics*, Vol. 98, No. 7, pp. 5648–5652, 1993.
7. Zhao, Y. and D. G. Truhlar, “The M06 Suite of Density Functionals for Main Group Thermochemistry, Thermochemical Kinetics, Noncovalent Interactions, Excited States, and Transition Elements: Two New Functionals and Systematic Testing of Four M06-class Functionals and 12 Other Functionals”, *Theoretical Chemistry Accounts: Theory, Computation, and Modeling (Theoretica Chimica Acta)*, Vol. 120, No. 1, pp. 215–241, 2008.
8. Runge, E. and E. K. U. Gross, “Density-Functional Theory for Time Dependent Systems”, *Physical Review Letters*, Vol. 52, pp. 997–1000, 1984.

9. Tapia, O. and J. Bertrán, *Solvent Effects and Chemical Reactivity*, Kluwer Academic Publishers, Dordrecht; Boston, 1996.
10. Tomasi, J., B. Mennucci and R. Cammi, “Quantum Mechanical Continuum Solvation Models”, *Chemical Reviews*, Vol. 105, pp. 2999–3093, 2005.
11. Cramer, C. J. and D. G. Truhlar, “Implicit Solvation Models: Equilibria, Structure, Spectra, and Dynamics”, *Chemical Reviews*, Vol. 99, pp. 2161–2200, 1999.
12. Barone, V., M. Cossi and J. Tomasi, “Geometry Optimization of Molecular Structures in Solution by the Polarizable Continuum Model”, *Journal of Computational Chemistry*, Vol. 19, pp. 404–417, 1998.
13. Barone, V. and M. Cossi, “Quantum Calculation of Molecular Energies and Energy Gradients in Solution by a Conductor Solvent Model”, *Journal of Physical Chemistry A*, Vol. 102, pp. 1995–2001, 1998.
14. Mennucci, B., E. Cancès and J. Tomasi, “Evaluation of Solvent Effects in Isotropic and Anisotropic Dielectrics and in Ionic Solutions with a Unified Integral Equation Method: Theoretical Bases, Computational Implementation, and Numerical Applications”, *The Journal of Physical Chemistry B*, Vol. 101, No. 49, pp. 10506–10517, 1997.
15. Mennucci, B. and J. Tomasi, “Continuum Solvation Models: a New Approach to the Problem of Solute’s Charge Distribution and Cavity Boundaries”, *The Journal of Chemical Physics*, Vol. 106, No. 12, pp. 5151–5158, 1997.
16. Yagci, Y., S. Jockusch and N. J. Turro, “Photoinitiated Polymerization: Advances, Challenges, and Opportunities”, *Macromolecules*, Vol. 43, No. 15, pp. 6245–6260, 2010.
17. Dietliker, K., T. J. Jung, J. Benkhoff, H. Kura, A. Matsumoto, H. Oka, D. Hristova, G. Gescheidt and G. Rist, “New Developments in Photoinitiators”, *Macro-*

- molecular Symposia*, Vol. 217, pp. 77–97, 2004.
18. Fouassier, J. and J. Lalevée, *Photoinitiators for Polymer Synthesis: Scope, Reactivity, and Efficiency*, Wiley-VCH Verlag GmbH Co. KGaA, Weinheim, 2012.
  19. Dietliker, K., R. Hüsler, J.-L. Birbaum, S. Ilg, S. Villeneuve, K. Studer, T. Jung, J. Benkhoff, H. Kura and A. Matsumoto, “Advancements in Photoinitiators—Opening up New Applications for Radiation Curing”, *Progress in Organic Coatings*, Vol. 58, No. 2, pp. 146–157, 2007.
  20. Corrales, T., F. Catalina, C. Peinado and N. Allen, “Free Radical Macrophotoinitiators: an Overview on Recent Advances”, *Journal of Photochemistry and Photobiology A: Chemistry*, Vol. 159, No. 2, pp. 103–114, 2003.
  21. Wang, H. Y., J. Wei, X. S. Jiang and J. Yin, “Novel Chemical-Bonded Polymerizable Sulfur-Containing Photoinitiators Comprising the Structure of Planar N-phenylmaleimide and Benzophenone for Photopolymerization”, *Polymer*, Vol. 47, No. 14, pp. 4967–4975, 2006.
  22. Nayak, B. R. and L. J. Mathias, “A novel Photoinimer for the Polymerization of Acrylates and Methacrylates”, *Journal of Polymer Science Part A-Polymer Chemistry*, Vol. 43, No. 22, pp. 5661–5670, 2005.
  23. Karahan, O., D. K. Balta, N. Arsu and D. Avci, “Synthesis and Evaluations of Novel Photoinitiators with Side-Chain Benzophenone, Derived from Alkyl alpha-Hydroxymethacrylates”, *Journal of Photochemistry and Photobiology A-Chemistry*, Vol. 274, pp. 43–49, 2014.
  24. Xiao, P., F. Dumur, M. Frigoli, M. A. Tehfe, B. Graff, J. P. Fouassier, D. Gigmes and J. Lalevee, “Naphthalimide Based Methacrylated Photoinitiators in Radical and Cationic Photopolymerization under Visible Light”, *Polymer Chemistry*, Vol. 4, No. 21, pp. 5440–5448, 2013.

25. Yang, J. L., R. F. Tang, S. Q. Shi and J. Nie, "Synthesis and Characterization of Polymerizable One-Component Photoinitiator Based on Sesamol", *Photochemical Photobiological Sciences*, Vol. 12, No. 5, pp. 923–929, 2013.
26. Balta, D. K., O. Karahan, D. Avci and N. Arsu, "Synthesis, Photophysical and Photochemical Studies of Benzophenone Based Novel Monomeric and Polymeric Photoinitiators", *Progress in Organic Coatings*, Vol. 78, pp. 200–207, 2015.
27. Cesur, B., O. Karahan, S. Agopcan, T. N. Eren, N. Okte and D. Avci, "Difunctional Monomeric and Polymeric Photoinitiators: Synthesis and Photoinitiating Behaviors", *Progress in Organic Coatings*, Vol. 86, pp. 71–78, 2015.
28. Corrales, T., C. Peinado, F. Catalina, M. G. Neumann, N. S. Allen, A. M. Rufs and M. V. Encinas, "Photopolymerization of Methyl Methacrylate Initiated by Thioxanthone Derivatives: Photoinitiation Mechanism", *Polymer*, Vol. 41, No. 26, pp. 9103–9109, 2000.
29. Angiolini, L., D. Caretti and E. Salatelli, "Synthesis and Photoinitiation Activity of Radical Polymeric Photoinitiators Bearing Side-Chain Camphorquinone Moieties", *Macromolecular Chemistry and Physics*, Vol. 201, No. 18, pp. 2646–2653, 2000.
30. Allonas, X., J. P. Fouassier, L. Angiolini and D. Caretti, "Excited-State Properties of Camphorquinone Based Monomeric and Polymeric Photoinitiators", *Helvetica Chimica Acta*, Vol. 84, No. 9, pp. 2577–2588, 2001.
31. Wei, J. and F. Liu, "Novel Highly Efficient Macrophotoinitiator Comprising Benzophenone, Coinitiator Amine, and Thio Moieties for Photopolymerization", *Macromolecules*, Vol. 42, No. 15, pp. 5486–5491, 2009.
32. Wang, J. S., J. Y. Cheng, J. C. Liu, Y. J. Gao and F. Sun, "Self-Floating Ability and Initiating Gradient Photopolymerization of Acrylamide Aqueous Solution of a Water-Soluble Polysiloxane Benzophenone Photoinitiator", *Green Chemistry*,

- Vol. 15, No. 9, pp. 2457–2465, 2013.
33. Jiang, X. S. and J. Yin, “Polymeric Photoinitiator Containing in-Chain Thioxanthone and Cointiator Amines”, *Macromolecular Rapid Communications*, Vol. 25, No. 6, pp. 748–752, 2004.
  34. Temel, G., B. Aydogan, N. Arsu and Y. Yagci, “Synthesis and Characterization of One-Component Polymeric Photoinitiator by Simultaneous Double Click Reactions and Its Use in Photoinduced Free Radical Polymerization”, *Macromolecules*, Vol. 42, No. 16, pp. 6098–6106, 2009.
  35. Wang, Y. L., X. S. Jiang and J. Yin, “Novel Polymeric Photoinitiators Comprising of Side-Chain Benzophenone and Cointiator Amine: Photochemical and Photopolymerization Behaviors”, *European Polymer Journal*, Vol. 45, No. 2, pp. 437–447, 2009.
  36. Wang, K. M., Y. H. Lu, P. H. Chen, J. S. Shi, H. N. Wang and Q. Yu, “Novel One-Component Polymeric Benzophenone Photoinitiator Containing Poly (Ethylene Glycol) as Hydrogen Donor”, *Materials Chemistry and Physics*, Vol. 143, No. 3, pp. 1391–1395, 2014.
  37. Cheng, L. L. and W. F. Shi, “Synthesis and Photoinitiating Behavior of Benzophenone-Based Polymeric Photoinitiators Used for UV Curing Coatings”, *Progress in Organic Coatings*, Vol. 71, No. 4, pp. 355–361, 2011.
  38. de Groot, J. H., K. Dillingham, H. Deuring, H. J. Haitjema, F. J. van Beijma, K. Hodd and S. Norrby, “Hydrophilic Polymeric Acylphospine Oxide Photoinitiators/Crosslinkers for in vivo Blue-Light Photopolymerization”, *Biomacromolecules*, Vol. 2, No. 4, pp. 1271–1278, 2001.
  39. Wei, J., R. Lu and F. Liu, “Effect of Photosensitive Groups on the Photoefficiency of Polymeric Photoinitiators”, *Journal of Polymer Research*, Vol. 18, No. 5, pp. 1001–1008, 2011.

40. Kork, S., G. Yilmaz and Y. Yagci, "Poly(vinyl alcohol)-Thioxanthone as One-Component Type II Photoinitiator for Free Radical Polymerization in Organic and Aqueous Media", *Macromolecular Rapid Communications*, Vol. 36, No. 10, pp. 923–928, 2015.
41. Akat, H., B. Gacal, D. K. Balta, N. Arsu and Y. Yagci, "Poly(ethylene glycol)-Thioxanthone Prepared by Diels-Alder Click Chemistry as One-Component Polymeric Photoinitiator for Aqueous Free-Radical Polymerization", *Journal of Polymer Science Part A-Polymer Chemistry*, Vol. 48, No. 10, pp. 2109–2114, 2010.
42. Tanikawa, M., T. Watanabe, Y. Oyama, T. Yamamoto and S. Uwagawa, "Curing Resin Composition, Sealing Material for Liquid Crystal Display Device and Liquid Crystal Display Device", US20090134358.
43. Liu, Y. and D. Bull, "Photoinitiators and UV-Crosslinkable Acrylic Polymers for Pressure Sensitive Adhesives", US7745505.
44. Warren, S. C. and L. J. Mathias, "Synthesis and Polymerization of Ethyl alpha-Chloromethylacrylate and Related Derivatives", *Journal of Polymer Science Part A-Polymer Chemistry*, Vol. 28, No. 6, pp. 1637–1648, 1990.
45. Mathias, L. J., R. M. Warren and S. Huang, "tert-Butyl alpha-(Hydroxymethyl)Acrylate and its Ether Dimer - Multifunctional Monomers Giving Polymers with Easily Cleaved Ester Groups", *Macromolecules*, Vol. 24, No. 8, pp. 2036–2042, 1991.
46. Xiao, P., J. Lalevee, X. Allonas, J. P. Fouassier, C. Ley, M. El Roz, S. Q. Shi and J. Nie, "Photoinitiation Mechanism of Free Radical Photopolymerization in the Presence of Cyclic Acetals and Related Compounds", *Journal of Polymer Science Part A-Polymer Chemistry*, Vol. 48, No. 24, pp. 5758–5766, 2010.
47. Frisch, M., G. Trucks, H. Schlegel, G. Scuseria, M. Robb, J. Cheeseman, G. Scalmani, V. Barone, B. Mennucci, G. Petersson *et al.*, "Gaussian 09, revision A. 2",

*Gaussian, Inc., Wallingford, CT.*

48. Tehfe, M.-A., F. Dumur, B. Graff, F. Morlet-Savary, J.-P. Fouassier, D. Gigmes and J. Laleve'e, "New Push-Pull Dyes Derived from Michler's Ketone For Polymerization Reactions Upon Visible Lights", *Macromolecules*, Vol. 46, No. 10, pp. 3761–3770, 2013.
49. Criqui, A., J. Lalevee, X. Allonas and J. P. Fouassier, "Electron Spin Resonance Spin Trapping Technique: Application to the Cleavage Process of Photoinitiators", *Macromolecular Chemistry and Physics*, Vol. 209, No. 21, pp. 2223–2231, 2008.
50. Moad, D., G.; Solomon, *The Chemistry of Radical Polymerization*, Elsevier Science, Oxford, U.K., 2nd edition, 2006.
51. Matyjaszewski, T., K.; Davis, *Handbook of Radical Polymerization*, Wiley-Interscience, New York, 2002.
52. Kloosterboer, J. G., "Network Formation by Chain Crosslinking Photopolymerization and its Applications in Electronics", *Advances in Polymer Science*, Vol. 84, pp. 1–61, 1988.
53. Decker, C., "Photoinitiated Crosslinking Polymerisation", *Progress in Polymer Science*, Vol. 21, No. 4, pp. 593–650, 1996.
54. Anseth, K. S., S. M. Newman and C. N. Bowman, "Polymeric Dental Composites: Properties and Reaction Behavior of Multimethacrylate Dental Restorations", *Biopolymers II*, Vol. 122, pp. 177–217, 1995.
55. Decker, C. and B. Elzaouk, "Laser-Induced Crosslinking Polymerization of Acrylic Photoresists", *Journal of Applied Polymer Science*, Vol. 65, No. 5, pp. 833–844, 1997.

56. Jansen, J., A. A. Dias, M. Dorschu and B. Coussens, “Fast Monomers: Factors Affecting the Inherent Reactivity of Acrylate Monomers in Photoinitiated Acrylate Polymerization”, *Macromolecules*, Vol. 36, No. 11, pp. 3861–3873, 2003.
57. Lee, T. Y., T. M. Roper, E. S. Jönsson, C. Guymon and C. Hoyle, “Influence of Hydrogen Bonding on Photopolymerization Rate of Hydroxyalkyl Acrylates”, *Macromolecules*, Vol. 37, No. 10, pp. 3659–3665, 2004.
58. Berchtold, K. A., J. Nie, J. W. Stansbury, B. Hacıoğlu, E. R. Beckel and C. N. Bowman, “Novel Monovinyl Methacrylic Monomers Containing Secondary Functionality for Ultrarapid Polymerization: Steady-State Evaluation”, *Macromolecules*, Vol. 37, No. 9, pp. 3165–3179, 2004.
59. Kilambi, H., J. W. Stansbury and C. N. Bowman, “Deconvoluting the Impact of Intermolecular and Intramolecular Interactions on the Polymerization Kinetics of Ultrarapid Mono (meth)Acrylates”, *Macromolecules*, Vol. 40, No. 1, pp. 47–54, 2007.
60. Karahan, O., D. Avci and V. Aviyente, “Structure-Reactivity Relationships of Alkyl alpha-Hydroxymethacrylate Derivatives”, *Journal of Polymer Science Part A-Polymer Chemistry*, Vol. 49, No. 14, pp. 3058–3068, 2011.
61. Karahan, O., V. Aviyente, D. Avci, H. Zijlstra and F. M. Bickelhaupt, “A Computational Study on the Reactivity Enhancement in the Free Radical Polymerization of Alkyl alpha-Hydroxymethacrylate and Acrylate Derivatives”, *Journal of Polymer Science Part A-Polymer Chemistry*, Vol. 51, No. 4, pp. 880–889, 2013.
62. Avci, D. and A. Z. Albayrak, “Synthesis and Copolymerization of New Phosphorus-Containing Acrylates”, *Journal of Polymer Science Part A: Polymer Chemistry*, Vol. 41, No. 14, pp. 2207–2217, 2003.
63. Avci, D. and L. J. Mathias, “Synthesis and Polymerization of Phosphorus-Containing Acrylates”, *Journal of Polymer Science Part A: Polymer Chemistry*,



Vol. 40, No. 19, pp. 3221–3231, 2002.

64. Zhao, Y., N. E. Schultz and D. G. Truhlar, “Design of Density Functionals by Combining the Method of Constraint Satisfaction with Parametrization for Thermochemistry, Thermochemical Kinetics, and Noncovalent Interactions”, *Journal of Chemical Theory and Computation*, Vol. 2, No. 2, pp. 364–382, 2006.
65. Günaydin, H., S. Salman, N. S. Tuzun, D. Avci and V. Aviyente, “Modeling the Free Radical Polymerization of Acrylates”, *International Journal of Quantum Chemistry*, Vol. 103, No. 2, pp. 176–189, 2005.
66. Dogan, B., S. Catak, V. Van Speybroeck, M. Waroquier and V. Aviyente, “Free Radical Polymerization of Ethyl Methacrylate and Ethyl  $\alpha$ -Hydroxy Methacrylate: A Computational Approach to the Propagation Kinetics”, *Polymer*, Vol. 53, No. 15, pp. 3211–3219, 2012.
67. Karahan, O., M. Isik, G. Cifci, I. Ugur, D. Avci and V. Aviyente, “Cyclization Tendencies in the Free Radical Polymerization of Allyl Acrylate Derivatives: A Computational Study”, *Journal of Polymer Science Part A: Polymer Chemistry*, Vol. 49, No. 11, pp. 2474–2483, 2011.
68. Decker, C. and K. Moussa, “Real-Time Kinetic-Study of Laser-Induced Polymerization”, *Macromolecules*, Vol. 22, No. 12, pp. 4455–4462, 1989.
69. Decker, C. and K. Moussa, “A New Class of Highly Reactive Acrylic-Monomers .2. Light-Induced Copolymerization with Difunctional Oligomers”, *Makromolekulare Chemie-Macromolecular Chemistry and Physics*, Vol. 192, No. 3, pp. 507–522, 1991.
70. Decker, C. and K. Moussa, “Photopolymerization of Multifunctional Polymers .5. Polyurethane-Acylate Resins”, *European Polymer Journal*, Vol. 27, No. 9, pp. 881–889, 1991.

71. Decker, C. and K. Moussa, "A New Class of Highly Reactive Acrylic-Monomers .1. Light-Induced Polymerization", *Makromolekulare Chemie-Rapid Communications*, Vol. 11, No. 4, pp. 159–167, 1990.
72. Moussa, K. and C. Decker, "Light-Induced Polymerization of New Highly Reactive Acrylic-Monomers", *Journal of Polymer Science Part A-Polymer Chemistry*, Vol. 31, No. 9, pp. 2197–2203, 1993.
73. Beckel, E. R., J. W. Stansbury and C. N. Bowman, "Evaluation of a Potential Ionic Contribution to the Polymerization of Highly Reactive (meth)Acrylate Monomers", *Macromolecules*, Vol. 38, No. 23, pp. 9474–9481, 2005.
74. Kilambi, H., S. K. Reddy, L. Schneidewind, J. W. Stansbury and C. N. Bowman, "Influence of the Secondary Functionality on the Radical-Vinyl Chemistry of Highly Reactive Monoacrylates", *Journal of Polymer Science Part A-Polymer Chemistry*, Vol. 47, No. 19, pp. 4859–4870, 2009.
75. Degirmenci, I., V. Aviyente, V. Van Speybroeck and M. Waroquier, "DFT Study on the Propagation Kinetics of Free-Radical Polymerization of alpha-Substituted Acrylates", *Macromolecules*, Vol. 42, No. 8, pp. 3033–3041, 2009.
76. Isik, M., O. Karahan, D. Avcı and V. Aviyente, "A Computational Approach to the Free Radical Polymerization Kinetics of Alkyl alpha-Hydroxymethacrylate Monomers: A Structure-Reactivity Relationship", *Journal of Polymer Science Part A-Polymer Chemistry*, Vol. 51, No. 11, pp. 2375–2384, 2013.
77. Tedder, J. M. and J. C. Walton, "The Importance of Polarity and Steric Effects in Determining the Rate and Orientation of Free-Radical Addition to Olefins - Rules for Determining the Rate and Preferred Orientation", *Tetrahedron*, Vol. 36, No. 6, pp. 701–707, 1980.
78. Giese, B., "Formation of CC Bonds by Addition of Free-Radicals to Alkenes", *Angewandte Chemie-International Edition in English*, Vol. 22, No. 10, pp. 753–

764, 1983.

79. Munger, K. and H. Fischer, "Separation of Polar and Steric Effects on Absolute Rate Constants and Arrhenius Parameters for the Reaction of tert-Butyl Radicals with Alkenes", *International Journal of Chemical Kinetics*, Vol. 17, No. 8, pp. 809–829, 1985.
80. Riemenschneider, K., H. M. Bartels, R. Dornow, E. Drechselgrau, W. Eichel, H. Luthe, Y. M. Matter, W. Michaelis and P. Boldt, "Free-Radical Additions .11. Kinetics of Free-Radical Additions of Bromomalononitrile to Alkenes and Pmo Treatment of The Reactivity and Regioselectivity", *Journal of Organic Chemistry*, Vol. 52, No. 2, pp. 205–212, 1987.
81. Heberger, K. and H. Fischer, "Rate Constants for the Addition of the 2-Hydroxy-2-Propyl Radical to Alkenes in Solution", *International Journal of Chemical Kinetics*, Vol. 25, No. 11, pp. 913–920, 1993.
82. Heberger, K. and A. Lopata, "Assessment of Nucleophilicity and Electrophilicity of Radicals, and of Polar and Enthalpy Effects on Radical Addition Reactions", *Journal of Organic Chemistry*, Vol. 63, No. 24, pp. 8646–8653, 1998.
83. De Vleeschouwer, F., V. Van Speybroeck, M. Waroquier, P. Geerlings and F. De Proft, "An Intrinsic Radical Stability Scale from the Perspective of Bond Dissociation Enthalpies: A Companion to Radical Electrophilicities", *Journal of Organic Chemistry*, Vol. 73, No. 22, pp. 9109–9120, 2008.
84. Morell, C., A. Grand and A. Toro-Labbe, "New Dual Descriptor for Chemical Reactivity", *Journal of Physical Chemistry A*, Vol. 109, No. 1, pp. 205–212, 2005.
85. De Vleeschouwer, F., P. Jaque, P. Geerlings, A. Toro-Labbe and F. De Proft, "Regioselectivity of Radical Additions to Substituted Alkenes: Insight from Conceptual Density Functional Theory", *Journal of Organic Chemistry*, Vol. 75, No. 15, pp. 4964–4974, 2010.

86. De Vleeschouwer, F., V. Van Speybroeck, M. Waroquier, P. Geerlings and F. De Proft, "Electrophilicity and Nucleophilicity Index for Radicals", *Organic Letters*, Vol. 9, No. 14, pp. 2721–2724, 2007.
87. De Vleeschouwer, F., P. Geerlings and F. De Proft, "Radical Electrophilicities in Solvent", *Theoretical Chemistry Accounts*, Vol. 131, No. 6, 2012.
88. De Vleeschouwer, F., F. De Proft and P. Geerlings, "Conceptual Density Functional Theory Based Intrinsic Radical Stabilities: Application to Substituted Silylenes and p-Benzynes", *Journal of Molecular Structure-Theochem*, Vol. 943, No. 1-3, pp. 94–102, 2010.
89. De Vleeschouwer, F., A. Chanlidsjijev, W. T. Yang, P. Geerlings and F. De Proft, "Pushing the Boundaries of Intrinsically Stable Radicals: Inverse Design Using the Thiadiazinyl Radical as a Template", *Journal of Organic Chemistry*, Vol. 78, No. 7, pp. 3151–3158, 2013.
90. Stewart, J. J. P., "Optimization of Parameters for Semiempirical Methods .1. Method", *Journal of Computational Chemistry*, Vol. 10, No. 2, pp. 209–220, 1989.
91. Stewart, J. J. P., "Optimization of Parameters for Semiempirical Methods .2. Applications", *Journal of Computational Chemistry*, Vol. 10, No. 2, pp. 221–264, 1989.
92. Deppmeier, B., A. Driessen, T. Hehre, W. Hehre, J. Johnson, P. Klunzinger, J. Leonard, I. Pham, W. Pietro, J. Yu *et al.*, "Spartan'08; Wavefunction, Inc", Irvine, CA, 2008.
93. Hehre, W. J., "AB-Initio Molecular-Orbital Theory", *Accounts of Chemical Research*, Vol. 9, No. 11, pp. 399–406, 1976.
94. Godineau, E., K. Schenk and Y. Landais, "Synthesis of Fused Piperidinones through a Radical-Ionic Cascade", *Journal of Organic Chemistry*, Vol. 73, No. 18,

- pp. 6983–6993, 2008.
95. De Dobbeleer, C., J. Pospisil, F. De Vleeschouwer, F. De Proft and I. E. Marko, “Unexpected Nucleophilic Behaviour of Free-Radicals Generated from Alpha-Iodoketones”, *Chemical Communications*, , No. 16, pp. 2142–2144, 2009.
  96. Godineau, E. and Y. Landais, “Radical and Radical-Ionic Multicomponent Processes”, *Chemistry-A European Journal*, Vol. 15, No. 13, pp. 3044–3055, 2009.
  97. Shih, H. W., M. N. Vander Wal, R. L. Grange and D. W. C. MacMillan, “Enantioselective alpha-Benzoylation of Aldehydes via Photoredox Organocatalysis”, *Journal of the American Chemical Society*, Vol. 132, No. 39, pp. 13600–13603, 2010.
  98. Pratsch, G., C. A. Anger, K. Ritter and M. R. Heinrich, “Hydroxy- and Aminophenyl Radicals from Arenediazonium Salts”, *Chemistry-A European Journal*, Vol. 17, No. 15, pp. 4104–4108, 2011.
  99. Liautard, V., F. Robert and Y. Landais, “Free-Radical Carboalkynylation and Carboalkenylation of Olefins”, *Organic Letters*, Vol. 13, No. 10, pp. 2658–2661, 2011.
  100. Kohls, P., D. Jadhav, G. Pandey and O. Reiser, “Visible Light Photoredox Catalysis: Generation and Addition of N-Aryltetrahydroisoquinoline-Derived alpha-Amino Radicals to Michael Acceptors”, *Organic Letters*, Vol. 14, No. 3, pp. 672–675, 2012.
  101. Jasch, H., S. B. Hoffing and M. R. Heinrich, “Nucleophilic Substitutions and Radical Reactions of Phenylazocarboxylates”, *Journal of Organic Chemistry*, Vol. 77, No. 3, pp. 1520–1532, 2012.
  102. Yoshioka, E., S. Kohtani, K. Sawai, Kentefu, E. Tanaka and H. Miyabe, “Polarity-Mismatched Addition of Electrophilic Carbon Radicals to an Electron-Deficient Acceptor: Cascade Radical Addition-Cyclization-Trapping Reaction”, *Journal of*

*Organic Chemistry*, Vol. 77, No. 19, pp. 8588–8604, 2012.

103. Debien, L. and S. Z. Zard, “From a Remarkable Manifestation of Polar Effects in a Radical Fragmentation to the Convergent Synthesis of Highly Functionalized Ketones”, *Journal of the American Chemical Society*, Vol. 135, No. 10, pp. 3808–3811, 2013.
104. Perkowski, A. J. and D. A. Nicewicz, “Direct Catalytic Anti-Markovnikov Addition of Carboxylic Acids to Alkenes”, *Journal of the American Chemical Society*, Vol. 135, No. 28, pp. 10334–10337, 2013.
105. O’Hara, F., D. G. Blackmond and P. S. Baran, “Radical-Based Regioselective C-H Functionalization of Electron-Deficient Heteroarenes: Scope, Tunability, and Predictability”, *Journal of the American Chemical Society*, Vol. 135, No. 32, pp. 12122–12134, 2013.
106. Parr, R. G., L. Von Szentpaly and S. B. Liu, “Electrophilicity Index”, *Journal of the American Chemical Society*, Vol. 121, No. 9, pp. 1922–1924, 1999.
107. Perdew, J. P., “Density-Functional Approximation for the Correlation-Energy of the Inhomogeneous Electron-Gas”, *Physical Review B*, Vol. 33, No. 12, pp. 8822–8824, 1986.
108. Brandrup, E. H., J.; Immergut, *Polymer Handbook*, Wiley-Interscience, New York, 2 edition, 1975.
109. Anseth, K. S., C. M. Wang and C. N. Bowman, “Kinetic Evidence of Reaction-Diffusion During the Polymerization of Multi(meth)acrylate Monomers”, *Macromolecules*, Vol. 27, No. 3, pp. 650–655, 1994.
110. Kobatake, S. and B. Yamada, “Severely Hindered Propagation and Termination Allowing Radical Polymerization of Alpha-Substituted Acrylate Bearing a Bis(Carbomethoxy)Ethyl Group”, *Macromolecules*, Vol. 28, No. 12, pp. 4047–

- 4054, 1995.
111. Kopeček, J., “Hydrogel Biomaterials: a Smart Future?”, *Biomaterials*, Vol. 28, No. 34, pp. 5185–5192, 2007.
  112. Lee, K. Y. and D. J. Mooney, “Hydrogels for Tissue Engineering”, *Chemical Reviews*, Vol. 101, No. 7, pp. 1869–1880, 2001.
  113. Oh, J. K., R. Drumright, D. J. Siegwart and K. Matyjaszewski, “The Development of Microgels/Nanogels for Drug Delivery Applications”, *Progress in Polymer Science*, Vol. 33, No. 4, pp. 448–477, 2008.
  114. Nguyen, K. T. and J. L. West, “Photopolymerizable Hydrogels for Tissue Engineering Applications”, *Biomaterials*, Vol. 23, No. 22, pp. 4307–4314, 2002.
  115. Scranton, A. B., C. N. Bowman and R. W. Peiffer, *Photopolymerization: Fundamentals and Applications*, ACS Publications, New Orleans, 1996.
  116. Fouassier, J.-P., *Photoinitiation, Photopolymerization, and Photocuring: Fundamentals and Applications*, Hanser Publishers, New York, 1995.
  117. Song, J., V. Malathong and C. R. Bertozzi, “Mineralization of Synthetic Polymer Scaffolds: a Bottom-Up Approach for the Development of Artificial Bone”, *Journal of the American Chemical Society*, Vol. 127, No. 10, pp. 3366–3372, 2005.
  118. Gong, J. P., Y. Katsuyama, T. Kurokawa and Y. Osada, “Double-Network Hydrogels with Extremely High Mechanical Strength”, *Advanced Materials*, Vol. 15, No. 14, pp. 1155–1158, 2003.
  119. Myung, D., W. Koh, J. Ko, Y. Hu, M. Carrasco, J. Noolandi, C. N. Ta and C. W. Frank, “Biomimetic Strain Hardening in Interpenetrating Polymer Network Hydrogels”, *Polymer*, Vol. 48, No. 18, pp. 5376–5387, 2007.
  120. Kopeček, J. and J. Yang, “Hydrogels as Smart Biomaterials”, *Polymer Interna-*

- tional*, Vol. 56, No. 9, pp. 1078–1098, 2007.
121. Chen, S., M. Liu, S. Jin and Y. Chen, “Synthesis and Swelling Properties of pH-Sensitive Hydrogels Based on Chitosan and poly-(Methacrylic Acid) Semi-Interpenetrating Polymer Network”, *Journal of Applied Polymer Science*, Vol. 98, No. 4, pp. 1720–1726, 2005.
  122. Kokubo, T. and H. Takadama, “How Useful is SBF in Predicting in vivo Bone Bioactivity?”, *Biomaterials*, Vol. 27, No. 15, pp. 2907–2915, 2006.
  123. Phadke, A., C. Zhang, Y. Hwang, K. Vecchio and S. Varghese, “Templated Mineralization of Synthetic Hydrogels for Bone-Like Composite Materials: Role of Matrix Hydrophobicity”, *Biomacromolecules*, Vol. 11, No. 8, pp. 2060–2068, 2010.
  124. Kahraman, M. V., G. Bayramoğlu, Y. Boztoprak, A. Güngör and N. Kayaman-Apohan, “Synthesis of Fluorinated/Methacrylated Epoxy Based Oligomers and Investigation of its Performance in the UV Curable Hybrid Coatings”, *Progress in Organic Coatings*, Vol. 66, No. 1, pp. 52–58, 2009.
  125. Quéré, D., “Surface Chemistry: Fakir Droplets”, *Nature Materials*, Vol. 1, No. 1, pp. 14–15, 2002.
  126. Tamada, Y. and Y. Ikada, “Effect of Preadsorbed Proteins on Cell Adhesion to Polymer Surfaces”, *Journal of Colloid and Interface Science*, Vol. 155, No. 2, pp. 334–339, 1993.
  127. Fringuelli, F., L. Minuti, F. Pizzo and A. Taticchi, “Reactivity and Selectivity in Lewis-Acid-Catalyzed Diels-Alder Reactions of 2-Cyclohexenones”, *Acta Chemica Scandinavica*, Vol. 47, pp. 255–255, 1993.
  128. Bodwell, G. J. and Z. Pi, “Electron Deficient Dienes I. Normal and Inverse Electron Demand Diels-Alder Reaction of the Same Carbon Skeleton”, *Tetrahedron Letters*, Vol. 38, No. 3, pp. 309–312, 1997.



129. Fringuelli, F. and A. Taticchi, *The Diels-Alder Reaction: Selected Practical Methods*, John Wiley Sons, 2002.
130. Carruthers, W., *Cycloaddition Reactions in Organic Synthesis*, Vol. 8, Elsevier, 2013.
131. Gao, H., X. Wu and J. Zhang, “Exo/endo Selectivity-Control in Lewis-Acid Catalyzed Tandem Heterocyclization/Formal [4+3] Cycloaddition: Synthesis of Polyheterocycles from 2-(1-alkynyl)-2-alken-1-ones and 1, 3-diphenylisobenzofuran”, *Chemical Communications*, Vol. 46, No. 46, pp. 8764–8766, 2010.
132. Liu, P., Y. Wu, C. C. Pye, P. D. Thornton, R. A. Poirier and D. J. Burnell, “Facial Selectivity in the Diels-Alder Reactions of 2, 2-Disubstituted Cyclopent-4-ene-1,3-dione Derivatives and a Computational Examination of the Facial Selectivity of the Diels-Alder Reactions of Structurally Related Dienes and Dienophiles”, *European Journal of Organic Chemistry*, Vol. 2012, No. 6, pp. 1186–1194, 2012.
133. Ma, M., R. Lu, S. A. Pullarkat, W. Deng and P.-H. Leung, “Steric Effects on the Control of endo/exo-Selectivity in the Asymmetric Cycloaddition Reaction of 3,4-dimethyl-1-phenylarsole”, *Dalton Transactions*, Vol. 39, No. 23, pp. 5453–5461, 2010.
134. Ruano, J. L. G., M. Alonso, D. Cruz, A. Fraile, M. R. Martin, M. T. Peromingo, A. Tito and F. Yuste, “Synthesis of Bicyclo 3.1.0 Hexanones via 1,3-Dipolar Cycloaddition of Diazoalkanes to Homochiral alpha-sulfinyl-2-cyclopentenones”, *Tetrahedron*, Vol. 64, No. 46, pp. 10546–10551, 2008.
135. Yoshitake, Y., H. Nakagawa, M. Eto and K. Harano, “Effect of  $\delta$  C=O Center Dot Center Dot Center Dot H-Ar Interaction on endo/exo Selectivity in the Diels-Alder Reaction of Phenyl-Substituted Cyclopentadienones”, *Tetrahedron Letters*, Vol. 41, No. 22, pp. 4395–4400, 2000.
136. Erol, S. and I. Dogan, “exo-Selective Inverse-Electron-Demand Hetero Diels-Alder

- Reactions of Norbornene with 5-benzylidene-2-arylimino-3-aryl-thiazolidine-4-thiones at Room Temperature”, *Tetrahedron*, Vol. 69, No. 4, pp. 1337–1344, 2013.
137. Erol, S. and I. Dogan, “Axially Chiral 2-arylimino-3-aryl-thiazolidine-4-one Derivatives: Enantiomeric Separation and Determination of Racemization Barriers by Chiral HPLC”, *The Journal of Organic Chemistry*, Vol. 72, No. 7, pp. 2494–2500, 2007.
138. Abhinit, M., M. Ghodke and N. A. Pratima, “Exploring Potential of 4-thiazolidinone: a Brief Review”, *International Journal of Pharmacy and Pharmaceutical Sciences*, Vol. 1, No. 1, pp. 47–64, 2009.
139. Li, W., Y. Lu, Z. Wang, J. T. Dalton and D. D. Miller, “Synthesis and Antiproliferative Activity of Thiazolidine Analogs for Melanoma”, *Bioorganic Medicinal Chemistry Letters*, Vol. 17, No. 15, pp. 4113–4117, 2007.
140. Best, M. D., “Click Chemistry and Bioorthogonal Reactions: Unprecedented Selectivity in the Labeling of Biological Molecules”, *Biochemistry*, Vol. 48, No. 28, pp. 6571–6584, 2009.
141. Gramlich, P. M. E., C. T. Wirges, A. Manetto and T. Carell, “Postsynthetic DNA Modification through the Copper-Catalyzed Azide-Alkyne Cycloaddition Reaction”, *Angewandte Chemie-International Edition*, Vol. 47, No. 44, pp. 8350–8358, 2008.
142. Weisbrod, S. H. and A. Marx, “Novel Strategies for the Site-Specific Covalent Labelling of Nucleic Acids”, *Chemical Communications*, , No. 44, pp. 5675–5685, 2008.
143. Becer, C. R., R. Hoogenboom and U. S. Schubert, “Click Chemistry Beyond Metal-Catalyzed Cycloaddition”, *Angewandte Chemie-International Edition*, Vol. 48, No. 27, pp. 4900–4908, 2009.

144. Kolb, H. C., M. G. Finn and K. B. Sharpless, "Click Chemistry: Diverse Chemical Function from a few Good Reactions", *Angewandte Chemie-International Edition*, Vol. 40, No. 11, pp. 2004–2021, 2001.
145. Tornøe, C. W., C. Christensen and M. Meldal, "Peptidotriazoles on Solid Phase: 1,2,3-triazoles by Regiospecific Copper(I)-Catalyzed 1,3-dipolar Cycloadditions of Terminal Alkynes to Azides", *Journal of Organic Chemistry*, Vol. 67, No. 9, pp. 3057–3064, 2002.
146. Kim, E. Y. L., C. Gronewold, A. Chatterjee, C. W. von der Lieth, C. Kliem, B. Schmauser, M. Wiessler and E. Frei, "Oligosaccharide Mimics Containing Galactose and Fucose Specifically Label Tumour Cell Surfaces and Inhibit Cell Adhesion to Fibronectin", *ChemBioChem*, Vol. 6, No. 2, pp. 422–431, 2005.
147. Seelig, B. and A. Jaschke, "Site-Specific Modification of Enzymatically Synthesized RNA: Transcription Initiation and Diels-Alder Reaction", *Tetrahedron Letters*, Vol. 38, No. 44, pp. 7729–7732, 1997.
148. Wombacher, R. and A. Jaschke, "Probing the Active Site of a Diels-Alderase Ribozyme by Photoaffinity Cross-Linking", *Journal of the American Chemical Society*, Vol. 130, No. 27, pp. 8594–8595, 2008.
149. Braun, K., M. Wiessler, V. Ehemann, R. Pipkorn, H. Spring, J. Debus, B. Didingler, M. Koch, G. Muller and W. Waldeck, "Treatment of Glioblastoma Multiforme Cells with Temozolomide-BioShuttle Ligated by the Inverse Diels-Alder Ligation Chemistry", *Drug Design, Development and Therapy*, Vol. 2, pp. 289–301, 2008.
150. Pipkorn, R., W. Waldeck, B. Didingler, M. Koch, G. Mueller, M. Wiessler and K. Braun, "Inverse-Electron-Demand Diels-Alder Reaction as a Highly Efficient Chemoselective Ligation Procedure: Synthesis and Function of a BioShuttle for Temozolomide Transport into Prostate Cancer Cells", *Journal of Peptide Science*, Vol. 15, No. 3, pp. 235–241, 2009.

151. Wiessler, M., E. Mueller, P. Lorenz, C. Kliem and H. Fleischhacker, *Deutsches Krebsforschungszentrum Stiftung Des Oeffentlichen Rechts*, Germany, 2007.
152. Blackman, M. L., M. Royzen and J. M. Fox, "Tetrazine Ligation: Fast Bioconjugation Based on Inverse-Electron-Demand Diels–Alder Reactivity", *Journal of the American Chemical Society*, Vol. 130, No. 41, pp. 13518–13519, 2008.
153. Devaraj, N. K., S. Hilderbrand, R. Upadhyay, R. Mazitschek and R. Weissleder, "Bioorthogonal Turn-On Probes for Imaging Small Molecules Inside Living Cells", *Angewandte Chemie (International ed. in English)*, Vol. 49, No. 16, p. 2869, 2010.
154. Devaraj, N. K., R. Upadhyay, J. B. Haun, S. A. Hilderbrand and R. Weissleder, "Fast and Sensitive Pretargeted Labeling of Cancer Cells through a Tetrazine/trans-Cyclooctene Cycloaddition", *Angewandte Chemie International Edition*, Vol. 48, No. 38, pp. 7013–7016, 2009.
155. Schoch, J., M. Wiessler and A. Ja"schke, "Post-Synthetic Modification of DNA by Inverse-Electron-Demand Diels–Alder Reaction", *Journal of the American Chemical Society*, Vol. 132, No. 26, pp. 8846–8847, 2010.
156. Clayden, J., W. J. Moran, P. J. Edwards and S. R. LaPlante, "The Challenge of Atropisomerism in Drug Discovery", *Angewandte Chemie International Edition*, Vol. 48, No. 35, pp. 6398–6401, 2009.
157. Paul, B., G. L. Butterfoss, M. G. Boswell, P. D. Renfrew, F. G. Yeung, N. H. Shah, C. Wolf, R. Bonneau and K. Kirshenbaum, "Peptoid Atropisomers", *Journal of the American Chemical Society*, Vol. 133, No. 28, pp. 10910–10919, 2011.
158. Sandstrom, J., "Topics in Stereochemistry", *Ed. HL Allinger, EL Eliel, SH Wilen, John Willey, New York*, Vol. 14, p. 83, 1983.
159. Vázquez, S. and P. Camps, "Chemistry of Pyramidalized Alkenes", *Tetrahedron*, Vol. 61, No. 22, pp. 5147–5208, 2005.

160. Koga, N., T. Ozawa and K. Morokuma, "Origin of exo Selectivity in Norbornene. An ab initio MO Study", *Journal of Physical Organic Chemistry*, Vol. 3, No. 8, pp. 519–533, 1990.
161. Mazzocchi, P. H., B. Stahly, J. Dodd, N. G. Rondan, L. Domelsmith, M. D. Rozeboom, P. Caramella and K. Houk, "pi-Facial Stereoselectivity: Rates and Stereoselectivities of Cycloadditions of Hexachlorocyclopentadiene to 7-Substituted Norbornadienes and Photoelectron Spectral and Molecular Orbital Computation Investigations of Norbornadienes", *Journal of the American Chemical Society*, Vol. 102, No. 21, pp. 6482–6490, 1980.
162. Rondan, N. G., M. N. Paddon-Row, P. Caramella, J. Mareda, P. H. Mueller and K. N. Houk, "Origin of Huisgen's Factor x: Staggering of Allylic Bonds Promotes Anomalously Rapid exo Attack on Norbornenes", *Journal of the American Chemical Society*, Vol. 104, No. 18, pp. 4974–4976, 1982.
163. Domingo, L. R., M. J. Aurell, M. Arnó and J. A. Sáez, "Toward an Understanding of the Acceleration of Diels-Alder Reactions by a Pseudo-Intramolecular Process Achieved by Molecular Recognition. A DFT Study", *The Journal of Organic Chemistry*, Vol. 72, No. 11, pp. 4220–4227, 2007.
164. Stephens, P. J., F. J. Devlin, C. F. Chabalowski and M. J. Frisch, "AB-Initio Calculation of Vibrational Absorption and Circular-Dichroism Spectra Using Density-Functional Force-Fields", *Journal of Physical Chemistry*, Vol. 98, No. 45, pp. 11623–11627, 1994.
165. Gonzalez, C. and H. Schelgel, "Reaction Path Following in Mass-Weighted Internal Coordinates", *Journal of Physical Chemistry*, Vol. 94, No. 14, pp. 5523–5527, 1990.
166. Reed, A. E., R. B. Weinstock and F. Weinhold, "Natural Population Analysis", *The Journal of Chemical Physics*, Vol. 83, No. 2, pp. 735–746, 1985.

167. Pieniazek, S. N., F. R. Clemente and K. N. Houk, "Sources of Error in DFT Computations of C-C Bond Formation Thermochemistries:  $\pi \rightarrow \sigma$  Transformations and Error Cancellation by DFT Methods", *Angewandte Chemie International Edition*, Vol. 47, No. 40, pp. 7746–7749, 2008.
168. Rao, L., H. W. Ke, G. Fu, X. Xu and Y. J. Yan, "Performance of Several Density Functional Theory Methods on Describing Hydrogen-Bond Interactions", *Journal of Chemical Theory and Computation*, Vol. 5, No. 1, pp. 86–96, 2009.
169. Thompson, J. D., C. J. Cramer and D. G. Truhlar, "Predicting Aqueous Solubilities from Aqueous Free Energies of Solvation and Experimental or Calculated Vapor Pressures of Pure Substances", *The Journal of Chemical Physics*, Vol. 119, No. 3, pp. 1661–1670, 2003.
170. Kelly, C. P., C. J. Cramer and D. G. Truhlar, "SM6: A Density Functional Theory Continuum Solvation Model for Calculating Aqueous Solvation Free Energies of Neutrals, Ions, and Solute-Water Clusters", *Journal of Chemical Theory and Computation*, Vol. 1, No. 6, pp. 1133–1152, 2005.
171. Sletten, E. M. and C. R. Bertozzi, "From Mechanism to Mouse: a Tale of Two Bioorthogonal Reactions", *Accounts of Chemical Research*, Vol. 44, No. 9, pp. 666–676, 2011.
172. Huisgen, R., L. Möbius, G. Müller, H. Stangl, G. Szeimies and J. M. Vernon, "1,3-Dipolare Cycloadditionen, XXII. Zur Anlagerung organischer Azide an winkelgespannte Doppelbindungen", *European Journal of Inorganic Chemistry*, Vol. 98, No. 12, pp. 3992–4013, 1965.
173. Gutsmedl, K., C. T. Wirges, V. Ehmke and T. Carell, "Copper-Free "Click" Modification of DNA via Nitrile Oxide– Norbornene 1, 3-Dipolar Cycloaddition", *Organic Letters*, Vol. 11, No. 11, pp. 2405–2408, 2009.
174. Hansell, C. F., P. Espeel, M. M. Stamenovic, I. A. Barker, A. P. Dove, F. E.

- Du Prez and R. K. O'Reilly, "Additive-Free Clicking for Polymer Functionalization and Coupling by Tetrazine–Norbornene Chemistry", *Journal of the American Chemical Society*, Vol. 133, No. 35, pp. 13828–13831, 2011.
175. Watson, W. H., J. Galloy, P. D. Bartlett and A. A. Roof, "Double-Bond Deformation in Two Crystalline Derivatives of syn-Sesquinorbornene (.DELTA. 4a, 8a-octahydro-1, 4, 5, 8-dimethanonaphthalene)", *Journal of the American Chemical Society*, Vol. 103, No. 8, pp. 2022–2031, 1981.
176. Lopez, S. A. and K. Houk, "Alkene Distortion Energies and Torsional Effects Control Reactivities, and Stereoselectivities of Azide Cycloadditions to Norbornene and Substituted Norbornenes", *The Journal of Organic Chemistry*, Vol. 78, No. 5, pp. 1778–1783, 2012.
177. Wang, H. and K. Houk, "Torsional Control of Stereoselectivities in Electrophilic Additions and Cycloadditions to Alkenes", *Chemical Science*, Vol. 5, No. 2, pp. 462–470, 2014.
178. Sakamoto, M., N. Utsumi, M. Ando, M. Saeki, T. Mino, T. Fujita, A. Katoh, T. Nishio and C. Kashima, "Breaking the Symmetry of Axially Chiral N-Aryl-2 (1H)-pyrimidinones by Spontaneous Crystallization", *Angewandte Chemie International Edition*, Vol. 42, No. 36, pp. 4360–4363, 2003.
179. Najahi, E., N. Vanthuyne, F. Nepveu, M. Jean, I. Alkorta, J. Elguero and C. Roussel, "Atropisomerization in N-aryl-2 (1 H)-pyrimidin-(thi) ones: A Ring-Opening/Rotation/Ring-Closure Process in Place of a Classical Rotation around the Pivot Bond", *The Journal of Organic Chemistry*, Vol. 78, No. 24, pp. 12577–12584, 2013.
180. van Zeist, W.-J. and F. M. Bickelhaupt, "The Activation Strain Model of Chemical Reactivity", *Organic Biomolecular Chemistry*, Vol. 8, No. 14, pp. 3118–3127, 2010.

181. Ess, D. H. and K. Houk, "Distortion/Interaction Energy Control of 1, 3-Dipolar Cycloaddition Reactivity", *Journal of the American Chemical Society*, Vol. 129, No. 35, pp. 10646–10647, 2007.
182. Schoenebeck, F., D. H. Ess, G. O. Jones and K. Houk, "Reactivity and Regioselectivity in 1,3-Dipolar Cycloadditions of Azides to Strained Alkynes and Alkenes: a Computational Study", *Journal of the American Chemical Society*, Vol. 131, No. 23, pp. 8121–8133, 2009.
183. Catak, S., M. D'hooghe, N. De Kimpe, M. Waroquier and V. Van Speybroeck, "Intramolecular  $\pi$ - $\pi$  Stacking Interactions in 2-Substituted N, N-Dibenzylaziridinium Ions and Their Regioselectivity in Nucleophilic Ring-Opening Reactions", *The Journal of Organic Chemistry*, Vol. 75, No. 3, pp. 885–896, 2009.
184. Ess, D. H. and K. Houk, "Theory of 1, 3-Dipolar Cycloadditions: Distortion/Interaction and Frontier Molecular Orbital Models", *Journal of the American Chemical Society*, Vol. 130, No. 31, pp. 10187–10198, 2008.
185. van Eis, M. J., F. M. Bickelhaupt, S. van Loon, M. Lutz, A. L. Spek, W. H. de Wolf, W.-J. van Zeist and F. Bickelhaupt, "Tricarbonylchromium Complexes of [5]-and [6] Metacyclophane: an Experimental and Theoretical Study", *Tetrahedron*, Vol. 64, No. 51, pp. 11641–11646, 2008.
186. de Jong, G. T. and F. M. Bickelhaupt, "Transition-State Energy and Position along the Reaction Coordinate in an Extended Activation Strain Model", *ChemPhysChem*, Vol. 8, No. 8, pp. 1170–1181, 2007.
187. Agopcan, S., N. Çelebi Ölçüm, M. N. Üçışık, A. Sanyal and V. Aviyente, "Origins of the Diastereoselectivity in Hydrogen Bonding Directed Diels–Alder Reactions of Chiral Dienes with Achiral Dienophiles: a Computational Study", *Organic Biomolecular Chemistry*, Vol. 9, No. 23, pp. 8079–8088, 2011.



188. Celebi-Olcum, N., A. Sanyal and V. Aviyente, "Understanding the Stereoselection Induced by Chiral Anthracene Templates in Diels–Alder Cycloaddition: A DFT Study", *The Journal of Organic Chemistry*, Vol. 74, No. 6, pp. 2328–2336, 2009.
189. Degirmenci, I., S. Eren, V. Aviyente, B. De Sterck, K. Hemelsoet, V. Van Speybroeck and M. Waroquier, "Modeling the Solvent Effect on the Tacticity in the Free Radical Polymerization of Methyl Methacrylate", *Macromolecules*, Vol. 43, No. 13, pp. 5602–5610, 2010.
190. McGettigan, P. and D. Henry, "Use of non-Steroidal anti-Inflammatory Drugs that Elevate Cardiovascular Risk: an Examination of Sales and Essential Medicines Lists in Low-, Middle-, and High-Income Countries", *PLoS Med*, Vol. 10, No. 2, p. e1001388, 2013.
191. Andreozzi, R., M. Raffaele and P. Nicklas, "Pharmaceuticals in STP Effluents and Their Solar Photodegradation in Aquatic Environment", *Chemosphere*, Vol. 50, No. 10, pp. 1319–1330, 2003.
192. Zhang, N., G. Liu, H. Liu, Y. Wang, Z. He and G. Wang, "Diclofenac Photodegradation under Simulated Sunlight: Effect of Different Forms of Nitrogen and Kinetics", *Journal of Hazardous Materials*, Vol. 192, No. 1, pp. 411–418, 2011.
193. Quintana, J. B., S. Weiss and T. Reemtsma, "Pathways and Metabolites of Microbial Degradation of Selected Acidic Pharmaceutical and their Occurrence in Municipal Wastewater Treated by a Membrane Bioreactor", *Water Research*, Vol. 39, No. 12, pp. 2654–2664, 2005.
194. Sacher, F., F. T. Lange, H.-J. Brauch and I. Blankenhorn, "Pharmaceuticals in Groundwaters: Analytical Methods and Results of a Monitoring Program in Baden-Württemberg, Germany", *Journal of Chromatography A*, Vol. 938, No. 1, pp. 199–210, 2001.

195. Laine, L., L. Goldkind, S. P. Curtis, L. G. Connors, Z. Yanqiong and C. P. Cannon, “How Common is Diclofenac-Associated Liver Injury? Analysis of 17,289 Arthritis Patients in a Long-Term Prospective Clinical Trial”, *The American Journal of Gastroenterology*, Vol. 104, No. 2, pp. 356–362, 2009.
196. Schwaiger, J., H. Ferling, U. Mallow, H. Wintermayr and R. Negele, “Toxic Effects of the non-Steroidal anti-Inflammatory Drug Diclofenac: Part I: Histopathological Alterations and Bioaccumulation in Rainbow Trout”, *Aquatic Toxicology*, Vol. 68, No. 2, pp. 141–150, 2004.
197. Ince, N. H. and I. G. Apikyan, “Combination of Activated Carbon Adsorption with Light-Enhanced Chemical Oxidation via Hydrogen Peroxide”, *Water Research*, Vol. 34, No. 17, pp. 4169–4176, 2000.
198. Suslick, K. S., “Sonochemistry”, *Science*, Vol. 247, No. 4949, pp. 1439–1446, 1990.
199. Ziylan, A. and N. H. Ince, “The Occurrence and Fate of Anti-Inflammatory and Analgesic Pharmaceuticals in Sewage and Fresh Water: Treatability by Conventional and non-Conventional Processes”, *Journal of Hazardous Materials*, Vol. 187, No. 1, pp. 24–36, 2011.
200. Ravina, M., L. Campanella and J. Kiwi, “Accelerated Mineralization of the Drug Diclofenac via Fenton Reactions in a Concentric Photo-Reactor”, *Water Research*, Vol. 36, No. 14, pp. 3553–3560, 2002.
201. Naddeo, V., V. Belgiorno, D. Ricco and D. Kassinos, “Degradation of Diclofenac during Sonolysis, Ozonation and their Simultaneous Application”, *Ultrasonics Sonochemistry*, Vol. 16, No. 6, pp. 790–794, 2009.
202. Ziylan, A., Y. Kolytyn, A. Gedanken and N. H. Ince, “More on Sonolytic and Sonocatalytic Decomposition of Diclofenac using Zero-Valent Iron”, *Ultrasonics Sonochemistry*, Vol. 20, No. 1, pp. 580–586, 2013.

203. Pérez-Estrada, L. A., S. Malato, W. Gernjak, A. Agüera, E. M. Thurman, I. Ferrer and A. R. Fernández-Alba, “Photo-Fenton Degradation of Diclofenac: Identification of Main Intermediates and Degradation Pathway”, *Environmental Science Technology*, Vol. 39, No. 21, pp. 8300–8306, 2005.
204. Hartmann, J., P. Bartels, U. Mau, M. Witter, W. Tümpling, J. Hofmann and E. Nietzsche, “Degradation of the Drug Diclofenac in Water by Sonolysis in Presence of Catalysts”, *Chemosphere*, Vol. 70, No. 3, pp. 453–461, 2008.
205. Martínez, C., M. Fernández, J. Santaballa and J. Faria, “Aqueous Degradation of Diclofenac by Heterogeneous Photocatalysis Using Nanostructured Materials”, *Applied Catalysis B: Environmental*, Vol. 107, No. 1, pp. 110–118, 2011.
206. Vogna, D., R. Marotta, A. Napolitano, R. Andreozzi and M. d’Ischia, “Advanced Oxidation of the Pharmaceutical Drug Diclofenac with UV/H<sub>2</sub>O<sub>2</sub> and Ozone”, *Water Research*, Vol. 38, No. 2, pp. 414–422, 2004.
207. Reddersen, K. and T. Heberer, “Formation of an Artifact of Diclofenac During Acidic Extraction of Environmental Water Samples”, *Journal of Chromatography A*, Vol. 1011, No. 1, pp. 221–226, 2003.
208. Drijvers, D., H. Van Langenhove and V. Herrygers, “Sonolysis of fluoro-, chloro-, bromo- and iodobenzene: a Comparative Study”, *Ultrasonics sonochemistry*, Vol. 7, No. 2, pp. 87–95, 2000.
209. Stavarache, C., B. Yim, M. Vinatoru and Y. Maeda, “Sonolysis of Chlorobenzene in Fenton-type Aqueous Systems”, *Ultrasonics Sonochemistry*, Vol. 9, No. 6, pp. 291–296, 2002.
210. Hofmann, J., U. Freier, M. Wecks and S. Hohmann, “Degradation of Diclofenac in Water by Heterogeneous Catalytic Oxidation with H<sub>2</sub>O<sub>2</sub>”, *Applied Catalysis B: Environmental*, Vol. 70, No. 1, pp. 447–451, 2007.

211. Ziylan, A., S. Dogan, S. Agopcan, R. Kidak, V. Aviyente and N. H. Ince, "Sonochemical Degradation of Diclofenac: Byproduct Assessment, Reaction Mechanisms and Environmental Considerations", *Environmental Science and Pollution Research*, Vol. 21, No. 9, pp. 5929–5939, 2014.
212. Adamo, C. and V. Barone, "Exchange Functionals with Improved Long-Range Behavior and Adiabatic Connection Methods without Adjustable Parameters: The mPW and mPW1PW models", *The Journal of Chemical Physics*, Vol. 108, No. 2, pp. 664–675, 1998.
213. Zhao, Y. and D. G. Truhlar, "Hybrid Meta Density Functional Theory Methods for Thermochemistry, Thermochemical Kinetics, and Noncovalent Interactions: the MPW1B95 and MPWB1K Models and Comparative Assessments for Hydrogen Bonding and van der Waals Interactions", *The Journal of Physical Chemistry A*, Vol. 108, No. 33, pp. 6908–6918, 2004.
214. An, T., Y. Gao, G. Li, P. V. Kamat, J. Peller and M. V. Joyce, "Kinetics and Mechanism of •OH Mediated Degradation of Dimethyl Phthalate in Aqueous Solution: Experimental and Theoretical Studies", *Environmental Science Technology*, Vol. 48, No. 1, pp. 641–648, 2013.
215. Galano, A. and J. R. Alvarez-Idaboy, "Guanosine+ OH Radical Reaction in Aqueous Solution: a Reinterpretation of the UV-vis Data Based on Thermodynamic and Kinetic Calculations", *Organic Letters*, Vol. 11, No. 22, pp. 5114–5117, 2009.
216. Coote, M. L., C. Y. Lin, A. L. Beckwith and A. A. Zavitsas, "A Comparison of Methods for Measuring Relative Radical Stabilities of Carbon-Centred Radicals", *Physical Chemistry Chemical Physics*, Vol. 12, No. 33, pp. 9597–9610, 2010.
217. Degirmenci, I. and M. L. Coote, "Comparison of Thiyl, Alkoxy, and Alkyl Radical Addition to Double Bonds: The Unusual Contrasting Behavior of Sulfur and Oxygen Radical Chemistry", *The Journal of Physical Chemistry A*, Vol. 120, No. 10, pp. 1750–1755, 2016.

218. “US EPA Estimation Programs Interface Suite for Microsoft Windows”, *United States Environmental Protection Agency, Washington DC, USA*, 2008.
219. Scheytt, T., P. Mersmann, R. Lindstädt and T. Heberer, “1-Octanol/Water Partition Coefficients of 5 Pharmaceuticals from Human Medical Care: Carbamazepine, Clofibrac Acid, Diclofenac, Ibuprofen, and Propyphenazone”, *Water, Air, Soil Pollution*, Vol. 165, No. 1, pp. 3–11, 2005.
220. Glaze, W. H. and J.-W. Kang, “Advanced Oxidation Processes. Test of a Kinetic Model for the Oxidation of Organic Compounds with Ozone and Hydrogen Peroxide in a Semibatch Reactor”, *Industrial Engineering Chemistry Research*, Vol. 28, No. 11, pp. 1580–1586, 1989.
221. Glaze, W. H., J.-W. Kang and D. H. Chapin, “The Chemistry of Water Treatment Processes Involving Ozone, Hydrogen Peroxide and Ultraviolet Radiation”, *Ozone: Science Engineering*, Vol. 9, No. 4, pp. 335–352, 1987.
222. Sehested, K., H. Corfitzen, H. Christensen and E. Hart, “Rates of Reaction of O-, OH, and H with Methylated Benzenes in Aqueous Solution. Optical Spectra of Radicals”, *Journal of Physical Chemistry*, Vol. 79, No. 4, pp. 310–315, 1975.
223. Mohan, H. and J. P. Mittal, “Pulse Radiolysis Investigations on Acidic Aqueous Solutions of Benzene: Formation of Radical Cations”, *The Journal of Physical Chemistry A*, Vol. 103, No. 3, pp. 379–383, 1999.
224. Gao, Y., Y. Ji, G. Li and T. An, “Mechanism, Kinetics and Toxicity Assessment of OH-initiated Transformation of Triclosan in Aquatic Environments”, *Water Research*, Vol. 49, pp. 360–370, 2014.
225. Song, W., T. Xu, W. J. Cooper, D. D. Dionysiou, A. A. d. l. Cruz and K. E. O’Shea, “Radiolysis Studies on the Destruction of Microcystin-LR in Aqueous Solution by Hydroxyl Radicals”, *Environmental Science Technology*, Vol. 43, No. 5, pp. 1487–1492, 2009.

226. Michael, I., A. Achilleos, D. Lambropoulou, V. O. Torrens, S. Pérez, M. Petrović, D. Barceló and D. Fatta-Kassinos, “Proposed Transformation Pathway and Evolution Profile of Diclofenac and Ibuprofen Transformation Products During (sono) Photocatalysis”, *Applied Catalysis B: Environmental*, Vol. 147, pp. 1015–1027, 2014.
227. Sein, M. M., M. Zedda, J. Tuerk, T. C. Schmidt, A. Golloch and C. v. Sonntag, “Oxidation of Diclofenac with Ozone in Aqueous Solution”, *Environmental Science Technology*, Vol. 42, No. 17, pp. 6656–6662, 2008.
228. Homlok, R., E. Takács and L. Wojnárovits, “Elimination of Diclofenac from Water using Irradiation Technology”, *Chemosphere*, Vol. 85, No. 4, pp. 603–608, 2011.
229. Salgado, R., V. Pereira, G. Carvalho, R. Soeiro, V. Gaffney, C. Almeida, V. V. Cardoso, E. Ferreira, M. Benoliel and T. Ternes, “Photodegradation Kinetics and Transformation Products of Ketoprofen, Diclofenac and Atenolol in Pure Water and Treated Wastewater”, *Journal of Hazardous Materials*, Vol. 244, pp. 516–527, 2013.
230. Lekkerkerker-Teunissen, K., M. J. Benotti, S. A. Snyder and H. C. Van Dijk, “Transformation of Atrazine, Carbamazepine, Diclofenac and Sulfamethoxazole by Low and Medium Pressure UV and UV/H<sub>2</sub>O<sub>2</sub> Treatment”, *Separation and Purification Technology*, Vol. 96, pp. 33–43, 2012.
231. Poiger, T., H. Buser and M. D. Müller, “Photodegradation of the Pharmaceutical Drug Diclofenac in a Lake: Pathway, Field Measurements, and Mathematical Modeling”, *Environmental Toxicology and Chemistry*, Vol. 20, No. 2, pp. 256–263, 2001.
232. Encinas, S., F. Bosca and M. A. Miranda, “Photochemistry of 2, 6-Dichlorodiphenylamine and 1-Chlorocarbazole, the Photoactive Chromophores of Diclofenac, Meclofenamic Acid and Their Major Photo-products”, *Photochemistry and Photobiology*, Vol. 68, No. 5, pp. 640–645, 1998.

233. Encinas, S., F. Bosca and M. A. Miranda, "Phototoxicity Associated with Diclofenac: a Photophysical, Photochemical, and Photobiological Study on the Drug and Its Photoproducts", *Chemical Research in Toxicology*, Vol. 11, No. 8, pp. 946–952, 1998.
234. Bae, S., D. Kim and W. Lee, "Degradation of Diclofenac by Pyrite Catalyzed Fenton Oxidation", *Applied Catalysis B: Environmental*, Vol. 134, pp. 93–102, 2013.
235. Sarasidis, V. C., K. V. Plakas, S. I. Patsios and A. J. Karabelas, "Investigation of Diclofenac Degradation in a Continuous Photo-catalytic Membrane Reactor. Influence of Operating Parameters", *Chemical Engineering Journal*, Vol. 239, pp. 299–311, 2014.
236. Fang, H., Y. Gao, G. Li, J. An, P.-K. Wong, H. Fu, S. Yao, X. Nie and T. An, "Advanced Oxidation Kinetics and Mechanism of Preservative Propylparaben Degradation in Aqueous Suspension of TiO<sub>2</sub> and Risk Assessment of its Degradation Products", *Environmental Science Technology*, Vol. 47, No. 6, pp. 2704–2712, 2013.
237. An, T., H. Yang, G. Li, W. Song, W. J. Cooper and X. Nie, "Kinetics and Mechanism of Advanced Oxidation Processes (AOPs) in Degradation of Ciprofloxacin in Water", *Applied Catalysis B: Environmental*, Vol. 94, No. 3, pp. 288–294, 2010.
238. An, T., H. Yang, W. Song, G. Li, H. Luo and W. J. Cooper, "Mechanistic Considerations for the Advanced Oxidation Treatment of Fluoroquinolone Pharmaceutical Compounds Using TiO<sub>2</sub> Heterogeneous Catalysis", *The Journal of Physical Chemistry A*, Vol. 114, No. 7, pp. 2569–2575, 2010.
239. Shu, Z., J. R. Bolton, M. Belosevic and M. G. El Din, "Photodegradation of Emerging Micropollutants Using the Medium-Pressure UV/H<sub>2</sub>O<sub>2</sub> Advanced Oxidation Process", *Water Research*, Vol. 47, No. 8, pp. 2881–2889, 2013.

240. Avdeef, A., K. Box, J. Comer, C. Hibbert and K. Tam, "pH-Metric logP 10. Determination of Liposomal Membrane-Water Partition Coefficients of Ionizable Drugs", *Pharmaceutical Research*, Vol. 15, No. 2, pp. 209–215, 1998.
241. Könemann, H., "Quantitative Structure-Activity Relationships in Fish Toxicity Studies Part 1: Relationship for 50 Industrial Pollutants", *Toxicology*, Vol. 19, No. 3, pp. 209–221, 1981.
242. Mayer, P. and F. Reichenberg, "Can Highly Hydrophobic Organic Substances Cause Aquatic Baseline Toxicity and Can They Contribute to Mixture Toxicity?", *Environmental Toxicology and Chemistry*, Vol. 25, No. 10, pp. 2639–2644, 2006.
243. Tay, K. S. and N. Madehi, "Ozonation of Ofloxacin in Water: By-products, Degradation Pathway and Ecotoxicity Assessment", *Science of the Total Environment*, Vol. 520, pp. 23–31, 2015.
244. Saxton, J. E., *The Chemistry of Heterocyclic Compounds, Indoles: the Monoterpene Indole Alkaloids*, Vol. 25, John Wiley Sons, 2009.
245. Southon, I. W. and J. Buckingham, *Dictionary of Alkaloids, with CD-ROM*, CRC Press, 1989.
246. Steyn, P. and R. Vlegaar, "Tremorgenic mycotoxins", *Fortschritte der Chemie organischer Naturstoffe/Progress in the Chemistry of Organic Natural Products*, pp. 1–80, Springer, 1985.
247. Gul, W. and M. T. Hamann, "Indole Alkaloid Marine Natural Products: An Established Source of Cancer Drug Leads with Considerable Promise for the Control of Parasitic, Neurological and Other Diseases", *Life Sciences*, Vol. 78, No. 5, pp. 442–453, 2005.
248. Abele, E., R. Abele, O. Dzenitis and E. Lukevics, "Indole and isatin oximes: Synthesis, reactions, and biological activity.(Review)", *Chemistry of Heterocyclic*



*Compounds*, Vol. 39, No. 1, pp. 3–35, 2003.

249. Sharma, V., P. Kumar and D. Pathak, “Biological Importance of the Indole Nucleus in Recent Years: A Comprehensive Review”, *Journal of Heterocyclic Chemistry*, Vol. 47, No. 3, pp. 491–502, 2010.
250. Kaushik, N. K., N. Kaushik, P. Attri, N. Kumar, C. H. Kim, A. K. Verma and E. H. Choi, “Biomedical Importance of Indoles”, *Molecules*, Vol. 18, No. 6, pp. 6620–6662, 2013.
251. Balon, M., M. C. Carmona, M. A. Munoz and J. Hidalgo, “The Acid-Base Properties of Pyrrole and its Benzolog Indole and Carbazole - A Reexamination from the Excess Acidity Method”, *Tetrahedron*, Vol. 45, No. 23, pp. 7501–7504, 1989.
252. Tewari, V. P. and A. K. Srivastava, “Calculation of HOMO Energy and Heat of Formation of Conjugated Systems Containing Nitrogen AND Oxygen”, *Indian Journal of Chemistry Section A-Inorganic Bio-Inorganic Physical Theoretical Analytical Chemistry*, Vol. 26, No. 6, pp. 449–452, 1987.
253. Carmona, C., J. Hidalgo, E. S. Marcos, R. R. Pappalardo, M. Munoz and M. Balon, “AM1 Study of a Beta-Carboline Set .2. Pyrrole-N Deprotonated Species”, *Journal of the Chemical Society-Perkin Transactions 2*, pp. 1881–1884, 1990.
254. Laws, A. P. and R. Taylor, “The Quantitative Electrophilic Reactivity of Annulenes .2. Partial Rate Factors for Hydrogen-Exchange of Azulene, Cycl 3,2,2 Azine, Indolizine, N-Methylisindole, Indole, And Pyrrolo 2,1-B Thiazole, and Attempted Exchange in Trans-9,10-Dimethyldihydropyrene - The Dramatic Effect of Creating Aromaticity in the Transition-State for Electrophilic Substitution, and the Importance of Valence Bond Theory”, *Journal of the Chemical Society-Perkin Transactions 2*, pp. 591–597, 1987.
255. Mancini, I., G. Guella, F. Pietra, C. Debitus and J. Waikedre, “From Inactive

- Nortopsentin D, a Novel bis(indole) Alkaloid Isolated from the Axinellid Sponge *Dragmacidon* sp. from Deep Waters South of New Caledonia, to a Strongly Cytotoxic Derivative”, *Helvetica Chimica Acta*, Vol. 79, No. 8, pp. 2075–2082, 1996.
256. Carbone, A., M. Pennati, B. Parrino, A. Lopergolo, P. Barraja, A. Montalbano, V. Spano`, S. Sbarra, V. Doldi and M. De Cesare, “Novel 1 H-pyrrolo [2, 3-b] Pyridine Derivative Nortopsentin Analogues: Synthesis and Antitumor Activity in Peritoneal Mesothelioma Experimental Models”, *Journal of Medicinal Chemistry*, Vol. 56, No. 17, pp. 7060–7072, 2013.
257. Alvarado, S., B. F. Roberts, A. E. Wright and D. Chakrabarti, “The Bis-(Indolyl) Imidazole Alkaloid Nortopsentin a Exhibits Antiplasmodial Activity”, *Antimicrobial Agents and Chemotherapy*, Vol. 57, No. 5, pp. 2362–2364, 2013.
258. Gu, X.-H., X.-Z. Wan and B. Jiang, “Syntheses and Biological Activities of bis (3-indolyl) Thiazoles, Analogues of Marine bis (Indole) Alkaloid Nortopsentins”, *Bioorganic Medicinal Chemistry Letters*, Vol. 9, No. 4, pp. 569–572, 1999.
259. Chan, W., D. Ho, C. Lau, K. Wat, Y. Kong, K. Cheng, T. Wong and T. Chan, “Structure Function Relationship Study of Yuehchukene. I. Anti-Implantation and Estrogenic Activities of Substituted Yuehchukene Derivatives”, *European Journal of Medicinal Chemistry*, Vol. 26, No. 4, pp. 387–394, 1991.
260. Ansari, N. H. and B. C. Söderberg, “Short Syntheses of the Indole Alkaloids Alocasin A, Scalaridine A, and Hyrtinadine AB”, *Tetrahedron*, Vol. 72, No. 29, pp. 4214–4221, 2016.
261. Kim, S. H. and J. Sperry, “Synthesis of Scalaridine A”, *Tetrahedron Letters*, Vol. 56, No. 43, pp. 5914–5915, 2015.
262. Netz, N. and T. Opatz, “Marine Indole Alkaloids”, *Marine Drugs*, Vol. 13, No. 8, pp. 4814–4914, 2015.

263. Lee, Y., D. Lee, H. S. Rho, V. B. Krasokhin, H. J. Shin, J. S. Lee and H. Lee, "Cytotoxic 5-[U+2010]Hydroxyindole Alkaloids from the Marine Sponge *Scalari-spongia* sp", *Journal of Heterocyclic Chemistry*, Vol. 50, No. 6, pp. 1400–1404, 2013.
264. Liu, Q. D., L. Thorne, I. Kozin, D. T. Song, C. Seward, M. D'Iorio, Y. Tao and S. N. Wang, "New Red-Orange Phosphorescent/Electroluminescent Cycloplati-nated Complexes of 2,6-bis(2'-indolyl)pyridine", *Journal of the Chemical Society-Dalton Transactions*, , No. 16, pp. 3234–3240, 2002.
265. Chao, W.-R., D. Yean, K. Amin, C. Green and L. Jong, "Computer-Aided Ra-tional Drug Design: a Novel Agent (SR13668) Designed to Mimic the Unique Anticancer Mechanisms of Dietary Indole-3-Carbinol to Block Akt Signaling", *Journal of Medicinal Chemistry*, Vol. 50, No. 15, pp. 3412–3415, 2007.
266. Palmieri, A., M. Petrini and R. R. Shaikh, "Synthesis of 3-substituted Indoles via Reactive Alkylideneindolenine Intermediates", *Organic Biomolecular Chemistry*, Vol. 8, No. 6, pp. 1259–1270, 2010.
267. Bandini, M. and A. Eichholzer, "Catalytic Functionalization of Indoles in a New Dimension", *Angewandte Chemie International Edition*, Vol. 48, No. 51, pp. 9608–9644, 2009.
268. Saracoglu, N., "Functionalization of Indole and Pyrrole Cores via Michael-type Additions", *Bioactive Heterocycles V*, pp. 1–61, 2007.
269. Mahadevan, A., H. Sard, M. Gonzalez and J. C. McKew, "A General Method for C3 Reductive Alkylation of Indoles", *Tetrahedron Letters*, Vol. 44, No. 24, pp. 4589–4591, 2003.
270. Rizzo, J. R., C. A. Alt and T. Y. Zhang, "An Expedient Synthesis of 3-substituted Indoles via Reductive Alkylation with Ketones", *Tetrahedron Letters*, Vol. 49, No. 48, pp. 6749–6751, 2008.

271. Lin, X., S. Cui and Y. Wang, "Mild and Efficient Synthesis of bis[U+2010]Indolylmethanes Catalyzed by Tetrabutylammonium Tribromide", *Synthetic Communications*, Vol. 36, No. 21, pp. 3153–3160, 2006.
272. Praveen, P., P. Parameswaran and M. Majik, "Bis (indolyl) Methane Alkaloids: Isolation, Bioactivity, and Syntheses", *Synthesis*, Vol. 47, No. 13, pp. 1827–1837, 2015.
273. Shiri, M., M. A. Zolfigol, H. G. Kruger and Z. Tanbakouchian, "Bis-and trisindolylmethanes (BIMs and TIMs)", *Chemical Reviews*, Vol. 110, No. 4, pp. 2250–2293, 2009.
274. Wu, L., H. Huang, P. Dang, Y. Liang and S. Pi, "Construction of Benzo [a] Carbazole Derivatives via Diels–Alder Reaction of Arynes with Vinylindoles", *RSC Advances*, Vol. 5, No. 79, pp. 64354–64357, 2015.
275. Cavdar, H. and N. Saraçoğlu, "Synthesis of New 2-Vinylation Products of Indole via a Michael-Type Addition Reaction with Dimethyl Acetylenedicarboxylate and Their Diels–Alder Reactivity as Precursors of New Carbazoles", *The Journal of Organic Chemistry*, Vol. 71, No. 20, pp. 7793–7799, 2006.
276. Kuo, C.-W., A. Konala, L. Lin, T.-T. Chiang, C.-Y. Huang, T.-H. Yang, V. Kavala and C.-F. Yao, "Synthesis of benzo [a] carbazole Derivatives from 3-ethylindoles by Exploiting the Dual Character of Benzoquinone as an Oxidizing Agent and Dienophile", *Chemical Communications*, Vol. 52, No. 50, pp. 7870–7873, 2016.
277. Kornblum, N. and H. E. DeLaMare, "The Base Catalyzed Decomposition of a Dialkyl Peroxide", *Journal of the American Chemical Society*, Vol. 73, No. 2, pp. 880–881, 1951.
278. Kelly, D. R., H. Bansal and J. G. Morgan, "The Mechanism of the Tertiary Amine Catalysed Isomerisation of Endoperoxides to Hydroxyketones: Synthesis and Chemistry of the Intermediate Postulated in the Peroxide Attack Mecha-

- nism”, *Tetrahedron Letters*, Vol. 43, No. 51, pp. 9331–9333, 2002.
279. Staben, S. T., X. Linghu and F. D. Toste, “Enantioselective Synthesis of  $\alpha$ -hydroxyenones by Chiral Base-Catalyzed Kornblum DeLaMare Rearrangement”, *Journal of the American Chemical Society*, Vol. 128, No. 39, pp. 12658–12659, 2006.
280. Cohen, R., C. R. Graves, S. T. Nguyen, J. M. Martin and M. A. Ratner, “The Mechanism of Aluminum-Catalyzed Meerwein–Schmidt–Ponndorf–Verley Reduction of Carbonyls to Alcohols”, *Journal of the American Chemical Society*, Vol. 126, No. 45, pp. 14796–14803, 2004.
281. Graves, C. R., K. A. Scheidt and S. T. Nguyen, “Enantioselective MSPV Reduction of Ketimines Using 2-Propanol and (BINOL) Al(III)”, *Organic Letters*, Vol. 8, No. 6, pp. 1229–1232, 2006.
282. Pratt, E. F. and L. W. Botimer, “Disproportionative Condensations. IV. The 3-Alkylation of Indoles by Primary and Secondary Alcohols<sup>1</sup>”, *Journal of the American Chemical Society*, Vol. 79, pp. 5248–5250, 1957.
283. Han, X. and J. Wu, “Redox Chain Reaction—Indole and Pyrrole Alkylation with Unactivated Secondary Alcohols”, *Angewandte Chemie International Edition*, Vol. 52, No. 17, pp. 4637–4640, 2013.
284. Chen, S., Y. Liao, F. Zhao, H. Qi, S. Liu and G.-J. Deng, “Palladium-Catalyzed Direct Arylation of Indoles with Cyclohexanones”, *Organic Letters*, Vol. 16, No. 6, pp. 1618–1621, 2014.
285. Taheri, A., B. Lai, C. Cheng and Y. Gu, “Brønsted Acid Ionic Liquid-Catalyzed Reductive Friedel–Crafts Alkylation of Indoles and Cyclic Ketones without Using an External Reductant”, *Green Chemistry*, Vol. 17, No. 2, pp. 812–816, 2015.